2019 SUMMER RESEARCH PROGRAM FOR HIGH SCHOOL JUNIORS

AT THE

UNIVERSITY OF ROCHESTER'S

LABORATORY FOR LASER ENERGETICS

STUDENT RESEARCH REPORTS

PROGRAM DIRECTOR

Dr. R. Stephen Craxton

August 2021 **Lab Report 430**

2019 SUMMER RESEARCH PROGRAM FOR HIGH SCHOOL JUNIORS

AT THE

UNIVERSITY OF ROCHESTER'S

LABORATORY FOR LASER ENERGETICS

STUDENT RESEARCH REPORTS

PROGRAM DIRECTOR

Dr. R. Stephen Craxton

LABORATORY FOR LASER ENERGETICS
University of Rochester
250 East River Road
Rochester, NY 14623-1299

During the summer of 2019, 14 students from Rochester-area high schools participated in the Laboratory for Laser Energetics' Summer High School Research Program. The goal of this program is to excite a group of high school students about careers in the areas of science and technology by exposing them to research in a state-of-the-art environment. Too often, students are exposed to "research" only through classroom laboratories, which have prescribed procedures and predictable results. In LLE's summer program, the students experience many of the trials, tribulations, and rewards of scientific research. By participating in research in a real

environment, the students often become more excited about careers in science and technology. In addition, LLE gains from the contributions of the many highly talented students who are attracted to the program.

The students spent most of their time working on their individual research projects with members of LLE's scientific staff. The projects were related to current research activities at LLE and covered a broad range of areas of interest including experimental diagnostic development, computer modeling of implosion physics, cryogenic target characterization, experimental design, irradiation uniformity, physical chemistry, and optical materials characterization. The students, their high schools, their LLE supervisors, and their project titles are listed in Table I. Their written reports are collected in this volume. By working through several iterations of their project reports, incorporating feedback from their supervisors and the Program Director, the students experience most of the steps involved in preparing a scientific paper for publication.

The students attended weekly seminars on technical topics associated with LLE's research. Topics this year included laser physics, fusion, fission, pulsed power, holography, and LLE's cryogenic target program. The students also received safety training, learned how to give scientific presentations, and were introduced to LLE's resources, especially the computational facilities.

The program culminated on 28 August with the "High School Student Summer Research Symposium," at which the students presented the results of their research to an audience including parents, teachers, and LLE staff. Each student spoke for approximately ten minutes and answered questions. At the symposium LLE presented its 23rd annual William D. Ryan Inspirational Teacher Award. The recipient this year was Mrs. Rebecca Berardino, a mathematics teacher at Barker Road Middle School in Pittsford. This award honors a teacher, nominated by alumni of the

LLE program, who has inspired outstanding students in the areas of science, mathematics, and technology. Mrs. Berardino was nominated by Margaret Rudnick, a participant in the 2018 Summer Program.

A total of 391 high school students have participated in the program from its inception in 1989 through 2019. The students in 2019 were selected from just over 40 applicants. Each applicant submitted an essay describing his or her interests in science and technology, a copy of his or her transcript, and a letter of recommendation from a science or math teacher.

In the past, several participants of this program have gone on to become scholars (formerly known as "semifinalists") and finalists in the prestigious Regeneron (formerly Intel) Science Talent Search. This tradition of success continued this year with the selection of Simon Narang as one of the 300 Regeneron Scholars chosen from nearly 2000 applicants nationwide. In addition, four participants in the 2019 program (Ji-Mi Jang, Simon Narang, Henry Berger, and Hanna Wiandt) were selected as finalists in the InspoScience Research and Innovation Competition (2020 Virtual Edition), which attracted over 400 entrants from the U.S., Canada, and Mexico.

LLE plans to continue this program in future years. The program is strictly for students from Rochester-area high schools who have just completed their junior year. Application information is mailed to schools and placed on the LLE web site in January with an application deadline near the middle of March. For more information about the program, please contact Dr. R. Stephen Craxton at LLE.

Table I: High School Students and Projects—Summer 2019.

Name	High School	Supervisor	Project Title
Henry Berger	Brighton	C. J. Forrest	Design of a Single-Hit Neutron Spectrometer for D–D Fusion
Adelyn Carney	Webster Schroeder	H. G. Rinderknecht	Optimization of X-Ray Prepulse Geometry for Imprint Mitigation in Directly Driven Implosions
Ji-Mi Jang	Pittsford Mendon	T. Z. Kosc	Micro-Raman Spectroscopy of Silica and Hafnia Laser Damage Sites
Christopher "Jude" Kukla	Pittsford Mendon	F. J. Marshall and S. T. Ivancic	Evaluation of Fresnel Zone Plate X-Ray Imagers for Inertial Confinement Fusion Applications
Michele Lin	Attica	M. McCluskey and R. Boni	A Comparative Study of the Effects of Methanol and Ethanol Solutions on the Bulk Etch Rate of CR-39
Anthony Mazzacane	Pittsford Mendon	P. B. Radha, O. M. Mannion, and S. Miller	Using *IRIS3D* to Simulate the Effects of Smoothing by Spectral Dispersion on Cryogenic Implosions
George Morcos	Rush Henrietta	K. L. Marshall	Glassy Liquid Crystals Based on Natural Products for High-Peak-Power Laser Optics
Adam Mroueh	Pittsford Sutherland	D. Broege	Schlieren Diagnostic for the Imaging of Thermal Turbulence
Ka-Hyun Nam	Brighton	C. Fagan and W. T. Shmayda	Comparative Analysis of Oxygen Uptake in Nickel and Copper-Zinc Beds
Simon Narang	Pittsford Sutherland	M. D. Wittman and D. Bredesen	Modeling for Direct-Drive Fusion Implosions: Cryogenic Target Filling at Arbitrary Viewing Angles and Yield Prediction
Max Neiderbach	Geneseo	M. A. Sharpe, V. Anand, and R. Peck	Enhancements to the Calorimetric Measurement System on the OMEGA Laser
Stephen Rosa	Eastridge	W. T. Shmayda and M. D. Sharpe	Investigations of the Hydrogen-Palladium and Deuterium-Palladium Systems
William Wang	Pittsford Sutherland	R. S. Craxton	Development of a Beam Configuration for the SG4 Laser to Support both Direct and Indirect Drive
Hanna Wiandt	Pittsford Mendon	R. S. Craxton	Optimization of the Uniformity of 12-Quad Direct-Drive Targets for the National Ignition Facility

Acknowledgment

This material is based upon work supported by the Department of Energy National Nuclear Security Administration under Award Number DE-NA0003856, the University of Rochester, and the New York State Energy Research and Development Authority.

This report was prepared as an account of work sponsored by an agency of the U.S. Government. Neither the U.S. Government nor any agency thereof, nor any of their employees,

Design of a Single-Hit Neutron Spectrometer for D-D Fusion

Henry Berger

Brighton High School

LLE Advisor: Chad Forrest

February 2020

Laboratory for Laser Energetics

University of Rochester

1 Abstract

A neutron spectrometer was designed and simulated for use with 2.45 MeV neutrons from fusion reactions with durations beyond the limits of current modes of time-of-flight-based spectroscopy. This diagnostic will be used to infer the apparent temperature of fusing ions. The spectrometer consists of two parts: a deuterated plastic converter foil, in which an incident neutron can transfer its energy to a deuteron, and a silicon complementary metal-oxide-semiconductor (CMOS) chip that measures the energy of deuterons. The shape of the observed deuteron energy spectrum was found to be strongly predictive of the shape of the incident neutron energy spectrum, enabling the determination of the fusing particles' apparent thermal energy. Many design parameters, including the converter's material, thickness, and distance from the detector, were optimized in order to maximize the detection rate and energy resolution. Simulations were used to determine the range of neutron yields and ion temperatures for which the spectrometer would be effective. The neutron yield at FuZE, the reactor for which the spectrometer was designed, is too low for the spectrometer to function, but other existing fusion reactors, such as JET, have sufficient neutron yields. A spectrometer based on this work will be built at LLE.

2 Introduction

2.1 Nuclear fusion

Nuclear fusion is the process by which two nuclei combine to form a single nucleus. All nuclei have positive charge, so fusion requires overcoming the Coulombic repulsion between the two nuclei. Once the two nuclei move close enough together, a nuclear force dominates, causing the nuclei to fuse. This effect is shown in Figure 1.

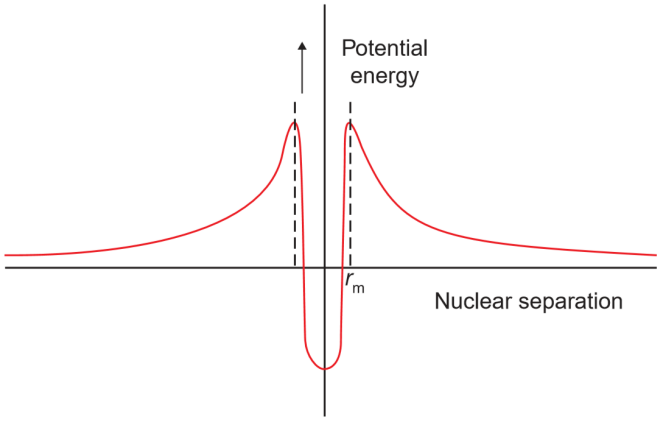

Figure 1: *Potential energy vs. separation for two positively charged nuclei. Above r_m, the Coulombic force is dominant, causing the two nuclei to repel. At distances less than r_m, the nuclear attraction exceeds the Coulombic repulsion, causing the two nuclei to fuse.*[1]

Most fusion research uses deuterium (hydrogen with one neutron, abbreviated D), often in combination with tritium (hydrogen with two neutrons, abbreviated T) or helium-3 (helium with only one neutron, abbreviated ^{3}He). Reactions with these isotopes are preferred because they have relatively high cross-sections, or likelihoods of occurrence. The three most likely candidates for fusion reactions are:

- D-D Fusion: $D + D \rightarrow {}^3He + n$ (2.45 MeV)
- D-T Fusion: $D + T \rightarrow {}^4He + n$ (14.1 MeV)
- D-^{3}He Fusion: $D + {}^3He \rightarrow {}^4He + p^+$ (14.7 MeV),

where n represents a neutron and p^+ represents a proton.[1]

The cross-section of a reaction depends on the energy of the fusing particles. If the ions have too little energy, they cannot overcome the Coulombic repulsion. If the ions have too much energy, they move so quickly that they are less likely to fuse. The dependence of cross-section on ion energy is shown in Figure 2.

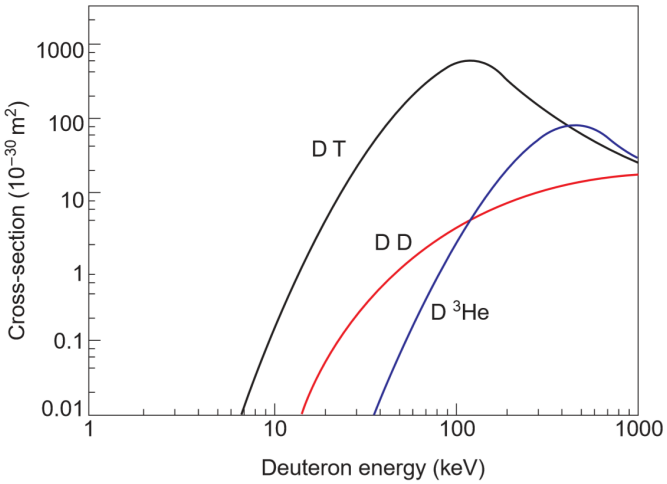

Figure 2: *Cross-sections of common fusion pathways vs. deuteron energy. The cross-section measures the probability of a fusion reaction occurring. Specifically, if the fusing ions were solid spheres that fuse whenever they touch, the cross-section would be their geometrical cross-section. Larger cross-sections indicated a greater probability of fusion.*[1]

2.2 Nuclear fusion reactors

Controlled nuclear fusion requires confining a plasma to a limited volume for enough time for fusion to occur. Nuclear fusion reactors are classified as either inertial confinement fusion (ICF) or magnetic confinement fusion (MCF), depending on the method of confining the plasma.

In ICF, a small capsule of fuel is compressed by a short, intense burst of radiation. The ablation of the outside of the capsule forces the contents inward, and fusion occurs at extremely high pressure and density. The fusion ends when the power released by the fusion causes the fuel to expand to a greater volume and lower density. Because only the fuel's inertia slows the expansion of the fuel, the duration of fusion is very

short, on the order of nanoseconds. Most ICF facilities, such as the National Ignition Facility (NIF) and the OMEGA facility, use laser pulses to compress the capsules.[1]

MCF uses magnetic fields to confine the fusing plasma. Current is passed through a plasma, generating a magnetic field that compresses the plasma. The magnetic field produced by the plasma is often enhanced by external magnets. Because a magnetic field confines the plasma, MCF reactors can maintain the temperature and density required for fusion for longer durations than ICF reactors can achieve. Many MCF reactors, such as the Joint European Torus (JET), use a toroidal design called a tokamak.[1] The spectrometer described in this work is intended for use at the Fusion Z-Pinch Experiment (FuZE), an experimental fusion reactor located at the University of Washington, Seattle. The reactor at FuZE is a variant of MCF called a Z-pinch reactor, in which the shape of the fusing plasma is linear, not toroidal.[2]

2.3 Neutron spectroscopy

Ion temperature directly affects the likelihood of fusion, so ion temperature is one of the most important diagnostics for evaluating how close a reactor is to achieving a sustained fusion reaction. A common method of determining the ion temperature of a fusing plasma is to analyze the neutron spectrum produced by the plasma. The temperature determined from the neutron spectrum is averaged over the entire time and volume of fusion, and it is also affected by which neutrons are able to escape the reactor. For this reason, this temperature is called the apparent, or neutron-averaged, temperature, as opposed to the true thermal temperature. The true thermal temperature of the fusing plasma varies with time and space and is more difficult to measure, so most diagnostics instead measure the apparent temperature.

The neutron spectrum produced by a plasma with ion temperature T_i is given by

$$f(E_n)dE_n = dE_n \exp\left[-\frac{(E_n - \langle E_n \rangle)^2}{\left(\frac{4m_n T_i \langle E_n \rangle}{m_n + m_\alpha}\right)}\right], \tag{1}$$

where E_n is neutron energy; $f(E_n)dE_n$ is the relative probability density of the neutron spectrum at E_n; $\langle E_n \rangle$ is the mean energy, which varies slightly based on T_i; m_n is the mass of a neutron; and m_α is the mass of the other particle produced by the reaction, which is a ^3He nucleus in the case of D-D fusion.[3] This is a Gaussian function, of the form

$$f(x)dx = \frac{dx}{\sigma\sqrt{2\pi}} \exp\left[-\frac{(x - \bar{x})^2}{2\sigma^2}\right].$$

It follows that the standard deviation, σ, is related to the temperature by

$$2\sigma^2 = \frac{4m_n T_i \langle E_n \rangle}{m_n + m_\alpha}, \tag{2}$$

and thus

$$T_i = \frac{\sigma^2 \left(m_n + m_\alpha\right)}{2 m_n \langle E_n \rangle}. \tag{3}$$

As a result, the apparent temperature can be inferred from knowledge of the σ and $\langle E_n \rangle$ of the neutron spectrum. Two of the most common methods of measuring the neutron spectrum are time-of-flight spectroscopy and charged particle spectrometry.[4]

Time-of-flight spectroscopy determines neutron energy by measuring the time taken for a neutron to travel a known distance. Dividing the distance by the time yields the neutron's velocity, which can be used to determine its energy. Time-of-flight measurement relies upon precise knowledge of the time and location at which neutrons are generated. As a result, time-of-flight spectroscopy is often used with fusion reactors that have very small targets that fuse over very short intervals. ICF reactors primarily use time-of-flight neutron spectroscopy.

Charged particle spectrometry, by contrast, detects neutron energy more indirectly. Neutrons hit a converter foil, where they produce charged particles in recoil reactions. The energy of the charged particle can be used to determine the energy of the incident neutron. The method of measuring the energy of the charged particle varies. The Magnetic Recoil Spectrometer (MRS), at the NIF and OMEGA facilities, uses a powerful magnet that bends the paths of protons and deuterons by angles dependent on their velocities. For high accuracy, charged particle spectrometers require very high yields, because they have low detection rates. For example, the MRS detects less than 1 out of every 10^9 neutrons created in the fusion volume.[5]

2.4 FuZE

The ion temperature at FuZE is estimated to be $1 - 2\ keV$.[2] However, a more precise measurement is difficult, because the long duration and low neutron yield of FuZE complicate the use of existing neutron spectrometers. FuZE uses D-D fusion, so the spectrometer was designed for the 2.45 MeV neutrons produced by D-D fusion.

FuZE has a fusion duration of approximately 5 μs.[2] A conventional time-of-flight spectrometer at a distance of around 10 m must know the time of flight to within a few picoseconds in order to make an accurate estimate of temperature.[6] Therefore, microseconds of uncertainty in the time of generation of a neutron make conventional neutron time-of-flight spectrometry extremely challenging. It might be possible to use a ^3He start/stop gate to measure the time of generation of each neutron, but such a method would be very difficult. With regard to charged-particle spectrometry, the yield at FuZE is on the order of 10^5 neutrons per pulse over 4π steradians.[2] This is multiple orders of magnitudes too low for the use of spectrometers like the MRS, with detection rates on the order of 10^{-9}. The spectrometer developed in this work was designed to accomodate the long duration and low yield of FuZE.

3 Design of the spectrometer

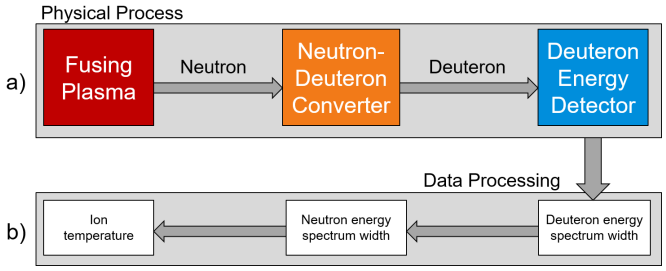

Figure 3: *Schematic of the neutron spectroscopy approach. a) The physical process. b) The post-processing of the data.*

The spectrometer investigated in this project uses a design similar to that of other charged particle spectrometers. First, incident neutrons encounter a converter foil. Neutrons collide with atoms in the foil, producing charged particles. Deuterated plastic, which produces deuterons when bombarded by neutrons, was chosen as the material for the converter foil, for reasons that will be discussed below. The deuterons then leave the foil and hit an energy detector, which registers the deuteron energy. The width of the deuteron energy distribution is then used to calculate the width of the neutron energy spectrum, which is used to calculate the apparent temperature of the fusing ions. This process is shown schematically in Figure 3 and physically in Figure 5 below.

The deuteron energy detector was chosen to be Icarus, a high-speed complementary metal-oxide-semiconductor (hCMOS) chip produced by Sandia National Laboratories, as shown in Figure 4(a). Icarus consists of a 9 μm-thick layer of silicon, which is divided into a 512×1024 array of pixels.[7] As deuterons pass through the silicon sheet, they deposit energy, which is converted into an electrical pulse. The sensor measures the height of this pulse, which can be used to determine the energy of the deuteron. The chip detects the energy of individual deuterons, hence the classification of the spectrometer as a single-hit spectrometer. Icarus has a frame duration of 1.5 ns,[7] so if two deuterons hit the same pixel of the chip within 1.5 ns, they will be counted as a single deuteron that creates a larger pulse. In the conditions examined in this work, the deuteron flux was low enough that double hits were extremely unlikely.

The Icarus chip is too thin to fully stop incident deuterons. The rate of energy loss, $\frac{-dE}{dx}$, of a particle in silicon is dependent on the particle's energy, E, by

$$\frac{-dE}{dx} = \frac{C_1}{E}\left[\ln\left(\frac{E}{C_2 - E}\right) + C_3 - \frac{E}{C_2}\right], \tag{4}$$

where C_1, C_2, and C_3 are constant with respect to E.[8] This relation is dominated by the $\frac{1}{E}$ term, so the higher the energy of the particle, the less energy it deposits. In the range of $1 - 2.5\ MeV$, deuterons deposit approximately $0.1 - 0.25\ MeV$. The relationship between deuteron energy and deposited energy is show in

Figure 4(b).

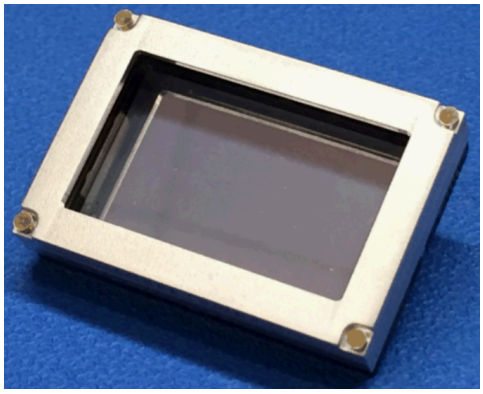

(a) The Icarus hCMOS chip, produced by Sandia National Laboratories, which was chosen as the deuteron detector.

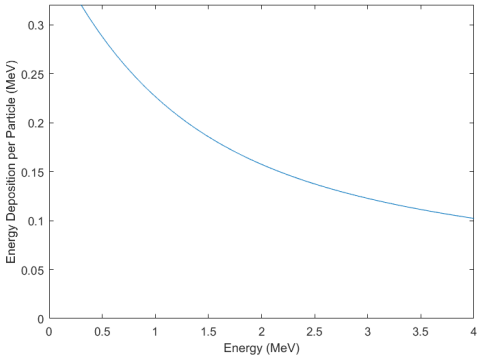

(b) Energy deposition of deuterons in the 9 μm silicon layer of Icarus, as predicted by Eq. 4. MCNP simulations confirmed these predictions. Deuterons with energies below approximately 0.3 MeV (not shown) deposit all their energy and do not escape the surface. This is called ranging out.

Figure 4: *The Icarus hCMOS chip, and the energy deposition of deuterons in the chip.*

4 Initial optimization of the spectrometer design

The optimization of the spectrometer design examined four characteristics of the spectrometer, as shown in Figure 5:

- The maximum observable scattering angle, θ_{max}. This is the maximum angle between the velocity of a deuteron hitting the detector surface and the velocity of the incident neutron that produced the deuteron. The maximum scattering angle was controlled by changing the distance between the converter foil and detector surface, labeled d in Figure 5.
- The material of the converter foil.
- The mass thickness, $\langle \rho l \rangle$, of the converter foil, which is the product of its density and thickness.
- The configuration of the detector surface relative to the converter foil. Figure 5 shows a planar configuration, which is optimal.

Due to dependencies of the different characteristics on each other, they were optimized in pairs. The converter foil material and the detector surface configuration were optimized in combination, and then the mass thickness of the converter foil and the maximum scattering angle were optimized in combination. All optimization of the spectrometer was performed using simulations using Monte Carlo N-Particle Code (MCNP).[9]

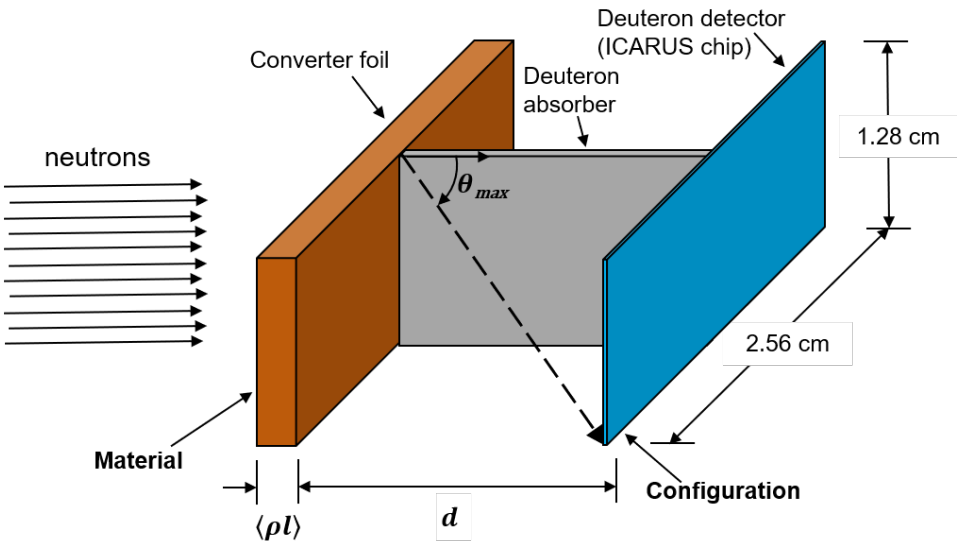

Figure 5: *Design of the spectrometer. The four parameters investigated were the maximum observable scattering angle, θ_{max}, the material of the converter foil, the mass thickness of the converter foil, $\langle \rho l \rangle$, and the configuration of the detector relative to the converter foil. The Icarus chip, shown here as a single detector, consists of 2^{19} independent pixels, each capable of detecting individual deuterons. The deuteron absorber is discussed in Section 4.3.*

4.1 Configuration of detector(s) around the converter

The spectrometer was originally designed as an array of macropixels, with each macropixel consisting of a converter foil and detector surface. The term macropixel is used to differentiate from the pixels of Icarus, which are contained within the macropixels. The detector surface could be configured in multiple different ways relative to the converter foil. The macropixels are arranged along the plane normal to the direction of neutron travel (henceforth the detection plane), so the ideal macropixel arrangement would maximize neutron detection while minimizing the area of the detection plane that is occupied. The following four arrangements were considered, as shown in Figure 6.

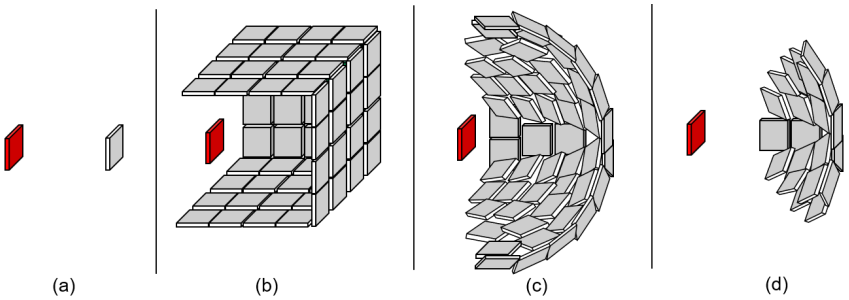

Figure 6: *The four arrangements considered. a) Planar. b) Rectangular prismic. c) Hemispherical. d) Spherical cap.*

1. **Planar.** In this arrangement, the detector surface is planar and is equal in shape and area to the converter foil.

2. **Rectangular prismic.** The converter foil and detector surface form a rectangular prism, where the converter foil is one base and the detector surface comprises the other five faces.
3. **Hemispherical.** The detector surface forms a hemisphere around the converter foil.
4. **Spherical cap.** The detector surface forms a section of a sphere, with the converter foil at its center.

All four arrangements are, in essence, variants of the spherical cap arrangement. A spherical cap with a large angle is a hemisphere; a spherical cap with a small angle approaches the planar arrangment. The rectangular prismic and hemispherical arrangements both capture 2π steradians of deuterons, so they have no relevant differences. Therefore, an examination of spherical cap arrangements with different maximum angles covered all cases.

The space-efficiency of each arrangement depends on how many particles the arrangement can detect. This depends on the angular distribution of the charged particles produced by the converter foil, which in turn depends on the material of the converter foil. For this reason, arrangements were considered in combination with materials.

4.2 Material of the converter foil

The purpose of the converter foil is to produce detectable charged particles when bombarded with neutrons. Therefore, the ideal converter foil material would produce as many charged particles as possible per incident neutron. Five materials were considered, as shown in Table 1.

Table 1: *Materials Investigated*

Converter Foil Material	**Charged Particle Produced**
Hydrogen (H_2)	Proton (p^+)
Plastic (CH_2)	Proton (p^+)
Deuterium (D_2)	Deuteron (np^+, or d^+)
Deuterated plastic (CD_2)	Deuteron (np^+, or d^+)
Helium-3 (^3He)	Helion (np_2^{2+}, or $^3He^{2+}$)

Each material has a different cross-section for charged particle-producing reactions, meaning that it produces different numbers of charged particles at each angle. To determine the ideal material and detector configuration, each material's performance was simulated with spherical cap configurations with central angles ranging from 2.5° to 90°. The simulations tracked the number of charged particles detected by the detector surface, divided by the area of the detector plane occupied by the detector surface. The simulation used a very thin converter foil, so that the charged particles would experience minimal energy loss while escaping the foil. The results are shown in Figure 7.

The simulations did not take into account any bonds between atoms. Therefore, CH_2 and CD_2 produced exactly 2/3 as many charged particles as H_2 and D_2, respectively. The plastics CH_2 and CD_2 are both solids

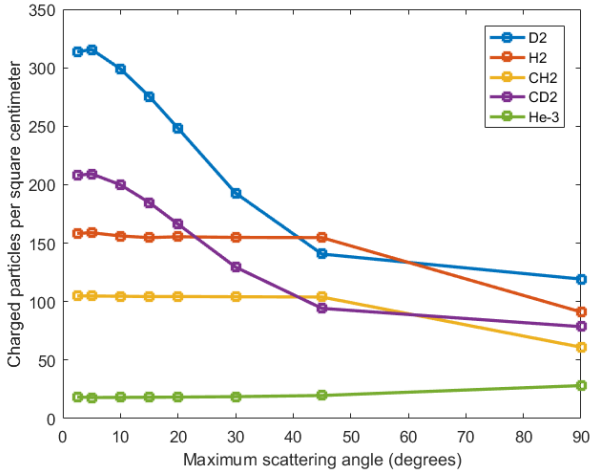

Figure 7: *Space-efficiency of spherical cap configurations for different angles and materials. The detection rate per unit area depends upon the number density of the atoms of the material, the number of incident neutrons, and the distance between the converter foil and the detector surface. These parameters were* 0.1 mol/cm^3, 10^7 *neutrons, and* 1 cm, *respectively, for all trials.*

at room temperature, whereas H_2, D_2, and ^3He are gases. Therefore, in order to reach comparable number densities, H_2, D_2, and ^3He would have to be cooled to liquids, at cryogenic temperatures. This would substantially increase the cost and difficulty of fabricating the converter foil. There is no overwhelming advantage to using H_2 or D_2, because the charged particle production rates of H_2, CH_2, D_2, and CD_2 are all within about a half order of magnitude of each other, and the production rate of ^3He is significantly lower. Therefore, further comparisons were limited to the solid materials, CH_2 and CD_2.

Between CH_2 and CD_2, CD_2 has a higher space-efficiency at angles less than 40 degrees; CH_2 is marginally better at 45 degrees, and CD_2 is better at 90 degrees. CD_2's greatest space-efficiency, which is at low angles, is twice the maximum space-efficiency of CH_2, and CD_2 is more space-efficient at most angles sampled. For this reason, CD_2 was chosen as the material for the converter foil.

The highest space-efficiency for CD_2 occurs at low angles. At low angles, the spherical cap configuration is very similar to a planar Icarus, so a planar configuration was chosen. The planar shape of the Icarus chip also facilitates the choice of a planar configuration.

The Icarus chip has dimensions 1.28 $cm \times 2.56$ cm, with a thickness of 9 μm.[7] The sensor is divided by a deuteron absorber into two square panels, or macropixels, as shown in Figure 5. Compared to a single rectangular macropixel, two square macropixels increase the ratio of lower-scattering angle to higher-scattering angle deuterons detected by the spectrometer. This improves the spectrometer's performance, as will be discussed below. The ideal material and mass thickness of the deuteron absorber were not investigated, and simulations assumed no cross-talk between the two macropixels.

4.3 Size of the macropixels

Within the planar configuration, one can vary the size of the macropixels. Given an approximately collimated neutron source, an array of small macropixels is functionally equivalent to a single, larger macropixel, scaled up in all three dimensions, with the same converter foil area as the array.

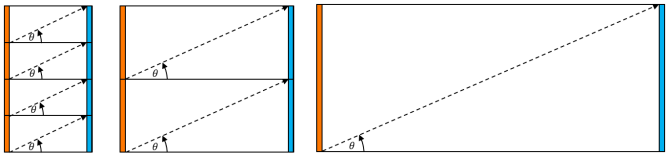

Figure 8: *Comparison of macropixel sizes. Macropixels of different sizes, if they are geometrically similar, have the same maximum angle. If they also have the same active area (in orange), they are functionally equivalent.*

As shown in Figure 8, an array of small macropixels and a single larger macropixel with the same area are equivalent in all relevant properties. The surface areas of the converter foils are the same, so the same number of neutrons will hit the converter foil, and the same number of deuterons will be produced, with the same energy and angle distributions. The small and large macropixels are geometrically similar to each other (in the technical sense), so the proportion of deuterons at each angle that reach the detector surface from the foil will be the same for both macropixel sizes. Thus, the energy and angle distribution of deuterons hitting the detector will be the same for an array of small macropixels as for a single, larger macropixel. The size of the CMOS pixels, which detect the individual deuterons, is independent of macropixel size, so macropixel size does not affect the spectrometer's ability to measure individual deuterons.

An array of small macropixels requires deuteron absorbers as walls between macropixels, to prevent cross-talk. These walls could introduce error. Some deuterons might penetrate the walls and enter other macropixels, or collide with the walls and lose energy, but still reach the detector. Additionally, neutrons that pass through the converter foil might interact with the walls and produce deuterons. An ideal wall material could minimize these concerns, but this was not investigated. Future work should determine the optimal material and thickness for the dividing walls.

The design with only two large macropixels was chosen for multiple reasons. The larger-macropixel design is simpler, because of its single dividing wall. Building a detector with many dividing walls would be more difficult and expensive. Secondly, in order to effectively absorb deuterons, the wall must have a non-trivial thickness. The wall must therefore occupy some of the geometrical cross-section of the spectrometer, reducing its active area and space-efficiency. Therefore, the fewer dividing walls, the greater the space-efficiency of the spectrometer.

5 Further considerations for optimization

In order for the spectrometer to have a high resolution, it must be able to determine the incident neutron spectrum. For this, two preconditions are necessary. First, the spectrometer must detect a large number of neutrons, so there are many points from which to determine the neutron spectrum. In optimizing the configuration of the detector surface and the material of the converter foil, maximizing the detection rate was the main concern. Second, the energy of each deuteron detected by the spectrometer must be predictive of the energy of the neutron producing the deuteron. Otherwise, the spectrometer would be unable to accurately measure the neutron spectrum. The ability to determine the energy of a neutron from the recoiled deuteron it produces will henceforth be called predictivity. The maximum scattering angle observed by the spectrometer and the mass thickness of the converter foil both present tradeoffs between the detection rate and the predictivity of the spectrometer.

5.1 Maximum observed scattering angle

The reaction producing the deuteron is an elastic collision between the incident neutron and the deuterium nucleus. Based on conservation of energy and momentum, the higher the scattering angle, the less energy the deuteron has, relative to the initial energy of the neutron. This is illustrated in Figure 9.

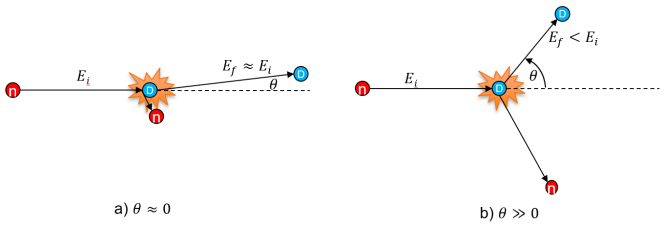

Figure 9: *Effects of scattering angle on deuteron energy. a) Low scattering angle. Deuterons at low scattering angles have energy close to that of the incident neutron. Because the deuteron has twice the mass of the neutron, the maximum energy transfer from the neutron to the deuteron is* $\frac{8}{9}E_i$*. b) High scattering angle. Deuterons at high scattering angles have substantially less energy than the incident neutron.*

For a spectrometer with perfect angular resolution, where the direction of each deuteron is known, this does not reduce predictivity, because the energy of the deuteron relative to the energy of the neutron is deterministically and exclusively based on the scattering angle. However, in a planar arrangement, where the detector surface is equal in size and shape to the converter foil, it is impossible to achieve high angular resolution, because any deuteron could have been produced anywhere on the converter foil. One potential solution would be making the detector surface much larger than the converter foil, but this would substantially reduce the space efficiency of the spectrometer. Therefore, only spectrometers without angular resolution were investigated.

The maximum scattering angle presents a tradeoff. Restricting the spectrometer to a low maximum scattering angle reduces the effects of energy loss from high scattering angle, which increases the predictivity; however, a low maximum scattering angle leads to a low detection rate. Conversely, a high maximum scattering angle leads to lower predictivity, but it allows a higher detection rate.

5.2 Mass thickness of the converter foil

The mass thickness of the converter foil also presents a tradeoff between the detection rate and predictivity of the spectrometer. In order to be detected, a neutron must collide with a deuterium atom in the converter foil. The greater the mass thickness of the converter foil, the more neutron-deuterium collisions, and the higher the detection rate.

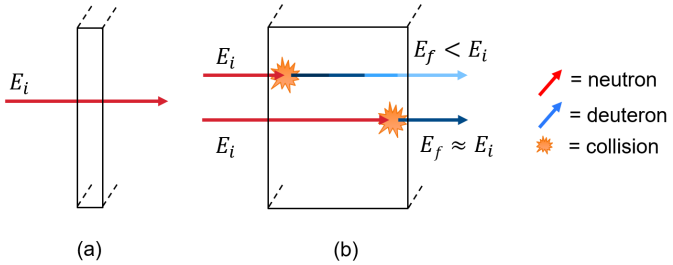

Figure 10: *Mass thickness considerations. a) Low mass thickness. If the mass thickness is too low, too many neutrons will pass through the foil without interacting. b) High mass thickness. If the mass thickness is too great, deuterons that are generated near the front of the foil will lose more energy in the foil than deuterons generated near the back of the foil, reducing the accuracy of energy measurements.*

Deuterons are charged particles, so as they travel through the converter foil, they lose energy.[8] Therefore, the greater the mass thickness through which a deuteron must travel, the more energy it loses. When a high-energy neutron produces a high-energy deuteron near the front of the converter foil, the deuteron loses energy before exiting the converter foil, and it is indistinguishable from a lower-energy deuteron produced by a lower-energy neutron towards the back of the converter foil. Thus, increasing the mass thickness decreases the predictivity of the the spectrometer. This tradeoff is illustrated in Figure 10. At large enough mass thicknesses, the energy loss is so great that the deuterons could fail to escape the foil, or range out. However, the foils investigated in this work were thin enough that the effects of deuterons ranging out were negligible, except at very high scattering angles.

5.3 Combinations of mass thickness and scattering angle

Mass thickness and scattering angle were tested in combination with each other because they are dependent on each other: the mass thickness affects the deuteron spectrum at each scattering angle. Simulations were run in MCNP to test combinations of mass thickness and scattering angle.

Each trial simulated a monoenergetic, collimated source, with an energy of 2.45 MeV and a total of 3×10^7 neutrons. The direction and energy of each deuteron produced were recorded as it left the converter foil. For each combination of mass thickness and maximum scattering angle, detection rate was calculated as the number of deuterons with scattering angles less than the maximum, divided by the number of incident neutrons. The predictivity was defined as the standard deviation divided by the mean for the energy spectrum of deuterons with scattering angles less than the maximum.

Simulations were performed for combinations of 15 maximum scattering angles, ranging from 2.5° to 90°, and 21 mass thicknesses, ranging from 15 $\mu g/cm^2$ to 4.8 mg/cm^2. The results are shown in Figure 11.

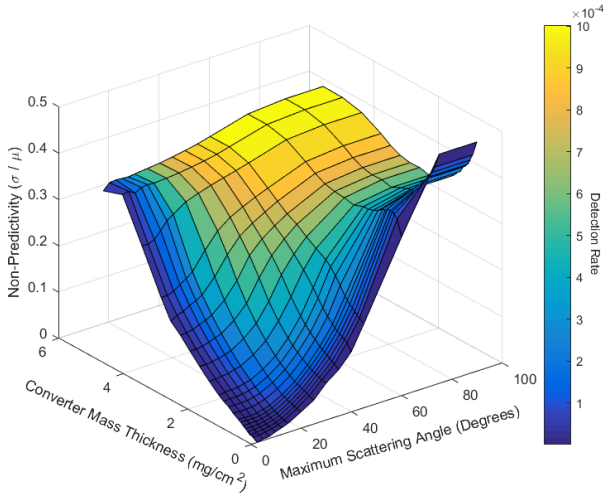

Figure 11: *Dependence of detection rate and predictivity on mass thickness and maximum scattering angle.*

These simulations matched the predicted effects of mass thickness and maximum scattering angle. Higher maximum scattering angles and higher mass thicknesses led to higher detection rates, but also to lesser predictivity. A plot of achievable combinations of predictivity and detection rates (Figure 12) shows an approximately linear bound separating achievable and unachievable combinations of predictivity and detection rate.

The geometry of these simulations differed from the geometry of an actual spectrometer with respect to the counting of deuterons at scattering angles close to the maximum. In the planar arrangement (Figure 6(a)), the converter foil and detector surface are placed at the two bases of a prism. The maximum scattering angle would be observed if a particle scatters from one corner of the converter foil to the opposite corner of the detector surface.

Most deuterons scattered at very small angles hit the detector surface, but few deuterons scattered close to the maximum scattering angle hit the detector surface, unless they are generated at the corner of the converter foil and scatter in exactly the right direction. Thus, even below the maximum scattering angle, deuterons at higher scattering angles are less likely to be detected than deuterons at lower scattering angles.

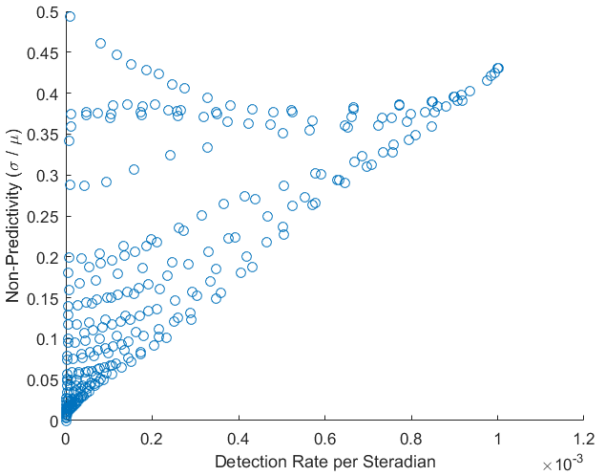

Figure 12: *Achievable predictivity-detection rate combinations, from the simulations shown in Figure 11. The ideal spectrometer would have low non-predictivity and high detection rate and would appear at the bottom right of the graph.*

Simulations indicated that for a square panel, the probability of detecting a deuteron decreases approximately linearly, from 100% detection at a scattering angle of 0° to approximately 0% detection at the maximum scattering angle.

The equal weighting of deuterons at all angles less than the maximum scattering angle artificially increases the detection rate and decreases the predictivity of each trial. However, it does not change the relative detection rate and predictivity of each trial, which were the purpose of this set of simulations. All subsequent simulations accounted for this issue.

6 Modeling the deuteron spectrum

As shown in Eq. 3, the relationship between the T_i, σ, and $\langle E_n \rangle$ of the neutron spectrum follows $T_i \propto \sigma^2 / \langle E_n \rangle$. The σ is squared and varies more than $\langle E_n \rangle$, so apparent temperature can be approximated using only σ. Therefore, the analysis of simulated data focused on determining the σ of the neutron spectrum.

The deuteron spectrum is equal to the convolution of the neutron spectrum with the energy spectrum of deuterons scattered by a deuterated plastic foil, taking into account the scattering angles observed. Based on kinematics, the energies of scattered deuterons at each angle should be proportional to the energy of the incident neutron. Thus, the spectra produced by neutrons of different energies should be geometrically similar to each other, but scaled along the energy axis. For small enough differences in neutron energy, this transformation can be approximated by a translation along the energy axis. In theoretical modeling, therefore, the same spectrum of scattered deuteron energies, with respect to the neutron energy, was used for all neutron energies.

As shown in Figure 13, there is a strong correlation between energy and scattering angle. Additionally,

the scattering spectrum of deuterium with respect to energy is approximately linear at high energies. At energies of below 1.5 MeV, the probability density is approximately constant. However, because the proportion of high-angle deuterons that hit the detector surface approaches zero near the maximum scattering angle, the spectrum observed by the spectrometer contains fewer high-angle, low-energy deuterons than the spectrum shown in Figure 13. As a result, the overall scattering spectrum of deuterium with respect to energy, accounting for the effects of the scattering angles observed, can be approximated as a right triangle, with one leg on the x-axis, one vertical leg, and the peak on the right.

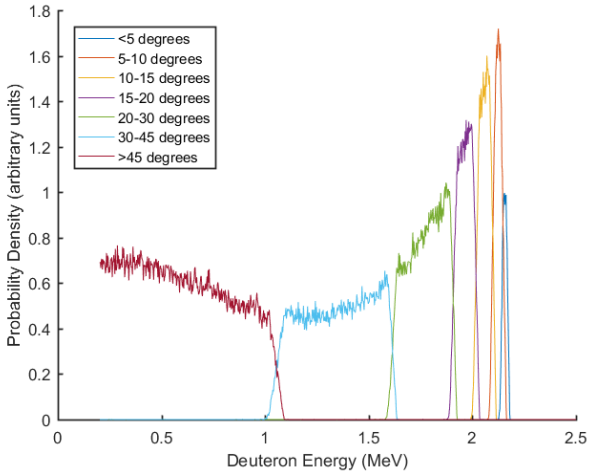

Figure 13: *Spectrum of scattered deuterons with respect to energy, as produced by 2.45 MeV neutrons incident on a very thin foil of deuterated plastic* ($\langle \rho l \rangle = 0.1\ \mu g/cm^2$). *The slight energy overlap between different angle bins is due to energy loss of deuterons within the foil. The under-*5° *bin has the fewest deuterons because it subtends the smallest solid angle. The simulation did not track deuterons with energies below* 0.2 MeV, *because they were unlikely to escape the foil and hit the detector.*

Convolutions of such a right triangle with Gaussian distributions of different widths (Figure 14) approximate the dependence of the observed deuteron spectrum on the width of the incident neutron spectrum. When the neutron spectrum is narrow compared to the triangle, the resultant deuteron spectrum is roughly triangular, with a long tail at low energies and very few particles more energetic than the peak of the distribution. When the neutron spectrum is wide compared to the triangle, the resultant deuteron distribution becomes more Gaussian in shape.

All of the theoretical deuteron distributions in Figure 14 have low-energy tails of similar width. However, the width of the high-energy tail of the deuteron distribution is highly sensitive to the width of the neutron distribution. Therefore, the spectrometer uses the deuteron spectrum's width to the right of its peak (WROP) to predict the width of the neutron distribution. Note that the *peak* of the observed deuteron distribution refers to the energy at which the probability distribution for detected deuteron energy is at a maximum, not the maximum observed deuteron energy. Even though all deuterons to the right of the peak have low scattering angles, arrangements with high maximum scattering angles were still considered, because deuterons

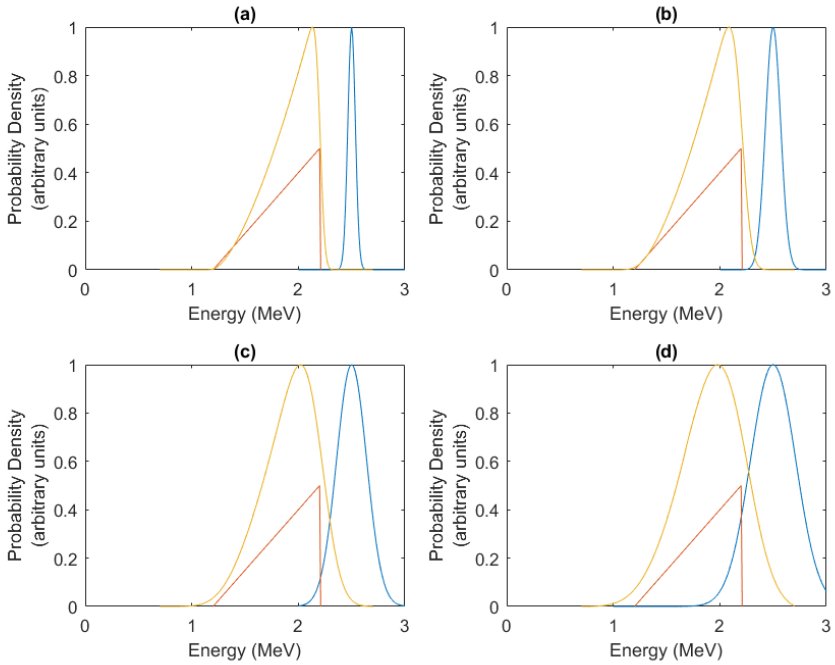

Figure 14: *Approximations of deuteron spectra (yellow) as convolutions of Gaussian neutron spectra of different widths (blue) with a right triangle (red) that roughly approximates the overall scattering spectrum of deuterium produced by 2.45 MeV neutrons. Subfigures a, b, c, and d show progressively wider neutron distributions.*

with higher scattering angles can increase the resolution for determining the peak of the distribution.

Calculating the WROP requires determining the peak of the deuteron distribution and the maximum energy. The maximum energy was defined as a high percentile of the distribution. After tests of multiple percentiles, the 99.5^{th} percentile was found to be the most reliable.

In trials with low neutron yields or thin foils, the number of deuterons detected was relatively low. As a result, the deuteron spectrum was noisy, so the mode of the measured distribution was not always an accurate representation of its peak. Therefore, the peak was calculated by finding the smallest energy intervals that contained 2, 4, 6, 8, and 10% of the observed deuterons. These intervals were assumed to be centered on the peak, so the midpoints of the five intervals were averaged together to determine the peak of the distribution. This method prevented noisiness in the spectrum from affecting the determination of the peak. The deuteron spectrum from 1 keV fusion in Figure 15 below provides an example. The spectrum had two local maxima, separated by a slight dip, and the algorithm determined the peak to be between the two local maxima.

7 Final optimization of the spectrometer design

To determine the optimal mass thickness and maximum scattering angle, simulations were done for combinations of 20 mass thicknesses, ranging from 1.0×10^{-5} to 2.0×10^{-2} g/cm^2, and 17 maximum scattering angles, in 5° increments from 5° to 85°. Each combination was evaluated for its performance over three temperature intervals: $0.1-1.0$ keV, $0.1-10$ keV, and $1.0-10$ keV. The simulations exhibited the predicted relation between the WROPs of the neutron and deuteron spectra. Figure 15 shows examples of the determination of the WROPs of deuteron and neutron spectra, and Figure 16 shows examples of the correlation between neutron WROP and deuteron WROP.

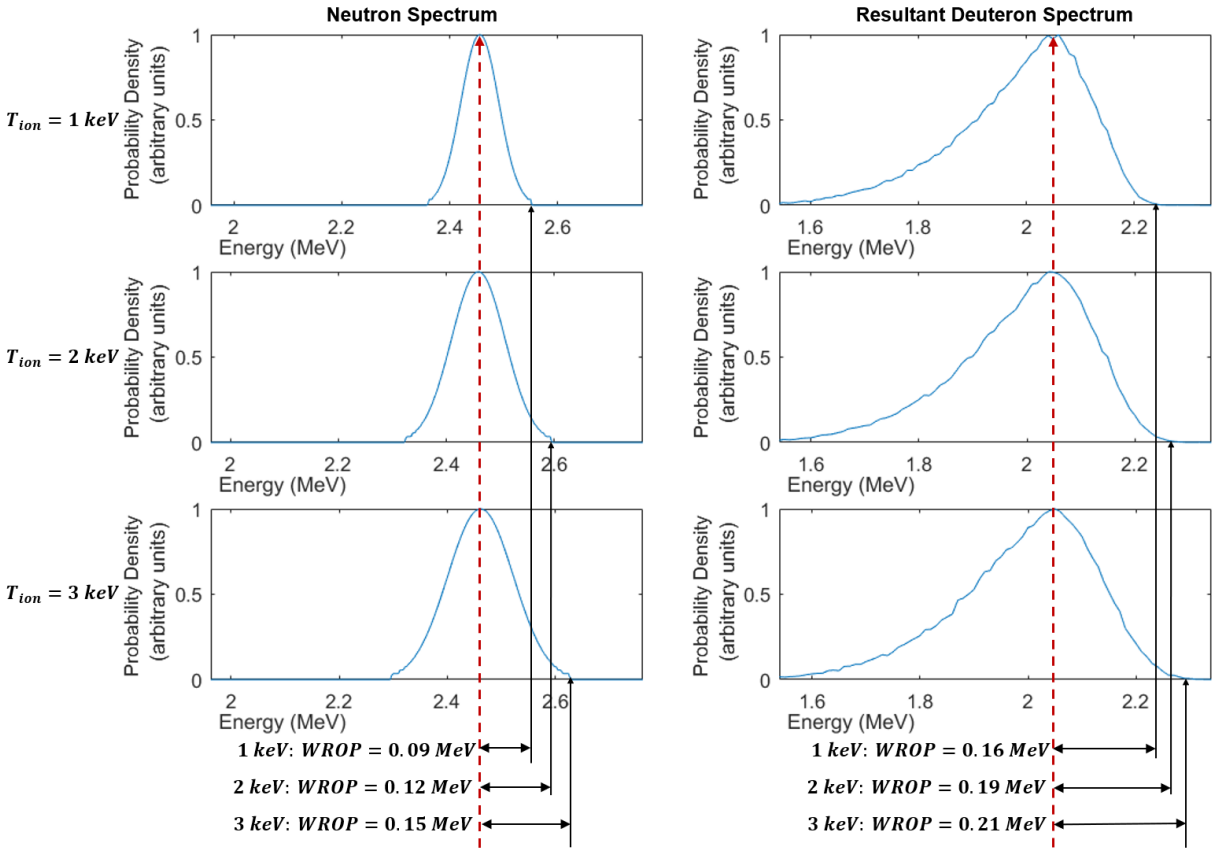

Figure 15: *Example of the use of WROP to differentiate between neutron spectra of different widths. The range of the energy axis is different between the neutron and deuteron spectra, but the scale is consistent. For all three examples, the mass thickness, maximum scattering angle, and neutron count were* 600 $\mu g/cm^2$, 35°, *and* 10^{10}, *respectively. These were among the least noisy deuteron spectra measured, due to the high neutron count and mass thickness.*

The performance of the spectrometer was evaluated for detection rate and sensitivity. The calculation of WROP focuses on the deuterons to the right of the peak, so the detection rate only considered deuterons to the right of the peak. The sensitivity is a measure of the ability of the spectrometer to discriminate

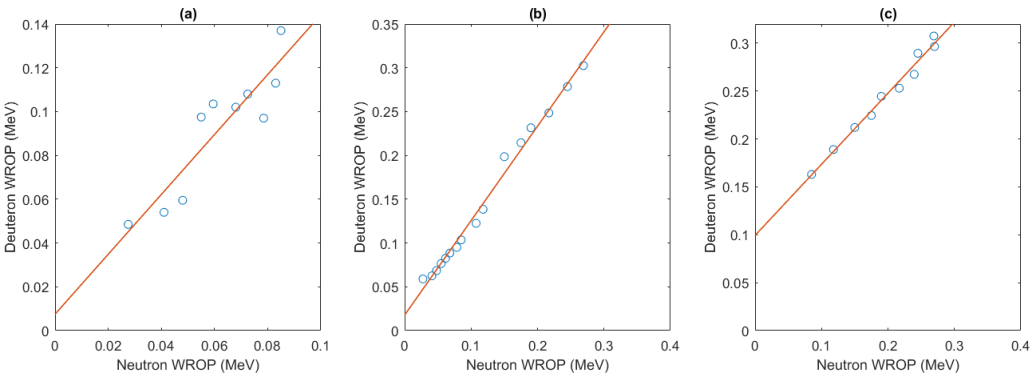

Figure 16: *Three examples of neutron and deuteron WROPs, with varying degrees of correlation. The regression lines from these three data sets had slopes of 1.37, 1.08, and 0.74 and R^2 values of 0.827, 0.991, and 0.983, respectively. The simulations used the optimized mass thicknesses and maximum scattering angles listed in Table 2 below. a) Neutron and deuteron WROPs from 10^8 neutrons at temperatures of 0.1-1.0 keV. b) Neutron and deuteron WROPs from 10^9 neutrons at temperatures of 0.1-10 keV. c) Neutron and deuteron WROPs from 10^{10} neutrons at temperatures of 1.0-10 keV. Subfigure c includes the examples shown in Figure 15.*

between different ion temperatures. The sensitivity was calculated based upon a regression between the deuteron WROP and the incident neutron WROP, as illustrated in Figure 16. To have a high sensitivity, the deuteron WROP must be highly correlated with the neutron WROP, and the deuteron WROP should respond as much as possible to changes in the neutron WROP. Therefore, the sensitivity was defined as the product of the slope of the regression line between neutron WROP and deuteron WROP $\left(\frac{d(WROP_{deuteron})}{d(WROP_{neutron})}\right)$ and the square of the R^2 value of the linear regression between neutron WROP and deuteron WROP.

The spectrometer design was optimized for each temperature range by choosing the mass thickness-maximum scattering angle combination that produced the highest detection rate while maintaining a high sensitivity. The detection rate value for each trial was reliable, but the sensitivity showed more fluctuation. The detection rate to the right of the peak ranged from 10^{-7} to 10^{-5} deuterons per incident neutron. The deuteron WROP was therefore based on a small quantity of deuterons, relative to the incident neutron count. This causes uncertainty in the determination of the deuteron WROP, which causes uncertainties in sensitivity. An anomolous deuteron WROP value could substantially change the $\frac{d(WROP_{deuteron})}{d(WROP_{neutron})}$, which would affect the measured sensitivity.

A comparison of the results from many trials of the same conditions would yield a more accurate measure of the sensitivity. However, performing many trials of each run was prohibitively computation-intensive. Instead, the reliability of the sensitivity measurement was determined by comparing each trial to the trials of the same mass thickness and slightly different scattering angles. Under the assumption that a small change in maximum scattering angle should produce only small changes in sensitivity, a trial's sensitivity was considered to be more reliable if it was similar to the sensitivity from trials with the same

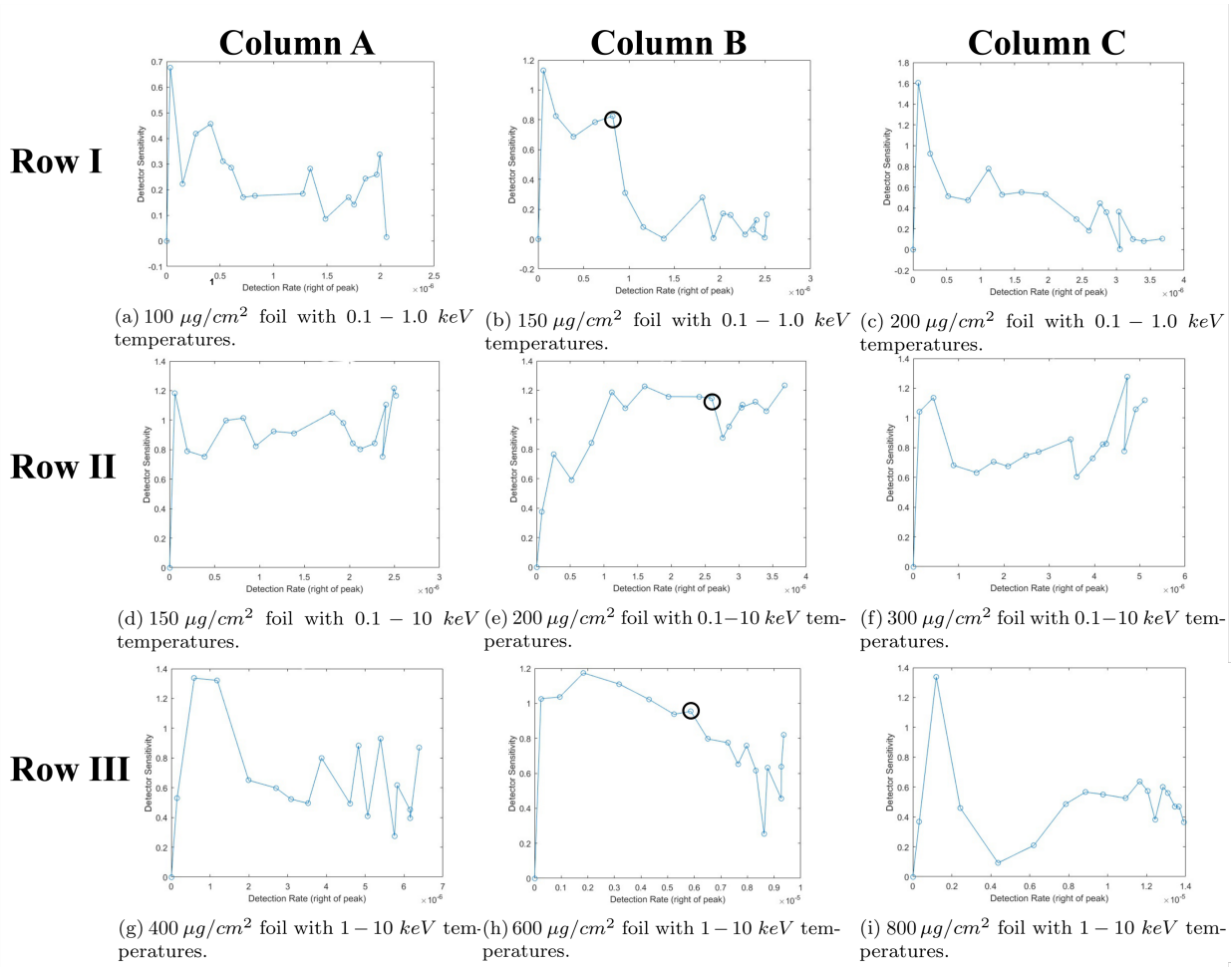

(a) 100 $\mu g/cm^2$ foil with $0.1 - 1.0$ keV temperatures.

(b) 150 $\mu g/cm^2$ foil with $0.1 - 1.0$ keV temperatures.

(c) 200 $\mu g/cm^2$ foil with $0.1 - 1.0$ keV temperatures.

(d) 150 $\mu g/cm^2$ foil with $0.1 - 10$ keV temperatures.

(e) 200 $\mu g/cm^2$ foil with $0.1-10$ keV temperatures.

(f) 300 $\mu g/cm^2$ foil with $0.1-10$ keV temperatures.

(g) 400 $\mu g/cm^2$ foil with $1-10$ keV temperatures.

(h) 600 $\mu g/cm^2$ foil with $1-10$ keV temperatures.

(i) 800 $\mu g/cm^2$ foil with $1 - 10$ keV temperatures.

Figure 17: *Detection rate and sensitivity for a range of maximum scattering angles, mass thicknesses, and temperatures. For each row, Column A shows a foil that is too thin, Column B shows the chosen foil, and Column C shows a foil that is too thick. Each graph shows data points at maximum scattering angles from* $0°$ *to* $85°$*, in* $5°$ *increments, beginning at the origin. In Column B, the circled data point represents the chosen maximum scattering angle. Row I (a-c): Optimization for 0.1-1.0 keV. Row II (d-f): Optimization for 0.1-10 keV. Row III (g-i): Optimization for 1.0-10 keV.*

mass thickness and similar maximum scattering angles.

For each temperature range investigated, the detection rate and sensitivity are shown in Figure 17 for a range of maximum scattering angles, at mass thicknesses just less than, equal to, and just greater than the chosen mass thickness. The chosen mass thickness-maximum scattering angle combinations are listed in Table 2.

Table 2: *Optimized Design Parameters*

Ion temperature range (keV)	Optimized mass thickness ($\mu g/cm^2$)	Optmizied maximum scattering angle ($°$)
0.1-1.0	150	25
0.1-10	200	50
1.0-10	600	35

8 Performance of the chosen spectrometer designs

Detailed simulations were carried out to evaluate the performance of these three spectrometer designs. Each spectrometer was simulated over 10-16 temperatures in the range for which the spectrometer was optimized, at incident neutron counts of 10^7, 10^8, 10^9, and 10^{10}.

For each design at each yield, a linear regression between the WROP of the incident neutron spectrum and the WROP of the deuteron spectrum was calculated, based on simulations at different temperatures. This regression was then used to calculate a predicted neutron WROP based on each deuteron WROP. To measure the accuracy of the spectrometer design, the mean percent error between the actual neutron WROP and the predicted neutron WROP was used. The results are shown in Figure 18.

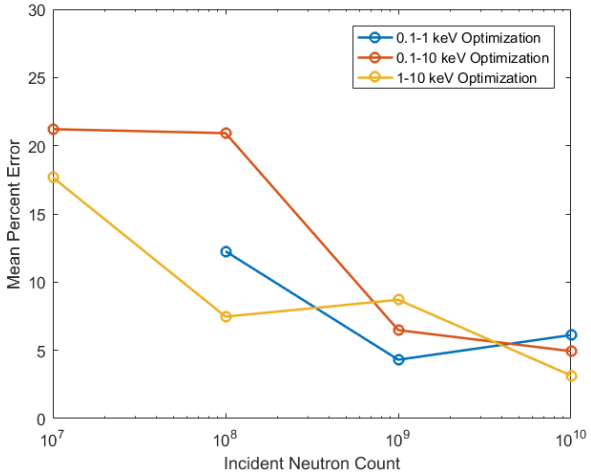

Figure 18: *The mean percent error for WROP prediction at different yields. Each mean percent error is based upon simulations at 10-16 temperatures within the temperature range for which the design was optimized. There was no meaningful ability to predict the WROP for 0.1-1.0 keV optimization at a yield of* 10^7*, so the mean percent error is not shown at that point.*

The mean percent error was under 25% for all cases studied, with the exception of 10^7 neutrons at ion temperatures of $0.1 - 1.0\ keV$. In that range, so few deuterons were detected that no useful measurements could be made. The trends in these results match theoretical predictions. The spectrometer designed for $1.0 - 10\ keV$ generally has lower error than the spectrometer designed for $0.1 - 1.0\ keV$, due to the greater WROPs at higher temperatures. Additionally, the error tends to decrease as the yield increases, because the greater number of deuterons detected reduces the uncertainty of the measurements.

The deuteron data was also used to estimate the ion temperature, using Eq. 3. The neutron spectrum is a normal distribution,[3] meaning that its 99.5^{th} percentile is 2.576 standard deviations above the mean. Therefore, a neutron distribution with a WROP of W has a standard deviation of $\sigma = W/2.576$, yielding a temperature equation of

$$T_i = \frac{W^2\,(m_n + m_\alpha)}{2\,(2.576^2)\,m_n \langle E_n \rangle}. \tag{5}$$

The determination of $\langle E_n \rangle$ was not investigated. The peak of the deuteron distribution was used, but this introduced substantial error, because the deuteron energy peak is significantly lower than the neutron energy peak *(see Figure 15)*. Therefore, a second linear regression was run on the calculated T_i values in order to account for the difference in neutron and deuteron peaks. This formula was used to generate a calculated ion temperature for each trial, and the mean percent error was calculated for each spectrometer design and yield. The results are shown in Figure 19.

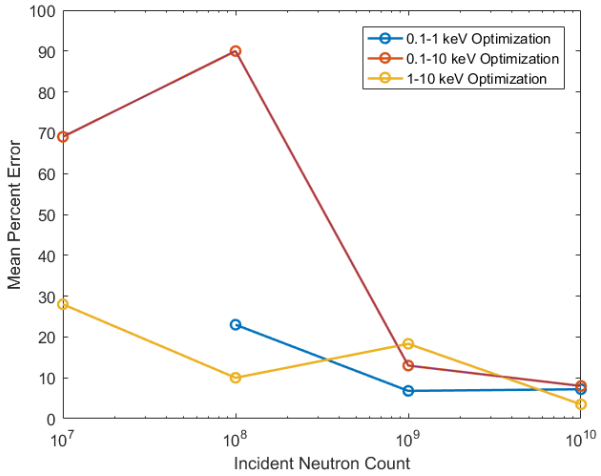

Figure 19: *The mean percent error for ion temperature prediction at different yields. There was no meaningful ability to predict the ion temperature for 0.1-1.0 keV optimization at a yield of* 10^7*, so the mean percent error is not shown. Developing a more accurate method of determining* $\langle E_n \rangle$ *would likely improve the temperature measurements.*

The trends for temperature prediction are similar to the trends for WROP prediction: higher temperatures and higher yields tend to reduce error. The error in temperature prediction is generally greater than the error in WROP prediction. One reason for this is that temperature is proportional to WROP squared, as shown in Eq. 5, so errors in WROP prediction are magnified. The lack of a reliable method of calculating $\langle E_n \rangle$ from the deuteron spectrum causes additional error. It is likely that the $\langle E_n \rangle$ can be deduced from the deuteron spectrum, and further work should explore this possibility.

The neutron yield at FuZE is on the order of 10^5 neutrons per pulse, over 4π steradians.[2] It follows that any spectrometer would observe many fewer than 10^5 neutrons per pulse. Given that the spectrometer described here must observe at least 10^7 neutrons to make useful measurements, it is not efficient enough to be used at FuZE. However, other existing fusion reactors have much higher yields. For example, JET has achieved neutron yields of over 10^{15} neutrons,[10] with ion temperatures of a few keV.[11] At such yields, the spectrometer could function even if the proportion of neutrons that hit the spectrometer is 10^{-5} or less. This would require a few tens of Icarus chips, which could be feasible.

9 Areas for further investigation

9.1 Measurement of the deuteron energy spectrum

This work did not investigate the process of determining the deuteron spectrum from the signal from the CMOS detector. The extraction of the deuteron spectrum could be a significant source of error, for multiple reasons.

The total energy deposited by a deuteron is the integral of $\frac{dE}{dx}$ over its path, or

$$\Delta E = \int_x dE = \int_x \left(\frac{dE}{dx}\right) dx. \tag{6}$$

Therefore, the longer the path length, the greater the energy deposition. The path length of a deuteron with angle ϕ from the normal is inversely proportional to $\cos\phi$. The chosen spectrometer arrangements have maximum scattering angles of 25°, 35°, and 50°, which permit variations in path length of up to 10%, 22%. and 55%, respectively. This effect could be modeled. However, compensating for the uncertainty introduced by angle variations could require a larger data sample, which requires a higher detection rate.

If multiple deuterons hit the same pixel of Icarus within 1.5 ns, the pixel does not have time to reset, and it records the two events identically to a single, higher-deposition event. Such double hits compromise the accuracy of the detector. Statistical analysis can be used to determine the maximum deuteron flux, and therefore the maximum neutron flux, that the detector can observe without substantial error from double hits. Given the low efficiency of the detector, the maximum flux is unlikely to be a limiting factor.

The CMOS detector is primarily designed to detect charged particles, such as protons and deuterons. However, it is possible for neutrons to interact with the CMOS detector as well. Considering that the optimal detector arrangements have efficiencies of less than 1.0×10^{-5}, the neutron flux on the detector surface will be much greater than the deuteron flux. If the neutrons interact with the CMOS detector at a non-negligible rate, it could produce background noise that limits the ability to observe the deuteron signal.

9.2 Accounting for shifts of the neutron and deuteron peaks

As previously discussed, a method of determining the $\langle E_n \rangle$ would substantially improve temperature prediction. Because the neutron spectrum is Gaussian, the mean energy is equivalent to the peak of the spectrum. Thus, $\langle E_n \rangle$ could be calculated by determining the relation between the peak of the deuteron spectrum and the peak of the neutron spectrum. Two factors complicate the determination of this relation.

Firstly, the peak of the neutron spectrum shifts depending on the temperature.[3] Secondly, as shown in Figure 14, the location of the peak of the deuteron spectrum with respect to the peak of the neutron spectrum changes based on the width of the neutron spectrum. Therefore, the relationship between the peaks is more

complex than the model used in this work, and future work should develop more accurate models for this relationship.

9.3 Discrimination between beam-target and thermonuclear fusion

Another use of neutron spectrometry is the discrimination between beam-target fusion, where all fusion reactions involve accelerated particles, and thermonuclear fusion, where the thermal energy is enough to cause fusion. Discrimination between the two requires the measurement of the location of the peak of the neutron distribution, separately from the measurement of the width of the neutron distribution. The ability to extract this value from the deuteron signal was not investigated.

10 Conclusion

A neutron spectrometer was designed for use with 2.45 MeV neutrons from D-D fusion. The spectrometer consists of a neutron-to-deuteron converter foil and an Icarus hCMOS chip, which measures the deuteron spectrum. Deuterated plastic was selected as the material of the converter foil, and the converter foil was placed parallel to the detector surface. Three optimal combinations of the mass thickness of the converter foil and the maximum observable deuteron scattering angle were developed, depending on the apparent ion temperature range of the fusing plasma.

A model was developed to determine the apparent ion temperature of the fusing plasma, by correlating the widths of the observed deuteron spectrum and the incident neutron spectrum. At incident neutron counts of 10^9 and above, apparent ion temperature prediction was accomplished with mean error of less than 20% across all temperature ranges studied.

The spectrometer is time-independent, enabling its use with reactors with durations beyond the limits of time-of-flight spectrometers. The accuracy of the spectrometer is highly dependent upon the incident neutron count, and although it is unusable at very low-yield reactors, such as FuZE, the design has the potential to be applied at higher-yield reactors. A prototype of the spectrometer will be built and tested at LLE, as a proof of concept.

11 Acknowledgements

This work would not have been possible without the help of many people. Most of all, I would like to thank my advisor, Dr. Chad Forrest. From framing this project to guiding me with the research process to providing feedback on this report, his help has been invaluable. I am also indebted to William Scullin, for handling all the technological challenges that arose during this project. Without his assistance setting

up and trouble-shooting the computer environment, I would never have been able to run all the simulations that formed the basis of this research.

I would also like to thank Jonathan Davies, for explaining the intended use of the spectrometer at FuZE; Steve Ivancic, for providing the specifications of the Icarus chip; and Vladimir Glebov, for giving me valuable feedback on my presentation. Lastly, I am grateful to Dr. Stephen Craxton, for managing the Summer Research Program. His supervision ensured that everything ran smoothly, and his guidance was essential to the oral and written presentation of my work.

References

[1] G. M. McCracken and P. E. Stott, *Fusion: the energy of the universe*. Burlington, MA: Elsevier Academic Press, 2005.

[2] Y. Zhang, U. Shumlak, B. A. Nelson, R. P. Golingo, T. R. Weber, A. D. Stepanov, E. L. Claveau, E. G. Forbes, Z. T. Draper, J. M. Mitrani, H. S. McLean, K. K. Tummel, D. P. Higginson, and C. M. Cooper, "Sustained neutron production from a sheared-flow stabilized Z pinch," *Physical Review Letters*, vol. 122, no. 13, p. 135001, 2019.

[3] H. Brysk, "Fusion neutron energies and spectra," *Plasma Physics*, vol. 15, no. 7, pp. 611–617, 1973.

[4] D. Thomas, "Neutron spectrometry," *Radiation Measurements*, vol. 45, no. 10, pp. 1178 – 1185, 2010.

[5] J. A. Frenje, D. T. Casey, C. K. Li, F. H. Séguin, R. D. Petrasso, V. Y. Glebov, P. B. Radha, T. C. Sangster, D. D. Meyerhofer, S. P. Hatchett, S. W. Haan, C. J. Cerjan, O. L. Landen, K. A. Fletcher, and R. J. Leeper, "Probing high areal-density cryogenic deuterium-tritium implosions using downscattered neutron spectra measured by the magnetic recoil spectrometer," *Physics of Plasmas*, vol. 17, no. 5, p. 056311, 2010.

[6] C. J. Forrest, V. Y. Glebov, V. N. Goncharov, J. P. Knauer, P. B. Radha, S. P. Regan, M. H. Romanofsky, T. C. Sangster, M. J. Shoup, and C. Stoeckl, "High-dynamic-range neutron time-of-flight detector used to infer the D(t,n)4He and D(d,n)3He reaction yield and ion temperature on OMEGA," *Review of Scientific Instruments*, vol. 87, no. 11, p. 11D814, 2016.

[7] L. D. Claus, "An overview of the Sandia Labs ultra-fast x-ray imager (UXI) program," 2015.

[8] W. R. Leo, *Techniques for nuclear and particle physics experiments: a how-to approach*. New York: Springer-Verlag, 1987.

[9] X-5 Monte Carlo Team, MCNP —A General Monte Carlo N-particle transport code, Version 5, Los Alamos National Laboratory, Los Alamos, NM, Report LA-UR-03-1987 (2008).

[10] P. van Belle, O. N. Jarvis, G. Sadler, S. de Leeuw, P. D'Hondt, and M. Pillon, "Calibration of the JET neutron yield monitors using the delayed neutron counting technique," *Review of Scientific Instruments*, vol. 61, no. 10, pp. 3178–3180, 1990.

[11] P. H. Rebut, R. J. Bickerton, and B. E. Keen, "The Joint European Torus: installation, first results and prospects," *Nuclear Fusion*, vol. 25, no. 9, pp. 1011–1022, 1985.

Optimization of X-Ray Prepulse Geometry for Imprint Mitigation in Directly Driven Implosions

Adelyn Carney

Webster Schroeder High School

Advisor: Hans Rinderknecht

Laboratory for Laser Energetics

University of Rochester Rochester

February 2020

1. Abstract

Laser imprint, when laser non-uniformities are imprinted onto the capsule at the beginning of the implosion, is a limiting factor in direct-drive inertial confinement fusion. One method to reduce imprint is x-ray pre-illumination, in which an additional x-ray source is used to "puff up" the outermost layer of the capsule before it is illuminated by the main laser pulse. Positioning metal foils around the capsule and using lasers to heat the foils so they produce x rays is one way to implement this technique. The optimal placement of x-ray prepulse foils was investigated. MATLAB functions were developed to generate foil geometries that correspond to the faces of a tetrahedron, cube, and octahedron, and verify that they satisfy beam clearance requirements. VisRad (J. J. MacFarlane, Journal of Quantitative Spectroscopy and Radiative Transfer **81**, 287 (2003)) models were constructed for selected foil configurations, and viewfactor simulations were run to optimize foil orientation. Three optimized foil configurations were examined: the first configuration optimized uniformity of x-ray distribution on the capsule, the second maximized incident flux by decreasing the foil radius, and the third maximized incident flux by breaking polyhedral symmetry. It was determined that the four-foil geometry would be the most convenient to implement, the six-foil geometry produces the highest mean incident flux with nonuniformity below 10%, and the eight-foil geometry provides the lowest nonuniformity (<8%).

2. Introduction

Because non-renewable energy sources such as coal release carbon dioxide into the atmosphere, a major contributor to global warming, and are projected to run out in only a few centuries, people have been turning to renewable energy sources. The idea of using lasers to initiate a nuclear fusion reaction in a controlled environment was first thought of in the 1960s and first published in 1972 [1, 2]. Since nuclear fusion is both safe and clean (compared to

nuclear fission), much effort has been put into making this idea a reality. Direct-drive inertial confinement fusion [1, 2], studied on the 60-beam OMEGA laser at the Laboratory for Laser Energetics, is one way to achieve it. In this approach, a spherical capsule, which typically has a plastic shell surrounding a layer of frozen deuterium and tritium, is irradiated using high-power laser beams. The capsule implodes, causing extreme temperatures and pressures to be reached. These extreme conditions cause the deuterium and tritium to combine, forming a helium atom and a neutron. If there is enough fusion to further heat the fuel, a chain reaction will occur, known as ignition.

For the best results, the capsule must be irradiated as uniformly as possible. However, uniformity is hard to achieve due to several factors that can worsen over time due to Rayleigh-Taylor instability [3]. One of these factors is laser imprint, in which laser non-uniformities are imprinted onto the surface of the capsule at the beginning of the implosion. As the capsule implodes, the perturbation gets worse, as can be seen in Fig. 1 (taken from Ref. 4). This can destroy the shell of the capsule, reducing capsule performance and the amount of fusion generated. X-ray pre-illumination is one way to reduce laser imprint [5]. In this technique, an additional x-ray source is used to “puff-up” the outermost layer of the capsule before the main laser beams are turned on. This increases the distance between the capsule surface and the region where the laser is initially absorbed, smoothing out the imprint. One way to produce the x-ray prepulse is to position foils around the capsule and hit the foils with laser beams. The foils will then radiate x rays onto the capsule. Figures 2 and 3 support this claim. Figure 2a shows the experimental design when the laser beam directly hits the target, and Fig. 3a shows the result of the laser imprint on the surface of the target when there is no x-ray prepulse. Figure 2b shows the experimental design when the laser beam first goes through a sheet of gold before hitting the target, and Fig. 3b shows the resulting laser imprint on the surface of the

target when there is an x-ray prepulse. When the surface is first pre-illuminated by x rays, a plasma layer is formed that smoothes out the small imprint speckles that are seen in Fig 3a.

In this work, foils will be driven by an OMEGA EP beam transported into the OMEGA target chamber, using a custom optic to split the OMEGA EP beam to focus onto multiple targets, as can be seen in Fig. 4a. Foil configurations made up of four, six, and eight foils were analyzed for optimized uniformity of x rays on the capsule and incident flux. Foil sets will be configured so that the faces of the polyhedra as shown in Fig. 4b correspond to a foil. Section 3 discusses how foil positions were found, including foil constraints, how sets of foils were defined, and how foil geometries and orientations were optimized. Section 4 analyzes the three optimized foil configurations.

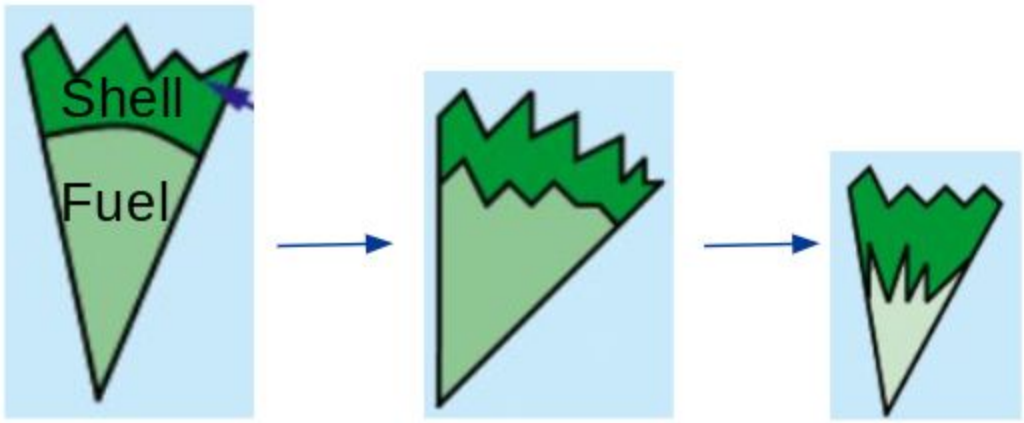

Image from Ref. 4

Figure 1: Series of images showing the effect of laser imprint on an imploding capsule. As time goes on, the perturbations get worse due to Rayleigh-Taylor instabilities.

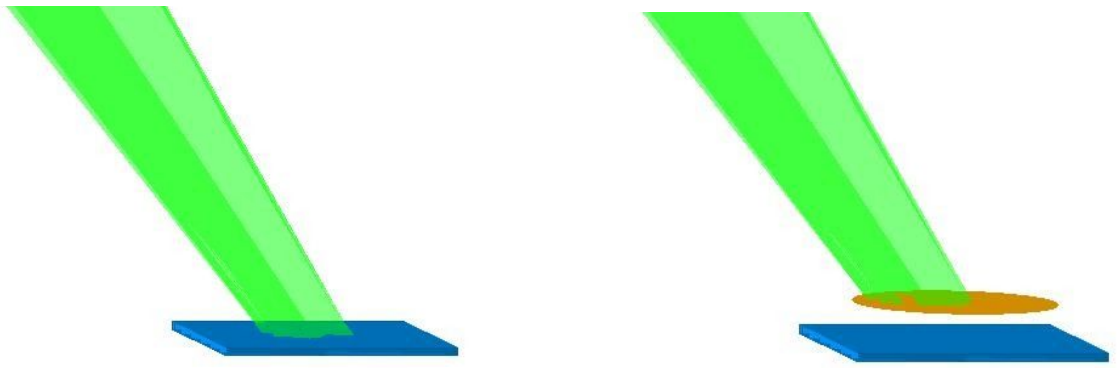

a **b**

Figure 2: Experimental setups to show how laser imprint can be reduced. In (a), the laser beam directly hits the target whereas in (b), the laser beam first goes through a thin gold foil before hitting the target.

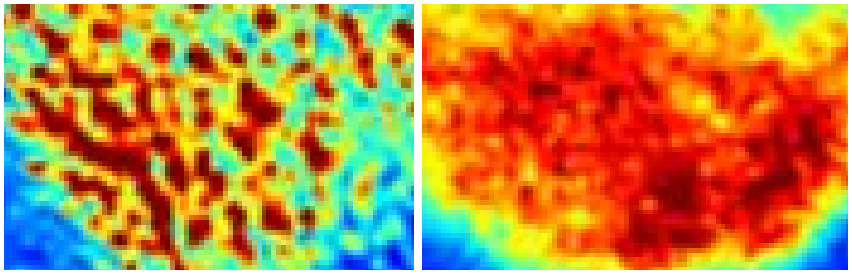

a **b**

Image from Ref. 6

Figure 3: Time resolved x-ray radiography of density modulations from laser imprint from the experiment described in Fig. 2. Color represents mass, with blue showing more mass and red showing less. Where density is greater, more x rays are absorbed. Image (a) shows the imprint left on a surface when the laser hits the surface directly. Image (b) shows the imprint left on a surface when the laser first goes through a thin layer of gold before hitting it. The imprint in image (b) is much smoother because the x-ray prepulse created a layer of plasma near the surface that served as a "buffer" for when the laser hit the surface directly.

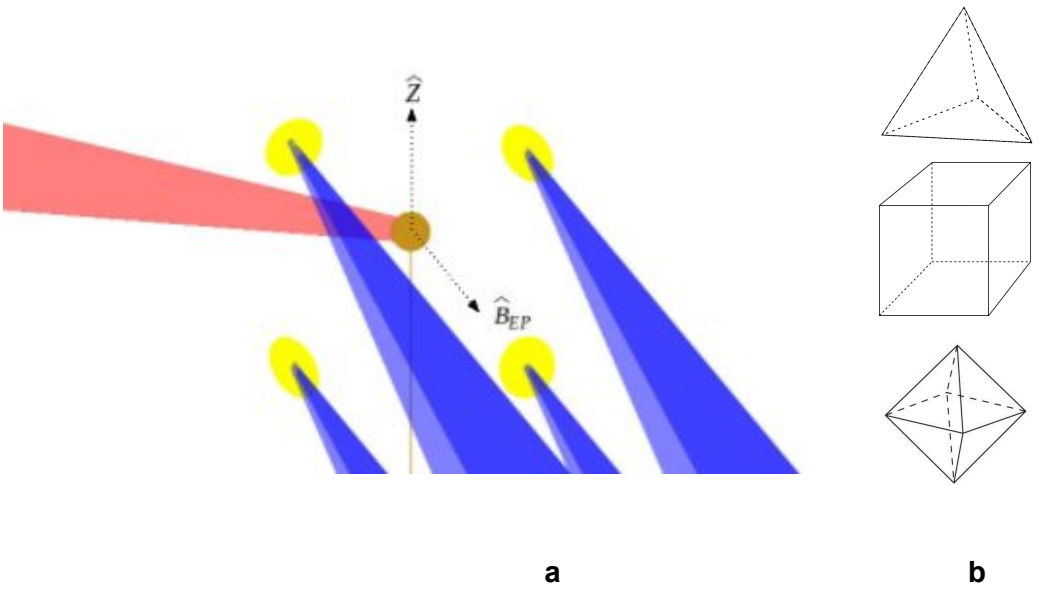

Figure 4: Schematic of foil arrangements. Figure (a) shows the OMEGA EP beam (blue) split up into four beams, each focused on a foil (yellow), and one of the 60 OMEGA laser beams (red) focused onto the capsule (gold). Unit vector, $\hat{B}_{EP}$ is also shown. Figure (b) shows the polyhedral geometry of the foils - the 4-foil geometry will correspond to the faces of the tetrahedron on the top, the 6-foil geometry will correspond to the faces of the cube in the middle, and the 8-foil geometry will correspond to the faces of the octahedron on the bottom.

3. Finding foil positions and orientations

In order to find potential locations where the foils could be placed, constraints on the foils were defined. Then mechanisms were set up to find sets of foils in tetrahedral, cubic, and octahedral geometries, and the most suitable sets of foil geometries were found. The best foil sets were then further analyzed by adjusting the tilt on the foils.

3.1 Foil constraints

Throughout this work, bold indicates vector notation, and the hat symbol, $\hat{}$, indicates a unit vector. For example, the vector **A** = $< A_x \hat{x} + A_y \hat{y} + A_z \hat{z} >$ points in the direction $\hat{A} = \frac{A}{|A|}$.

Constraints on the foils must be satisfied in order for the foils and capsule stalk to not be in the way of any of the OMEGA laser beams and to minimize the risk associated with scattered laser energy. Below are three of these constraints.

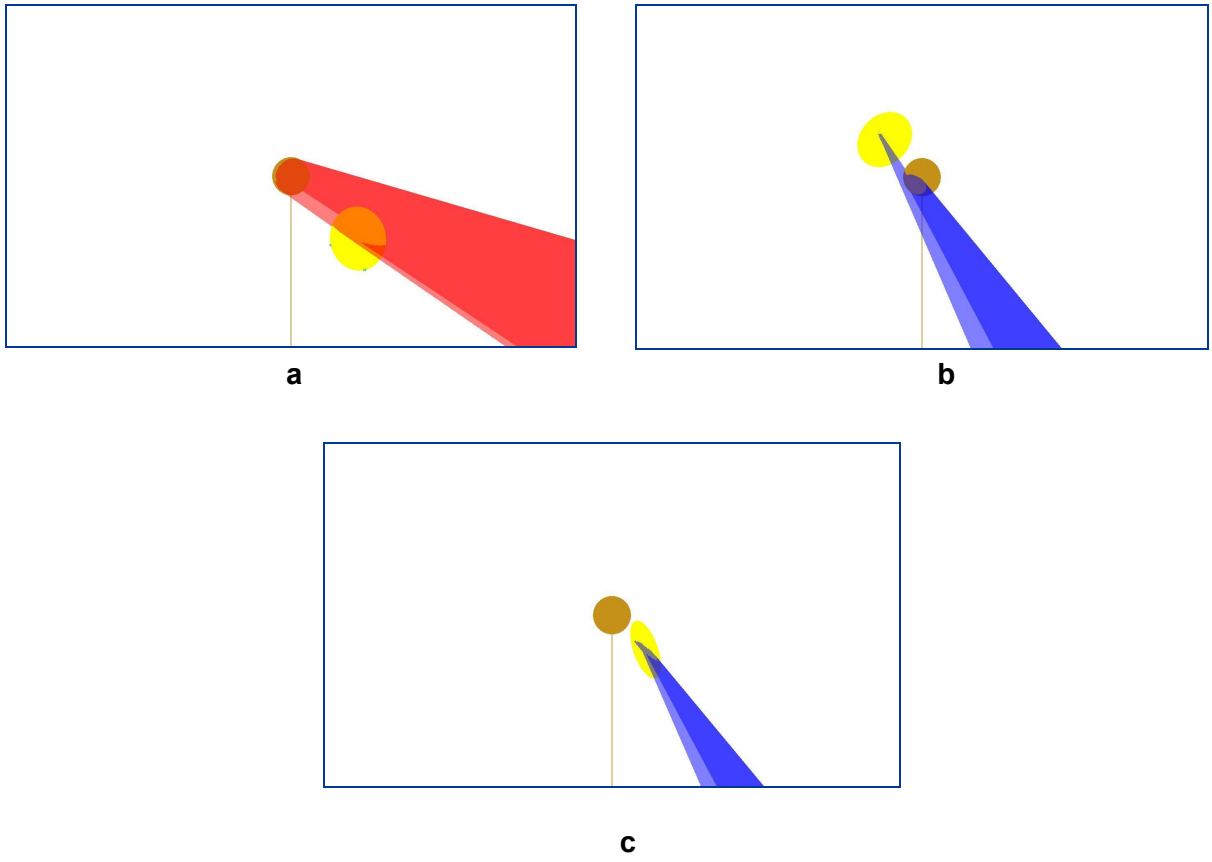

Figure 5: Constraints on the foils. Figure (a) shows an example of when a foil does not clear one of the OMEGA laser beams. Figure (b) shows an example of the target stalk being positioned between an OMEGA EP beam and a foil. Figure (c) shows a large OMEGA EP beam incidence angle.

1) The foils must be clear of all 60 OMEGA laser beams. If the foil is clear of the closest OMEGA beam, then it is clear of all of the beams. An example of a foil not clearing one of the OMEGA laser beams can be seen in Fig. 5a. So, a MATLAB function was generated to loop through all of the OMEGA laser beams and return the Beam ID of the closest beam. The half-angular size is defined as the angle formed by the center of the foil (or beam), the center of

the capsule, and the edge of the foil (or beam). The foil was defined to be clear of the closest beam if the sum of the half-angular sizes of the foil and the beam was less than the angular distance between the center of the foil and the beam. Rotation of the foil will reduce the angular size of the foil, so this condition is an overestimate of the limit which will serve as a safety buffer. The half-angular size of the foil is arctan($\frac{F_r}{r}$) where F_r is the radius of the foil and r is the distance of the foil from the capsule, assuming that the foil is oriented to face the capsule (the worst case). OMEGA beams typically have an f/#, which is the focal length divided by the lens diameter, of 6.65 and a radius at best focus of $R_{spot} \approx 360\ \mu m$. The radius of the OMEGA beam at a distance of r from the focus is approximately $\sqrt{{R_{spot}}^2 + \frac{1}{4}(\frac{r}{6.65})^2}$. Then the half-angular size of the beam at a distance of r from the capsule is approximately arctan($\frac{1}{2}\sqrt{(\frac{R_{spot}}{r})^2 + \frac{1}{4}(\frac{1}{6.65})^2}$). So,

$$\Delta(F,B) \geq \text{arctan}(\tfrac{F_r}{r}) + \text{arctan}(\tfrac{1}{2}\sqrt{(\tfrac{C\,R_{spot}}{r})^2 + \tfrac{1}{4}(\tfrac{1}{6.65})^2}), \qquad [1]$$

where $\Delta(F,B)$ is the angular distance between the center of the foil and the beam and C (≥ 1) is some safety constant, must be satisfied in order for none of the lasers to hit the foil.

2) The capsule stalk cannot be positioned between an OMEGA EP beam and a foil. For this constraint to be satisfied, the foil must be in front of the stalk from the perspective of the beam, the point of closest approach from the beam to the Z (vertical) axis must have a positive Z value (we can assume that the condition that the OMEGA EP beam doesn't hit the capsule has been satisfied), or the beam radius must be smaller than the distance to the stalk at the point on the beam that is closest to the stalk. Fig. 5b shows an example of a foil placed behind the capsule from the perspective of the OMEGA EP beam and as a result, the beam hits the capsule and stalk before it reaches the foil. The points on the beam axis directed at the center

of foil **F** can be defined parametrically as **B**(t) = **F** + t$\widehat{B}_{EP}$, where $\widehat{B}_{EP}$ is the unit vector in the direction the beam comes from (see Fig. 4 for a visual representation). The distance from the beam to the stalk is D(t) = $\sqrt{\widehat{B}_x(t)^2 + \widehat{B}_y(t)^2}$. To find the point of closest approach, $\frac{d(D^2)}{dt}$ = 0 is solved for t, resulting in $t_c = -\frac{F_x\widehat{B}_x + F_y\widehat{B}_y}{\widehat{B}_x^2 + \widehat{B}_y^2}$. The radius of the beam here is $\frac{|t_c|}{2f}$, where *f* is the f-number of the OMEGA-EP beam (f = 6.65). So, the foil is in front of the stalk from the perspective of the beam when

$$t_c < 0.$$

The point of closest approach from the beam to the Z axis has a positive Z value when

$$F_z + t_c\widehat{B}_z > 0.$$

The beam radius is smaller than the closest distance to the stalk when

$$\frac{|t_c|}{2f} < \sqrt{(F_x + t_c\widehat{B}_{EP,x})^2 + (F_y + t_c\widehat{B}_{EP,y})^2} . \qquad [2]$$

The condition is satisfied if any of these are true.

3) The angle of incidence between the OMEGA EP beam and the foil cannot exceed 65°. The laser energy is absorbed best by the foils when they are hit head-on by the laser, so as the angle of incidence increases, less laser energy is absorbed and more scatters, potentially hitting and damaging other equipment in the chamber. This constraint is controlled by the tilt of the foils with respect to the incident laser. A beam-foil coordinate system defined by unit vectors (B_1, B_2, $B_{\parallel}$) was created in which the z-axis ($B_{\parallel}$) is parallel to the direction of the laser beam, the x-axis (B_1) is perpendicular to both the position of the foil with respect to the capsule and the beam direction, and the y-axis (B_2) is perpendicular to the x- and z-axes (see Fig. 6).

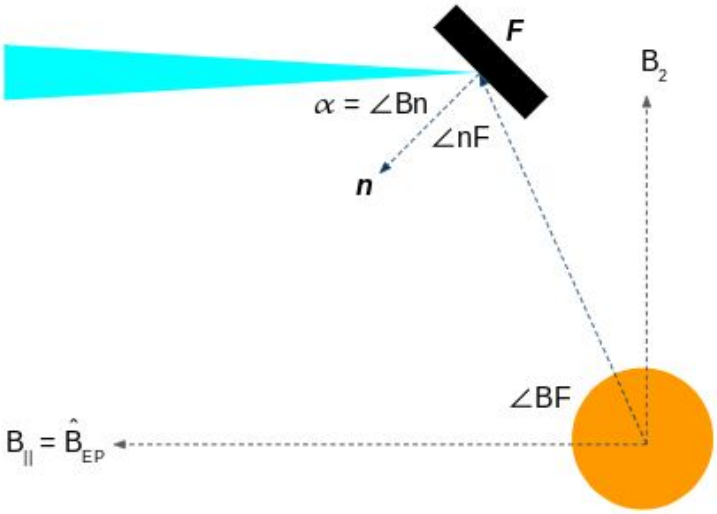

Figure 6: Schematic of OMEGA EP beam (blue), foil (black), and capsule (orange), showing vectors and angles. The unit vector B_1 is directed out of the page.

The orientation angles of the beam with respect to the target chamber axes are polar angle = 116.6° and azimuthal angle = 18°. Let **F** be the position of the foil in cartesian coordinates. Then the new axes can be defined by

$$B_{\parallel} = \widehat{B}_{EP}\,, \qquad [3a]$$

$$B_1 = \frac{F \times B_{\parallel}}{\left| F \times B_{\parallel} \right|}\,, \qquad [3b]$$

and

$$B_2 = B_{\parallel} \times B_1\,, \qquad [3c]$$

where $\times$ is the vector cross product.

Let *p* and *a* be the polar and azimuthal angles of the normal to the foil $\widehat{n}$ with respect to the target chamber. Define $\widehat{n}$ = <x, y, z> to be the cartesian coordinates in the chamber coordinate system when converted from the spherical coordinates <1, *p*, *a*>. Then the normal $\widehat{n}$ is given with respect to the new axes by

$$\widehat{n}(\alpha, \beta) = B_{\parallel} \cos\alpha - (B_1 \sin\beta + B_2 \cos\beta) \sin\alpha \qquad [4]$$

where α is the angle between $\hat{n}$ and $B_{\parallel}$, and β is the angle between the projection of $\hat{n}$ into the (B_1, B_2) plane and the (-B_2) axis. The tilt of the foil can be defined by two angles,

$$\alpha = \arccos(\hat{n} \cdot B_{\parallel}) \qquad [5a]$$

and

$$\beta = \arctan\left(\frac{\hat{n} \cdot B_1}{\hat{n} \cdot B_2}\right), \qquad [5b]$$

where α is the in-plane angle (the angle of incidence), β is the out-of-plane angle, and $\cdot$ is the vector dot product. The case where $\beta = 0$ ($\hat{n} \cdot B_1 = 0$) corresponds to the normal $\hat{n}$ lying in the plane of Fig. 6. In order for the angle of incidence between the OMEGA EP beam and the foil to not exceed 65°, α must not exceed 65°. There is no constraint on β. Fig. 5c shows how the α limit makes it difficult to direct the x rays onto the capsule when it has a small $\angle BF$ (from Fig. 6).

3.2 Defining and Generating Sets of Foils

Each set of foil locations can be defined by four parameters, r, θ, ϕ, and η, where r, θ, and ϕ define the position of the first foil, F_1, in spherical coordinates, and η defines the rotation of the remaining foils about the F_1 axis. To determine the positions of the other foils from these four parameters, an axis parallel ($\hat{Z}'$) and axes perpendicular ($\hat{X}'$, $\hat{Y}'$) to F_1 must be defined. $\hat{Z}'$ is a unit vector parallel to F_1, which is defined by

$$\hat{Z}' = \frac{<F_{1x}, F_{1y}, F_{1z}>}{F_{1r}}, \qquad [6]$$

where $F_{1r} = \sqrt{F_{1x}^2 + F_{1y}^2 + F_{1z}^2}$ is the distance of the first foil from the capsule.

To get the perpendicular vectors, a reference vector must be chosen. If <0, 0, 1> is the reference vector, then the perpendicular vectors can be defined as

$$\hat{X}' = \frac{<0, 0, 1> \times \hat{Z}'}{\left| <0, 0, 1> \times \hat{Z}' \right|} \qquad [7]$$

And

$$\widehat{Y}' = \widehat{Z}' \times \widehat{X}'. \qquad [8]$$

If F_1 is parallel to <0, 0, 1>, then $\widehat{X}'$ = <1, 0 ,0>, and $\widehat{Y}'$ = <0, 1, 0>.

The position of foil *j* in the tetrahedral, cubic, and octahedral geometries with a rotation η about the F_1 axis can be written as

$$F_j = F_{1r}[(T_{jx}\cos\eta + T_{jy}\sin\eta)\widehat{X}' + (T_{jy}\cos\eta - T_{jx}\sin\eta)\widehat{Y}' + T_{jz}\widehat{Z}']. \qquad [9]$$

The coefficients T_{ji} are defined in Table 1.

Geometry	*j*	T_{jx}	T_{jy}	T_{jz}
Tetrahedron	1	0	0	1
	2	$\sqrt{8/9}$	0	-1/3
	3	$-\sqrt{2/9}$	$\sqrt{2/3}$	-1/3
	4	$-\sqrt{2/9}$	$-\sqrt{2/3}$	-1/3
Cube	1	0	0	1
	2	1	0	0
	3	0	1	0
	4	-1	0	0
	5	0	-1	0
	6	0	0	-1
Octahedron	1	0	0	1
	2	$\sqrt{2/3}$	$\sqrt{2/9}$	1/3
	3	$-\sqrt{2/3}$	$\sqrt{2/9}$	1/3
	4	0	$-\sqrt{8/9}$	1/3
	5	0	$\sqrt{8/9}$	-1/3
	6	$\sqrt{2/3}$	$-\sqrt{2/9}$	-1/3
	7	$-\sqrt{2/3}$	$-\sqrt{2/9}$	-1/3
	8	0	0	-1

Table 1: Locations of vertices for unit polyhedrons where F_1 *= (0,0,1).*

3.3 Process to find optimal foil geometries

The goal of this study was to find a foil geometry that maximizes mean x-ray intensity on the capsule as well as uniformity. VisRad [7], a view factor code, was used to simulate the radiation flux onto a capsule for each foil geometry. The x-ray uniformity was assessed by calculating the ratio of the incident flux standard deviation to the mean incident flux. Ease of implementation should also be taken into account in the future. So, even though an 8-foil geometry will yield higher uniformity than a 4-foil geometry, it is possible that the 4-foil geometry will be chosen over an 8-foil geometry because it is more practical to field 4 foils than 8. Some actions improved one of these parameters while worsening others, so foil geometries were sought that had a balance between these parameters.

For example, putting the foils closer to the capsule generally increased their x-ray intensity and uniformity. However, this wasn't always the case. For the tetrahedron, since there were only four foils to irradiate the capsule, if the foils got too close, uniformity decreased, contrary to what happened with the cubic and octahedral geometries.

At a given foil-to-capsule distance, the maximum flux was limited by the smallest value of the angle ∠BF (see Fig.6 for these angles) within each set of foils. Since there is an upper limit on ∠Bn (65°), the foil with the smallest ∠BF necessarily has the largest ∠nF, and therefore limits the incident flux on the capsule. The minimum value of ∠BF was found for each set of foils, and the set with the largest minimum value was expected to produce the largest x-ray flux. The largest possible ∠BF was constrained by geometry, and was 70.5° for the tetrahedron and 54.7° for the cube and octahedron. However, due to the constraints described in Section 3.1, these largest possible minimum ∠BF 's could not be achieved in practice. The largest minimum ∠BF that were found were in the 50°s for the tetrahedron and in the 40°s for the cube and octahedron.

A MATLAB function was written to randomly generate sets of foils for each foil geometry given a distance between the foils and the capsule. So, a distance between the foils and the capsule and the number of generated sets of foils that was to be returned would be input into the function, and foil sets with the θ, Φ, and η values along with the smallest ∠BF were returned. In general, the goal was to minimize the distance between the foils and the capsule while also retaining a large, smallest ∠BF. The best sets of foils found for each foil geometry by this random generator were then put into VisRad.

To maximize the smallest ∠BF, an iterative MATLAB function was written to return the range of θ, Φ, or η values (defined in Section 3.2) for a specific foil geometry that satisfied all of the constraints given a foil-to-capsule distance and two of the three parameters, θ, Φ, and η . For example, r, θ, and Φ would be input and ranges, to the nearest hundredths place, of η values that satisfied all of the constraints were output. The previous η value would then be replaced by the value in that output range that produced the largest, smallest ∠BF. This was then done with the other two parameters, θ and Φ: r, Φ, and η would be input and ranges, to the nearest hundredths place, of θ that satisfied all of the constraints were output, and the previous θ value would then be replaced by the value in that output range that produced the largest, smallest ∠BF. Likewise, r, θ, and η would be input and ranges, to the nearest hundredths place, of Φ that satisfied all of the constraints were output, and the previous Φ value would then be replaced by the value in that output range that produced the largest, smallest ∠BF. Starting from a randomly selected foil configuration defined by the four parameters (r, θ, Φ, η) that satisfied the conditions, ranges for θ, Φ, and η were found, and the previous θ, Φ, and η values were replaced by the values in that range that produced the largest, smallest ∠BF. Then the distance between the foils and the capsule would be increased, and this process would be

repeated until the smallest ∠BF was as large as possible while still fulfilling the clearance conditions described in Section 3.1.

3.4 Normal vector optimization

The tilts on the foils were varied in VisRad to optimize intensity and uniformity. The same beam-foil coordinate system was used as in Section 3.1. The normal vector $\hat{n}(\alpha, \beta)$ defined in Eq. (4) can be used in VisRad by converting $\hat{n}$ shown in Fig. 6 to spherical coordinates, (r, polar, azimuthal) with respect to the target chamber axes and inputting the polar and azimuthal angles. A MATLAB function was written that returns the polar and azimuthal angles given the coordinates of the foil and its α and β.

For foils with a small angle $\angle BF$, it is harder for x rays to reach the capsule. So to start, the foil with the smallest $\angle BF$ had its tilt set. α was set to 65°, the maximum tilt allowed in the target chamber, and β was set to 0°. This would maximize the amount of x rays generated by that foil that would be directed towards the capsule since this foil was the limiting factor for the foil set in terms of x-ray intensity.

The alphas and betas of the other foils were determined by manual iteration. The α and β of the other foils were initially set to 65° and 0°, respectively. Then the α and/or β of one of the foils was changed by a small amount. The simulation was then run. If nonuniformity, which was calculated by dividing the standard deviation by the mean incident flux, decreased, the tilt was moving in the right direction and it was further changed in that same direction. If nonuniformity increased, the tilt was changed in the opposite direction. The tilt on each foil was altered a little bit before moving onto the next foil. The foils' tilts were optimized in a rotating pattern, excluding the foil with the smallest $\angle BF$. No foil was altered too much at once. In the end, each foil's tilt was altered multiple times with the goal of maximizing uniformity. This procedure did not guarantee that an optimal radiation intensity and uniformity was reached for each foil geometry.

However, by inspection, reasonable illumination symmetry was achieved for all geometries, as described in the next section.

4. Optimized foil geometries

Three approaches were taken to optimize foil geometries. The first approach optimized x-ray uniformity on the capsule. The other two approaches maximized incident flux by decreasing the distance between the foils and the capsule, either by decreasing the radius of the foils or by breaking the polyhedral symmetry.

4.1 Optimized Uniformity with Foil Radius of 0.8 mm

This approach worked on decreasing the nonuniformity of the x-ray distribution on the capsule by finding good foil geometries as described in section 3.3 and then optimizing the normal vector through the process described in section 3.4. The results can be found in Table 2. Incident flux and uniformity can be visually compared between the three foil geometries in Fig 7. (The same total beam power, which is energy per unit time of a beam, was used for the 4-foil, 6-foil, and 8-foil geometry in all three scenarios. In this simulation, 1 TW of total beam power was used and a conversion efficiency of 60% into x rays was assumed.) The cubic geometry produced the highest mean incident flux, while the octahedral geometry produced the most uniform distribution of x rays onto the capsule. The octahedral geometry had the lowest mean incident flux because this geometry utilized the highest number of foils so in order to satisfy all of the constraints, it needed a bigger r value, decreasing x-ray intensity. However, this geometry had the best uniformity because its large number of foils allowed it to irradiate the capsule the most evenly.

	(r, theta, phi, eta) (r in mm and θ, Φ, and η in °)	Mean incident flux (TW/ cm^2)	$\frac{standard\ deviation}{mean}$
Tetrahedron	(9.2, 64.4, 340.6, 97.9)	0.036	0.096
Cube	(6.6, 56.8, 336.6, 96.3)	0.047	0.095
Octahedron	(11.4, 117.5, -125.8, 69.9)	0.014	0.08

Table 2: Location, mean incident flux, and uniformity measure for the most uniform tetrahedral, cubic, and octahedral foil geometries found. Of these three, the cubic geometry had the highest mean incident flux, and the octahedral geometry had the lowest. The octahedral geometry was also the most uniform, although all had uniformity better than 10%.

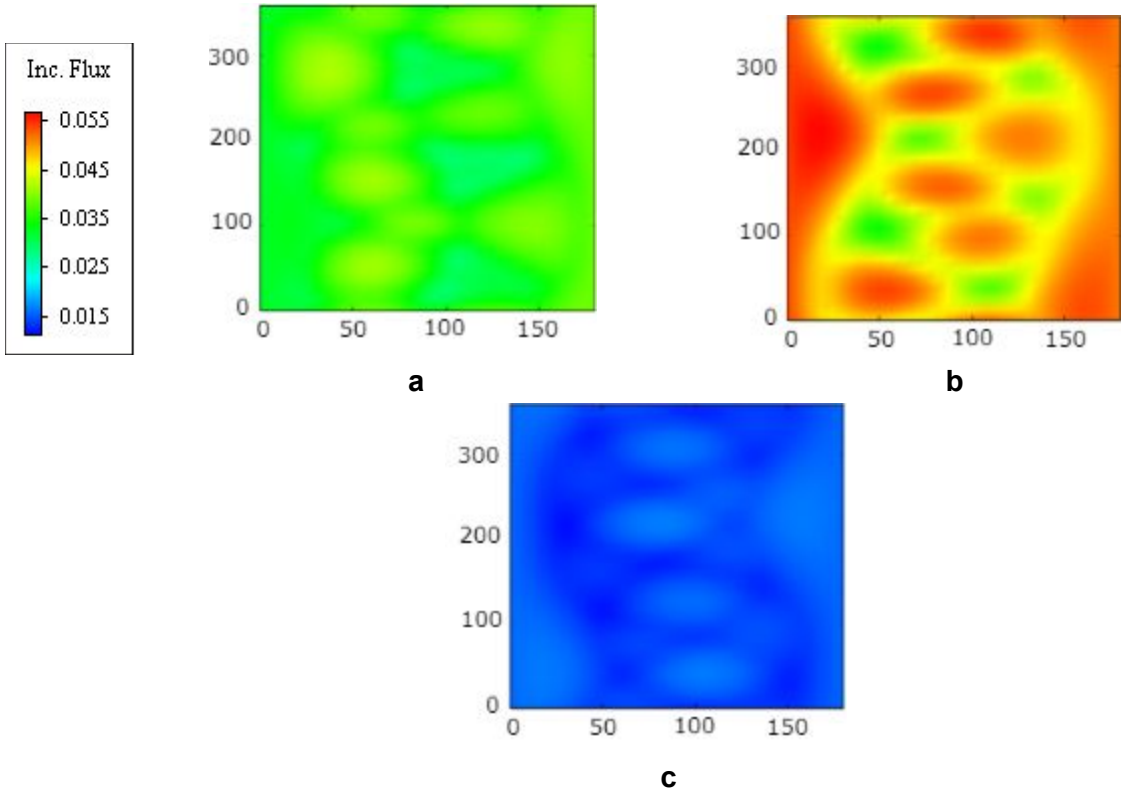

Figure 7: Incident flux plots (TW/cm^2) versus location on the capsule surface for the (a) tetrahedral, (b) cubic, and (c) octahedral foil geometries with θ on the horizontal axis (in degrees) and Φ on the vertical axis.

4.2 Maximized Incident Flux by Decreasing Radius

This approach used the foil positions found in Section 4.1 as the baseline. The radii of the foils were decreased, allowing them to sit closer to the capsule. Since uniformity decreased as the foils got closer to the capsule for the tetrahedral foil geometry, the cubic and octahedral foil geometries were the only polyhedra analyzed using this technique. The radii of the foils were decreased from 0.8 mm to 0.5 mm, although it is unknown how small the foils can actually get. (Ease of implementation and practicality must be taken into account.) Then the same approach as used in Section 4.1 was used to maximize uniformity. The results can be found in Table 3. The increase in incident flux intensity can be seen visually in Fig. 8, with a 61% increase for the cubic geometry and a 74% increase for the octahedral geometry. Uniformity improved as well but not by much.

	(r, theta, phi, eta) (r in mm and θ, Φ, and η in °)	Mean incident flux (TW/ cm^2)	$\frac{standard\ deviation}{mean}$
Cube	(5.2, 56.8, 336.6, 96.3)	0.076	0.092
Octahedron	(8.7, 1, 354, 82)	0.025	0.079

Table 3: Location, mean incident flux, and uniformity measure for the cubic and octahedral foil geometries found that maximized incident flux by decreasing the foil radius from 0.8 mm to 0.5 mm. The mean incident flux increased greatly for both geometries with a 61% increase in the cubic geometry and a 74% increase in the octahedral geometry while maintaining almost the same uniformity. The cubic geometry still had the highest mean incident flux, and the octahedral geometry was still the most uniform.

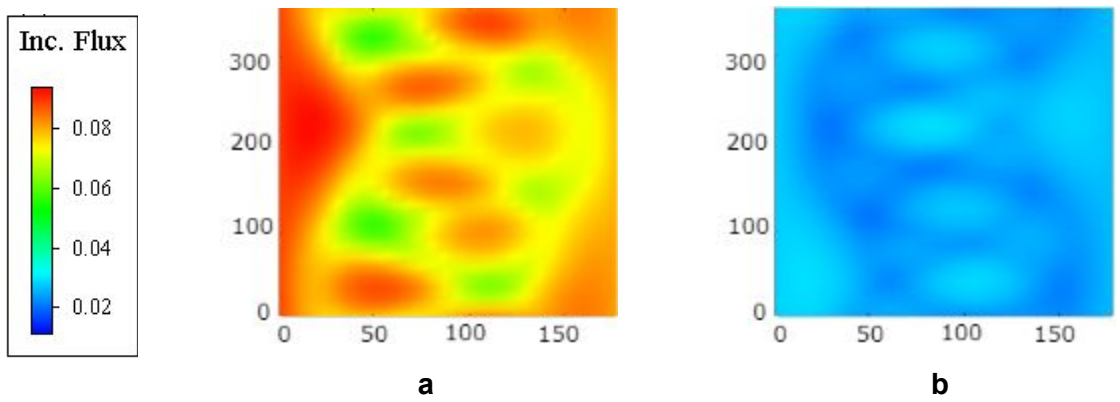

Figure 8: Incident flux plots (TW/cm^2) versus location on the capsule surface for the (a) cubic geometry and (b) octahedral geometry with θ on the horizontal axis and Φ on the vertical axis after the foil radius was decreased from 0.8 mm to 0.5 mm.

4.3 Maximized Incident Flux by Breaking Symmetry

This approach also used the foil positions found in Section 4.1 as a baseline. The radii of the foils was held at 0.8 mm in this approach, the same as in Section 4.1. From there, the position of any foil that was so close to any of the OMEGA beams that the distance between the foil and capsule couldn't be decreased any more was moved slightly away from whichever beam it was closest to. This allowed for the distances between the foils and the capsule to be decreased even more, increasing the incident flux but also increasing nonuniformity. The process of breaking polyhedral symmetry and decreasing the distance between the foils and the capsule was continued until $\frac{standard\ deviation}{mean}$ equalled 0.1. The results can be found in Table 4. The change in incident flux intensity and uniformity can be seen visually in Fig. 9. When Sections 4.1 and 4.3 are compared, a dramatic increase in incident flux intensity can be seen for both geometries. The foils for the cubic geometry were able to get slightly closer to the capsule (the r value decreased from 6.6 mm to 5.7 mm), while the foils for the octahedral geometry were able to get much closer to the capsule (the r value decreased from 11.4 mm to 6.5 mm). This allowed for the cubic geometry to experience a 34% increase in incident flux and

the octahedral geometry to experience a large, 273% increase. Nonuniformity increased slightly for both, with a 5% increase for the cubic geometry and a 25% increase for the octahedral geometry.

	(r, theta, phi, eta) (r in mm and θ, Φ, and η in °)	Mean incident flux (TW/ cm^2)	$\frac{standard\ deviation}{mean}$
Cube	(5.7, 56.8, 336.6, 96.3)	0.063	0.1
Octahedron	(6.5, 1, 354, 82)	0.053	0.1

Table 4: Location, mean incident flux, and uniformity measure for the cubic and octahedral foil geometries found that maximized incident flux by breaking the symmetry of the foils while keeping $\frac{standard\ deviation}{mean}$ *below 0.1. (The (x, y, z) coordinates for each foil don't match exactly with the given (r, theta, phi, eta) values because their positions were moved in order to avoid the beams.) This approach increased the incident flux by 34% for the cube and 273% for the octahedron.*

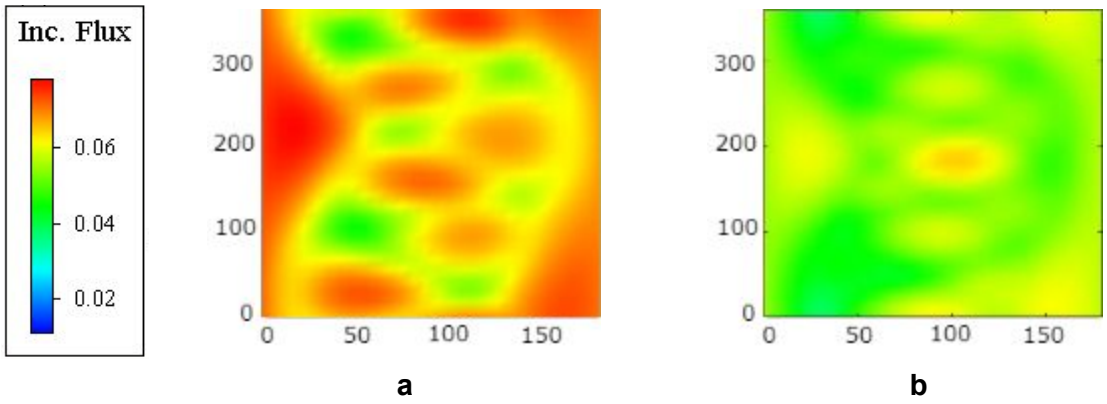

Figure 9: Incident flux plots (TW/cm^2) versus location on capsule surface for the (a) cubic geometry and (b) octahedral geometry with θ on horizontal axis and Φ on vertical axis after polyhedral symmetry was broken.

5. Conclusion

In direct-drive inertial confinement fusion, it is important that the capsule be irradiated as uniformly as possible in order to maximize the amount of fusion generated during the implosion.

Laser imprint is one cause of capsule nonuniformities. This project explored the x-ray pre-illumination technique in which metal foils are heated to produce x rays onto the capsule before the main lasers are turned on. MATLAB functions were written to find optimal foil locations; these foils were then put into VisRad where foil locations and tilts were analyzed in order to optimize the incident flux and uniformity on the capsule. Foil positions were found three different ways: the first optimized uniformity, the second maximized incident flux by decreasing the radii of the foils to allow the distance between the foils and the capsule to be decreased, and the third allowed the foils to come closer to the capsule by breaking polyhedral symmetry. The six-foil geometry produced the highest mean incident flux in all three cases with nonuniformity below 10%. The eight-foil geometry provided the lowest asymmetry (<8%) at the expense of a greatly reduced incident flux. However, the four-foil geometry would be easiest to implement. Future work includes realistic mounting for the foils, calculations of absorbed flux using real x-ray spectra, and ultimately experimental tests.

6. Acknowledgements

I would like to thank my advisor, Dr. Hans Rinderknecht, for his guidance throughout my project. I couldn't have done it without his patience and endurance. I would also like to thank Dr. Jonathan Peebles for sharing his experimental results with me to assist with my project report. Lastly, I would like to thank Dr. Stephen Craxton for making possible this once-in-a-lifetime opportunity of working in this world-renowned laboratory.

7. References

1. J. Nuckolls, L. Wood, A. Thiessen, and G. Zimmerman, "Laser compression of matter to super-high densities: Thermonuclear (CRT) applications," Nature, **239**, 139 (1972).
2. R.S. Craxton et al., "Direct-Drive Inertial Confinement Fusion: A Review," Physics of Plasmas **22**, 110501 (2015).

3. D.H. Sharp, “An Overview of Rayleigh-Taylor Instability,” Physica D. **12**: 3-18 (1948).
4. O. Willi “Lecture 2: Symmetry issues”, Institut für Laser - und Plasmaphysik
5. M. Nishikino, et al., “Imprint reduction in a plasma layer preformed with x-ray irradiation,” Phys. Plasmas **9**, 1381 (2002).
6. J. Peebles, private communication, Sept 2019.
7. J. J. MacFarlane, “VISRAD – A 3-D view factor code and design tool for high-energy density physics experiments,” Journal of Quantitative Spectroscopy and Radiative Transfer 81, 287 (2003).

Micro-Raman Spectroscopy of Silica and Hafnia Laser Damage Sites

Ji-Mi Jang

Pittsford Mendon High School

Advisor: **Dr. Tanya Kosc**

Laboratory for Laser Energetics

University of Rochester

Rochester, New York

January, 2020

Abstract

Micro-Raman spectroscopy was used to characterize laser-induced material modification of silica and hafnia thin films, which are used to produce critical multi-layer dielectric thin film coatings for the Omega Laser Facility at the Laboratory for Laser Energetics. Several parameters relevant to laser-induced damage, such as laser fluence, testing protocols (1-on-1 versus N-on-1 tests), and thin film materials have been probed and compared through the analysis of their Raman spectra. The spectra obtained for silica and hafnia thin films are similar, both showing Raman features and photoluminescence (PL), but easily discernible. Clear distinctions in PL intensity help differentiate between low and high fluence damage sites as well as between damaged and undamaged areas. This information could be applied to the future design and manufacturing of thin film coatings.

1. Introduction

Micro-Raman spectroscopy is a non-damaging technique that studies vibrational modes of molecules to analyze molecular interaction and structure. During the process, a laser beam irradiates a test site, and some of the laser energy is absorbed by certain bonds, providing energy to start a vibration between two atoms. The different vibrational modes are specific to certain bonds, allowing the modes to be used as identifying characteristics useful for analyzing molecular structures. Different types of scattering can occur, each resulting in a different wavelength (λ) of the reemitted signal (Figure 1). The first type is Rayleigh scattering, which occurs when none of the laser energy is lost to initiating vibrations, and the reemitted light has the same wavelength as that of the incident beam. The second type is scattering due to the Raman effect, from which, depending on the frequencies of the vibrations, the reemitted

wavelengths differ from the incident laser beam wavelength. The unit (quantum) of energy transferred to atomic or molecular vibrations is referred to as a phonon. The energy of the incident photon that was not transferred to a phonon becomes the energy of the scattered photon and determines the new wavelength of the reemitted light that produces the Raman signal. These new wavelengths are represented by a shift from the wavelength of the incident laser beam and are quantified in terms of the wavenumber shift (cm^{-1}). Wavenumber is a measure of spatial frequency and is defined as $1/\lambda$. Zero wavenumber shifts correspond to the wavelength of the incident (pump) laser beam, so any wavelength deviation indicates a shift in frequency of the reemitted light from the incident beam. Compared to Rayleigh scattering, the Raman effect is much weaker. Nonetheless, it produces essential information that this work uses to investigate material modifications.

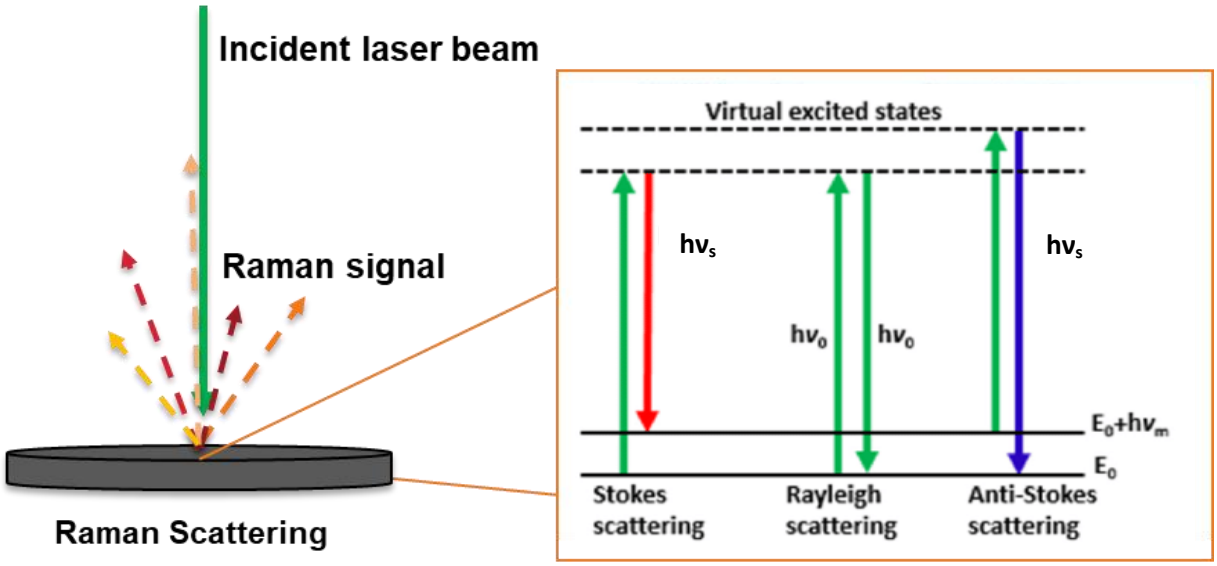

Figure 1: Diagram representing different forms of scattering. Left: A 532 nm green laser beam is incident upon the sample site where scattering occurs. A scattering signal consisting of different wavelengths is reemitted, with the signal at each of the wavelengths depending on the amount of energy lost to molecular vibrations. Right [1]: An energy diagram indicates the difference between Stokes and Anti-Stokes Raman scattering. Stokes scattering is much more common than Anti-Stokes scattering, and the reemitted light has lower or higher wavelength, respectively, than the original laser beam.

Raman scattering is further classified as Stokes and Anti-Stokes scattering. The absorption of an incident photon with energy $h\nu_0$ (note: this is not the absorption of the whole incident laser beam) is followed by the emission of a scattered photon with energy $h\nu_s$. Figure 1 shows different energy levels of the excited electronic state after absorption. The arrows pointing up depict laser energy absorbed, differing from the arrows pointing down, which show reemitted photon energy. Stokes scattering, which occurs much more frequently than Anti-Stokes scattering, arises after energy has been lost to molecular vibrations. In this situation, the reemitted photon has less energy than the initial photon. A lower-energy photon will oscillate at a lower frequency and therefore have a longer wavelength. Anti-Stokes scattering occurs when photons are reemitted with more energy than what was initially absorbed. In this case, the molecule is already vibrating and in an excited state. The energy from the excited state is added to the energy of the absorbed (pump) photon, so the reemitted photon is more energetic and therefore oscillates at a higher frequency (and has a shorter wavelength). The type of scattering occurring is depicted by the directions in which the Raman peaks are shifted – Stokes to the right of the origin with positive wavenumber shifts, and Anti-Stokes to the left with negative wavenumber shifts. In this experiment, Stokes scattering is considered (Figure 2). Had there been observations of leftward (negative) shifts of the signal wavenumber, they would have indicated Anti-Stokes scattering.

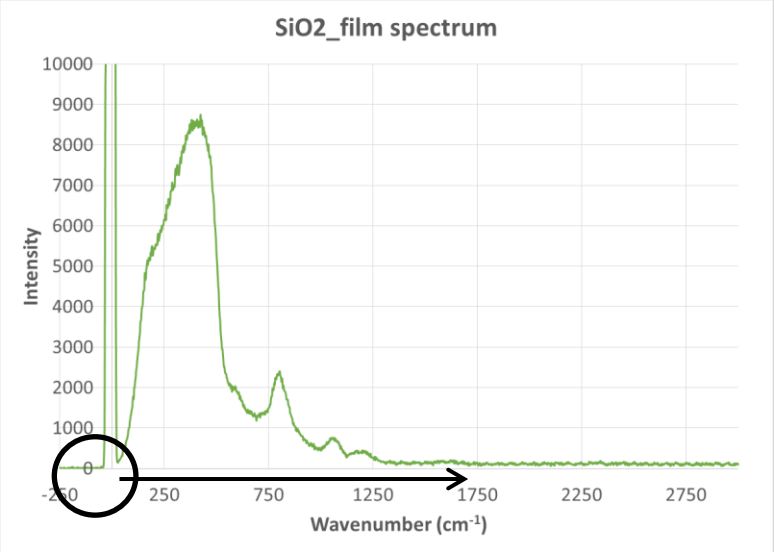

Figure 2: A neat (undamaged) silica film spectrum. The black circle indicates the origin at which zero wavenumber shift is located. The black arrow points to the rightward shift of the signal wavenumbers (i.e. Stokes scattering). In this and similar figures, "wavenumber" indicates wavenumber shift.

The main immediate purpose of this work is to better understand how damage forms. Most fundamentally, this work strives to answer the questions of how material (silica or hafnia) and its density change. Fused silica is supposed to be amorphous (as opposed to crystalline quartz), but previous research shows that silicon dioxide polymorphs (a solid material that can exist in more than one form or crystal structure) form at extreme conditions [2]. If polymorphs are determined to be present, then a following question would involve further research on which polymorphs (shistovite, coesite) form, why, and how. This information would be useful to learn about the conditions that exist during damage as certain polymorphs require a specific temperature or pressure to form. Micro-Raman spectroscopy is an alternative method to detect damage and provide information on how the material might be changing.

2. Background

In previous studies at the Laboratory for Laser Energetics (LLE), abnormal peaks were observed on a spectrum taken on a silica damage site. As can be seen in Figure 3, a strange spike is apparent at approximately 495 cm^{-1}, where other spectra slope down in a smooth curve.

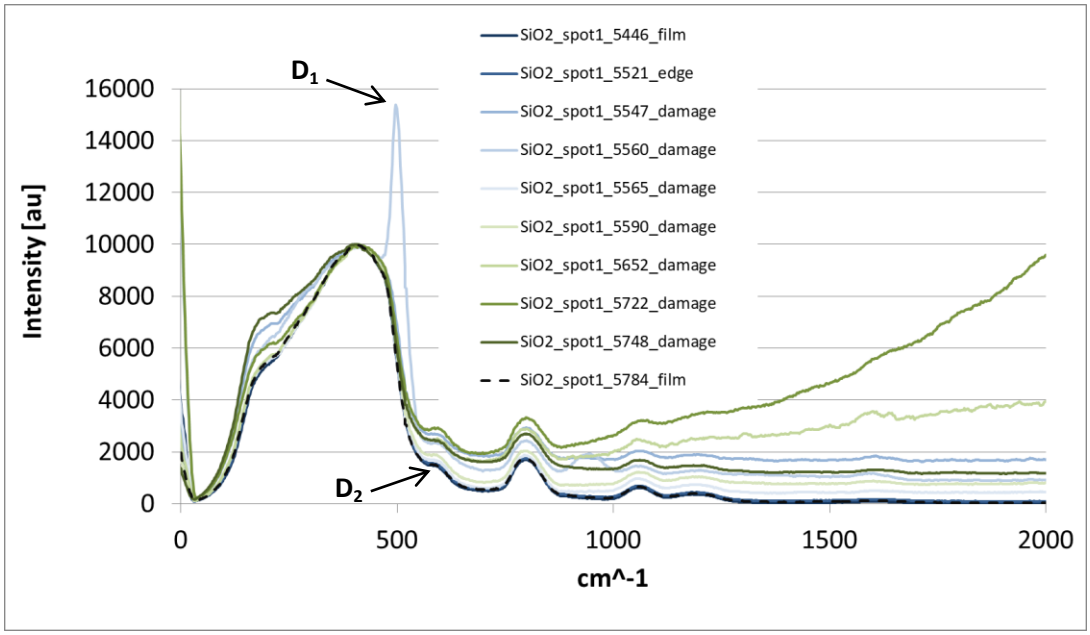

Figure 3: Graph depicting the abnormal peak on a spectrum taken from a silica damage site. Comparison with literature data identifies the peak as a defect, D_1. The emerging peak to the right of it is identified as another defect, D_2 [3]. The dashed curve (for readability) and the dark blue curve are undamaged film spectra. Their close overlap with each other indicates that undamaged film spectra are reproducible. Other solid curves are damaged film spectra (previous data acquired by Dr. T. Kosc). The D_1 defect feature is not observed on other damage film spectra as it is a rare material modification detected at only that location.

To investigate these defects, spectra obtained at LLE were compared with data presented in the literature. It was determined that the peaks arise as a result of molecular defects. The spike at 495 cm^{-1} is identified as a defect, D_1 [3]. In Figure 3, emerging peaks at approximately 600 cm^{-1} consistently appear in each of the spectra produced. This defect feature also appears on the two undamaged film spectra in figure 3 because this feature is commonly occurring and is not a modification due to the laser pulse. This feature could be strengthened by laser irradiation.

According to data from the literature (see Figure 4), these peaks at 600 cm^{-1} are identified as a defect, D_2 [3]. However, unlike the distinct peaks presented in Figure 4, the D_2 peak in Figure 3 is less obvious and is more characteristically similar to a knee feature than a Raman defect peak. Yet, its location and consistent appearance suggest that it is a defect peak riding on photoluminescence signals. Photoluminescence (PL) is also the reemission of absorbed light at lower wavelengths, but the mechanism of energy loss differs from Raman processes. After light has been absorbed by an irradiated sample and molecules enter a higher (excitation) electronic state, PL is the emission of light that occurs when photons are released as molecules return to a lower energy level.PL signals can often mask the Raman signal.

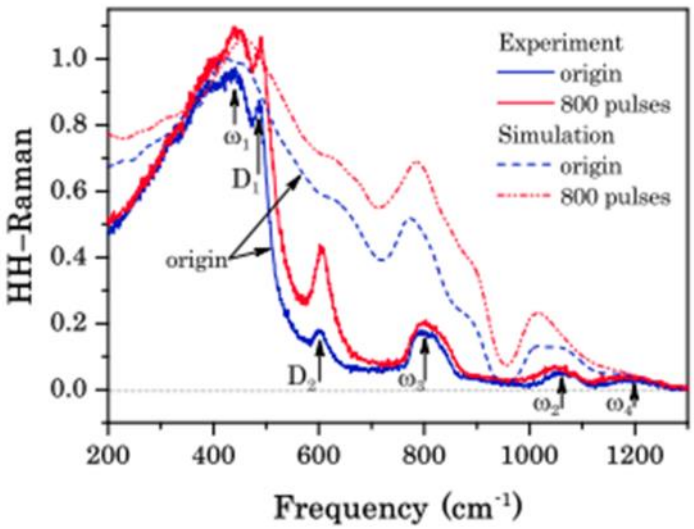

Figure 4: Identification of defect peaks. This graph, published by Shcheblanov [3], identifies D_1 and D_2 peaks along with other reference wavenumbers that are also found in LLE data (Figure 3) and produces evidence that the sharp peak (D_1) at 495 cm^{-1} is reproducible.

According to the literature, the D_1 and D_2 Raman defect spectra are due to the symmetric stretch of four- and threefold rings in the structure of vitreous silica [3, 4]. It is probable that the damage in silica results in a laser-induced densification [3]. Due to the similarities of traits

presented on the spectra, an analogous process could be inferred about the laser-induced damage spots produced at LLE.

3. Experimental Setup

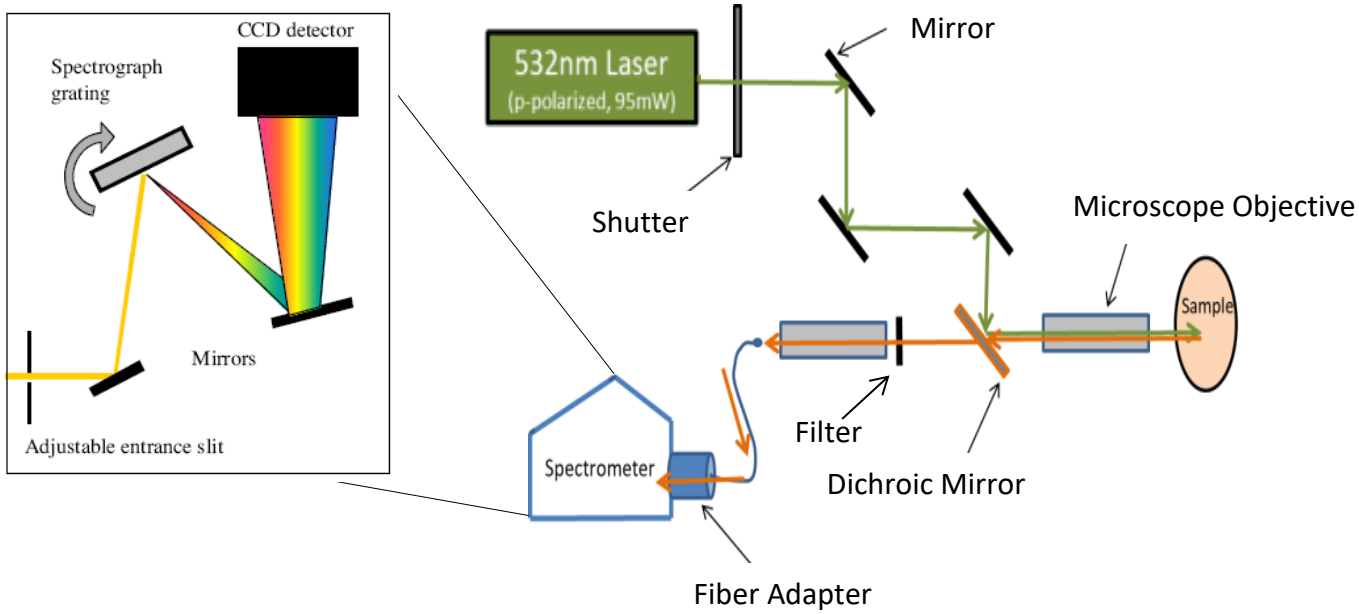

Figure 5: Experimental setup. The path that the laser beam takes from the laser source to the thin film sample is depicted by the green arrows. The path of the reemitted signal from the sample is represented by the orange arrows.

To conduct this research, a Laser Quantum GEM532 continuous laser (p-polarized, 95 mW) is used to probe silica and hafnia sample damage sites. As shown in Figure 5, the laser beam passes through a shutter and is then aligned by three consecutive mirrors positioned at 45 degrees. Reflected off the third mirror, the 532 nm laser beam hits a Razor Edge 532 dichroic mirror, designed for maximum reflection of 532 nm light at a 45-degree angle of incidence. (All other wavelengths are transmitted.) The dichroic mirror reflects green light and directs the laser beam to its target site on the sample. The laser beam is focused by a Mitutoyo WE835003118 M Plan Apo microscope objective onto specific locations on damage sites.

The laser beam is focused on silica damage sites of approximately 200 microns or hafnia damage sites ranging from approximately 70 to 400 microns. Upon radiation, the Raman scattering is collected by the same microscope objective and passes back through the dichroic mirror. Since the Raman scattering consists of wavelengths other than 532 nm, it is transmitted through the dichroic mirror. Unfortunately, this mirror does not filter out the 532 nm light entirely. Hence, a Razor Edge 532 filter is installed to filter out as much of the 532 nm wavelength from the scattering signal as possible to prevent overwhelming the Raman spectra with a strong green laser beam signal.

After the filter, the laser beam passes through an Opto Sigma, PAL-10-A, J11406689, 10x Plan, microscope objective, which focuses the scattering signal into a fiber optic. The light enters a fiber adapter where two lenses collimate the light and then properly focus the rays onto the 100-micron entrance slit of the Horiba iHR320 spectrometer. In the Horiba spectrometer, the signal is dispersed by a 600 lines/mm diffraction grating. The dispersed light is projected onto the pixels of a charge-couple device (CCD) detector to capture the signal spectrum.

4. Results

4.1 Silica Laser-Induced Damage Spots and Site Mapping

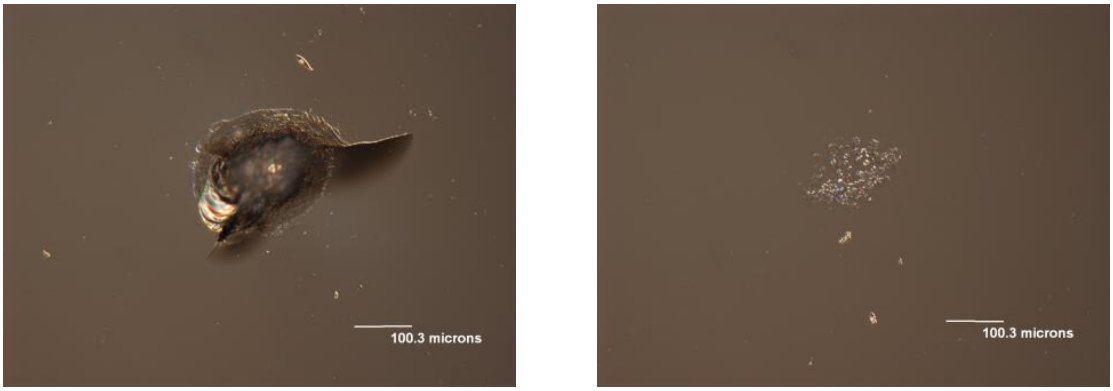

(a) **(b)**

Figure 6: (a) Damage spot 15 on the silica sample, damaged under high fluence. (b) Damage spot 21 on the silica sample, damaged under low fluence.

Using a Leica microscope, damage sites on both silica and hafnia samples were mapped out. Under the microscope, consecutive damage sites are in lines, increasing in visibility from one end to the other. This pattern is evidence that these sites were created with increasing laser fluences. Sites were distinguished from dust on the samples by their rounded shapes, organized formation for silica sites, and coloration for hafnia sites. Using one easily identifiable spot on the samples as the origin, the relative positions of each site were noted. Each damage site was labeled with a number and images similar to Figure 6a and 6b were captured.

Sample damage spots are produced with high and low fluences as well as with different testing protocols, including 1-on-1 and N-on-1 testing [5]. 1-on-1 testing involves irradiating a test site once at a specific laser fluence. N-on-1 testing involves irradiating a test site multiple times, each time with an increased fluence, until damage is created. Under the microscope, the sites are distinguished by their damage widths and features. Certain damage spots are observed with cracks that extend beyond the edges (Figure 6a). Some damage spots created under higher

fluences are observed to contain melted material, which creates depth to the damage site. Figure 6b shows a light damage spot with low material modification, which was created using a low fluence.

4.2 Silica Data Spectral Analysis

To better understand the unique characteristics present in the spectra of damaged spots, undamaged, or "neat," silica films were probed and compared. As depicted in Figure 7, it is evident that the neat films are characteristically similar. Normalized data result in nearly identical spectra that overlap each other. This confirms the hypothesis that neat silica films will have a similar molecular composition. Slight signal intensity discrepancies are noted at approximately 200 cm^{-1} and from 550 cm^{-1} to 1050 cm^{-1}, which are indicated by the red circles in Figure 7. These discrepancies are hypothesized to be caused by slightly different interactions of the sample surface with its environment, which are probably insignificant in the study of laser-induced damage.

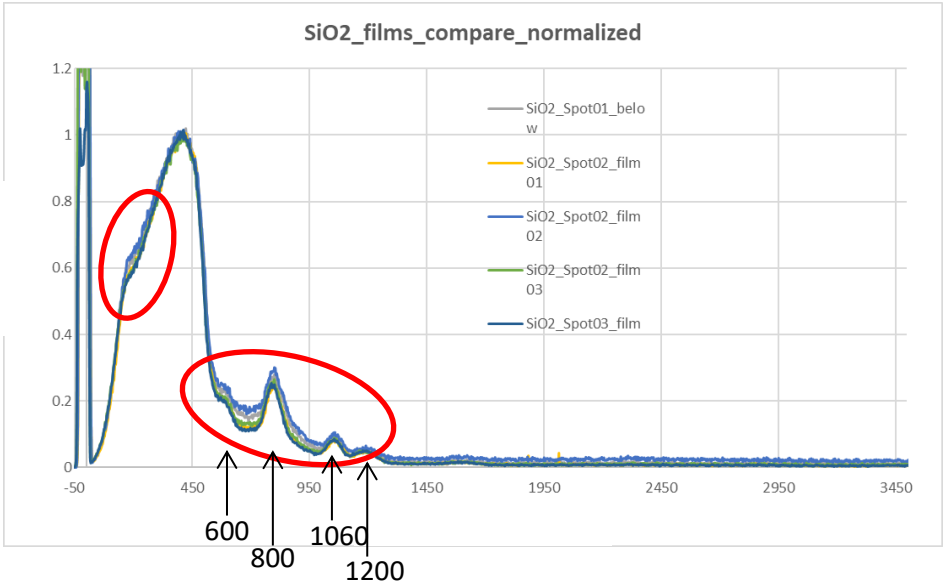

Figure 7: Comparison of normalized neat film spectra probed in various areas on the silica sample. Subtle differences in spectral feature intensities are observed (indicated by the red circles).

To identify material modifications on silica thin films resulting from laser-induced damage, spectra from neat films were compared with damage site spectra. Two damage spots on the silica sample were selected and probed at various positions within each spot. No additional peaks were noted in the damage sites to indicate defects. Looking at the spectra from damaged spot 02 shown in Figure 8, it is observed that while the main characteristics of the Raman signal, such as the Raman peaks prior to 1750 cm^{-1}, are present in each spectrum, the intensities of the spectra taken at the same location on spot 02 differ largely within the range from approximately 550 cm^{-1} to 7000 cm^{-1}. In Figure 8, the differences in magnitude are obvious when the spectra from two damaged sites (try1 and try75) are compared with the neat film spectrum (flat green curve). These variations likely arise due to PL resulting from the laser irradiation.

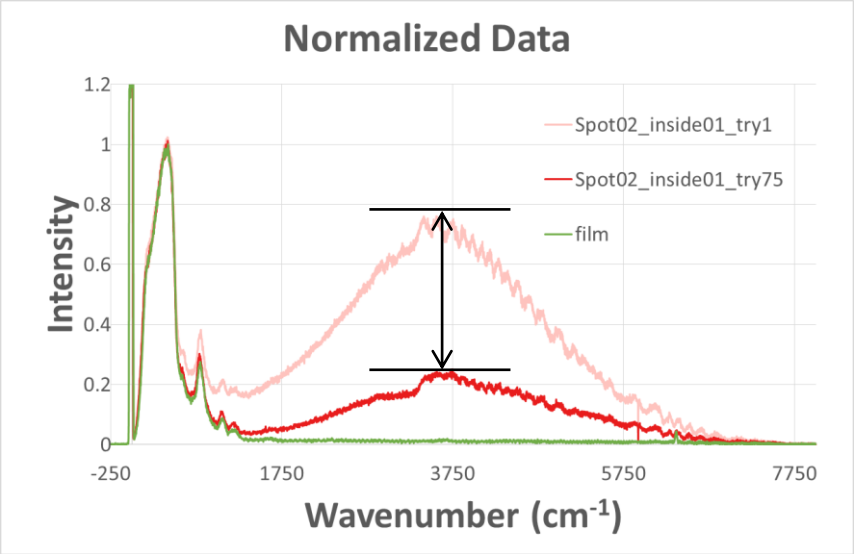

Figure 8: Decay of silica PL signals. The pink curve represents data collected from the first laser irradiation at spot 02. The red curve represents data collected from the last laser irradiation (the seventy-fifth spectrum) at the same location in spot 02. The spectra of damage spot 02 are normalized to the main Raman peak to facilitate data comparison and to account for the effect of PL. The black arrow outlines the decrease in PL in a single position in silica damage spot 02. The green curve is a neat film spectrum.

The magnitude of the PL was investigated as a function of time. A total of seventy-five spectra were collected from spot 02 over three days, with a total of approximately six hours of

irradiation to study PL decay. Each day, the damage site in spot 02 was probed with an acquisition time of ten seconds for each spectrum. On the first day, the site was probed consecutively for nearly one hour. The setting was left exactly the same to continue laser irradiation on the second day for approximately four hours of acquiring spectra with the laser turned off between each day. The same process was repeated the third day to acquire the remaining spectra. There were twenty-minute rest intervals and five-minute rest intervals in between each acquisition on the second and third days, respectively. In Figure 8, the pink and red spectra represent the investigated net decay over time. While the intensity at that particular sample position continued to decay, its rate of decay was minimal compared to the first few spectra that were taken. The changing signal intensities could be due to prolonged laser irradiation (exposure) over the duration of acquiring the 75 spectra as well as reaction to the environment. When comparing all spectra taken from silica damage spots, the main Raman features are all present and similar. Yet, the levels of PL appear to vary from one position within the damage site to another. These data suggest that somewhat different PL signatures are produced by laser-induced damage at various sites. Note that aside from PL signals in the spectra, the Raman features (see Figure 8 at <1750 cm^{-1}) are all relatively uniform without notable abnormal features. In three inspected silica damage sites, though various positions were probed and analyzed, a strong D_1 (~495 cm^{-1}) or D_2 (~600 cm^{-1}) peak was not found other than the identified D_1 peak in figure 3, underscoring their rarity in being observed.

4.3 Hafnia Laser-Induced Damage Spots

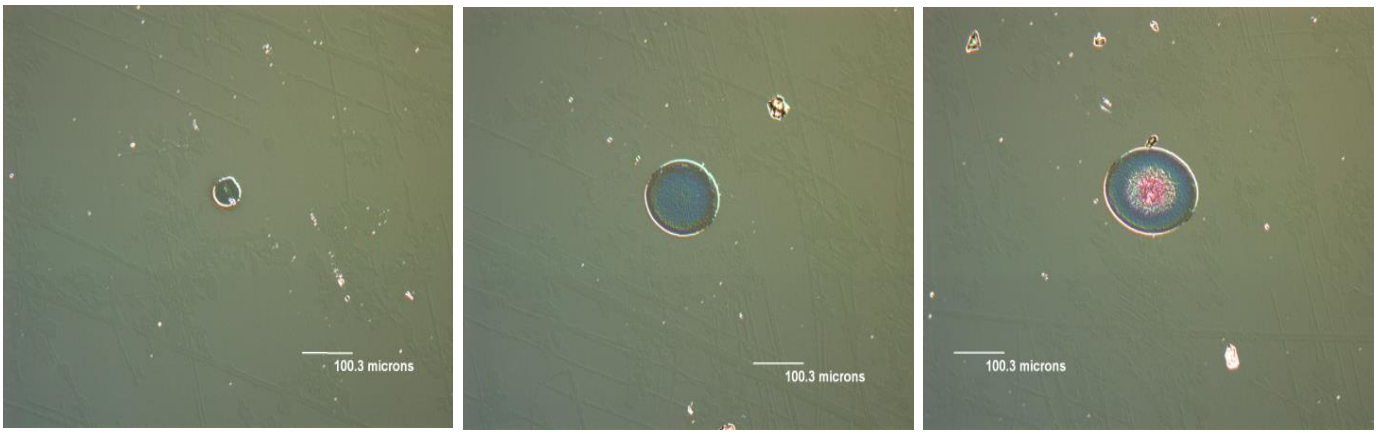

Figure 9: A series of hafnia damage sites created with increasing fluence, starting from the leftmost image to the right. The images depict spots 20, 21, and 22, respectively.

Overall, hafnia damage spots have greater variability in their sizes compared to those of silica. Differences due to fluence levels in addition to other test protocols are distinguishable through the damage areas, which are depicted in Figure 9. The most notable difference is the varying sizes of each site. Considering all hafnia damage sites, they range from approximately 30 microns to 400 microns in width (Figure 9 depicts a range of 30 to 200 microns).

4.4 Hafnia Data Spectral Analysis

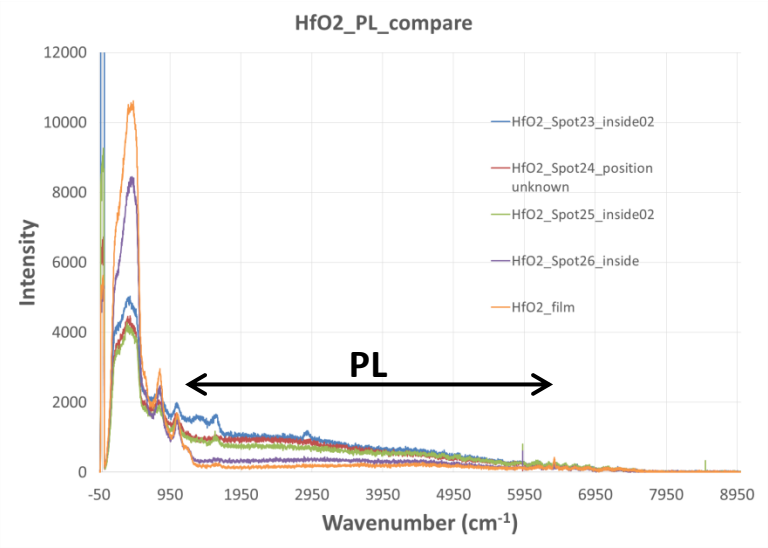

Figure 10: A study of hafnia PL signals. Damaged site PL spectra are all relatively low in intensity, yet greater in intensity compared to the film spectrum and span approximately from 1000 cm^{-1} to 6000 cm^{-1}.

Most spectra produced from damaged sites show similar features, with relatively low intensity PL signals that span from 1000 to 6000 cm^{-1} (Figure 10). Note that the spectrum for spot 23 (blue curve) has two unusual features at ~1500 and 2900 cm^{-1}. These peaks have not yet been identified and could yield interesting information.

An unusual signal behavior is observed in spectra from spot 29 shown in Figure 11. The first spectrum taken at spot 29 on the first day shows a very large PL signal. With a 10-second acquisition time for each spectrum, this same position was again probed over the course of three days in half-hour intervals for a total of six hours. The laser was turned off at the end of each day while the setup was kept exactly the same to continue probing at that position the next day. It was observed that the first spectrum taken at the spot each day increased in intensity slightly above the last spectrum taken from the previous day. The final spectra of each day all eventually declined to about the same level of intensity. The decreasing rate of PL signal decline is presented in Figure 11.

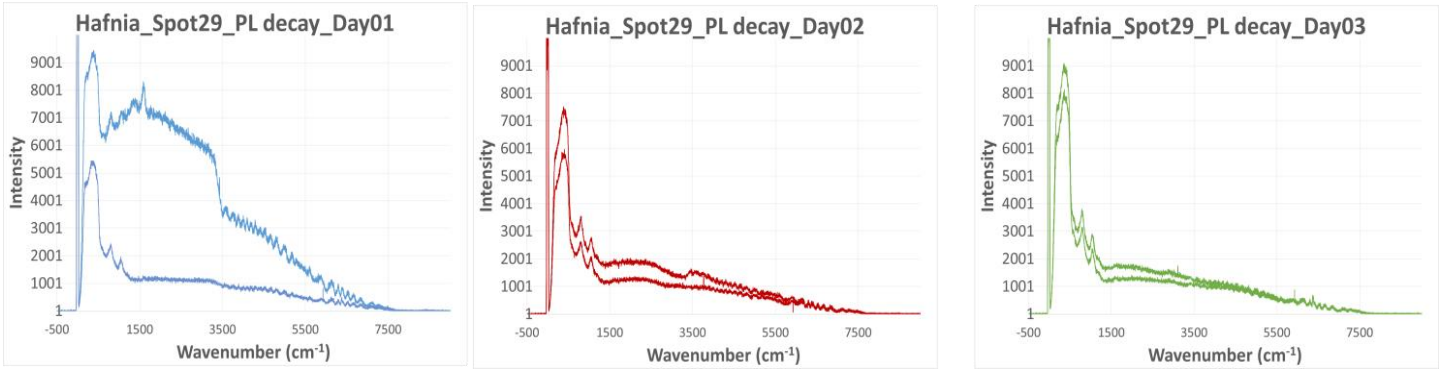

Figure 11: Signal intensity decay of an unusually large signal at spot 29 of the hafnia sample. This figure illustrates the decreasing signal intensity at a slowing rate. The spectra in each graph represent the differences in intensity between the first and last spectra obtained in a day.

To study the PL signal decrease, a comparison between data taken on the three separate days was created (Figure 12). It is noted that each PL signal eventually decayed to approximately the same intensity level, which reflects consistent material modification at that particular damage spot. However, through this comparison, it is observed that although PL signals have decayed, the relative intensity of the Raman signal appears to have increased over time, though the exact reason for this remains unclear.

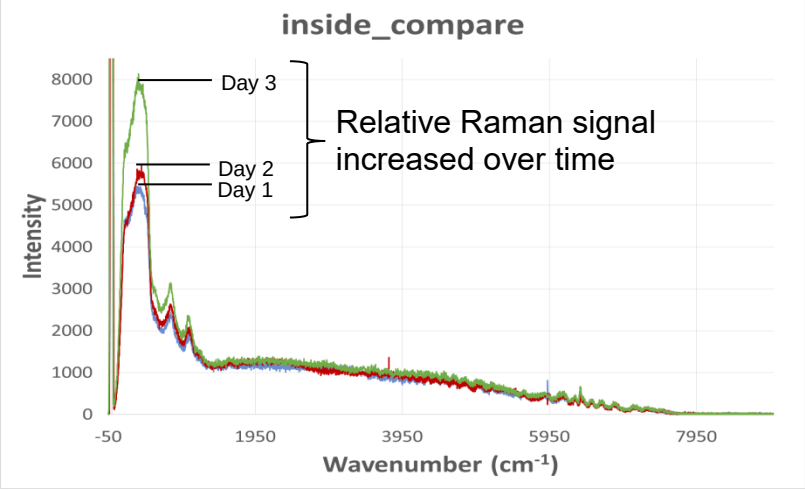

Figure 12: Comparison of the last spectra taken from spot 29 from day 01, day 02, and day 03 of observations (the three lower spectra from Figure 11).

To compare the differences between hafnia damage test sites created with high versus low fluence, damage sites from both were probed. The damage spots representing high fluence are spots 24, 25, 26, and 29 [Figure 13(a)]. The damage spot representing low fluence is spot N1, created with an N-on-1 test, with data taken from various locations within the site [Figure 13(b)]. In spot N1, similar spectra are reproduced repeatedly, with spectra closely overlapping each other. This suggests that little material change occurred in this spot despite the slight damage. Apparent in Figure 13, the spectra acquired from high fluence damage spots demonstrate significantly larger intensity levels whereas the damage test spots created by N-on-1 tests at low fluence depict low intensity levels and relatively little deviation from the neat film spectrum.

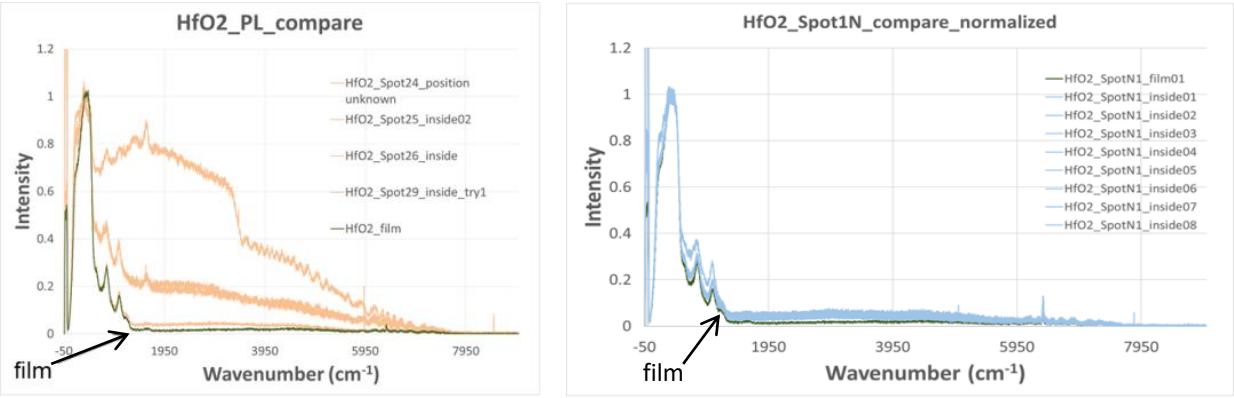

(a) **(b)**

Figure 13: Comparison of signal intensity levels between the spectra of low and high fluence laser-induced damage in the hafnia sample. Figure 13(a) depicts the spectra of a high fluence damage site, which shows high intensity signals with the exception of the bottom yellow curve (spot 26), which is similar to the film spectrum. Figure 13(b) represents the spectra of a low fluence damage site, which shows low intensity signals, resembling the neat film spectrum.

4.5 Comparing Silica and Hafnia Data Spectra

When comparing silica data with hafnia data, certain features are highlighted. For instance, neat film spectra from both samples were compared to observe potential differences between undamaged films. Normalized data (Figure 14) show that while silica neat film spectra are fairly reproducible, with flat curves consistently overlapping each other, hafnia neat film spectra suggest some PL that spans from approximately 400 cm^{-1} to 7000 cm^{-1}. When hafnia neat film spectra are compared to hafnia damage site spectra, they appear to be flat. However, when the spectra from both samples are placed together on the same graph, as in Figure 14, the PL signals become distinct. Potentially, the hafnia film spectra could be riding on a small PL signal, leading to raised features. When normalized to the main Raman peak, the two subsequent hafnia Raman peaks at 810 and 1065 cm^{-1} are also raised in comparison to those of silica.

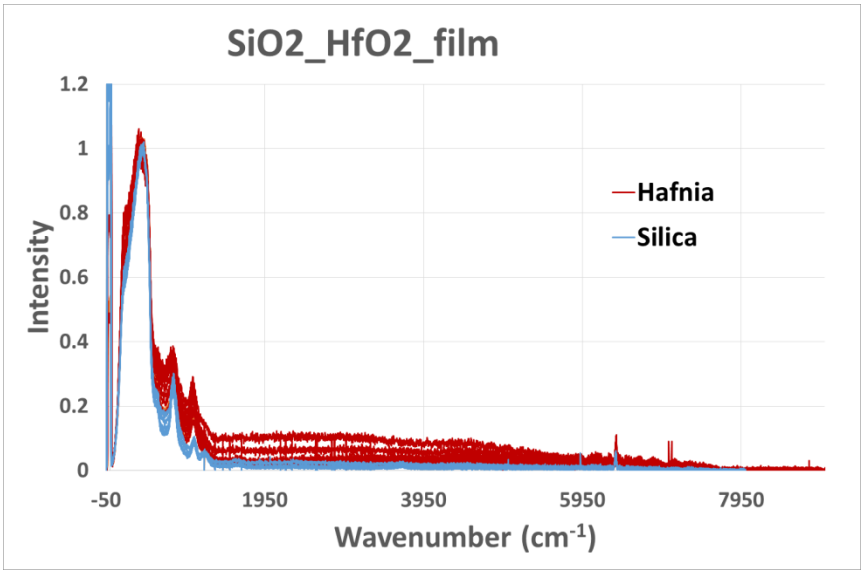

Figure 14: Comparison of silica and hafnia neat film spectra. The PL signals in the hafnia data are highlighted when placed together with the silica data.

Results from the spectral comparison shown in Figure 15 reveal two additional features that are observed in silica spectra but not hafnia spectra. These two features, a knee and a peak,

are observed in silica neat film spectra as well as inside damaged spots. The knee feature is visible around 600 cm^{-1}, and the peak is visible around 1200 cm^{-1}.

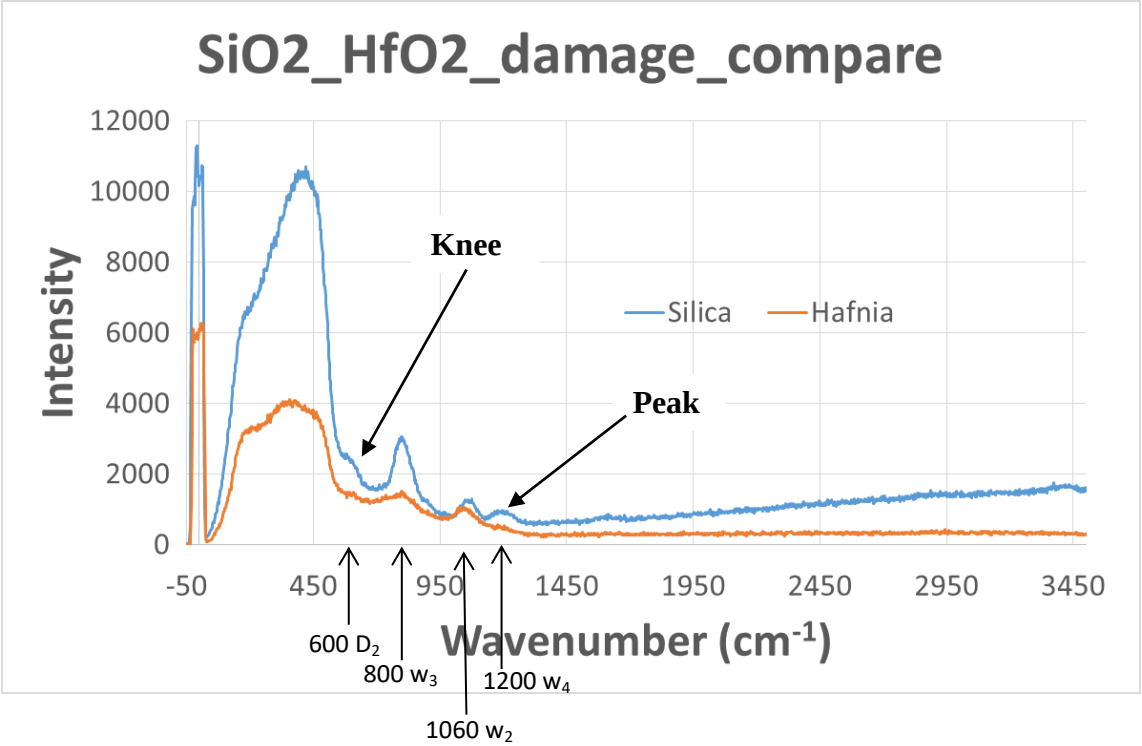

Figure 15: Comparison of silica and hafnia damaged site spectra. The black arrows point to additional knee and peak features that are not visibly observed in hafnia spectra. Note that the four silica peaks (D_2, w_3, w_2, and w_4) match those in figure 4 exactly.

From Figure 15 it appears that the knee and peak are unique characteristics of silica. However, a close-up study of the curves reveals emerging knee and peak features on hafnia spectra as well, though much weaker. This observation was made on nearly all hafnia spectra, be it on neat film or damage sites. These spectral features are clearly identifiable in some hafnia spectra while barely visible in most others. A proposed explanation is that the visibility of these spectral features depends on the proximity of the excitation laser to the silica substrate, which is used for both film samples. To test this hypothesis, a depth study was conducted on the hafnia

sample. This involved probing the sample in the air above the target site, on the surface, and beyond the surface.

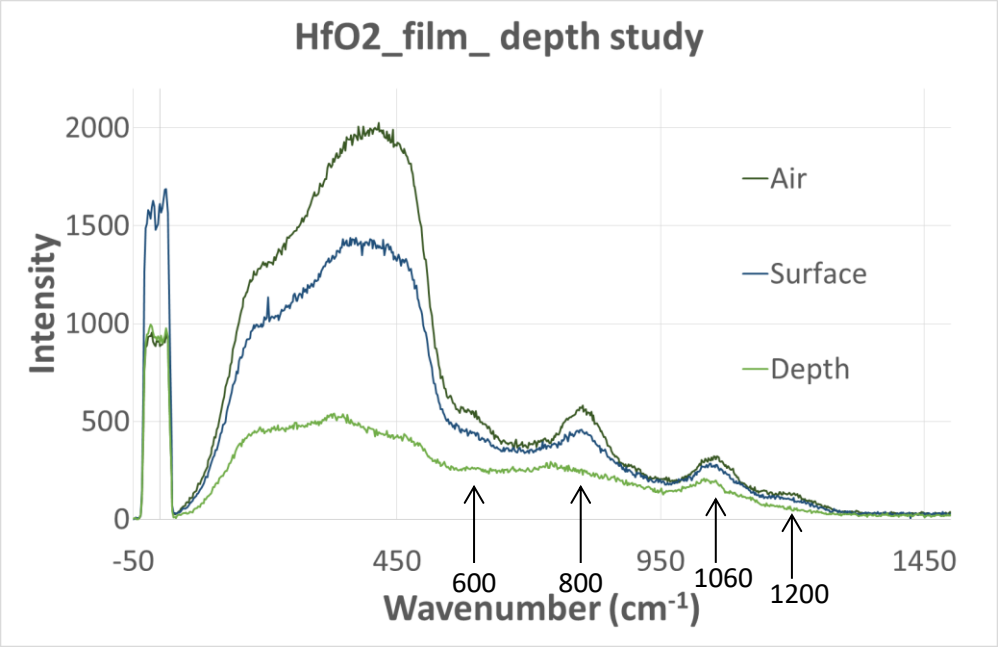

Figure 16: Comparison of depth study spectra. The three representative spectra show resulting data taken from air (above), surface (on the same dimension as the sample), and depth (past the surface). The specific measurements for the spectra in this figure use the surface as the standard position. The focal point of the excitation laser beam is moved out 0.105 mm above the surface and moved 0.145 mm past the surface.

Depth study results suggest that the visibility of the spectral features at 600 and 1200 cm^{-1} can be affected by the position of the excitation source. As the laser beam probes below the surface of the sample, the knee and peak features are no longer visible on the spectra. As seen in Figure 16, the lowest-intensity spectrum (probed beneath the surface) has no knee at 600 cm^{-1} and no peak at 1200 cm^{-1}, whereas the top two spectra, acquired at and above the sample surface, show both features at the indicated wavenumbers. This observation is repeatedly seen on other spectra, which are taken from other positions with varying depths. This may indicate different material compositions (or interactions) beneath the surface of damage sites.

Summary

Micro-Raman spectroscopy was used to identify material modifications in silica and hafnia laser-induced damage sites. By probing the damage sites with an incident laser beam, spectra with identifying characteristics were produced. These spectra allow for comparisons between damaged and undamaged film materials and have identified transient features, such as the disappearing hafnia features. Raman spectra of silica and hafnia proved to be similar, but not identical. The main difference between silica and hafnia lies in their signal intensity levels. Hafnia spectra tend to have higher PL signals, which tend to obscure some spectral features more than in silica spectra. Damaged and undamaged spectra in silica portray similar characteristics, and the previously observed rare D_1 and D_2 features at 495 cm^{-1} and 600 cm^{-1}, respectively, were not found in any new spectra. The main Raman peaks are present in all spectra, though PL signals are evident in most damaged spectra. A depth study showed that the distance above or below the sample surface at which the sample is probed affects the signal intensity. Research on material modifications using micro-Raman spectroscopy could be applied to improve understanding of the laser-damage process and future manufacturing of laser thin film coatings.

Acknowledgements

I would like to thank Dr. Tanya Kosc, my advisor, for her endless help and support throughout this project. Her patience during discussions offered invaluable insight and inspiration. Thank you to Dr. Stephen Craxton, who offered me this opportunity to learn about micro-Raman spectroscopy. I would also like to thank Dr. Stavros Demos and Mr. Alexei Kozlov for giving me much appreciated suggestions on my project. Many thanks to the Optical Material

Technologies group members for making it possible for me to spend extensive time working with lasers in the lab.

References

[1] Lohumi, Santosh & Kim, Moon Seok & Qin, Jianwei & Cho, Byoung-Kwan. (2017). Raman imaging from microscopy to macroscopy: Quality and safety control of biological materials. TrAC Trends in Analytical Chemistry. 93. 10.1016/j.trac.2017.06.002.

[2] K. J. Kingma, R. J. Hemley; Raman spectroscopic study of microcrystalline silica. *American Mineralogist* ; 79 (3-4): 269–273.

[3] N. S. Shcheblanov, M. E. Povarnitsyn, K. N. Mishchik, and A. Tanguy; Raman spectroscopy of femtosecond multipulse irradiation of vitreous silica: Experiment and simulation. Phys. Rev. B 97, 054106 (2018)

[4] A. E. Geissberger, F. L. Galeener; Raman studies of vitreous SiO_2 versus fictive temperature. Phys. Rev. B 28, 3266 (1983)

[5] A. A. Kozlov *et al*. Study of the picosecond laser damage in HFO_2/SiO_2-based thin-film coatings in vacuum. *Proc. SPIE* 10014, (100141Y (2017).

A Comparative Study of the Effects of Methanol and Ethanol Solutions on the Bulk Etch Rate of CR-39

Michele Lin

Attica High School

Advisors: Michelle McCluskey, Robert Boni

Laboratory for Laser Energetics

University of Rochester

April 2020

1. Abstract

CR-39 is a plastic polymer detector used on the magnetic recoil spectrometer (MRS) diagnostic on the OMEGA laser system. Charged particles produced by neutrons emitted from fusion reactions disrupt chemical bonds within the plastic, leaving tracks. The detectors undergo a series of three chemical etching processes to reveal the tracks. The tracks are recorded using an optical microscope in conjunction with image processing software, which uses a coincidence counting technique to distinguish true tracks from background noise. This project investigates a new bulk etching technique using a methanol/NaOH solution with the goal of increasing the etch rate. Varied concentrations of methanol/NaOH solutions were tested. Using a 2.5 molar concentration of methanol/NaOH solution compared to the standard ethanol/NaOH solution increased the bulk etch rate from ~18 microns removed/hour to ~37 microns removed/hour. This promises to decrease the amount of time needed to process MRS and other data.

2. Introduction

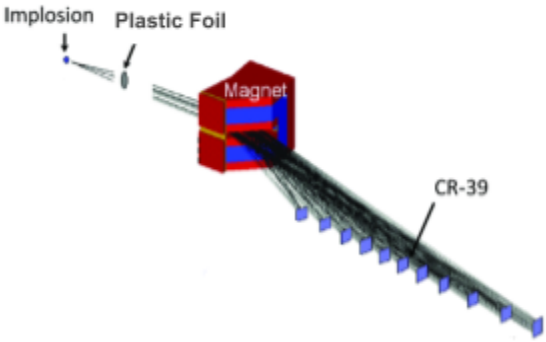

Figure 1: A schematic illustration of the magnetic recoil spectrometer (MRS). Neutrons emitted from the implosion hit the foil, producing charged particles that are selected to be momentum analyzed by an aperture in front of the magnet. The charged particles are then directed onto the CR-39 detectors located on the windows of the MRS.

A nuclear fusion reaction occurs when two light atomic nuclei fuse together to form a heavier nucleus with the release of energy in the form of particles. Although various isotopes of light elements can be paired, the Laboratory for Laser Energetics (LLE) uses the hydrogen isotopes deuterium (D) and tritium (T) to produce the most energetically efficient results. Inertial confinement fusion (ICF) is a method implemented at LLE that uses high-power lasers to uniformly irradiate a cryogenic capsule containing DT fuel.[1] The energy from laser beams ablates the surface of the capsule and causes an implosion, which means the inner fuel quickly collapses inward. As a result, the target is compressed and heated to the extreme temperature and pressure necessary to initiate the DT reaction. When the interior fuel undergoes fusion, helium is formed and a high energy neutron is released.

The magnetic recoil spectrometer (MRS) on the OMEGA laser system shown in Figure 1 consists of three main parts: a plastic foil, a focusing magnet, and an array of CR-39 plastic detectors.[2] Neutrons emitted from an implosion hit the plastic foil and produce recoil charged particles (deuterons or protons). An aperture in front of the magnet selects some of the particles to be momentum analyzed and focused onto the CR-39 detectors.[3] Although the neutrons are generated at a fixed energy, the energies with which they reach the MRS vary. The energies of the recoil particles vary correspondingly. The recorded energies thus indirectly create a neutron spectrum that can quantify the energy lost between neutron production and the detectors.[4] Almost all the energy loss is caused by collisions between ejected neutrons and particles of the unfused fuel between the DT fuel core of the implosion and the detector. This energy loss depends on the fuel areal density (product of density and radius), which is a measure of the radial compression and

determines how much fuel was fused.[5] Measurements of fuel areal density from cryogenic DT implosions are essential to the National Ignition Campaign of achieving ignition. Ignition is attained when the output of energy from a fusion reaction exceeds the input of energy used to create fusion conditions. Thus, CR-39 detectors provide a means to quantify the success of individual reactions.

CR-39 is a special type of plastic (polyallyl diglycol carbonate) designed to be clear with high optical quality. When charged particles pass through the sensitive material, they leave molecular damage that can be observed and recorded under a digital microscope using MIT's charged particle spectroscopy (CPS) scanning program. The Laboratory for Laser Energetics receives CR-39 detectors from Track Analysis Systems Ltd in England. During manufacturing, the plastic is compromised by defects known as background noise or noise pits. Other detector manufacturers also produce noise-pitting CR-39, which means that background noise is not specific to Track Analysis Systems Ltd. Although the CPS scanning program is usually able to recognize valid data points, analyzed noise pits may show similar eccentricity and contrast to ejected particles.[6] To reduce background noise, irradiated CR-39 detectors go through a successful coincidence counting technique (CCT) that takes advantage of the fact that particles penetrate deep within CR-39, while noise pits only show up on one surface or the other.

The CCT uses a standard 6 N NaOH track etch, a bulk etch, and a final 6 N NaOH track etch, along with track microscope scans and analysis. Figure 2 shows the series of etches and their effects on CR-39. In the first standard track etch, the detectors are placed in a hot water bath at 80°C in a beaker containing 6 N NaOH. The chemical etchant infiltrates the broken chemical bonds in the irradiated plastic material, opening the tracks of particles and background noise. After six hours, the detectors are removed from the hot water bath, dried, and placed on the stage of an optical microscope for the pre bulk etch (PRBE) scan. The CPS scanning program records the surface of the CR-39, which can take 1.5 hours to over a day to complete.

In the bulk etch, the detectors are placed in a hot water bath at a temperature of 55°C in a beaker containing 2 M ethanol/NaOH. The aggressive chemical etchant removes the bulk of the material and erases all the opened particle and noise tracks. After 12 hours, the detectors are removed, dried, and measured before reopening the tracks in the final standard track etch.

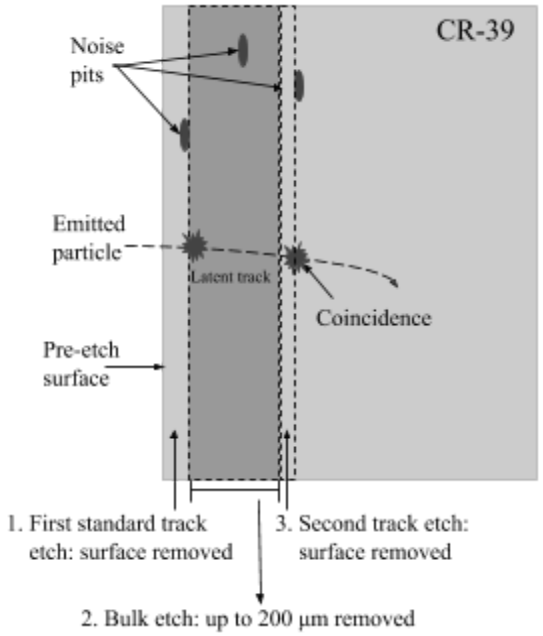

Figure 2: A schematic drawing of the three-series etch process of CR-39 used in the coincidence counting technique (CCT). Emitted particles leave tracks of molecular damage that travel deep within the plastic as opposed to the noise pits that appear sporadically throughout. The standard NaOH track etch reveals the trails. The bulk etch removes much of the bulk of the material and erases the trails. The second track etch reopens the trails. The points that coincide with each other before and after bulk etching are valid data.

The second standard track etch follows the same procedure as the first standard track etch. Figure 3 shows a generalized track profile of molecular damage in the plastic after the two etch processes occur. A conical pit forms in the place of both embedded background noise and true data points on the etched surface.[7]

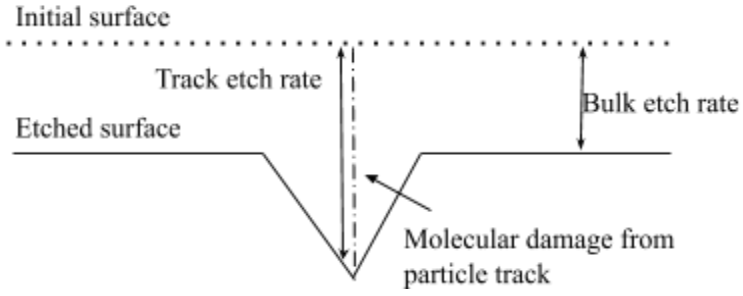

Figure 3: A generalized track profile. During the standard track etches, the solution infiltrates the molecular damage and opens the particle track. During bulk etching, the aggressive etchant removes the bulk of the material. The simultaneous action of the two etches in which the track etch rate is greater than the bulk etch rate results in a conical pit.

The final step in the time-consuming CCT is the CCT scan, which can take 1.5 hours to over a day to complete. The reopened tracks are again recorded under an optical microscope with the CPS scanning program. As shown in Figure 4, the surface of CR-39 from the PRBE scan is aligned and compared with the CCT scan. The points that coincide with each other before and after are true data points because noise has been eliminated.

In this study, a different chemical etchant, methanol/NaOH solution, was chosen to improve the bulk etch technique and decrease the data processing time. While the hot water bath was maintained at 55°C, the concentration of the solutions was manipulated to investigate if the methanol/NaOH solution has a faster bulk etch rate and produces the same quality of CCT data as the ethanol/NaOH solution.

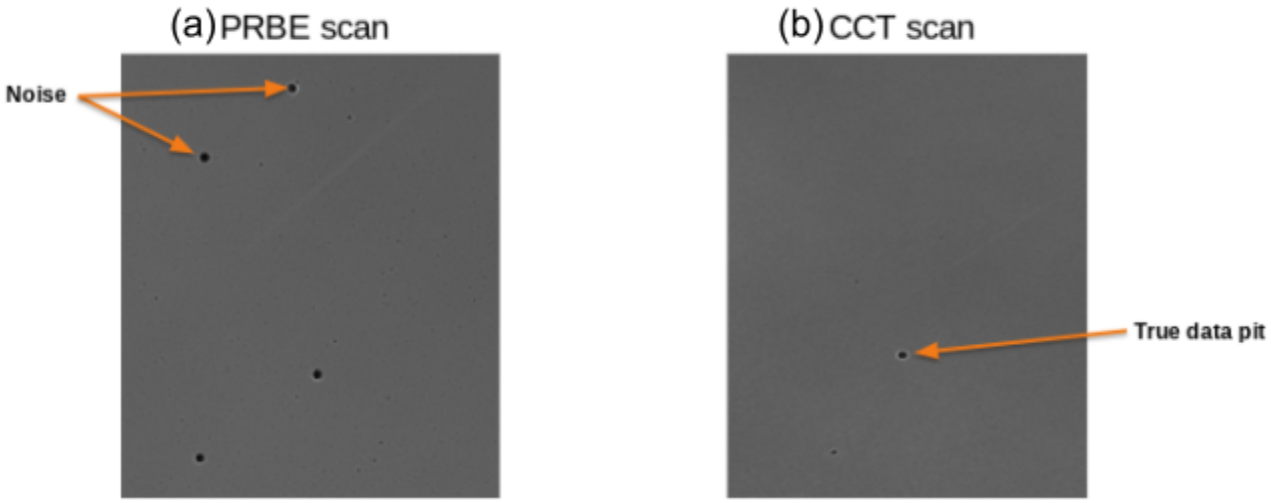

Figure 4: Pre bulk etch (PRBE) and CCT images of a CR-39 surface under an optical microscope after standard track etches. The noise on image (a) appears similar to the true data pits and would be identified as a true data pit by the scanning program. On image (b), the noise has disappeared and only a true data pit remains.

3. Methods and Materials

Prior to the present experiment, the detectors had been subjected to the first standard track etch. They were placed in a 6 N NaOH standard track etch at 80°C. After six hours, they were removed from the hot water bath, dried, and placed under an optical microscope that recorded an image of the CR-39 surface.

After the first standard etch, a micrometer was used to measure the thickness of each CR-39 detector at eight locations. The measurements were averaged and recorded to ensure that ~180 to 200 microns of plastic material would be removed during bulk etching. If less than 180 microns of bulk were removed, the noise pits seen in the first scan would not be eliminated. If more than 200 microns of bulk were removed, then all the particle tracks would be lost.[8]

In the present experiment, the bulk etch rates of four irradiated CR-39 samples were tested in 2 M ethanol/NaOH solution and compared to twenty irradiated CR-39 samples tested in methanol/NaOH solutions ranging from 1 M to 4 M. These chemical etchants were prepared in beakers using 10 N NaOH. The beakers were placed in a hot water bath maintained at a constant temperature of 55°C and covered to prevent evaporation.

Every few hours, the detectors were removed from the hot water bath and the thickness of each sample was measured at eight locations. The average thickness measured was subtracted from the initial average thickness to determine how much bulk was removed. The samples continued to undergo bulk etching until the average bulk removed was between 180 and 200 microns. Then, the bulk etch rate was calculated by dividing the average thickness of the material removed by the number of hours it took to bulk etch. The averages were plotted on a graph (Figure 5) with x-values representing time in hours and y-values representing the bulk etch rate in microns removed/hour. Figure 6 compares the bulk etch rate using various concentrations of methanol/NaOH solutions. Overall, a 2.5 M methanol/NaOH solution reduced the approximately ten-hour procedure using the 2 M ethanol/NaOH solution to under six hours.

Although the efficiency of bulk etching nearly doubled, the final steps of the CCT were executed to ensure that the methanol/NaOH solution produced the same quality of data as the ethanol/NaOH solution.

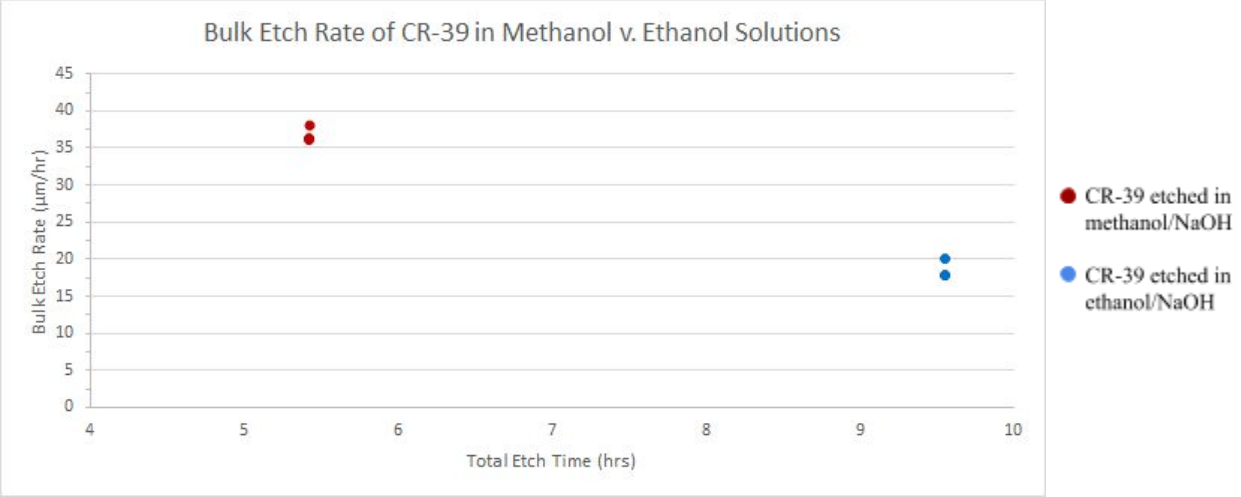

Figure 5: Scatterplot of the bulk etch rate of CR-39 comparing methanol/NaOH solutions and ethanol/NaOH solutions. Time is plotted on the x-axis and the bulk etch rate is plotted on the y-axis. The bulk etch rate of CR-39 in methanol/NaOH is about twice as fast as it is in ethanol/NaOH.

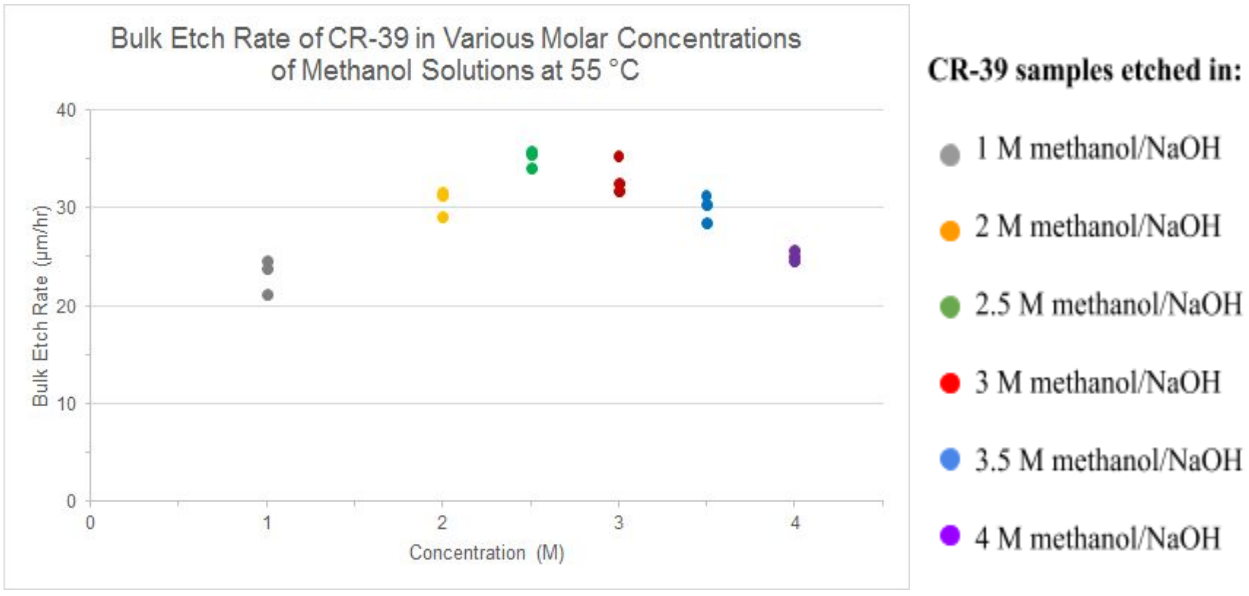

Figure 6: Scatterplot of the bulk etch rate of CR-39 in methanol/NaOH solutions. Molarity is plotted on the x-axis and bulk etch rate is plotted on the y-axis. The bell-shaped curve shows that the fastest bulk etch rate was ~37 microns removed/hour at a molar concentration of 2.5 methanol/NaOH.

4. Results

After completing the CCT, the methanol/NaOH solution produced comparable particle track results to the ethanol/NaOH solution. Figure 7 shows the track counts from PRBE scans and CCT scans of methanol and ethanol etches. The total track counts from ethanol etches compared to methanol etches is greater because the total neutron yield was higher on those implosions. After analyzing the scans, the difference in tracks between PRBE and CCT scans of methanol etches is comparable to the difference in tracks between PRBE and CCT scans of ethanol etches. The ethanol bulk etches have been shown to work with accelerator exposures to a known number of protons.[9] One specific shot (94008) shows a greater track count in the CCT scan than in the PRBE scan, which is most likely due to the background noise being over-subtracted in the PRBE analysis. Separating tracks from background noise is not always straightforward, which is why there is not a perfect agreement between the PRBE and CCT analysis.[10]

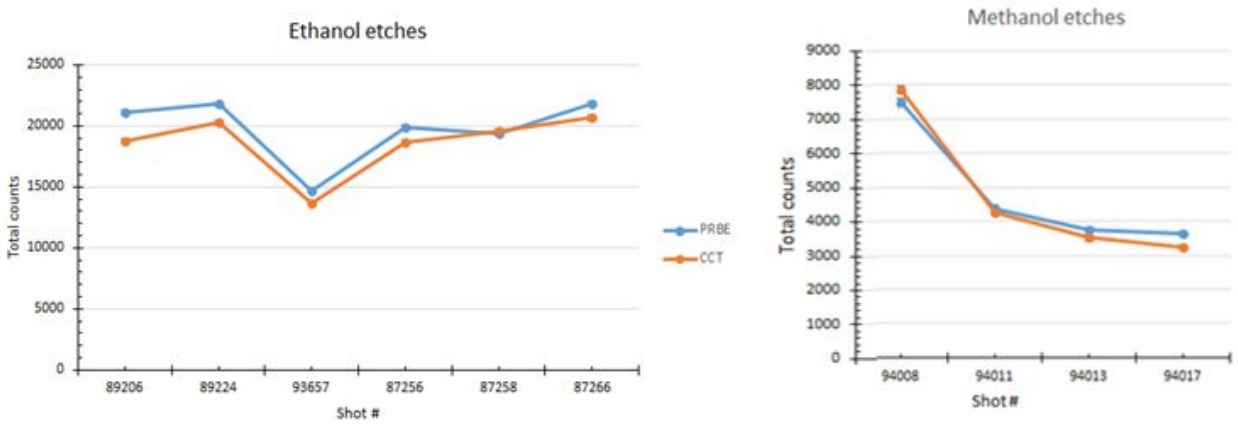

Figure 7: A comparison of the total counts of tracks from PRBE and CCT scans between methanol/NaOH bulk etches and ethanol/NaOH bulk etches. The implosion shot number is plotted on the x-axis and the total count of tracks is plotted on the y-axis. Methanol/NaOH bulk etches reproduce the PRBE and CCT track number estimate trend seen on the ethanol etch graph.

The two contour plots that are shown in Figure 8 graph the number of tracks as a function of diameter and contrast. Based on previous experience with CR-39 response, the tight region highlighted in red is a cluster of tracks with similar diameter and contrast identified as the signal deuterons. Because the signal characteristics are very similar for the two etch scenarios, the methanol etch does not negatively impact CR-39 response. Other contour clusters, such as the cluster stretching from ~10-85 in contrast at small diameters, represent noise tracks in the CR-39. A negative result would show fainter tracks (higher contrast) or smaller tracks (lower diameter), which would have been harder to separate from background tracks in the analysis. This allows us to be confident that the methanol/NaOH does not anomalously fade or shrink tracks.[11]

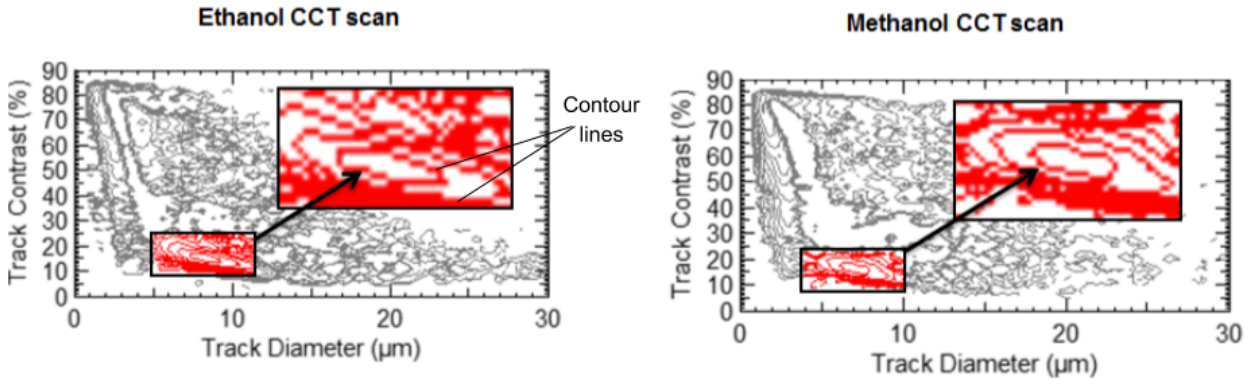

Figure 8: Contour plots of track counts comparing ethanol/NaOH and methanol/NaOH CCT scans. Track diameter is plotted on the x-axis and track contrast is plotted on the y-axis. The areas boxed off in red are the signals picked up from the CPS program. The signal characteristics (track contrast and diameter) are comparable post ethanol and methanol bulk etches, which shows that methanol/NaOH does not negatively impact CR-39 response.

5. Conclusion

In this project, the etching properties of methanol/NaOH solutions have been investigated and compared to the standard 2 M ethanol/NaOH solution. The goals were to verify that methanol/NaOH etchants have a faster bulk etch rate than the standard ethanol/NaOH etchant, find the optimal concentration of the methanol/NaOH etchant that yields the fastest bulk etch rate, and determine if the methanol/NaOH etchant produced the same quality of CCT data as the ethanol/NaOH etchant. Originally, the standard 2 M ethanol/NaOH solution at 55°C had a bulk etch rate of ~18 microns removed/hour with a total etch time of ~10 hours. It was found that a 2.5 molar concentration of methanol/NaOH solution at 55°C more than doubled the efficiency of bulk etching to ~37 microns removed/hour. According to Figures 7 and 8, the data from ethanol etches were comparable to the data from methanol etches. Based on the evidence from this study, the methanol/NaOH bulk etch decreased the amount of time to process data and has replaced the ethanol/NaOH bulk etch as the preferred CR-39 processing method.

6. Acknowledgments

I want to start by thanking my advisors Michelle McCluskey and Robert Boni for encouraging me to do my best work and providing me with invaluable guidance throughout my project. I thank Dr. Maria Gatu Johnson for taking time out of her day to answer my questions regarding MRS data processing. I am grateful to graduate student Beth Bogart for everything she has done to help me succeed in a real research environment. Thank you to Dr. Stephen Craxton, Program Director, for providing this amazing opportunity. Finally, here is a special shoutout to my fellow colleagues for making this summer an unforgettable experience.

7. References

1. R. S. Craxton et al., "Direct-Drive Inertial Confinement Fusion: A Review," Phys. Plasmas 22, 110501 (2015).
2. D.T. Casey, "Diagnosing Inertial Confinement Fusion Implosions at OMEGA and the NIF Using Novel Neutron Spectrometry," Ph. D. thesis, *Massachusetts Institute of Technology*, pp. 43, 44, 94-95 January 2012.
3. "The OMEGA Magnetic Recoil Spectrometer," University of Rochester - Laboratory for Laser Energetics, *Around the Lab*, April 2009. <http://www.lle.rochester.edu/around_the_lab/index.php?month=04&year=2009 >.
4. J. A. Frenje et al., Rev. Sci. Instrum. 72 (1), 854-858 (2001).
5. Séguin, F.H., et al. "Spectrometry of Charged Particles from Inertial-Confinement-Fusion Plasmas." Rev. Sci. Instrum. 74, 975 (2003).
6. D. Hicks, "Charged Particle Spectroscopy: A New Window on Inertial Fusion," Ph. D. thesis, *Massachusetts Institute of Technology*, pp. 115-120 June 1999.
7. D. Hicks. ibid pp. 105.
8. D.T. Casey, "Diagnosing Inertial Confinement Fusion Implosions at OMEGA and the NIF Using Novel Neutron Spectrometry," Ph. D. thesis, *Massachusetts Institute of Technology*, pp. 104 January 2012.
9. D.T. Casey et al., Rev. Sci. Instrum. 82, 073502 (2011).
10. M. Gatu Johnson, Massachusetts Institute of Technology, private communication (2020).
11. M. Gatu Johnson, Massachusetts Institute of Technology, private communication (2019).

Glassy Liquid Crystals Based on Natural Products for High-Peak-Power Laser Optics

George Morcos

Rush-Henrietta Senior High School

Henrietta, NY

Advisor: Kenneth L. Marshall

Laboratory for Laser Energetics

University of Rochester

Rochester, NY

Summer High School Research Program 2019

February 2020

Abstract

Glassy liquid crystals (GLCs) are of interest for potential application as circular polarizers for high-peak-power lasers such as OMEGA. One new material based on the natural product cholesterol, GLC-Bz3CholC5, is of particular interest because it shows a ten-fold increase in laser-induced damage threshold values as compared to previous GLC materials - a prerequisite for large-scale laser optics applications. The feasibility of using this material for the fabrication of practical, large-area polarization control devices for high-peak-power laser applications was investigated by preparing mixtures of this GLC material with nematic and long-pitch polymer cholesteric liquid crystal (LC) host materials and evaluating their LC phase behavior and optical properties by hot-stage polarizing microscopy. Near-planar alignment of these new materials in assembled devices was achieved by melt-processing and thermal quenching on glass substrates, although significant optical scatter due to LC domain defects remains evident, especially in mixtures containing the long-pitch cholesteric host. A mixture containing 50% GLC-Bz3CholC5 in the nematic host GLC-CChxn3N4 was formulated and used to generate a two-inch-aperture device with few defects, excellent alignment, and blue selective reflection, all of which are promising attributes for future laser applications.

1. Introduction

Liquid crystals (LC's) are a form of condensed matter, intermediate in molecular order between a crystalline solid and an isotropic liquid. There are several phases of LC's including the nematic, cholesteric, and several smectic phases. [1] The helical structure of the cholesteric phase and relative ease of generating uniform molecular alignment makes it useful for laser optics applications as circular polarizers. The length of the helical structure in a given cholesteric LC is called the pitch length (p) as shown in Fig. 1. Liquid crystals are known for their unique optical and electromagnetic properties, including birefringence and selective reflection. Birefringence, also known as double refraction or optical anisotropy, is an optical effect that occurs when light strikes a birefringent material or surface and diverges into two rays, defined as the ordinary and extraordinary rays. [2] This effect results in double refraction, as illustrated in Fig. 2.

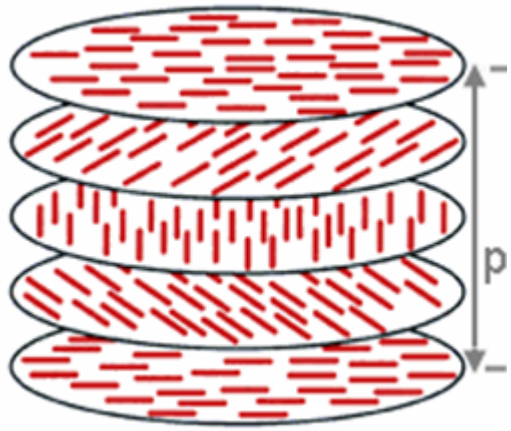

Figure 1: *Cholesteric LC with pitch length, p. Cholesteric LC's have the ability to circularly polarize light, a useful optical property in laser systems.*

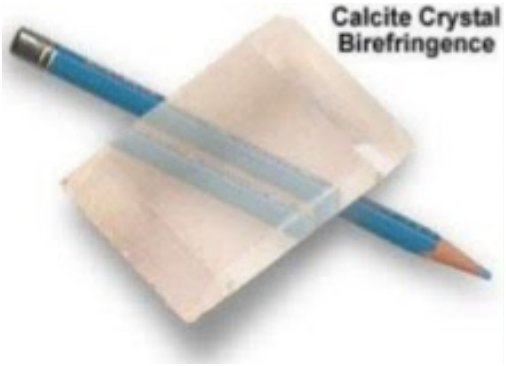

Figure 2: *Optical birefringence effect in a calcite crystal. In this case, the extraordinary and ordinary waves are separated allowing for the double image of the pencil.*

Another optical property of interest of cholesteric LC's is selective reflection, which occurs only for incident wavelengths that satisfy the relationship

$$\lambda = \bar{n}p \tag{1}$$

where $\bar{n}$ is the average refractive index and p is the helical pitch length. At this point, it is also important to define un-polarized light as light waves vibrating in multiple planes or axes as opposed to polarized light,

which only vibrates in one plane. [3] All natural and artificial light is un-polarized but can be converted to polarized light through the use of linear or circular polarizers. As un-polarized light enters a material exhibiting birefringence and selective reflection, it is separated into two components with opposite handedness (left- or right-handed). One circularly polarized component is reflected from the circular polarizer at its selective reflection wavelength, while the opposite handedness at the selective reflection wavelength is transmitted. All other wavelengths outside of the selective reflection bandwidth (except those that experience intrinsic electronic or vibrational absorbance bands in the LC material) pass through and remain un-attenuated, keeping their polarization states. These optical properties are responsible for generating circularly polarized light, which is useful for maximizing power output and preventing the back-reflection of laser light that can propagate down the laser beam lines and cause damage to optical components, as illustrated in Fig. 3. [1,4] If a laser system propagates right-handed circular polarized light (RHC), as shown in Fig. 3, its right-handed component will pass through the LC device and strike the target; any laser energy that is not absorbed by the target will undergo a 180^{o} phase shift (with a resultant change in handedness) and be reflected from the surface of the target as left-handed circularly polarized light (LHC). This LHC light is unable to pass through the LC device and back to the laser system, and is reflected diffusely from the LC circular polarizer, which reduces the intensity of the reflected light significantly.

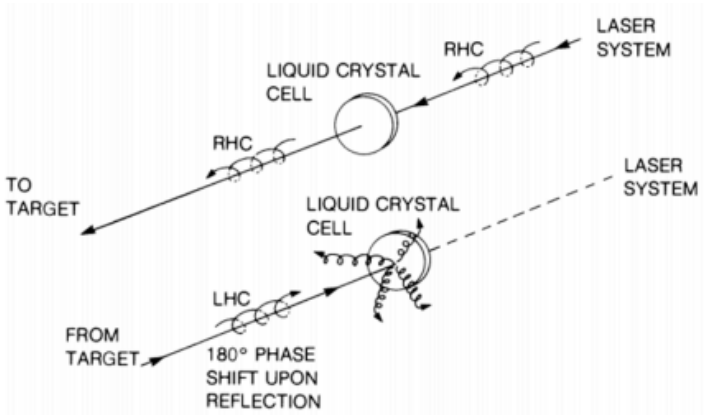

***Figure 3**: Illustration of the use of LC devices to prevent laser damage by changing the handedness of incident light when reflected back from the target. [1]*

Current LC laser optics applications employ a low-molar-mass (LMM) LC fluid to produce devices with high optical quality and contrast. The device shown in Fig. 4 demonstrates uniformity in both selective reflection and texture. LMM LC fluids also offer large-aperture device scalability (up to 200 mm), and excellent laser-induced damage threshold (LIDT) values of >30 J/cm^2 at 1053 nm and 1 ns pulse width. These LC devices have been used since 1985 on the OMEGA laser system for many device applications including circular polarizers and wave plates. [1]

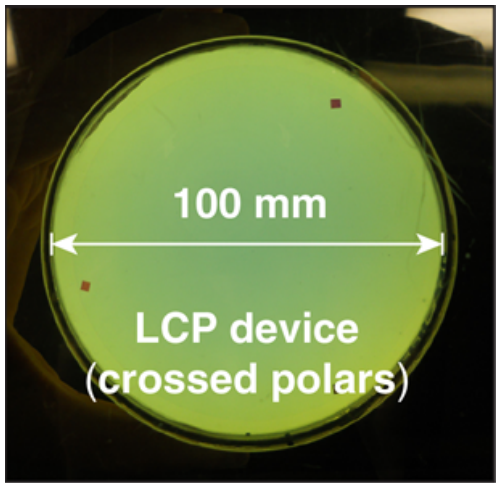

Figure 4: *A large aperture, LMM LC fluid device viewed under crossed polarizers. Devices such as these are currently in use on OMEGA.*

Glassy liquid crystals (GLCs) are a special type of LC that offer the unique optical properties of LMM LC fluids in the form of a solid film below the material's glass transition temperature T_g. They also offer significant advantages by eliminating LC fluid leakage and thick substrate requirements and may ultimately enable single-substrate devices.

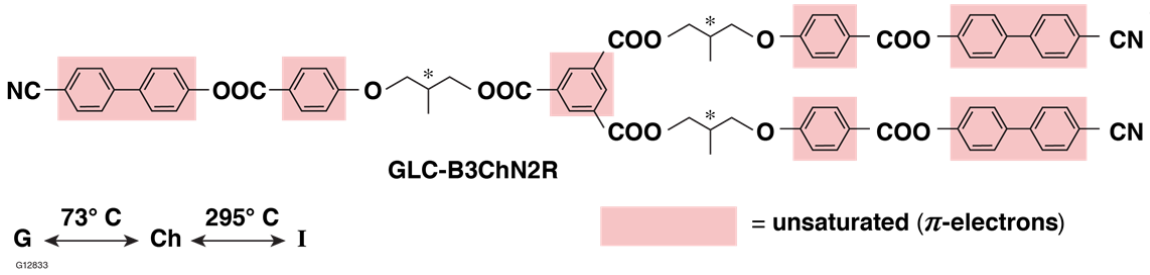

Figure 5: *A molecular diagram of a first-generation GLC material with ten aromatic rings containing delocalized π-electrons due to the presence of carbon-carbon double bonds.*

Previously synthesized "first generation" GLC materials contain large numbers of aromatic or unsaturated carbon rings as shown in Fig. 5. [5] This **π**-electron delocalization has been shown to favor formation of nematic and cholesteric LC phases, stabilize T_g, and enhance birefringence, all of which are benefits of this GLC. However, these materials have also shown significantly lower LIDT values

($\leq$ 1 J/cm^2 at 1053 nm and 1 ns pulse width) than their LMM LC counterparts. [6] The work reported here focused on developing viable GLC mixtures using a second-generation GLC compound (GLC-Bz3CholC5) based on cholesterol. As shown in Fig. 6, this material has an unsaturated benzene core, with three saturated cholesterol pendants and only one isolated double bond in each pendant. In order to fabricate circular polarizer devices from GLC materials, the cholesteric structure observed between 118 and 122^o C must be "trapped" by cooling the device rapidly (i.e., "quenching") to below its T_g (29^o C).

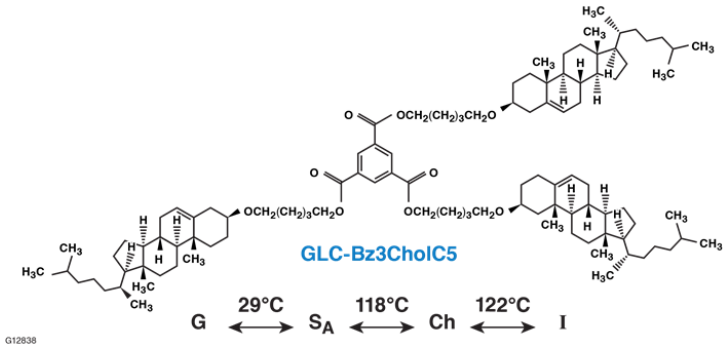

Figure 6: *A second-generation GLC compound GLC-Bz3CholC5. This material has a significantly higher saturation level, which is beneficial for laser damage resistance, and a wide LC temperature range (T_g at 29^{o}C, smectic A from 29 - 118^{o}C, cholesteric from 118-122^{o}C, and isotropic above 122^{o}C). The presence of the smectic A phase makes the material more difficult to work with.*

Previous work with GLC-Bz3CholC5 has shown that it favors the homeotropic orientation [5] (i.e., the GLC molecules align perpendicular to the glass substrates they are placed on instead of parallel to the substrate, which is required in order to observe selective reflection). This tendency toward homeotropic alignment is due to the presence of the smectic A phase, which adopts this orientation naturally. Another consequence of this underlying smectic A phase is that it produces significant optical scattering effects as the device is cooled rapidly from the cholesteric phase to room temperature (Fig. 7). These optical non-uniformities not only compromise consistent absorbance and transmittance measurements but also hamper device performance in many laser optics applications.

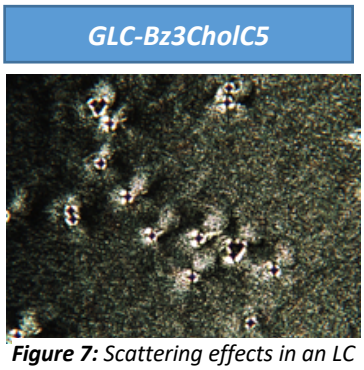

Figure 7: *Scattering effects in an LC cell made with GLC-Bz3CholC5.*

Several mixtures with different GLC nematic or long-pitch cholesteric hosts were used in device fabrication and illustrate that GLCs with natural products are capable of creating well-aligned LC devices for future use in laser optics applications. Figure 8 shows a generalized schematic of the components of the GLC mixtures evaluated. A chiral molecule (e.g., GLC-Bz3CholC5) and a glassy nematic host combine to create a cholesteric GLC with the ability to reflect (and transmit) one handedness of circularly polarized light and function as a circular polarizer. In addition, a procedure for GLC device fabrication was developed using GLC-Bz3CholC5 combined with an inexpensive, commercially available long-pitch polymer cholesteric liquid crystal (PCLC) as a surrogate for the glassy nematic host.

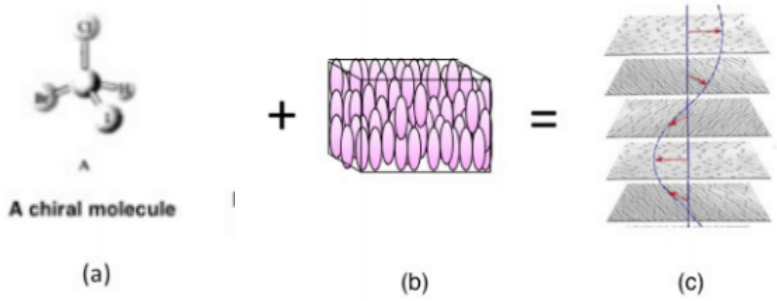

Figure 8: *Addition of a chiral molecule (GLC-Bz3CholC5) (a) to a nematic host (b) to form a chiral nematic or cholesteric LC (c) that has the ability to reflect one handedness of light and perform the function of a circular polarizer.*

GLC-Bz3CholC5 was utilized in this research because it showed a much higher UV transmission and LIDT than GLC-B3ChN2R (Fig. 5). Tables 1 and 2 summarize this data calculated using the Beer-Lambert Law:

$$A = \varepsilon bc \qquad (2)$$

where A is absorbance, ε is the extinction coefficient or molar absorptivity, b is the path length, and c is the concentration of the absorbing species. From the first generation GLC material to the second generation GLC material, nine aromatic rings were replaced with saturated rings leading to a sharp decline in the extinction coefficient. The lower the extinction coefficient, the lower the UV absorption. [5] To use these devices for UV laser applications, a low UV absorption and a high UV transmission are desired. Table 2

indicates an almost ten-fold improvement in LIDT values from the first generation GLC to the second material - a clear effect of eliminating the nine aromatic rings. [6]

GLC Material	Generation	# of Aromatic rings	Solvent	Extinction Coefficient (ε)
GLC-Bz3ChN2R	1	**10**	THF	**4600**
GLC-Bz3CholC5	2	**1**	THF/Isooctane	**220**

Table 1: *Comparison of the extinction coefficients (m^2/mole) of two GLC materials from different generations. Replacing 9 aromatic or unsaturated rings with saturated analogs yields a much lower extinction coefficient and thus a higher UV transmission/lower UV absorbance. This substantial difference in ε is promising for laser applications.*

GLC Material 22 μm thick sample	LIDT (J/cm^2)	
	351 nm, 1 ns	1053 nm, 1.4 ns
GLC-Bz3ChN2R	0.61	-
GLC-Bz3CholC5	**4.89**	**38.87**

Table 2: *Comparison of the LIDT of the same two GLC materials shown in Table 1. Replacing 9 aromatic or unsaturated rings with their saturated counterparts yields a much higher LIDT value at the 351 nm wavelength. Very large LIDT values are seen at 1053 nm, comparable to those observed for LMM LC fluids. [6]*

2. Experimental Procedures

This section describes the development of experimental procedures leading to the fabrication of a GLC device. Section 2.1 describes the creation of surrogate devices used to develop melt-processing techniques. Section 2.2 compares different mixtures and processing techniques used with the surrogate devices of Sec. 2.1. Section 2.3 describes the final processing procedure in detail and Sec. 2.4 describes the formation of the final GLC device.

2.1 PCLC Surrogate Device Fabrication

Two types of commercially available and cost-effective Wacker PCLC polysiloxanes were used to fabricate several surrogate devices with the intention being to demonstrate the basic melt-processing techniques that will ultimately be required to make GLC devices. These PCLC's have very similar chemical

properties but exhibit different selective reflection wavelengths in the blue (510 nm) and green (535 nm). Figure 8 shows several PCLC devices viewed under crossed polarizers. Each of these devices was fabricated using only one type of PCLC. The melt-processing technique used to create each of these devices involves melting the PCLC and applying it onto the central region of a single glass substrate. A portion of the melted PCLC is mixed with a small amount of glass microspheres or fibers, which are then carefully placed into four regions in the shape of a cross to control the cell thickness. The newly applied PCLC is sandwiched between the first substrate and another clean glass substrate and is allowed to cool and solidify (see Fig. 11 in Sec. 2.3: Final Procedure, on Page 14). The two PCLCs used to fabricate these devices have high viscosities and thus trap air bubbles as they are mixed and applied onto the glass substrate, as is evident from the tiny spots in these devices (Fig. 8). Device A was constructed incorrectly by using excessive numbers of glass beads, which resulted in the presence of many microspheres in the empty area surrounding the PCLC in the center of the device. For the other devices, smaller quantities of microspheres were used and limited to only four regions in order to help outline the desired circular shape and prevent excess PCLC material from escaping the device during filling. It is important to note that since microspheres are very small, many microspheres were placed in four specific regions and then allowed to spread out once the device was sandwiched. Ultimately, a high-quality device contains few to no air bubbles, fills the entire substrate with PCLC fluid, and is uniform in color. Because the PCLCs are viscous substances, stirring the materials for an extended period of time further contributes to the air bubbles shown in the devices. In addition, the different shades of the same color in each device show uneven heating and cooling of the PCLC material, which is most clearly visible in Device D.

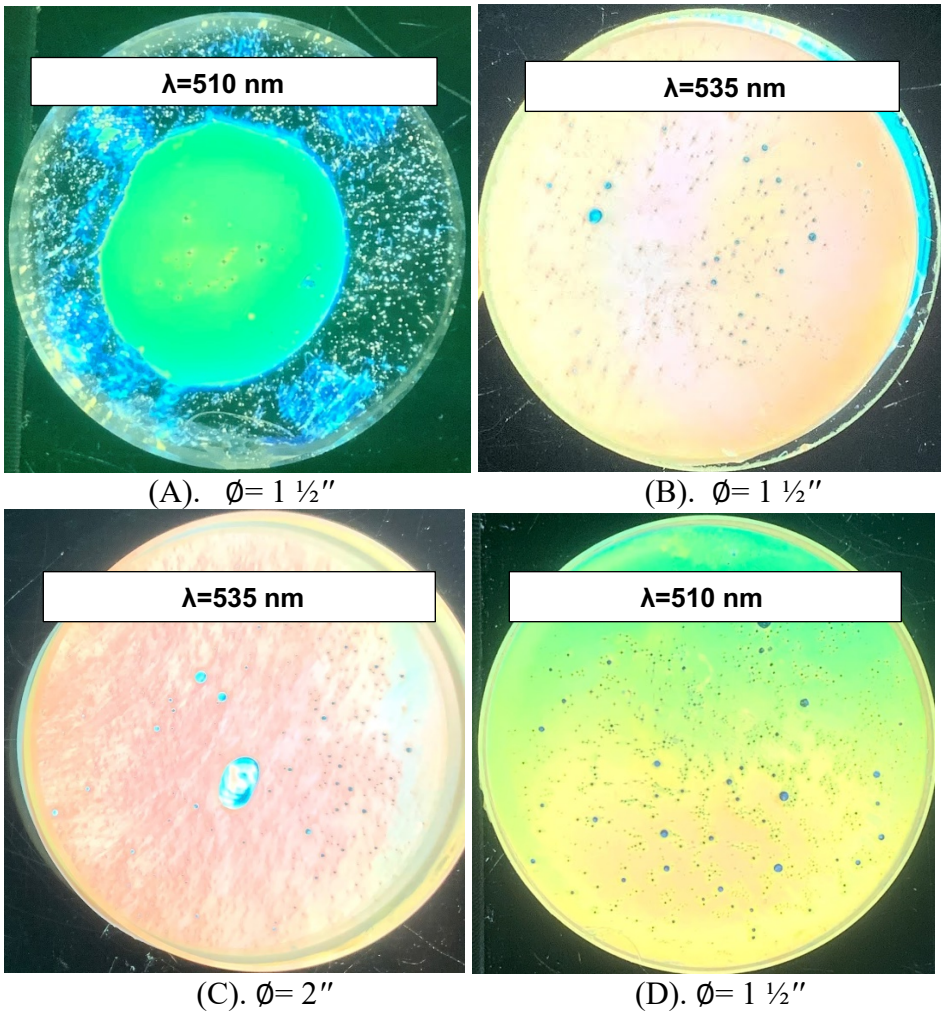

(A). Ø= 1 ½″ (B). Ø= 1 ½″

(C). Ø= 2″ (D). Ø= 1 ½″

Figure 8: *Four PCLC surrogate devices and their diameters (Ø) shown under crossed polarizers. Devices A and D exhibit a blue color in normal light while B and C display green.*

2.2 Procedural Development

For procedural development, Wacker LC-4627, another commercially available long pitch PCLC (2200 nm), was used as a surrogate host. The GLC-Bz3CholC5 was used as the chiral substance and combined with LC-4627 in different mass ratios and with different solvents to create several different mixtures (Table 3) that were then used to create devices using the melt processing technique described in Sec. 2.1. Because different ratios of GLC's and PCLC's were employed in the development of the devices, the procedure for each mixture (especially the preparation phase) was different and specific. Two different solvents (dichloromethane and chloroform) were used to dissolve the GLC materials for more efficient mixing and

to allow microfiltration for elimination of extrinsic particulate contamination. Evaporation of the solvents was accomplished in a fume hood using a nitrogen stream, followed by high-vacuum drying using a LabConCo freeze dryer. These samples showed a grainy texture with extensive scattering and as such would not be useful for GLC laser optics applications. As in Sec. 2.1, they were mainly used to develop a complete procedure for device fabrication.

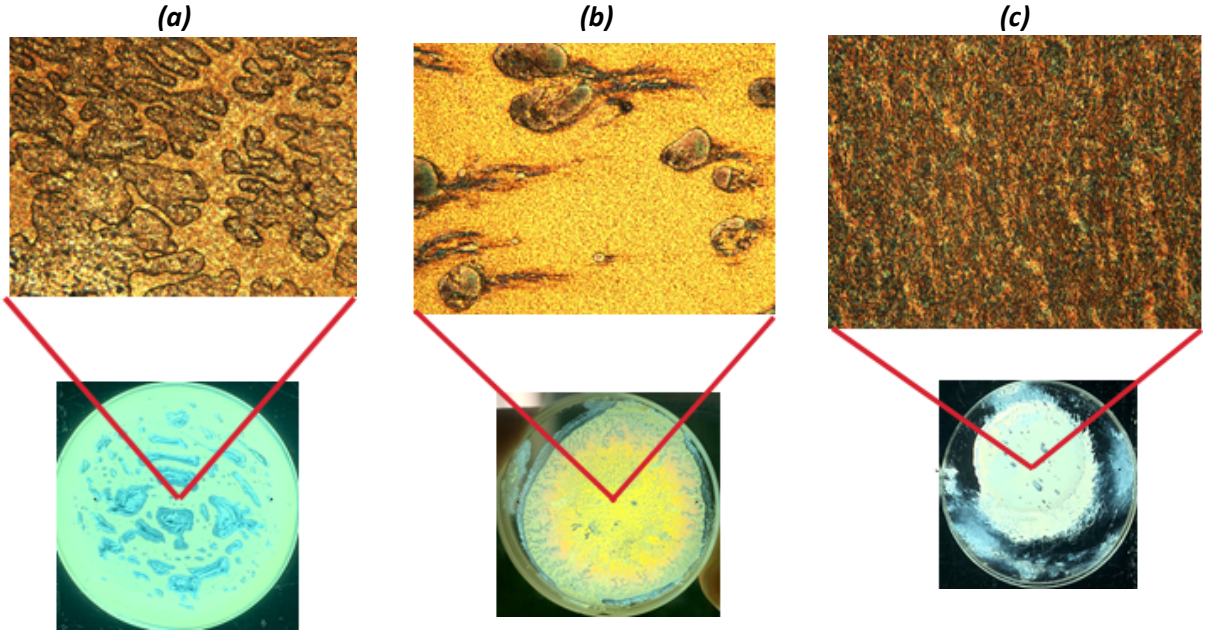

Figure 9: *Three separate devices (bottom) viewed under crossed polarizers; above each device is shown a photomicrograph of a specific area in that device viewed under crossed polarizers using a polarizing microscope.*

Mix #	% GLC-Bz3CholC5 in host	Solvent	Melt Temp (^{o}C)	Processing
1	50	Cloroform ($CHCl_3$)	180	1). Anneal 2 hours at 180^{o} C
2	25	Dichloromethane (CH_2Cl_2)	170	1). Quench to 25^{o} C
3	25	Cloroform ($CHCl_3$)	170	1). Anneal to 155^{o} C 2). Quench to 25^{o} C

Table 3: *The three different mixtures used to fabricate the devices shown in Fig. 9 along with their processing temperatures and how they were cooled. Quenching is an immediate cooling method in which the device is placed on a cool metal block; annealing is where the sample is cooled slowly to the designated temperature and held there for a prolonged period.*

Figure 9 shows that small variations in processing techniques for the three different mixtures shown in Table 3 can make a substantial difference in the final device. [7] For example, Mix #'s 2 and 3 were both processed at the same temperature and contained the same 25% GLC-Bz3CholC5 in the host; however, after dissolving them in different solvents (dichloromethane and chloroform, respectively) and altering the device processing technique by slow cooling of Mix 3 to 155^{o} C and then quenching the device (instead of immediately quenching as was done for Mix 2), the two devices showed distinctly different textures under the optical microscope. While Device 2 has several imperfections and a small grainy texture, Device 3 has a more uniform but larger grainy texture with few to no imperfections. The grainy texture in all three devices produced a high degree of optical scattering that prevented any conclusive birefringence or selective reflection testing. All processing temperatures were determined experimentally using hot stage polarizing microscopy, in which small amounts of each mixture were melted to determine their clearing point and glass transition temperature. This procedure allowed determination of viable temperatures for processing each unique mixture using a minimum amount of GLC material.

2.3 Final Procedure

The final procedure consists of three main phases: (1) preparation of the two glass substrates; (2) mixture preparation and filtration; and (3) device assembly using melt processing. On average, it takes roughly two to three days to complete all three phases and assemble a GLC cell. During substrate preparation, two clean glass substrates with the same diameter are selected and cleaned thoroughly using deionized water, detergent, and an ultrasonic cleaner. Next, the cleanest side of each substrate is coated with a polyimide alignment coating, which helps promote parallel alignment of the GLC material. Finally, the coating is buffed in order to promote more uniform alignment. When fabricating an optical device, the GLC molecular alignment needs to be parallel to the substrate in order to achieve the highest quality device. The next process phase was to prepare a uniform mixture by dissolving the GLC nematic (or long-pitch PCLC) and GLC-Bz3CholC5 into either dichloromethane or chloroform to ensure uniform mixing of the individual components. Next, the solution was filtered several times through a sub-micron particle filter

and dried using a simple gas evaporation apparatus (Fig. 10) followed by high vacuum drying overnight. The final phase was device assembly, which consisted of melt processing followed by quenching (rapid cooling), annealing (slow cooling), or a combination of both.

1). *Substrate Preparation*

- Wash substrates in an ultrasonic cleaner using a detergent and deionized (DI) H_2O
- Rinse substrates with DI H_2O
- Dry substrates in air for several hours
- Spin-deposit polyimide alignment coating onto the substrates and bake at elevated temperature
- Buff the alignment coating using a buffing machine to establish the LC alignment direction

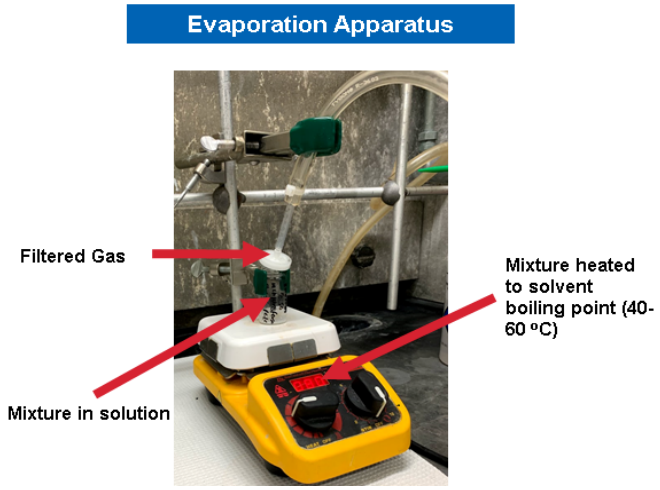

Figure 10: *The evaporation apparatus used to thoroughly evaporate the solvent from the mixture by running nitrogen or argon gas over it.*

2). *Mixture Preparation*

- Dissolve the GLC and PCLC in either CH_2Cl_2 or $CHCl_3$
- Filter through an 0.45 μm particle filter
- Evaporate solvent using N_2 or Ar (see Fig. 10)
- Dry using a high-vacuum freeze dryer

3). *Melt-Processing (Fig. 11)*

- Set hot plate to 10-15^{o} C above T_c (clearing temperature)
- Melt mixture onto microscope slide and stir until clear
- Transfer the mixture onto the middle of a single substrate, making sure not to touch the substrate
- Mix the remaining clear mixture with glass microspheres and transfer onto 4 corners of the same substrate
- Carefully sandwich the GLC material with the second substrate's coated surface facing the GLC material
- Using previous observations from hot stage polarizing microscopy, decide which cooling method to use

  - ***quenching***: quickly transfer the device onto a cool metal surface

  - ***annealing***: set hot plate timer to desired time and temperature and monitor cooling

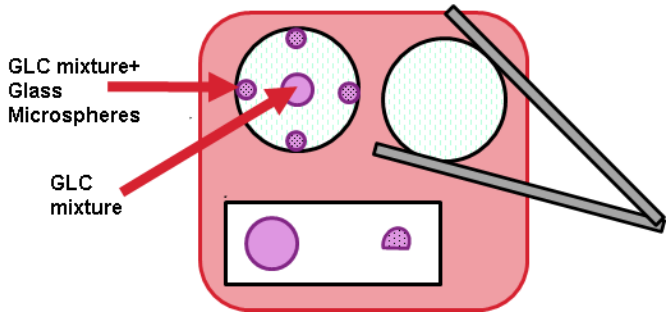

Figure 11: *Schematic showing the basic melt processing technique, which takes place on a hot plate.*

2.4 Final Device Development

After the procedure described in Sec 2.3 was developed, a new nematic host, GLC-CChxn3N4 that had been synthesized in very small quantities was mixed with GLC-Bz3CholC5 to fabricate a mixture and device employing only GLC materials. Figure 12 shows the nematic properties and chemical composition of the new host. Nematic LCs possesses high orientational order and low positional order; they have many of the optical properties of a crystalline solid, but because they are fluids while in the nematic phase they cannot support a shear stress. When combined with a chiral "dopant", the resultant mixture inherits the chirality of the dopant, along with associated optical properties such as selective reflection.

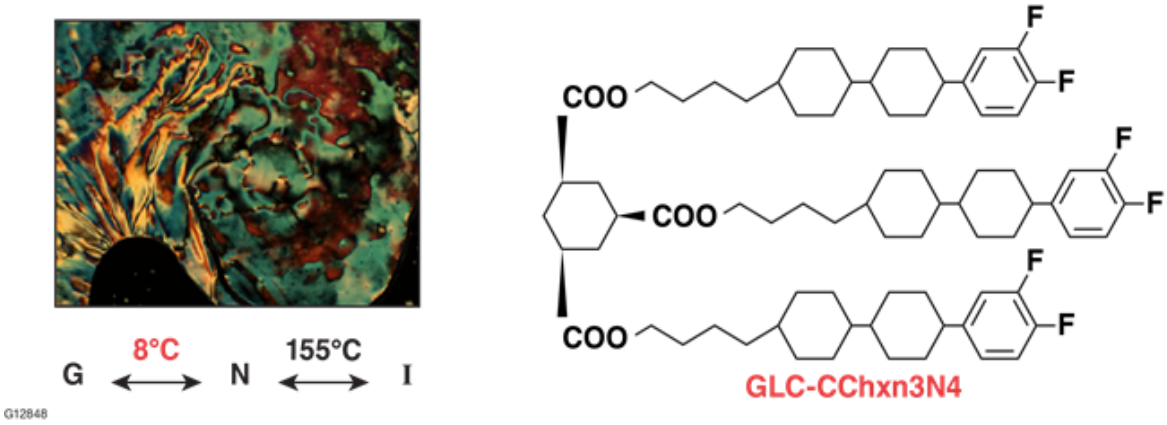

Figure 12*: Nematic texture of the new GLC host viewed under crossed polarizers in transmission using a polarizing optical microscope (left) and its chemical structure (right). The nematic phase has a broad temperature range of 8° to 155°C. The compound has a cyclohexane core with pendants that contain fluorine atoms (F).[6]*

The advantage of this host is that its fluorine-containing groups suppress the formation of smectic phases when mixed with GLC-Bz3CholC5. Other advantages are that it (1) allows for a wide temperature range for the mixture's cholesteric phase; (2) induces parallel alignment (see Sec. 1), thus counteracting the natural tendency of GLC-Bz3CholC5 to align homeotropically; and (3) reduces the overall mixture viscosity, which results in fewer bubbles into the device and makes device fabrication much simpler. The new mixture (50% by weight of GLC-Bz3CholC5 in the nematic host GLC-CChxn3N4) was processed at 160^{O}C followed by slowly cooling to 120^{O}C and then the top substrate was moved repeatedly back and forth in the buffing direction to promote homogenous alignment. The device was allowed to cool slowly to room temperature overnight. Figure 13 shows the device under crossed polarizers and regions of the device viewed under crossed polarizers using a polarizing optical microscope. The device has a clear blue selective reflection and few defects (seen in black). The much tinier black specks distributed within the device (right) are most likely trapped air bubbles, which can be eliminated with further processing improvements.

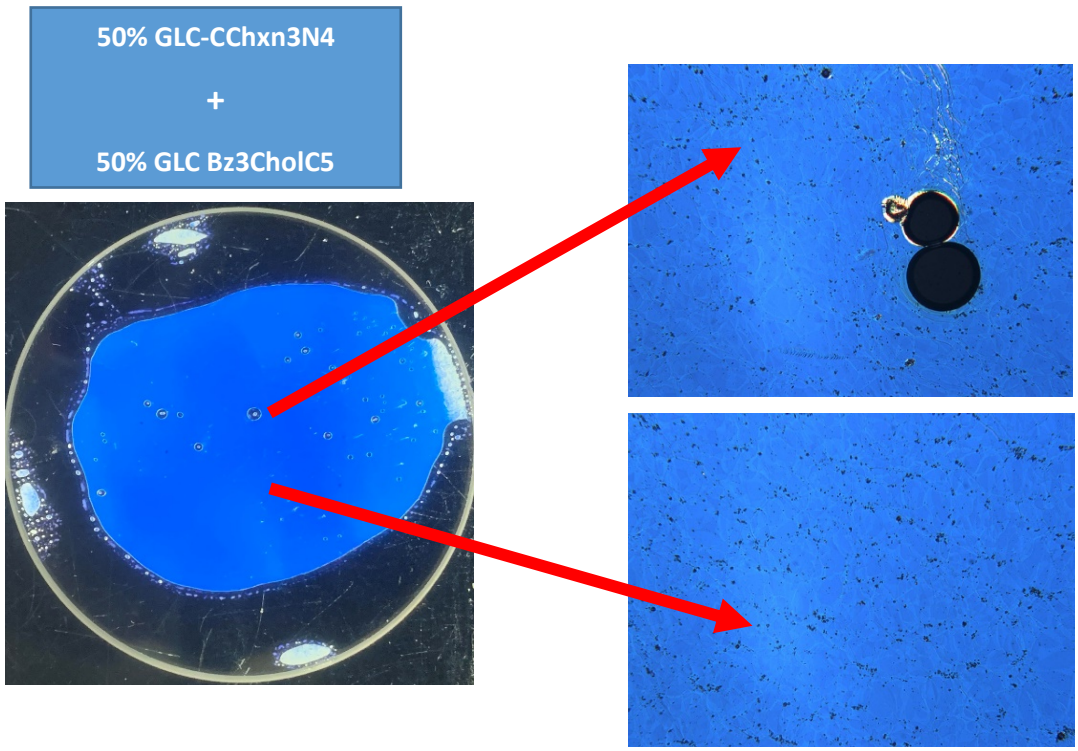

Figure 13: *Left: the new GLC circular polarizer device viewed under crossed polarizers. Right: Two regions of the device viewed under the polarizing optical microscope. The device is well aligned (as indicated by its uniform blue selective reflection) and shows few major defects (particulates and large air bubbles). The microscopic black objects are air bubbles introduced during shearing of the substrates. The device was fabricated using two thin fused silica substrates with a 2" radius.*

3. Results and Discussion:

Several tests and measurements were conducted on the device shown in Fig 13 to determine the optical quality and properties of the device [8]. If a linearly polarized incident light beam passes through a birefringent material, two polarized components exit the material with a phase difference called the linear retardance. The retardance map (Fig. 14), the optical rotation map (Fig. 15), and the polarization map (Fig. 16), all obtained using a Hinds Mueller Matrix polarimeter, indicate very good LC alignment and little optical scattering. Measurements of linear retardance, optical rotation, and output polarization were taken within the elliptical area of the device where there was GLC material present, as shown in Figs. 14-16. In these three maps, “x-position” and “y-position” indicate the value of retardance, optical rotation, and polarization measured at specified horizontal and vertical distances (in millimeters) from the center of the sample. Because the mixture used to fabricate the device contains chiral material, one would expect a small

value of linear retardance and largely consistent optical rotation values, both of which are clearly evident (Figs. 14 and 15, respectively). The average linear retardance is 2.15 ±0.65 nm, with one small area of higher retardance (6.5 nm) shown as a small red spot in the lower region of the outlined device. The retardance map's upper region shows generally lower linear retardance values than its lower region. These results show that there is some residual linear polarization in the device, which must be addressed in future mixtures and device fabrication.

Figure 15 shows the optical rotation of linearly polarized light as it passes through the device. The optical rotation values measured prove that the device is indeed chiral and optically active. Chiral LC materials separate circularly polarized light into two distinct components of opposite handedness (left or right). The output polarization map (Fig. 16) plots the directionality (handedness) of circular polarization. Right-handed circularly polarized light passes through the device while left-handed circularly polarized light is rejected and only present in a few outer regions of the device. The inner region (vertical lines) in Fig. 16 reveals the output polarization rotation produced by chiral GLC material; the outer region (45^{o} lines) shows the rotation of the incident light polarization passing through the empty regions of the device (essentially identical to the input polarization direction, shown as a black double-headed arrow in Fig. 16). The polarization rotation imparted by the chirality of the GLC is the difference in optical rotation angles between the two sets of lines, which is (-) 36.2 ^{o}. This result is significant in that it shows that the device has the desired optical properties to be used as a circular polarizer in that it effectively allows only right-handed circularly polarized light to pass through it.

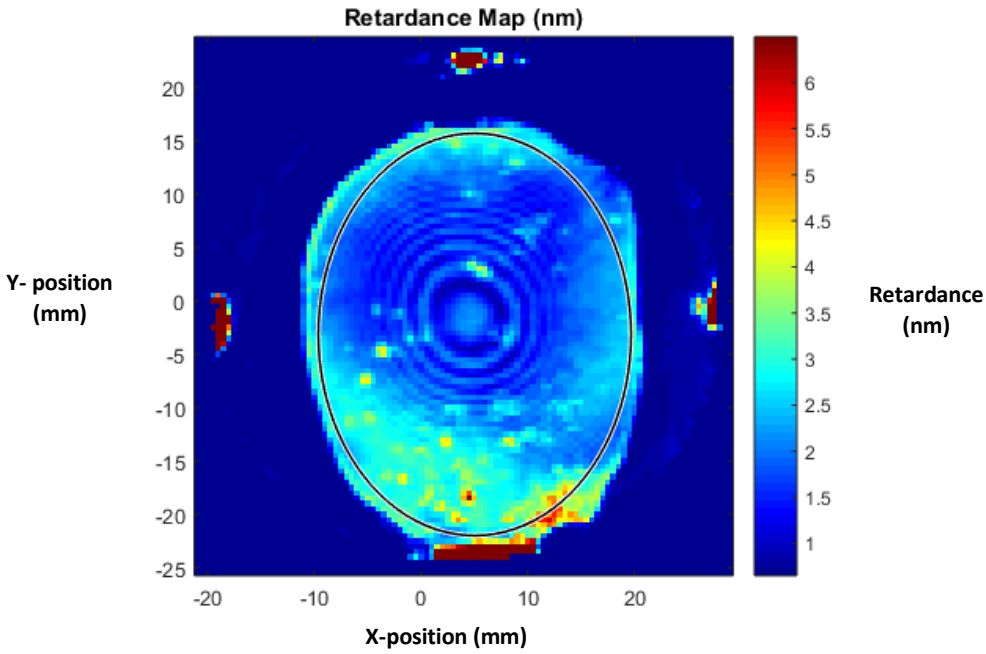

Figure 14: *Retardance map of the device with an average linear retardance of* 2.15 ± 0.65 *nm [8].*

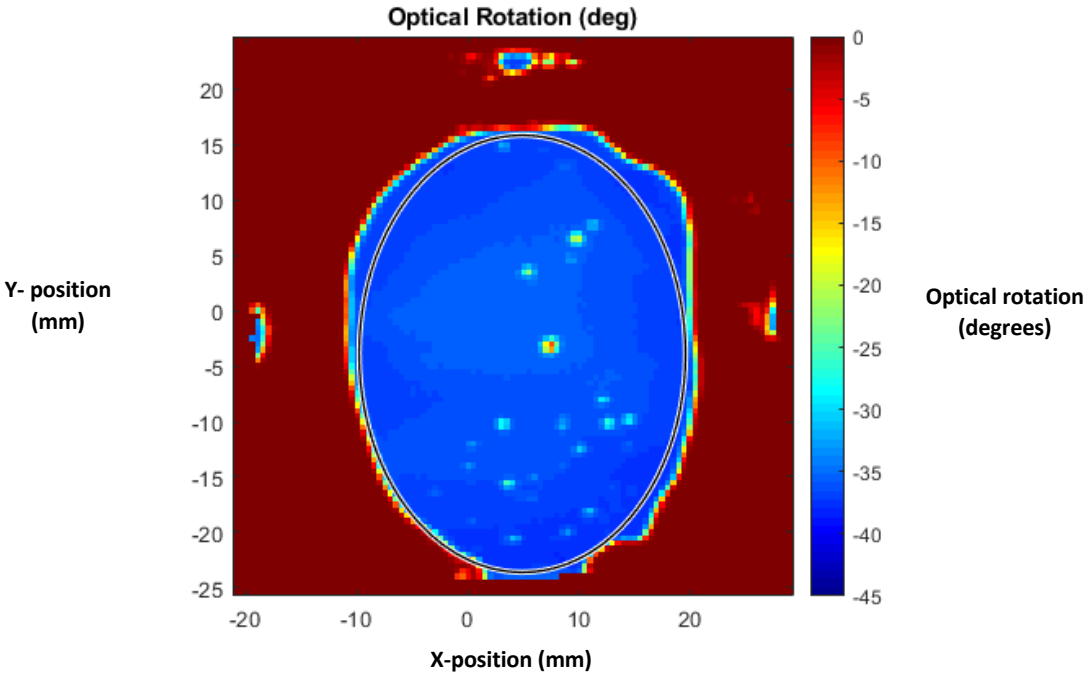

Figure 15: *Optical rotation map, indicating that the chiral material in the device is rotating light by a consistent amount of (-) 36.2* $\pm 1.3^{o}$*. [8]*

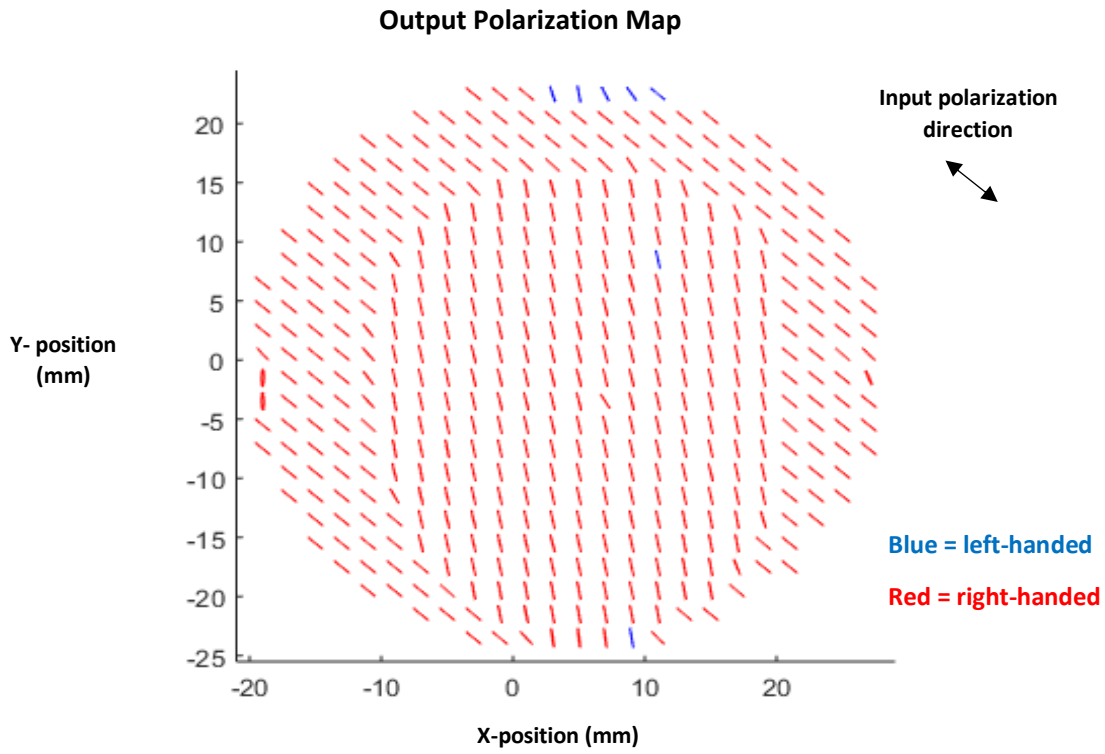

Figure 16: *Output polarization map giving the direction of rotation of the incident light after it passes through the GLC device. [8]*

4. Conclusions

Glassy liquid crystals (GLCs) with saturated natural product pendants such as cholesterol can be used effectively to create well-aligned circular polarizer cells with few imperfections, high optical quality and uniformity, high damage thresholds, and excellent alignment. The procedure developed in this work will provide the basis for ongoing GLC mixture development and device fabrication efforts. A 50:50 mixture of GLC-Bz3CholC5 and GLC-CChxn3N4 was developed that showed promising alignment and optical qualities. Processing conditions for the mixture were determined experimentally using hot stage polarizing microscopy; in this manner, phase transition temperatures and alignment quality for different mixture compositions could be observed using very small amounts of material and this information used to determine processing conditions for the fabrication of well-aligned devices. Results showed some desired

optical properties of these GLC materials, but there is certainly more work to be done in eliminating residual linear polarization and scattering effects, as well as microscopic extrinsic particles and trapped atmospheric gases.

In the future, additional mixtures will be developed to reduce scattering and improve GLC alignment. Different alignment techniques such as photo-alignment coatings will be evaluated during device fabrication. Finally, new GLC's with fully saturated cores and pendants based on other natural products (such as the steroid epiandrosterone) are under development and will undergo similar device fabrication techniques as the ones developed in the procedures described here. If a viable mixture composition is developed, future research will involve the fabrication of single substrate devices, which would be a significant benefit to laser systems such as OMEGA and even the National Ignition Facility.

5. Acknowledgments

I thank Dr. Stephen Craxton for providing this great opportunity to conduct this research and meet other like-minded peers; Ms. Jean Steve for organizing this program; my project advisor Mr. Ken Marshall for his endless help, support, and guidance throughout; Ms. Lonnie Garrett, my chemical engineering undergraduate mentor who helped me gain familiarity and purpose for my project; Ms. Brittany Hoffman for conducting the retardance and polarization measurements on my samples; and Mr. Eugene Kowaluk for his photography. Finally, I acknowledge the U.S. Department of Energy, the National Nuclear Security Administration, and the University of Rochester for providing the funding for this research.

6. References

[1] S. D. Jacobs, K. A. Cerqua, K. L. Marshall, A. Schmid, M. J. Guardalben, and K. J. Skerrett, "Liquid-Crystal Laser Optics: Design, Fabrication, and Performance," Journal of the Optical Society of America B, 5(9), 1962; 1988.

[2] D. B. Murphy, K. R Spring, T. J. Fellers, & M. W. Davidson, (n.d.), *Principles of Birefringence*, retrieved July 16, 2019, from https://www.microscopyu.com/techniques/polarized-light/principles-of-birefringence

[3] Physics Tutorial: *Polarization* (n.d.), retrieved July 23, 2019, from https://www.physicsclassroom.com/class/light/Lesson-1/Polarization

[4] J. Bonadonna, (2016, March), "Next Generation Liquid Crystal Mixtures for OMEGA Circular Polarizer/Isolator devices", retrieved July 2019, from http://www.lle.rochester.edu/media/publications/high_school_reports/documents/hs_reports/2015/Bonadonna_James.pdf

[5] K. L. Marshall, D. J. Batesky, J. U. Wallace, L. Garrett, T. Z. Kosc, S. Papernov, B. N. Hoffman, and J. Shojaie, "UV-Transmissive Glassy Liquid Crystals Employing Chiral Synthons Based on Natural Products," SPIE Optics and Photonics, Liquid Crystals XXIII, San Diego, CA, 11–15 August 2019 (invited).

[6] J. U. Wallace, K. L. Marshall, T. Z. Kosc, D. J. Batesky, B. N. Hoffman, S. Papernov, L. Garrett, J. Shojaie, and S. G. Demos, "Laser-Induced–Damage Behavior of Novel Glassy Liquid Crystal Materials at 1 ns and Multiple Wavelengths," Laser Damage 2019, Boulder, CO, 22–25 September 2019.

[7] Londrea Garrett, private communication.

[8] Brittany Hoffman, private communication.

Schlieren Diagnostic for the Imaging of Thermal Turbulence

Adam Mroueh

Pittsford Sutherland High School

Advisor: Dr. Douglas Broege

Laboratory for Laser Energetics

University of Rochester

August 2019

I Abstract

Turbulence and refractive index gradients arise from heat or gas flow through air and have long been an issue, disrupting the propagation of laser beams as well as their stability and ability to focus on a tight spot. Schlieren, a type of imaging used to visualize gradients in indices of refraction, has been proposed as a possible way to identify turbulence such as that occuring in CLARA amplifiers used at the Laboratory for Laser Energetics. In this experiment, through the setup of a Schlieren system consisting of a pinhole light source, a concave parabolic mirror and a razor blade it was possible to record the flow of heat and gas through air. Using the Schlieren system, a hot plate was analyzed at various temperatures ranging from 40-50 degrees Celsius. Videos were taken at a given temperature and a MATLAB script was devised to average these videos into a composite image. The script then finds the root-mean-square deviation between the averaged image and each individual frame in the video. The resulting matrix when displayed as an image represents turbulence from the hot plate. This process was repeated for nitrogen flow at varying pressures. Upon comparing the hot plate and nitrogen, it was explored whether the effects from turbulence could be reduced through heating nitrogen. Finally, various laser parts were analyzed such as a laser crystal cell and a gas diffuser to see how they may be contributing to gas-related turbulence.

II Introduction

The Laboratory for Laser Energetics (LLE) is home to two of the world's most powerful lasers–the 60 beam OMEGA and four beam OMEGA EP. Analysis of laser systems at the lab has revealed disruptions in the propagation of beams around CLARA amplifiers. Figure 1 shows an image of a laser beam before and after it passes through an amplifier. These images reveal how the laser beam changes from its square shape shown on the left to the more irregular shape on the right. Figure 2 shows an image of the CLARA amplifier, which the beam in Figure 1 is passing through. An image taken with a thermal imager shows this to be an area of high thermal activity relative to room temperature. This leads to the belief that it is turbulence coming from this heat that causes the breakdown in the laser beam's form shown in Figure 1.

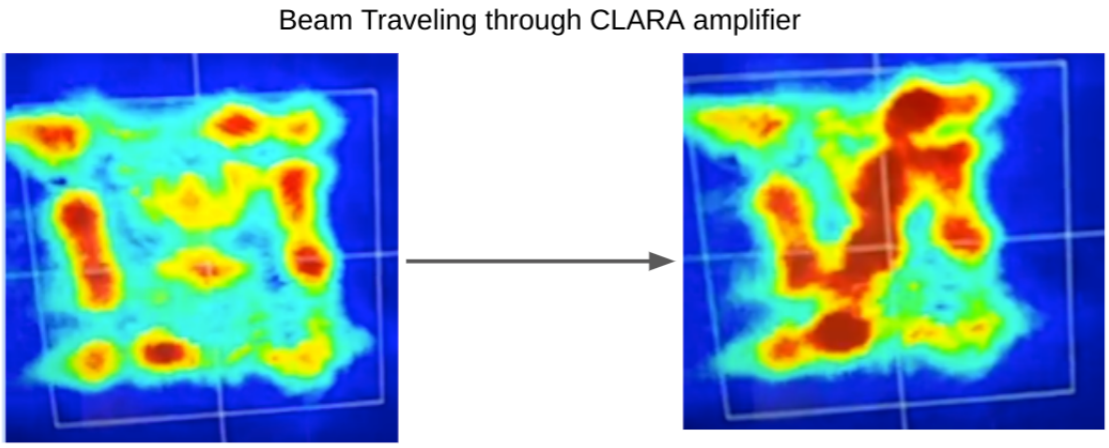

Figure 1: Intensity maps of a square laser beam before and after it passes through a CLARA amplifier. The image on the left shows a square beam with a relatively even distribution of intensities. The beam on the right shows the beam as it exits the amplifier. This image of the beam shows a breakdown in its shape as well as an uneven distribution in the beam's intensity as shown by the change in the red, green and blue spots.

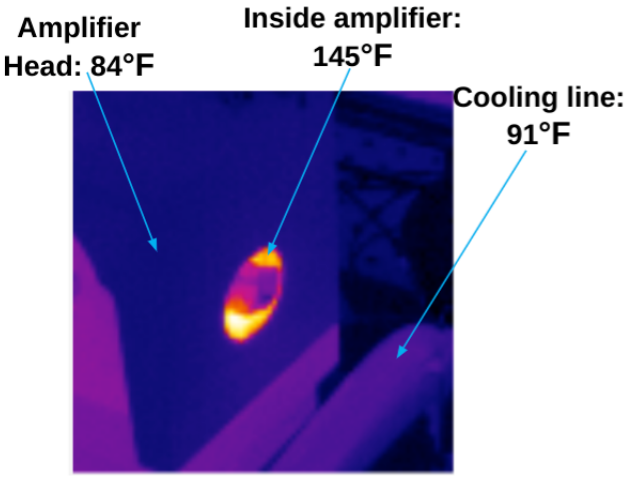

Figure 2: A picture of a CLARA amplifier, which is a rod surrounded by flash lamps with the beam propagating along its axis, that increases the intensity of a laser. This image is taken with a thermal imager, which shows the temperature of the various parts of the amplifier. This helps one understand a potential source of the disruptions seen in Figure 1.

In fluid mechanics there are two predominant types of flow, laminar and turbulent. Laminar flow is characterized by a streamlined flow, lacking irregularities, in which fluid layers move

parallel to each other. Laminar flow is also typical of fluids moving at a slower velocity. Turbulent flow in contrast is disorderly and occurs when fluid layers cross each other, moving at high velocities [1]. Any deflections caused by a refractive index gradient–coming from either laminar or turbulent flow–can disrupt the travel of lasers. However, those caused by turbulent flow are the most problematic.

Schlieren is a method of imaging originating from the German word *Schliere*, meaning streak. Historically, Schlieren has been used to visualize the flow of fluids which form a refractive index gradient, finding application in aerospace engineering and glass making [2]. Modern computers and programming languages such as MATLAB, however, allow for novel forms of analyzing and quantifying a Schlieren image. With this in mind, the goal of this project is to visualize nonuniformities in the index of refraction, including those coming from turbulent flow, through building a Schlieren system and writing a MATLAB script. In doing this work, LLE has gained insight into disturbances which affect laser systems as well as information which will allow for possible solutions to these problems.

III Experimental Setup

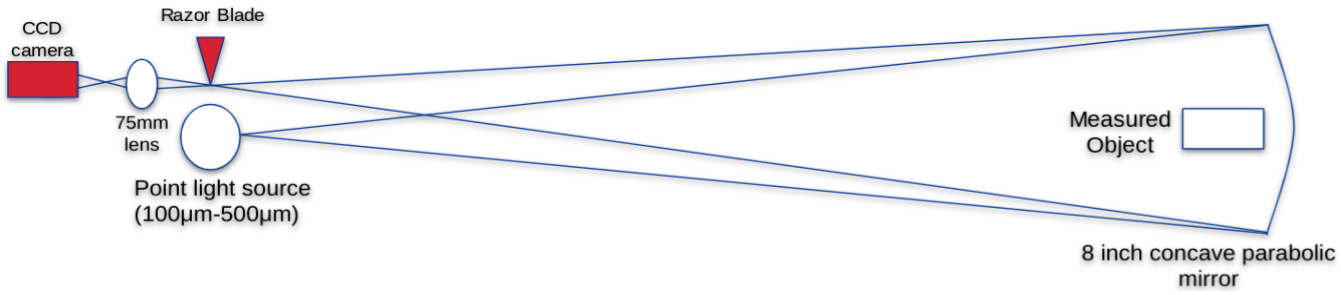

Figure 3: Experimental setup. A light source of diameter 100-500 microns expands and is reflected off a concave parabolic mirror, causing it to refocus near the original point. A razor blade is inserted at the new focus, cutting off exactly half of the refocused light. The remaining light passes through and is imaged by a 75 mm lens onto a CCD camera which displays the Schlieren image of the measured object onto a computer. The point light source is placed 2 focal distances away (400 cm) from the mirror at half the mirror's height (10 cm)

The optical basis behind Schlieren comes from Snell's law, which indicates that as a wave, in our case light, passes between two optical media it refracts or bends relative to the interface normal based on the change in index of refraction. Snell's law can be stated as the equation: $N_1 Sin\theta_1 = N_2 Sin\theta_2$ where N_1 is the index of refraction of the first medium, N_2 is that of the second medium, θ_1 is the angle of incidence relative to the interface normal, and θ_2 is the angle of refraction. Changes in temperature lead to small changes in index of refraction, somewhere on the order of one thousandth of a percent for each degree. In Figure 3 as light passes through the point labeled "measured object," it refracts relative to the amount of heat–or type and amount of gas–it passes through. The light having been refracted, the new focus will be moved by an infinitesimally small amount, invisible to the human eye. The position of the razor blade can then block a portion of this refracted light, preventing it from reaching the camera. The opposite is also true in that refracted light can shift part of the focus sideways, off the razor blade, allowing more light to reach the camera. These slight changes in the position of the focus create dark and light regions respectively where there are nonuniformities in refractive index [2]. A Schlieren image of a hot plate, placed in the area labeled "measured object," is seen in Figure 4 showing the dark and light spots created by the flow of heat through air.

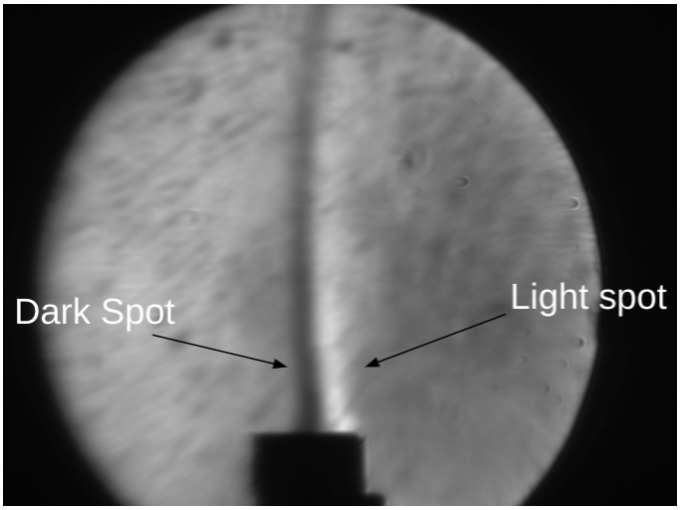

Figure 4: Schlieren image of a hot plate, illustrating dark and light regions caused by the refraction of light as it passes through the warm air. The hot plate is the rectangular black object in the middle of the bottom of the figure, beneath the light and dark regions.

Various light sources were utilized in this work including white light, a monochromatic

flashlight and a helium neon (HeNe) laser. Each source had various pros and cons associated with the Schlieren image it produced.

III.I Light sources: White Light

White light was the original light source used with the Schlieren setup. A Thorlabs adjustable lamp was placed against a pinhole ranging from 100-500 microns in diameter. The white light was advantageous in that it could be placed against a pinhole, didn't require focusing, and had an adjustable intensity. This was useful as pinholes can be interchanged, yielding different results as deemed necessary while light intensity could be adjusted as needed to procure the sharpest image. The primary downside to using white light was that the 75 mm imaging lens seen in Figure 3 was a monochromatic lens while white light contains many wavelengths. This led to somewhat of a smearing effect in the images due to the uneven focusing of light.

III.II Light Sources: Monochromatic Flashlight

To alleviate the smearing effect from the white light, an attempt was made to use a monochromatic green flashlight. While the smearing was eliminated, focusing the flashlight–a device fitted with its own optics–through a pinhole was difficult. In addition there was insufficient light illuminating the mirror and it was impossible to record a detailed image.

III.III Light Sources: HeNe Laser

To fix the problem of smearing while still maintaining sufficient illumination of the mirror, a HeNe laser was used. Since laser light is highly collimated a system of lenses as seen in Figure 5 was used to expand the beam so that it could cover the entirety of the mirror.

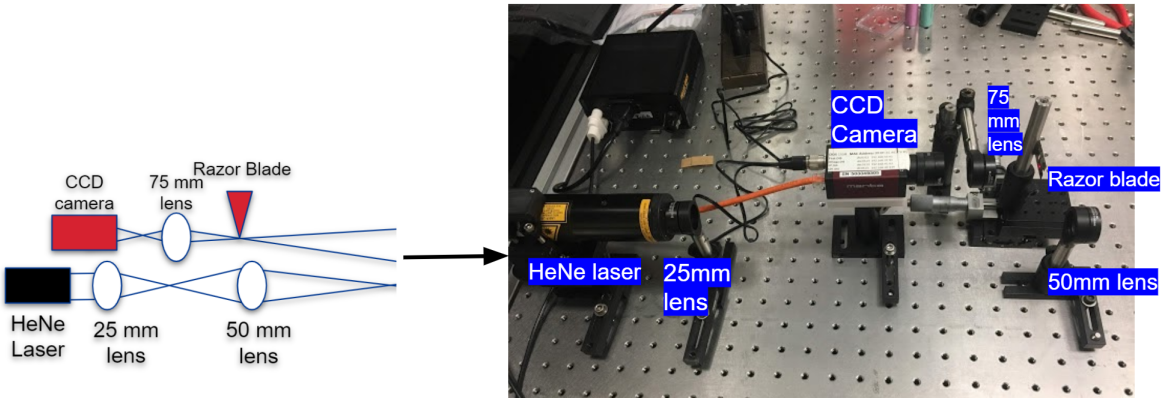

Figure 5: *The setup with the HeNe laser. In this setup, the 50 mm lens represents the point light source. The image on the left breaks down the components of the setup.*

While the HeNe laser had the advantage of eliminating smearing, issues arose regarding the lack of anti-reflection coatings on the various lenses. This led to issues with the image quality leading to a sort of smearing effect. In the end, it was determined that white light with a 500 micron pinhole was ideal for data collected using the hot plate, while either the HeNe system or white light with a 200 micron pinhole was best for collecting data from a nitrogen tube, which will be discussed more in depth in the next section.

IV Data Collection

IV.I Hot Plate

The first set of data was collected using white light and a 500 micron pinhole. The Schlieren signal from the hot plate shown in Figure 4 was analyzed at a set of five temperatures ranging from 40 to 50 degrees Celsius. Using Streampix software, videos were taken of the signal emitted from the hot plate. The CCD camera recorded for 30-45 seconds at a frame-rate of 3 frames per second, garnering videos of around 100 frames. Due to the relatively laminar appearance of the hot plate signal this low frame-rate was deemed acceptable. Single frame examples of the data collected are shown in Figure 6.

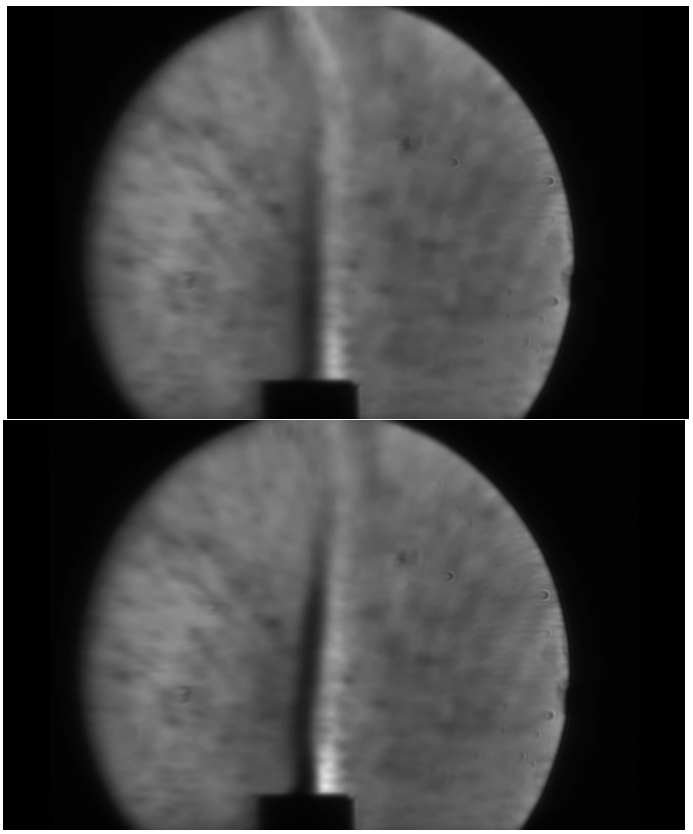

Figure 6: *Two individual frames from videos taken at 40 degrees (top image) and 50 degrees (bottom image). The hot plate is the rectangular black region in the middle of the bottom of the images.*

Air currents caused by human movement, a nearby computer and the room's cooling system contributed to fluctuations in the hot plate signal, causing it to move around and vary its intensity. To account for this, the videos were taken and averaged using a MATLAB function into a single composite image (see Section V).

IV.II Nitrogen Tube

Nitrogen is used in laser systems as a purging gas to eliminate humidity, with little thought given to the disturbances it may cause. As for the heat source, Schlieren has been proposed as a way to identify how nitrogen flow may be affecting laser propagation. To test this, a nitrogen tube was run across the room and mounted in front of the Schlieren system using Thorlabs posts and mounts. Nitrogen flow was controlled by a knob on which three distinct pressures were marked; the initial valve point, quarter turn and half turn. The initial valve point featured a

moderate streamlined flow, the quarter turn showed an increase in the nitrogen flow's intensity, and the half turn showed a chaotic fast flowing stream of nitrogen. The signal from nitrogen flow was sharp and unlike the hot plate its shape varied little from convections from the room. With this in mind the sharpest Schlieren images were obtained by recording videos at 18 frames per second for 10-15 seconds.

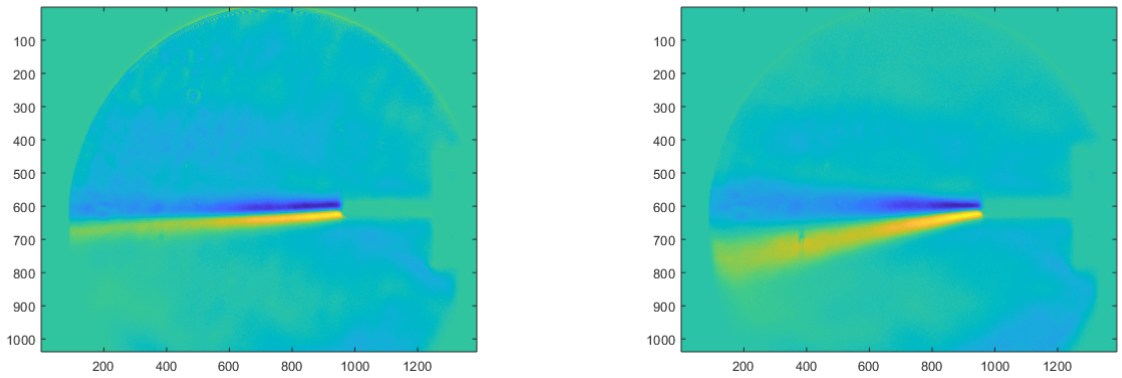

Figure 7: *Two individual frames from videos taken at the initial valve point (left image) and half turned valve (right image). Images have been background subtracted in MATLAB for greater clarity. The darker blue and yellow regions represent areas of nitrogen flow and the turquoise region directly to the right of that represents the nitrogen tube.*

V Analysis in MATLAB

A MATLAB script was created, aiming to complete the following goals for the data discussed in Section IV.

1. Average all frames of the Schlieren video into a composite image.

   (a) To accomplish this, a for loop was written which individually reads each frame of the video as a matrix and then finds the average of all of the matrices. The final matrix represents an averaged image of all the frames in the video.

2. Eliminate background noise from the image discussed in step 1.

(a) To accomplish this step, an image is taken with the Schlieren system without any signal (no hot plate or nitrogen flow). This data is then subtracted from the averaged image from step 1. This step removes stationary sources of signal (air currents, heat from computer, etc.) that are not the direct result of the source being studied. This ultimately provides a clearer image of the targeted signal.

3. Identify specific areas of both uniform (laminar) index gradients and turbulent index gradients.

(a) Stopping after step 2 reveals areas of laminar index gradients. To identify areas of turbulent flow a for loop was written in MATLAB to find the root-mean-square deviation between the image from step 2 and each individual frame in the video.

$$RMSDeviation = \sqrt{\frac{1}{n}\Sigma_{i=1}^{n}(AVG. - f_i)^2}$$

where n is the number of frames in a video, $AVG.$ is the background subtracted average image from step 2, and f_i is an individual frame from the video. The background is again subtracted, and the resulting image depicts turbulent flow (see Figure 8).

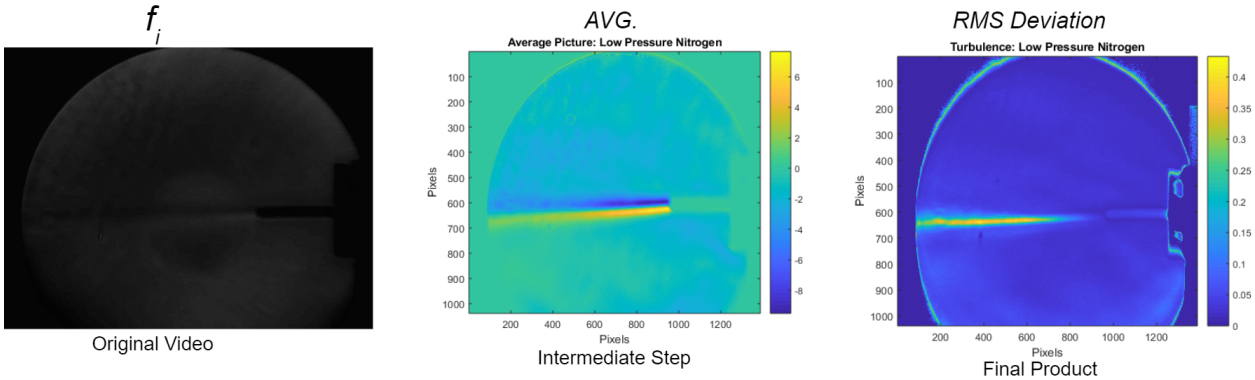

Figure 8: *A frame from a Schlieren video of nitrogen flow as it goes through the MATLAB program. The leftmost image shows a frame of a video taken with the Schlieren system. The middle image depicts an averaged video with the background subtracted (see step 2 above). The rightmost image shows the root-mean-square deviation between the middle image and the video with adjustment for background subtraction (see step 3).*

VI Comparison of the Nitrogen and Hot Plate

Upon recording data for both the nitrogen flow and the hot plate, various observations were made regarding the two and differences in their respective signals. Differences in the appearances of light and dark regions provide information about refractive index gradients. Figure 9 illustrates some of these differences. The nitrogen tube is mounted vertically in Figure 9 rather than horizontally as in Figure 7, in order to more directly compare it to the hot plate.

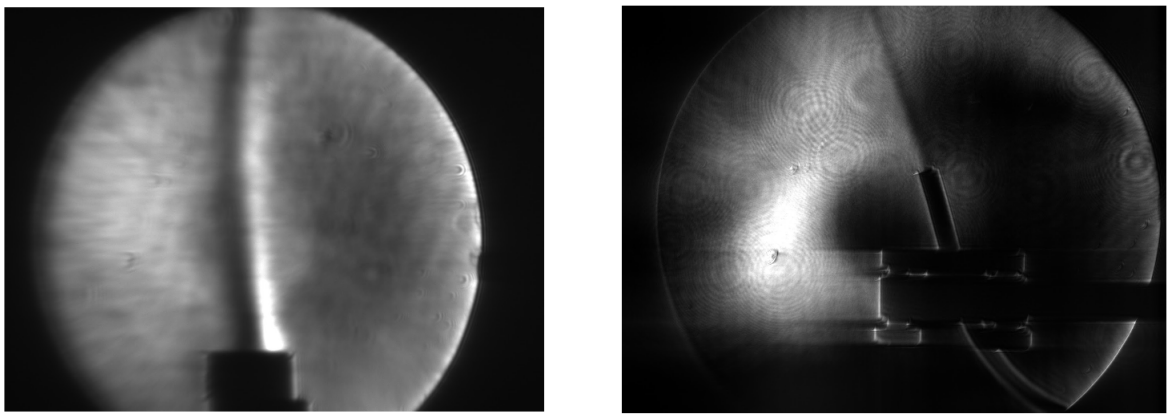

Figure 9: *Images of the hot plate (left) and nitrogen flow (right). The hot plate signal is dark on the left and white on the right while this is the opposite for the nitrogen flow (the faint signal coming off the end of the tube) which is at the initial valve point setting.*

This difference in the position of light and dark regions is due to differences in index of refraction between the nitrogen and the warm air from the hot plate. Figure 10 illustrates this in terms of Snell's law: $N_1 * Sin\theta_1 = N_2 * Sin\theta_2$.

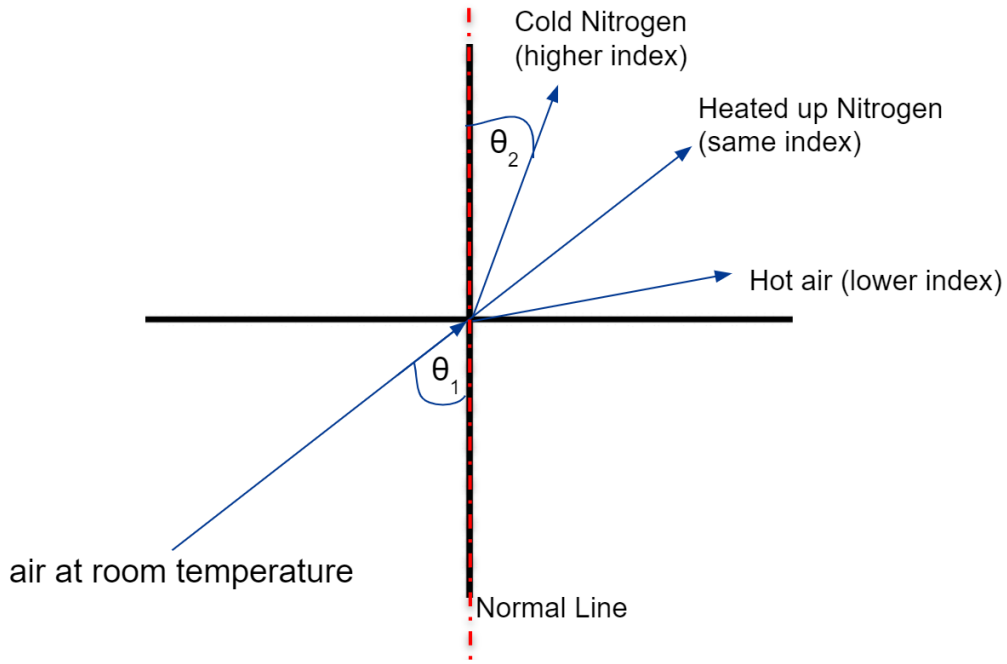

Figure 10: *Light refracting as it goes between two media. The x-axis represents the border between the media and the y-axis represents the interface normal which the light refracts relative to. As light passes from air at room temperature to cold nitrogen, it refracts at a smaller angle relative to the normal, while as light passes from air at room temperature to hot air, it refracts at a larger angle. The area below the x-axis represents air at room temperature and that above the x-axis represents the listed media.*

Cold nitrogen has a higher index of refraction than hot air and therefore light refracts at a smaller angle relative to the normal line. The index of refraction of a given medium is dependent on temperature. Heating a medium lowers its index of refraction and therefore increases the angle that light refracts to relative to the normal. It should therefore be possible to eliminate a signal from the nitrogen through heating it until its index of refraction is the same as that of room temperature air. If heating nitrogen eliminates the signal, than this tactic could be used in laser systems where nitrogen is present in order to avoid problems caused from turbulence related to nitrogen. Using data from Ref. 3 the required temperature of nitrogen was found to be around 20 degrees more than room temperature (23 degrees Celsius). It was then attempted to heat the nitrogen to this temperature, but, with limited time and materials, it was not possible to heat the nitrogen by a significant amount. Future work can be done in this area to find the exact temperature at which the signal from the nitrogen disappears.

VII Testing Laser Parts

Nitrogen is often used as a purging gas to reduce humidity in laser systems. Various laser parts were tested using nitrogen and the Schlieren system to see how they may be contributing to gas-related turbulence. Two examples of devices that use nitrogen are laser crystal cells and a gas diffuser, shown in Figure 11. Both parts were put in front of the Schlieren system and nitrogen was run through them to see how they interact with the gas. This test helped users understand how the parts may contribute to turbulence, before using them in a laser system.

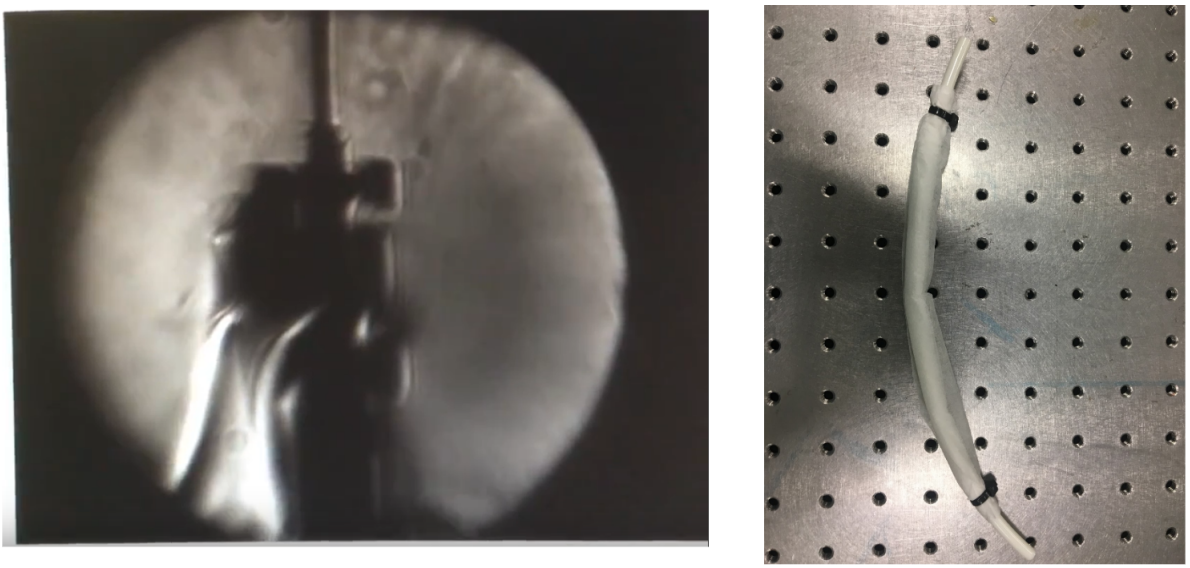

Figure 11: *Two laser parts that were tested. A Schlieren image of a laser crystal cell with nitrogen going through it (left) and a gas diffuser (right). The gas diffuser is a piece of a plastic tube with holes poked in it and mesh wrapped around it. The one pictured is used to release nitrogen in a laser system.*

VIII Pinhole Images and Aberrations

A concern with Schlieren imaging is that optical aberrations may distort the final image. In the setup used here (Figure 3) a concave parabolic mirror was used, avoiding spherical aberrations. However, the mirror is subject to comatic aberrations. Comatic aberrations come when light rays from any one of the sources hit the mirror at a nonzero angle to the normal, causing individual rays to not reflect back to the desired point at the edge of the razor blade. To

test the effect of this on the imaging system the mirror was placed at an angle and images were recorded of the pinhole light sources' reflection to see how aberrations affected their image.

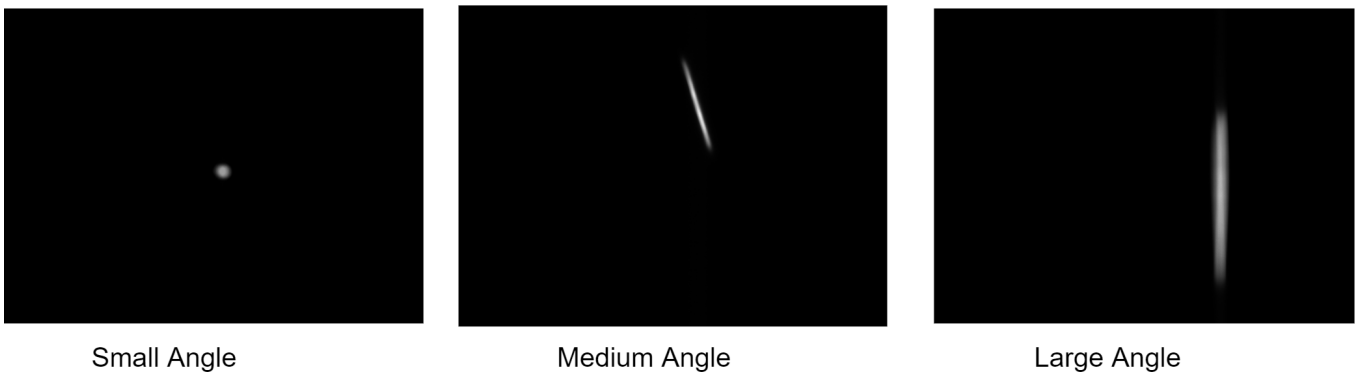

Figure 12: *Images showing the relationship between mirror angle and the image of the pinhole light source reflected in the mirror of Figure 3.*

The small angle image shown in Figure 12 accurately depicts the pinhole image when light rays are reflected 2.5-13 cm to the side of the original light source. The image becomes distorted, as shown in the middle image, when light rays are reflected at a medium angle 15-25 cm to the side of the light source. Beyond this, at 25+ cm to the side of the original light source, the pinhole reflection becomes quite distorted and difficult to focus as shown in the large angle picture in Figure 12. To alleviate the effect of these distorted pinhole images, the Schlieren system was typically set up with the pinhole reflection around 2.5-7.6 cm to the side of the original light source.

IX Conclusions

A Schlieren imaging system was built and various parameters were experimented with to optimize it. The system was also demonstrated using a hot plate and nitrogen gas flow. A MATLAB program was written which together with the Schlieren reveals areas of thermal and gaseous turbulence. Future work could be done to explore whether the effects from turbulence from nitrogen and other gasses can be accurately and consistently reduced through heating them. Work could also be done with the Schlieren system to reduce its size and increase its portability, enabling it to be implemented into laser systems to better understand and quantify

how disturbances may be affecting them.

X Acknowledgments

I would like to thank my advisor, Dr. Douglas Broege, for the countless hours he spent guiding me through this research. His time and effort in helping me understand the theory behind what I was doing made this experience incredibly educational and a lot of fun. I would also like to thank Dr. Stephen Craxton and Ms. Jean Steve for helping set up this incredible program which inspired me to continue pursuing and exploring science. Lastly, I must thank my fellow interns and everyone at LLE for creating an incredible work environment and always being there to help.

XI References

References

[1] "Difference between laminar and turbulent flow - mechanical booster." https://www.mechanicalbooster.com/2016/08/difference-between-laminar-and-turbulent-flow.html. (Accessed on 08/29/2019).

[2] A. Mazumdar, "Principles and techniques of schlieren imaging systems — academic commons." https://academiccommons.columbia.edu/doi/10.7916/D8TX3PWV, 06 2013.

[3] H. Johns and J. Wilhelm, "The refractive indices of liquid oxygen, nitrogen, and hydrogen," *Canadian Journal of Research*, vol. 15, pp. 101–108, 04 2011.

Comparative Analysis of Oxygen Uptake in Nickel and Copper-Zinc Beds

Ka-Hyun Nam

Brighton High School

LLE Advisors: Cody Fagan and Walter Shmayda

Laboratory for Laser Energetics

University of Rochester

Summer High School Research Program 2019

November 2019

Abstract

Nickel (Ni) and copper-zinc (CuZn) getter beds were analyzed for their relative efficiency in extracting oxygen from inert gas streams. The Ni bed was oxidized at various temperatures and carrier-gas flow rates. These results were compared with previously collected CuZn data. The length of the mass transfer zone (MTZ) was used as a measure of effective use of the beds' capacity for oxygen gettering. It was found that the Ni bed at 350°C has a shorter MTZ over the carrier gas flow rates examined in comparison to the CuZn bed at 150°C. Additionally, the MTZ was found to decrease in length as the temperature of the Ni bed increased from 350°C to 450°C. The shorter MTZ length of the Ni bed is indicative of a greater oxygen breakthrough capacity in comparison with the CuZn bed.

1. Introduction

Tritium (T_2) handling equipment is encased in gloveboxes to minimize environmental releases. The inert gas flow circulating through the glovebox is processed by a system designed to remove gaseous T_2, a radioactive isotope of hydrogen, from the gas flow. In this system, a zirconium-iron (ZrFe) alloy is utilized to capture T_2. Trace amounts of oxygen that permeate the glovebox environment through the elastomeric glove material can irreversibly oxidize the ZrFe alloy, preventing the absorption of T_2 and reducing the alloy's capacity for T_2 storage.[1] To prevent this degradation, a getter bed removes O_2 from the gas stream prior to the ZrFe alloy as shown in Fig.1.

Figure 1: Schematic of the glovebox inert gas flow cleanup system.

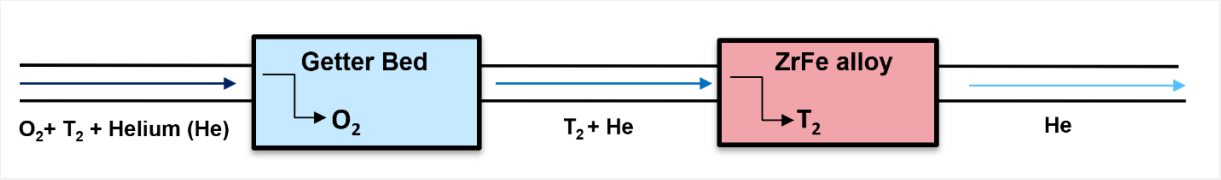

Two getter bed options that capture oxygen through oxidation are Ni and CuZn alloy. After the full oxygen capacity of the getter bed is reached, the bed is removed from the system and regenerated through reduction by creating water with hydrogen gas.

$$\text{Oxidation: } 2Ni + O_2 \rightarrow 2NiO$$
$$\text{Reduction: } NiO + H_2 \rightarrow Ni + H_2O \quad (1)$$

or

$$\text{Oxidation: } 2CuZn + O_2 \rightarrow 2CuO + 2Zn$$
$$\text{Reduction: } CuO + Zn + H_2 \rightarrow CuZn + H_2O \quad (2)$$

As the getter bed undergoes oxidation, a mass transfer zone is developed immediately upon introduction of oxygen flow to the bed and progresses down the length of the bed (Fig. 2). The MTZ is defined as the oxygen-getter reaction zone in which getter is being oxidized.[2] As the MTZ progresses down the length of the bed, it creates a saturated zone in which the getter bed is fully oxidized. The MTZ was previously measured for CuZn for areal flow rates from 0.1 to 3.5 cm/s at 150°C.[3] In this work, data was collected to characterize the MTZ of Ni at similar flow rates for two temperatures: 350°C and 450°C. This data was then compared with the CuZn bed data for the purpose of determining which of the two is the more efficient oxygen getter bed.

Figure 2: Mass transfer zone of the getter bed.

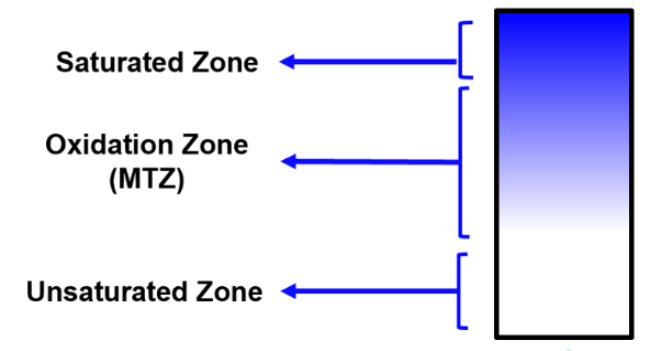

2. Experimental

The experimental set up shown in Fig. 3 allowed for control of the route and rate of the gas flow in order to simulate the flow conditions of a typical glove box inert gas stream. The bypass, which provided an alternative path for the gas flow around the Ni bed, was used for calibration prior to oxidation data collection. After traveling through either the bypass or the Ni bed, a small portion of the gas flow was siphoned off with capillary tubing in order to sample the composition of the gas leaving or bypassing the Ni bed. The chemical composition of the bed's outlet gas stream was measured with a residual gas analyzer (RGA). In the RGA system, the gas molecules were ionized by a hot cathode, then accelerated through an oscillating electric field (provided by the radio frequency quadrupole) for the purpose of finding the mass to charge ratio of the gas ions.[4] The remainder of the gas was released to the stacks. A turbomolecular system was used to create the high vacuum conditions necessary for the operation of the RGA. The bed was heated to temperatures ranging from 350°C to 450°C for the experiments while the overall system was kept at 150°C and insulated to prevent water condensation. The temperature was measured by thermocouples. The pressure of the system was monitored by a cold cathode gauge (not shown in Fig. 3) and a capacitance manometer (not shown in Fig. 3).

Figure 3: Schematic of experimental set up.

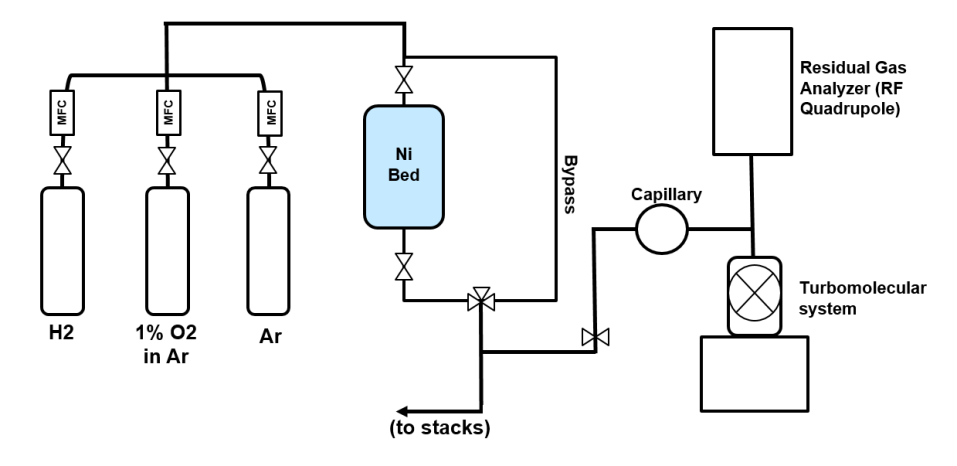

2.1 Getter Bed

The Ni bed used in this experiment consisted of a cylinder with diameter and length dimensions of 5.4 cm × 9.144 cm packed with 1.2 mm × 3 mm Ni pellets. The bed, shown in Fig. 4, was surrounded by insulation to minimize heat loss. To make the data gathered in this project applicable to any Ni bed rather than exclusively to the Ni bed dimensions used, the MTZ was measured as a function of areal velocity, defined as total gas flow rate (cm^3/s) ÷ bed cross sectional area (cm^2).

Figure 4: Schematic of Ni bed.

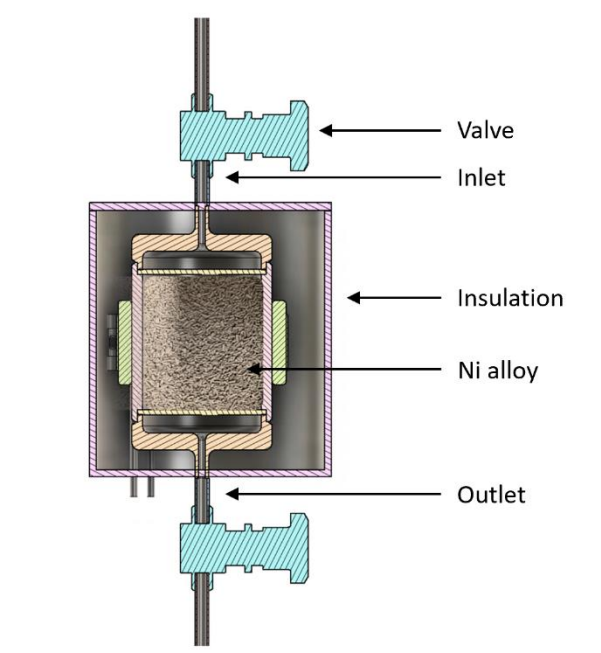

2.2 Gases and Gas Flow

Argon, 1% oxygen in argon, and hydrogen were used in this experiment. Argon, an inert gas, was used for purging the system of residual gases between oxidations and as a carrier gas for oxygen and hydrogen. The flow rate of argon was adjusted for each oxidation to make areal velocity an independent experimental variable. The total gas flow rate considered in the calculation of areal velocity is the sum of the 0.97 LPM 1% O_2 in Ar (or 0.0238 mol O_2 per hour) and the varied Ar flow rate (0.1 to 2.75 LPM). After the bed was oxidized, 50 standard cubic centimeters per minute (sccm) of hydrogen gas reduced the bed by creating water in the regeneration process.

Within the flow rate range used for this experiment (0.1 to 2.75 liters per minute (LPM) of Ar + 0.97 LPM O_2 in Ar), the areal velocity through the bed is 0.7 to 2.7 cm/s and the residence time in the bed (bed volume ÷ volumetric flow rate) is 1.4 to 52 s. Under these flow rate conditions and the temperature range used (350°C to 450°C) the modified Reynolds number (particle diameter × areal velocity × density of fluid ÷ gas viscosity) is 0.17 to 0.46. This value indicates that the gas flow is laminar and its velocity profile can be visualized as a plug flow.

2.3 Oxidation

The graph of the partial pressure of oxygen over time throughout a typical oxidation cycle of the Ni bed is shown in Fig. 5. Before oxidizing the bed, the bypass line and bed were purged with an argon flow to remove trace gases from the previous run. This is shown by the low levels of oxygen at the start of the graph. After the argon purge, a fixed flow rate of 1% oxygen in argon was passed through the bypass for calibration of the RGA, creating a sudden increase in oxygen partial pressure near the beginning of the graph. After half an hour of calibration, the gas flow route was switched to the Ni bed, resulting in a rapid decrease in the partial pressure of the oxygen flow in the outlet stream as the Ni bed began consuming oxygen through oxidation of the alloy. As the Ni bed nears maximum oxygen capacity (see "breakthrough" in Fig. 5), it is no longer able to absorb the majority of the oxygen flow, causing a gradual increase in the partial pressure of oxygen that is able to flow past the Ni bed to the outlet stream.

Figure 5: Partial pressure of oxygen as a function of time during oxidation at 350°C with 1 LPM Ar and 0.97 LPM 1% O_2 in Ar.

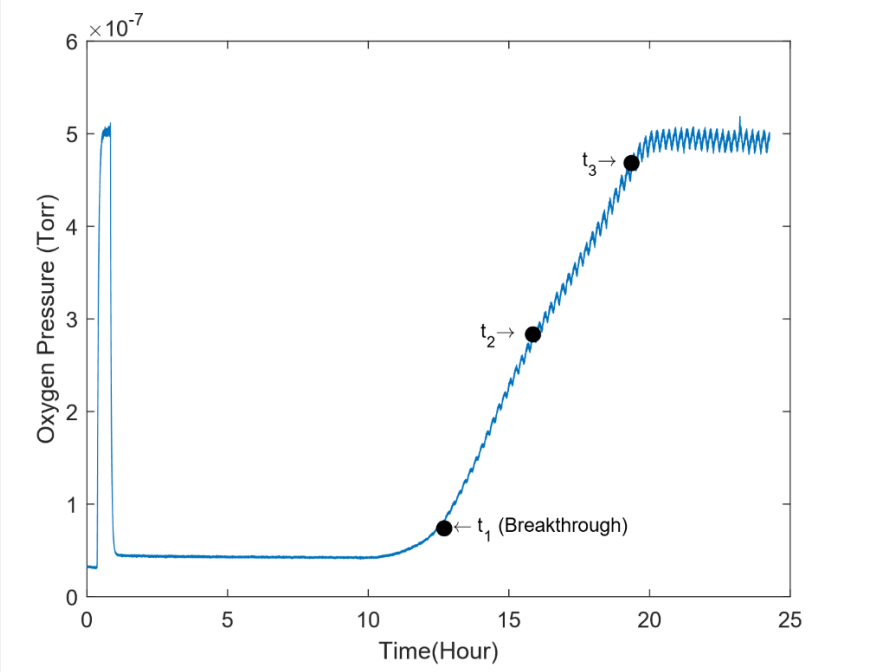

2.4 Mass Transfer Zone

Prior to breakthrough (see Fig. 2), there exists a region of the bed below the MTZ in which there is little to no oxygen present, resulting in a low partial pressure of oxygen in the outlet. The length of the MTZ is calculated with three specific time markers on the MTZ curve, shown in Fig. 5. The first time marker t_1 (i.e., breakthrough) is defined as the time at which the oxygen concentration in the outlet is 15% of the feedstock and t_3 when the oxygen concentration is 85%. The second time marker t_2 is when

$$\int_{t1}^{t2} P(t)\, d(t) = \int_{t2}^{t3} (P(t_3) - P(t))\, d(t)\,, \tag{3}$$

where P(t) is the partial pressure of oxygen in the carrier gas over time. From the values of t_2 and t_1, the MTZ length can be calculated by:

$$MTZ\ length = \frac{length\ of\ bed}{(t_2)} \times (t_2 - t_1) \times 2\,. \tag{4}$$

Beds 1 and 2 represent two different getter beds at breakthrough in Fig. 6. The MTZ length of Bed 1 is shorter than that of Bed 2. Correspondingly, the volume of the bed which is incompletely saturated is smaller in Bed 1 in comparison to Bed 2. This indicates that Bed 1 has utilized the oxygen capacity of the bed more effectively than Bed 2 because a greater fraction of the bed is used to capture

oxygen. For the purposes of this work, the effective use of the beds' oxygen capacity, or MTZ length, was used as a comparative measure of the beds' efficiency.

Figure 6: MTZ length comparison of two different getter beds at breakthrough.

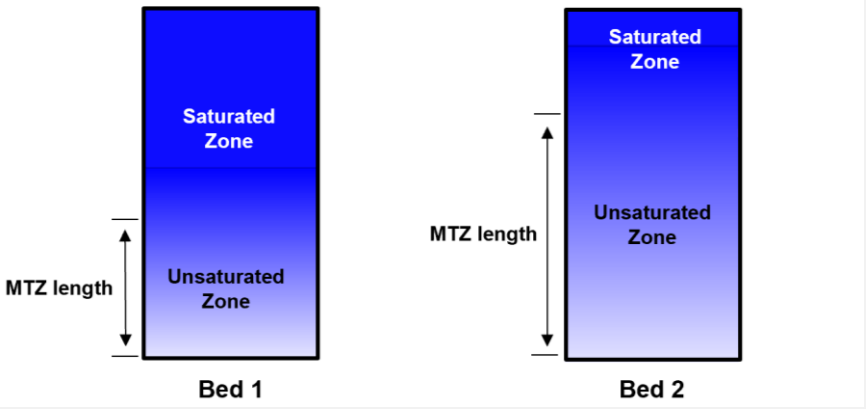

2.5 Oxygen Gettering Capacity

Capacity is defined as the maximum number of moles of oxygen that the bed can absorb at a given flow rate and temperature. The flow rate of oxygen was kept constant at 0.0238 mol/hour throughout all of the oxidation experiments. The fraction of the oxygen flow rate that is unabsorbed by the bed is proportional to the pressure of oxygen at the outlet of the bed (Fig. 5). The bed is absorbing the majority of the flow rate before t_1 and gradually decreases in the amount of oxygen absorbed from t_2 to t_3. The oxygen capacity in moles was approximated to be

$$Oxygen\ Capacity = 0.0238 \times t_2 \qquad (5)$$

where t_2 is measured in hours.

3. Results and Discussion

The MTZ length and capacity calculated from the Ni oxidations gathered throughout this work are shown below in Table 1.

Table 1: Data collected for the Ni bed capacity and MTZ length for various flow rates/areal velocities and temperatures.

Temperature (°C)	Argon Flow Rate (L/min)	Areal Velocity (cm/s)	Capacity (moles oxygen)	MTZ length (cm)
350	0.1	0.78	0.36	0.93
350	0.5	1.07	0.28	1.73
350	1	1.43	0.35	2.79
350	2.75	2.71	0.33	3.59
450	2.75	2.71	0.31	3.2

3.1 Comparison of MTZ length in the Ni and CuZn beds

The dependency of the MTZ length on areal velocity for nickel at 350°C was compared with the CuZn data at 150°C in Fig. 7. It was found that the Ni bed has the shorter MTZ for areal velocities from 0.78 to 2.7 cm/s. These results suggest that that the Ni bed has a greater oxygen adsorption capacity prior to breakthrough, with the concession that the CuZn bed operates at a lower temperature.

Figure 7: Comparison of MTZ lengths of CuZn and Ni beds. The CuZn data was collected in previous research.[3]

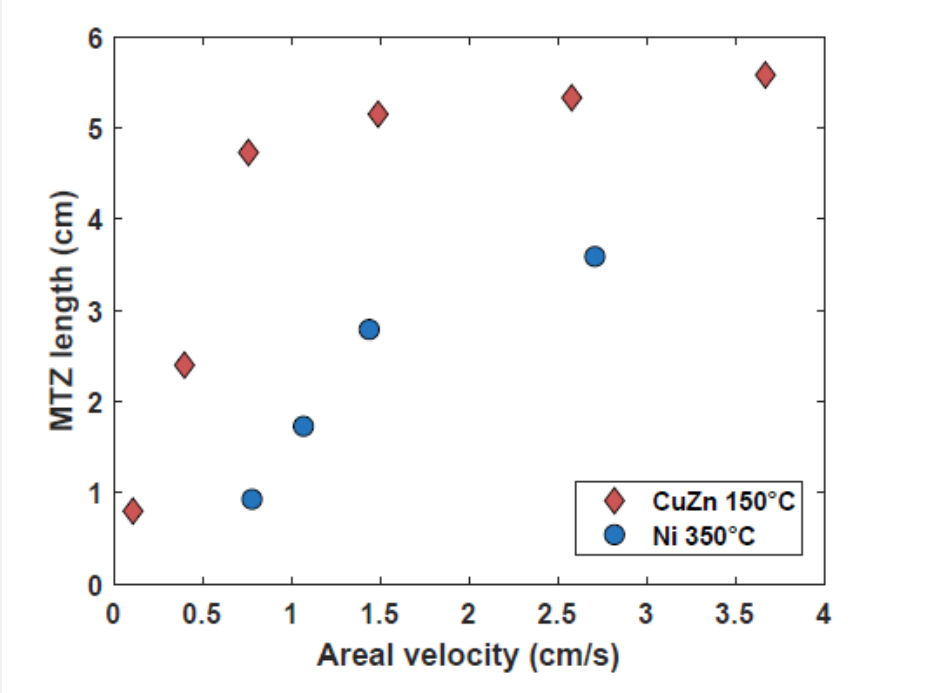

3.2 Temperature Dependence of the MTZ length of the Ni bed

The MTZ length of the Ni bed was measured at 350°C and 450°C at the areal velocity of 2.71 cm/s (or argon flow rate of 2.75 L/min). This areal velocity was chosen to find the temperature dependency as the divergence of MTZ lengths was expected to become more evident at higher areal velocities. As shown in Fig. 8, the slope of the O_2 pressure-versus-time curve at 450°C is greater than in the 350°C oxidation case, indicating that the MTZ for the 450°C case is shorter. Table 1 shows the calculated MTZ lengths for these two operating temperatures; the MTZ length in the 450°C case is 3.2 cm in comparison to the 3.59 cm for the 350°C oxidation case.

Figure 8: Oxygen partial pressure over time in 350°C and 450°C oxidation of Ni bed at an argon flow rate of 2.75 LPM.

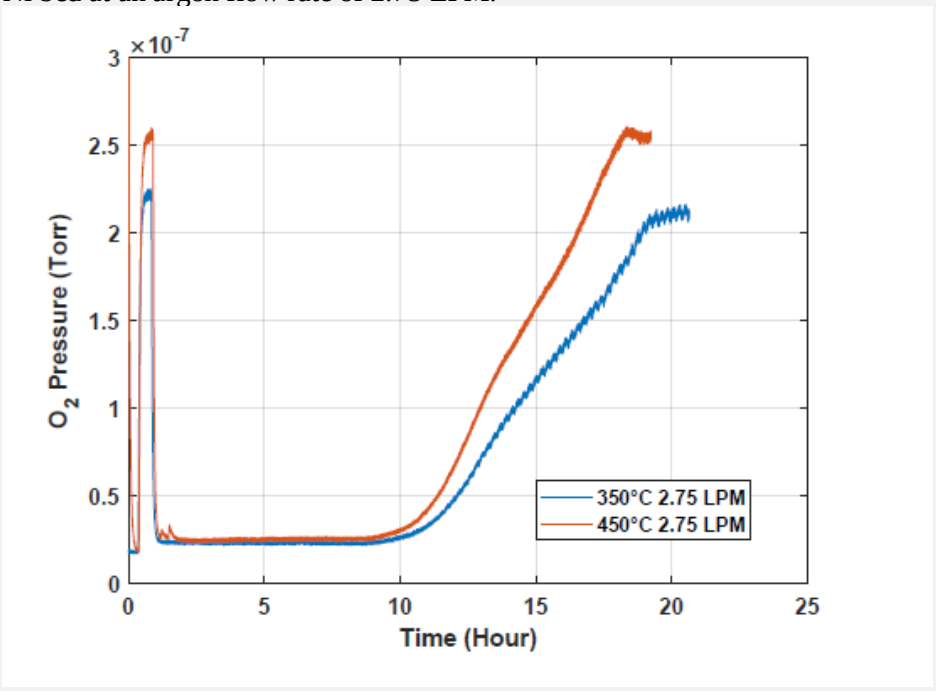

3.3 Temperature and Flow Rate Dependency of the Ni Bed's Capacity

The dependence of the nickel bed capacity on flow rate and temperature is shown in Fig. 9. The data show a trend of decreasing oxygen capacity with increasing flow rate. This is expected because, from Fig. 7, the MTZ length increases with increasing flow rate. As discussed earlier, the capacity is expected to decrease with increasing MTZ length. The data point at 0.5 LPM is an outlier within the trend with a lower oxygen capacity suggesting that the reduction prior to the experiment was incomplete, resulting in a partially oxidized bed at the start of the oxidation. The decreased capacity of the Ni bed at 450°C in

comparison to 350°C differs from the observations for the CuZn bed,[3] for which the oxygen capacity was found to increase with temperature. Further data collected from the Ni bed at 450°C may clarify the source of this difference.

Figure 9: Oxygen capacity of the Ni bed at 350°C and 450°C as a function of Argon flow rate.

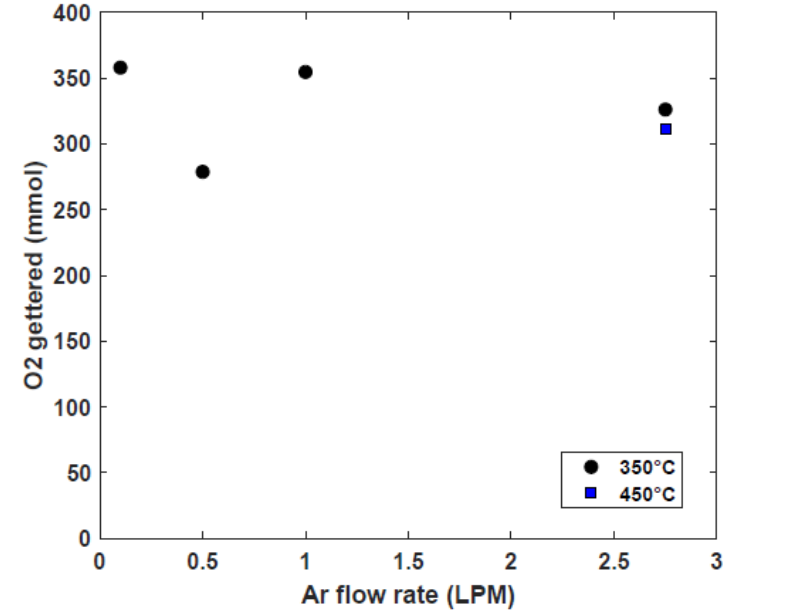

4. Conclusion

The purpose of this work was to compare the efficiency of the Ni and CuZn getter beds in removing oxygen from inert gas streams. The MTZ length of the Ni at 350°C and CuZn at 150°C were compared for various areal velocities. It was observed that the MTZ of the Ni bed is shorter within the areal velocity range of 0.78 to 2.71 cm/s, suggesting that the Ni bed has greater oxygen gettering efficiency within this range. Additionally, the MTZ length of the Ni bed was found to decrease as temperature increases from 350°C to 450°C. These results suggest that the Ni bed at 350°C can be implemented within tritium glovebox systems for increased oxygen adsorption performance in comparison to the CuZn bed at 150°C.

5. Acknowledgements

I would like to thank my advisors, Cody Fagan and Dr. Shmayda, for all the time and effort they invested to make this project possible, and Maia Raynor for her invaluable mentorship and advice throughout this summer. They contributed enormously to the growth of my knowledge in scientific research. In addition, I would like to thank Dr. Craxton for offering me the opportunity to participate in this incredible program and Jean Steve for her administrative organization.

References

1. Hanchett, MaryKate. (2012). *Oxygen Uptake Using a Nickel Catalyst.* LLE Summer High School Program Project Report
2. Gabelman, Alan. (2017). *Absorption Basics: Part 1*. Gabelman Process Solutions, LLC
3. Raynor, Maia. (2018). *Oxidation of Copper-Zinc Alloy,* LLE Summer High School Research Program Project Report
4. O'Hanlon, John F. (1980). *A User's Guide to Vacuum Technology.*

Modeling for Direct Drive Fusion Implosions: Cryogenic Target Filling at Arbitrary Viewing Angles and Yield Prediction

Simon Narang

Sutherland High School

Pittsford, New York

November 2019

Advisors: M. D. Wittman, D. Bredesen

Laboratory for Laser Energetics

University of Rochester

Rochester, New York

Abstract

Cryogenic targets for nuclear fusion are cooled to produce solid deuterium-tritium (DT) layers on their interiors. A new system, the fill tube, is being developed to improve cryogenic target quality and thus plasma compression. Due to physical constraints on the OMEGA target chamber, the fill tube can only be fielded on the laser at an angle not perpendicular to gravity. In this work, a new model, *SPARROW*, was developed to predict the final layer thickness of uncooled DT-liquid-filled targets viewed from arbitrary angles. In previous work, x-ray micrographs of liquid-filled targets were studied to obtain equations relating the size of the bubble above the liquid meniscus to the target's volume of fuel; this volume correlates with final DT layer thickness. With these equations, this work's newly developed model can automate cryogenic filling to a desired thickness within $\pm$2-μm accuracy. This will enable the final thickness to be determined prior to solidification. Further, a machine learning model was created to quantify the increase in neutron yield that can be attained if cryogenic target quality is improved. Nineteen models were trained on OMEGA data. The models were then compared for accuracy. Testing of the most accurate model revealed that target quality has a 17% impact on yield.

1 Introduction

Nuclear inertial confinement fusion (ICF) occurs between hydrogen atoms when the strong nuclear forces concentrated in nuclei overcome the repulsive electrostatic forces of protons. When enough atoms fuse, energetic neutrons are released that can be used for energy production. At the Laboratory for Laser Energetics (LLE), fusion is achieved with the sixty beam, 30 kJ OMEGA laser. LLE conducts ICF experiments with the OMEGA laser by concentrating energy on a target of $\sim$860 μm diameter to uniformly compress the fuel inside. Targets are filled with a composite fuel of deuterium and tritium (DT) due to the high nuclear cross-section of the fuel.[1]

Two indicators of progress toward ignition are the neutron yield (Y), the number of neutrons emitted by the fused DT in a target, and the areal density (ρR), a figure of merit as to how much fuel has been compressed. Target and layer imperfections are known to decrease Y and ρR.

Condensable hydrocarbons are created by the radioactive and high pressure environment in which targets are currently permeated with DT fuel. The tritium that dissolves through the target wall during permeation results in β-electron damage, breaking bonds in the polymer target and releasing short-chain hydrocarbons. These condense on the target when it is cooled to liquid and solid hydrogen temperatures. These target imperfections impact Y and ρR.[2] A new "fill-tube" system seeks to increase Y and ρR by reducing these imperfections such that targets are uniform enough to be pressurized to 100 Gbar. The fill-tube system also decreases particulate contamination. Targets are currently transferred to multiple locations before implosion. The fill tube will fill targets directly on OMEGA, eliminating points of contamination. Liquid DT enters the target through the fill tube and forms a liquid meniscus that is imaged by an x-ray camera. When the target is frozen, the DT forms into a uniform solid layer. This works seeks to predict the thickness of that solid layer based on x-ray images of the meniscus taken at any angle. A model was built for this purpose and tested on targets imaged in the horizontal view. These tests show the model's predictions to be within the 2 μm accuracy specification of LLE's experimental program.

This work also seeks to quantify the improvement to Y that these target and layer quality

improvements will provide using a machine learning model. Nineteen machine learning models were compared for accuracy against each other as well as two "control" models. The most accurate model showed an accuracy improvement of 17% over previous models.

The outline of this report is as follows. Section 2 describes the importance of cryogenic targets to nuclear fusion, how they are formed, how they are characterized, and the purpose of the new cryogenic fill-tube system. Section 3 describes how this work's first code, *SPARROW*, was developed and tested to enable the formation of cryogenic targets on the fill tube. Section 4 describes how this work's machine learning model was developed and tested to quantify the significance of the fill-tube to nuclear fusion.

2 Cryogenic Target Formation

2.1 Layering

Cryogenic targets contain frozen DT. As compared to targets filled with gaseous DT, cryogenic targets enable a higher density of fuel to be contained in the target[3] which increases Y and ρR. The current method for fielding cryogenic targets on OMEGA involves filling targets over 18 hours; during this period, DT is gradually compressed to high pressure (up to 1000 atm). A pressure gradient across the shell wall causes DT to diffuse through the target's polymer shell and fill the interior.

After permeation, the temperature is lowered to ∼20 K. This reduces the permeability of the target walls; hence, the gaseous fuel cannot escape. Next, the target is transferred to a "layering sphere" where its temperature is decreased ("ramped down") further over several hours until the fuel solidifies into a spherical layer, starting as a single crystal and becoming uniform in a process known as β-layering.[4] In β-layering, radioactive tritium in the DT emits high-energy β particles that locally heat the region where they are produced. Thus, thicker regions heat more than thinner regions. The result is a uniform solid layer on the interior of the target.[5] This layer is quantified by how radially thick it is. At present, it is yet to be determined what layer thickness is ideal for plasma compression.

2.2 Characterization

While targets are layered, a charged-coupled device (CCD) camera takes optical shadowgraphy images. The CCD camera captures images formed by light rays reflected by the inner surface of the solid DT layer. These images show a narrow bright ring that is currently used on OMEGA to measure target layer thickness and uniformity.[6]

The CCD also measures various target parameters (e.g., the initial location of the DT crystal). The initial location of the crystal is described by the observed horizontal and vertical offset of the crystal from the target center. This measurement is used in the machine learning model in Section 4.

X-ray cameras are not currently in use for target characterization on the OMEGA laser. However, they will be used on the new fill-tube system. X-ray images were used to develop this work's filling model. Images are formed by x rays that are emitted from a 60-kVp, 4-μm spot size point source and pass through the target and into the camera, as shown in Figure 2.1. X rays 1 and 2 are deflected because they are nearly tangential to interfaces. Due to this deflection, these x rays are not detected by the camera where they would be if they traveled in a straight line from the point source. Dark regions are thus formed. These dark regions form shapes (circles and ellipses).

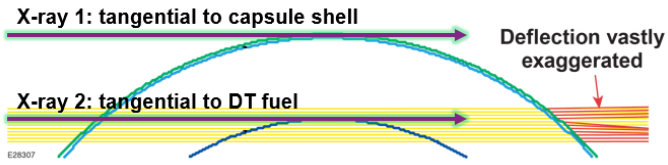

Figure 2.1: Rays tangential to (1) the target and (2) the inner surface of the solid DT. Although they are shown nearly parallel, they both originate from the same x-ray point source. After propagating through the target, they hit the camera. Rays are refracted close to the interfaces. As a result, the camera sees two dark circles (in the case of a uniform solid layer).

The dark areas in the images of Figure 2.2 indicate interfaces between different media. The "bubble" in liquid fuel shows a dark circle (the target shell), and the contained region of gas (the interface between gas and liquid DT). A good approximation of this meniscus bubble can be represented as an ellipse. The final fuel layer shows the same target shell and a concentric circle (the interface between gas and solid DT).

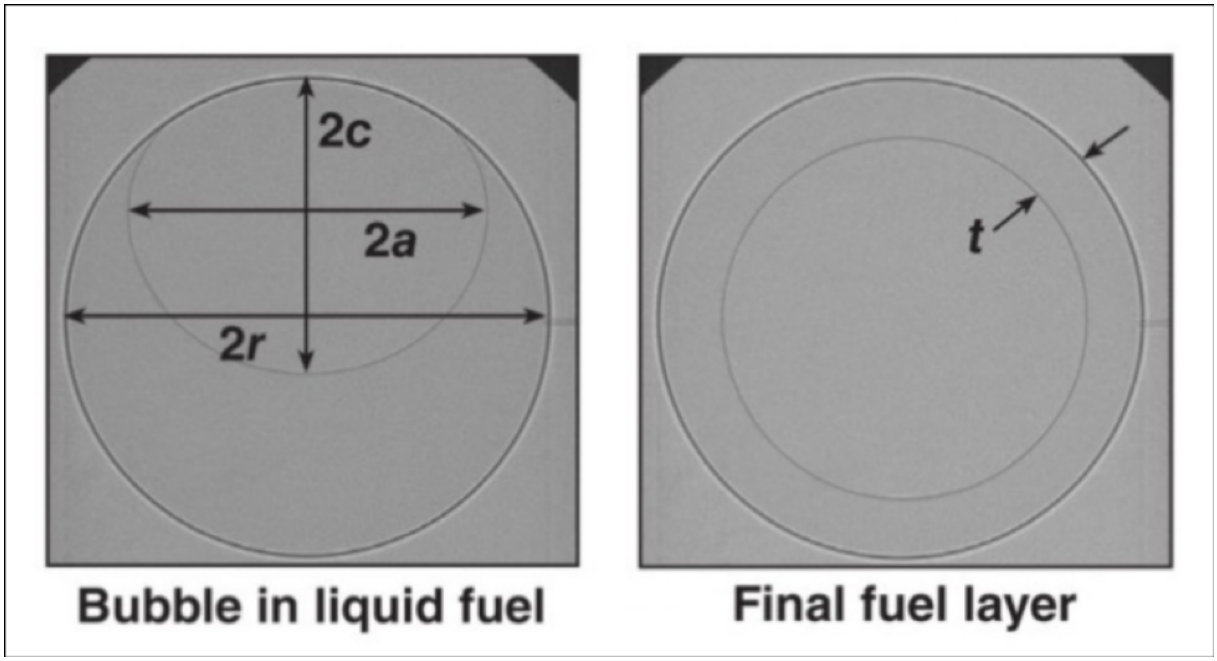

Figure 2.2: X-ray images of a liquid-filled target before and after freezing.[7]

2.3 New Cryogenic Fill-Tube System for OMEGA

The cryogenic fill-tube system is shown schematically in Figure 2.3. The target is filled with liquid DT from the tritium glovebox through the fill tube. The fill-tube heater is used to control the temperature at the interface between the layering sphere and the fill tube. When the interface drops below the freezing point, a solid freeze-plug forms. This stops liquid DT from moving into or out of the target. The target then begins to freeze. The target is viewed with an x-ray camera and an optical shadowgraphy camera.

The new fill-tube filling process was previously automated using a proportional-integral-derivative (PID) control loop that leverages the x-ray camera to adjust the temperature according to the difference between the amount of fuel currently contained in the target and the amount of fuel desired, such that the desired amount enters.[7]

The cryogenic fill-tube fixture to be fielded on OMEGA is shown in Figure 2.4a, and a mounted prototype is shown in Figure 2.4b, viewed perpendicular to gravity. A viewing angle perpendicular to gravity is not geometrically possible. Laser entrances, indicated by blue cylinders, block the x-ray camera from lying horizontally. Thus, $\theta = 23.97°$ below

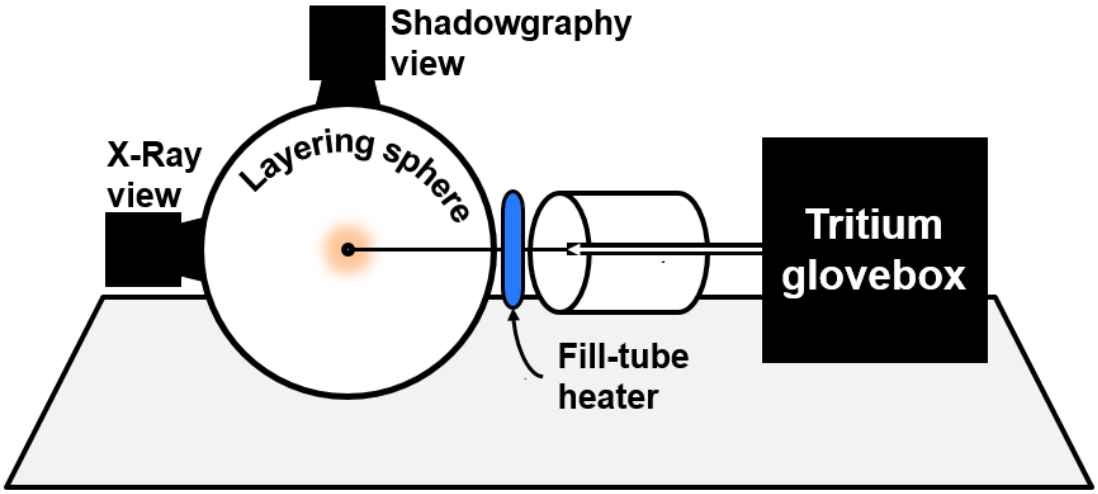

Figure 2.3: Cryogenic fill-tube schematic. The target is filled with DT through a 10-μm-diameter tube; DT is formed in the tritium glovebox shown on the right.

horizontal (position 3) was selected as the optimal choice of the options available because it is closest to horizontal. However, there is currently no experimental setup to image targets at angles other than the horizontal. Ergo, it remains unknown if a greater viewing angle impacts the accuracy of a fill level.

When the vertical angle θ is different from 0, the image of the elliptical meniscus changes location and eccentricity. The reason for this is that x rays passing through the liquid project different cross-sections of the meniscus bubble on the camera depending on the angle. This is addressed in the following section.

3 Layer Thickness Control Model

3.1 Ray-Tracing Simulation

The target-filling automation software must function with x-ray images taken at any angle to the horizontal because in the future the cryogenic fill-tube mechanism may be mounted at angles other than 23.97°. This work addresses this task by modifying a *Matlab* code to simulate the images of targets at all angles. This simulation was run at an array of distinct thicknesses and viewing angles in order to create a model for the predetermination of layer

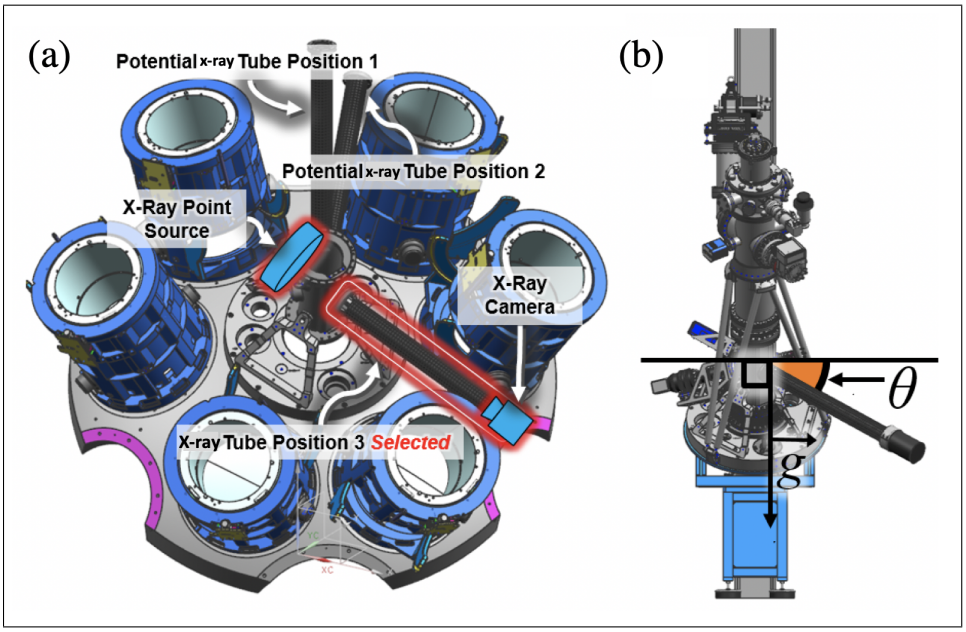

Figure 2.4: Cryogenic fill-tube fixture to be fielded on port H5 of OMEGA. The x-ray camera is located at the end of a black carbon fiber tube. The three black tubes in (a) represent potential x-ray tube mounting positions. The selected tube position will angle down at $\theta = 23.97°$.

thickness as a function of viewing angle and the size of the gaseous bubble in an unfrozen target.

In previous work, final thickness data from deuterium-filled targets had been used to establish the relationship between three measurements of the meniscus bubble and the final layer thickness. Note that these relationships *only* apply to OMEGA targets ($r = 430$ μm in Figure 2.2). The vertical offset Δy between the centers of the meniscus ellipse and target circle as a function of thickness T is

$$\boldsymbol{\Delta y(T) = 1.17T + 21.72} \tag{1}$$

where Δy and T are in μm. The semi-major axis of the ellipse a as a function of T is

$$\boldsymbol{a(T) = -1.27T + 437.14} \tag{2}$$

where a is in μm. The semi-minor axis of the ellipse c as a function of T is

$$\boldsymbol{c(T) = -1.27T + 432.79} \tag{3}$$

where c is in μm. Note that these equations were developed using only OMEGA targets

over the range $19.6 \leq t \leq 115.8$ μm. This work used Equations (1), (2) and (3) to develop a thickness predetermination ray-tracing code, *SPARROW*. For a given thickness T, *SPARROW* forms an elliptical meniscus given by Equations (1), (2) and (3).

To predetermine thickness, *SPARROW* simulates the x-ray images of targets taken at arbitrary angles for a number of thicknesses T. It simulates the target sphere and x-ray point source as objects in 3D space (see Figure 3.1). Then, the "orthogonal plane" is drawn. This goes through the target center and is orthogonal to the line of sight between the x-ray camera and point source. When *SPARROW* is run, the intersection circle between the target and this orthogonal plane is calculated. Iterating around this circle, the code calculates the locus of points where x rays are tangential to the outer target shell (depicted in Figure 2.1).

The points are calculated by minimizing the dot product between the x rays from the source and lines drawn normal to the target surface using the *fmincon* function in Matlab. While the tangent points to the outer circle can be calculated from Figure 3.1 using elementary trigonometry, *fmincon* was used to test the algorithm. The dot-product-minimization routine is subsequently re-executed on the ellipsoidal region of space above the liquid fuel, defined by Equations (1), (2) and (3). The simulation does not factor in the small deflection experienced by the rays passing through the target. However, it meets the accuracy specification of LLE's experimental program regardless.

fmincon is required because the meniscus bubble is vertically offset from the center of the target (about which the x-ray camera is angled). It is also not spherically symmetric. Therefore, each x ray needs to be traced to calculate a locus of points to form the simulated image. *fmincon* locates the point of tangency between each ray and the bubble.

For certain random x rays, *fmincon* fails to calculate their point of tangency to the target. It thus outputs a point of tangency very far away from the target. *SPARROW* removes these by discarding tangency points whose perpendicular distance to the orthogonal plane is greater than 50 μm. After outlier point removal, the two loci represent the x-ray image of a target for a specified thickness, viewing angle and target diameter.

Cryogenic targets on OMEGA have been shot with solid layer thicknesses between 40 and 60 μm. The simulation was run at distinct thicknesses of 5, 20, 40, 60, 80 and 100 μm.

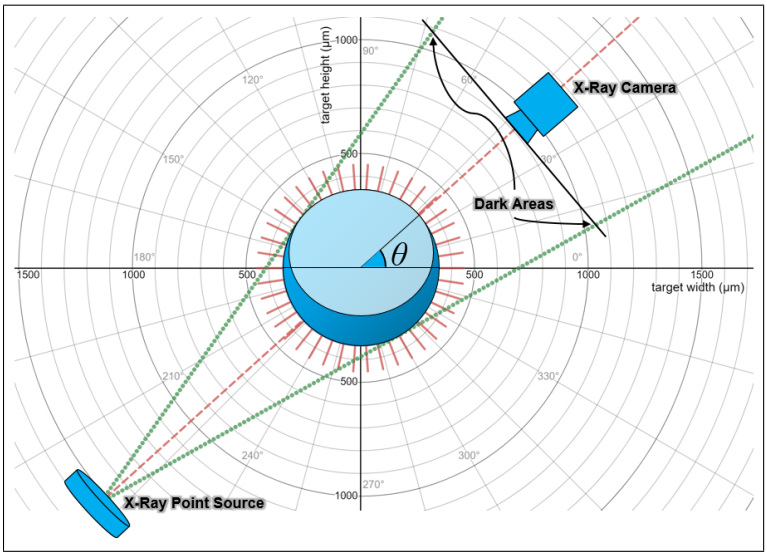

Figure 3.1: Cryogenic x-ray target characterization simulated by *SPARROW*. The dark blue meniscus in the target represents liquid DT fuel that has entered from the fill tube. The light blue region above indicates the bubble. The x-ray camera is represented as viewing from $\theta = 42°$. The red lines (each 8.66° apart) show the angles that the simulation was run at for each of the distinct thicknesses.

However, the 5 μm run was outside the range of thicknesses over which Equations (1), (2) and (3) were developed. For each thickness, the simulation was run with the point source placed every 8.66° (see Figure 3.1) with θ going from $-90°$ to 90°, with 0° being perpendicular to gravity and level with the target center.

3.2 Analysis of Simulated Data

The data collected from running *SPARROW* simulations are shown in Figure 3.2. c' is the semi-minor axis of the elliptical meniscus bubble; $r = 430$ μm is the radius of the target. Thus, $\frac{c'}{r}$ represents the normalized semi-minor axis. $\frac{c'}{r}$ was calculated for an array of viewing angles and thicknesses. Figures 3.2a and 3.2b show different regressions of the same data. The vertical black line in both plots signifies the viewing angle, -23.97°, from which the x-ray camera will view the target on OMEGA.

The linear fit in Figure 3.2a provides a complete solution to the problem of how to predetermine the final layer thickness of an OMEGA fill tube target where θ will be $-23.97°$. Based on the $\frac{c'}{r}$ obtained from fitting an ellipse to a target x-ray image, the vertical black line will be interpolated along to calculate the final thickness.

The collected data revealed a sinusoidal relationship between viewing angle and the normalized semi-minor axis. Results also showed that the amplitude of the sinusoidal rela-

tionship correlates directly with thickness. The data was fitted to the form

$$\frac{c'}{r}(T,\theta) = \big[P(T)\big]cos(A\theta) - BT + D \tag{4}$$

where T represents the final thickness of the frozen ice layer; θ represents the viewing angle; and A, B, and D represent constants to be fit. $P(T)$ represents a polynomial of thickness.

The Cryogenic Fill-tube Test Facility (CFTF) was previously built at LLE to test the possibility of using a fill tube. The CFTF includes x-ray and shadowgraphy cameras for characterization. Unlike the prototype shown in Figure 2.4, the x-ray camera on the CFTF views the target from the horizontal. Previous experiments conducted on the CFTF verified the linear relationship between semi-minor axis and thickness for $\theta = 0$ only. However, it is unknown what kind of association exists between $P(T)$ and thickness at other angles. To investigate this, the data was fit using both linear and quadratic polynomials to see if one fit better than the other.

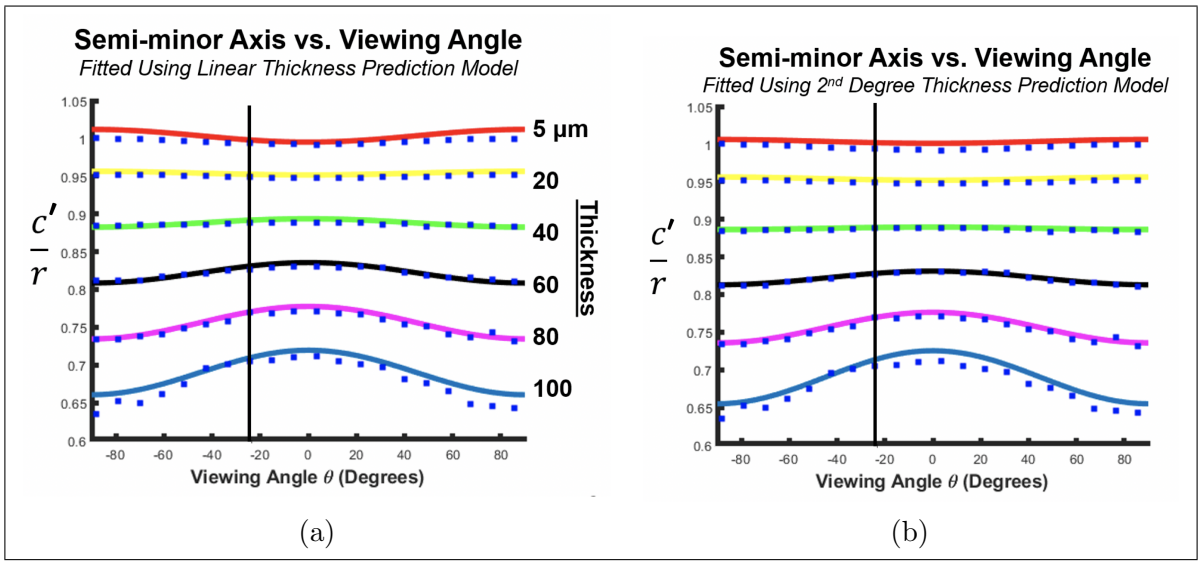

Figure 3.2: Simulated $\frac{c'}{r}$ as a function of θ for each of six distinct ice thicknesses. $\theta = 0$ represents viewing the target directly from horizontal. The simulated data were fit using both (a) first- and (b) second-degree polynomials.

Regression was used to fit Equation (4) using first- and then second-degree polynomials to determine which (linear or quadratic) fit better. The results depicted in Figure 3.2

produced the fits

$$\frac{\boldsymbol{c'}}{\boldsymbol{r}}(\boldsymbol{T},\boldsymbol{\theta}) = \big[(\mathbf{3.99}\text{e-}\mathbf{4})\boldsymbol{T} - \mathbf{1.04}\text{e-}\mathbf{2})\big]\boldsymbol{cos}(\mathbf{2}\boldsymbol{\theta}) - \mathbf{0.0033}\boldsymbol{T} + \mathbf{1.02} \tag{5}$$

$$\frac{\boldsymbol{c'}}{\boldsymbol{r}}(\boldsymbol{T},\boldsymbol{\theta}) = \big[(\mathbf{4.66}\text{e-}\mathbf{6})\boldsymbol{T}^{\mathbf{2}} - (\mathbf{9.09}\text{e-}\mathbf{5})\boldsymbol{T} - (\mathbf{2.21}\text{e-}\mathbf{3})\big]\boldsymbol{cos}(\mathbf{2}\boldsymbol{\theta}) - \mathbf{0.0033}\boldsymbol{T} + \mathbf{1.02} \tag{6}$$

where T is measured in μm. Both equations fit with a coefficient of determination of 0.997. Figure 3.2 shows that below a certain thickness threshold, the semi-minor axis of the bubble viewed switches from appearing largest when viewed horizontally to appearing largest when viewed from 90° to horizontal. Note how the sinusoidal relationship between viewing angle and normalized semi-minor axis inverts between $T = 20$ μm and $T = 40$ μm.

To calculate the threshold, Equations (5) and (6) were solved for T such that the expression $P(T) = 0$. $P(T)$ is the bracketed expression that $cos(2\theta)$ is scaled by. From Equation (5), the threshold is $T = 25.92$ μm in the linear model. However, it is $T = 33.62$ μm in the quadratic model in Equation (6). To determine where the actual inversion was, the simulation was rerun at closer thicknesses of 25.92, 29.77, and 33.62 μm. The results from this were then fit both linearly and quadratically with Equation (4). The linear fit produced an inflection point at 30.346 μm; the quadratic fit produced 30.75 μm. The mean of these two was 30.55 μm. Therefore, 30.55 μm was assumed to be the inflection point.

To gain some insight into the threshold behavior, the simulation was run at $\theta = 90°$ and $\theta = 0$ for thicknesses below, at, and above the threshold, shown in Figure 3.3. In the simulated x-ray images, the midpoint of the bubble does not fall on the midpoint of the target. However, the bubble transitions from having a horizontal major axis when viewed at $\theta = 0$ in (a) to having it vertically in (c). So, the bubble transitions from being wider than it is tall to taller than it is wide.

3.3 Model Testing

The linear and quadratic models each performed more accurately for different viewing angles and thicknesses. Below the threshold of $T = 30.55$ μm, the linear model made more accurate predictions within 45° of perpendicular to gravity. For angles greater than 45°, the quadratic

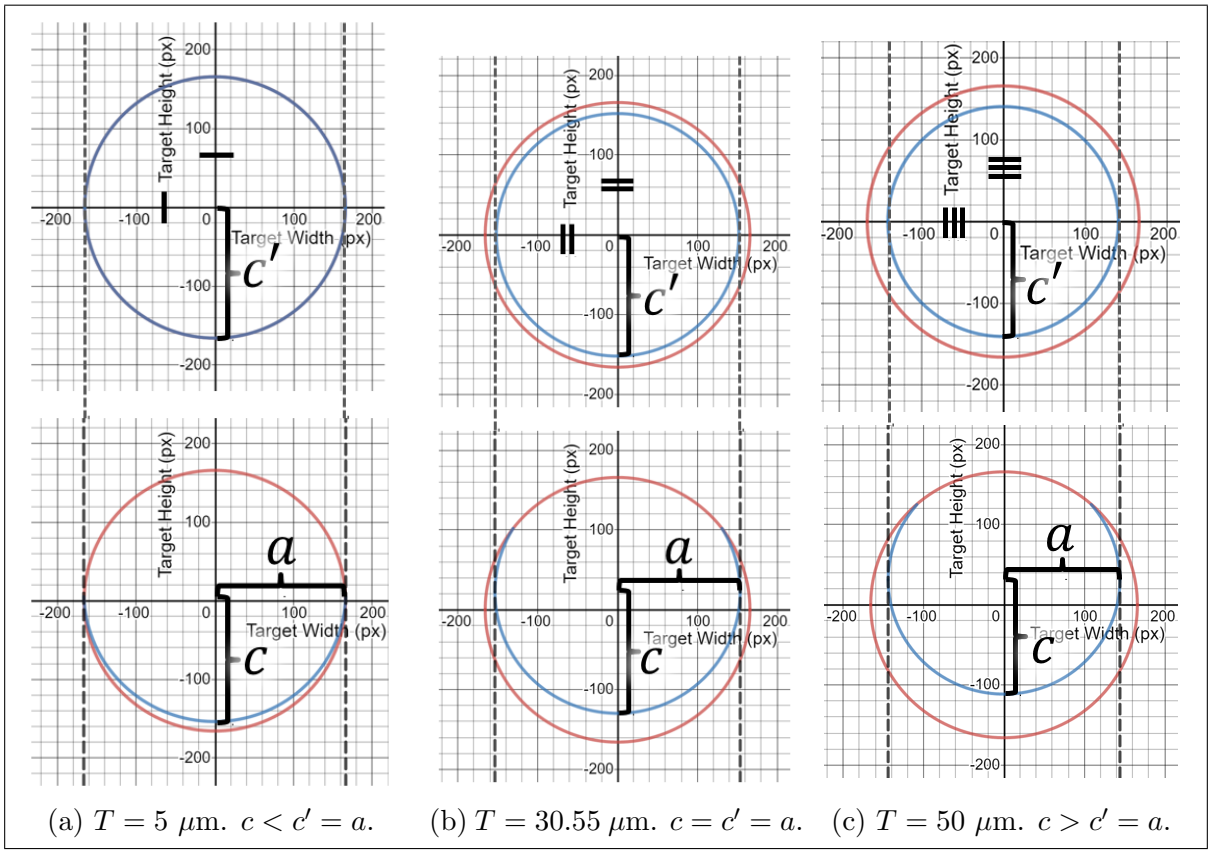

(a) $T = 5$ μm. $c < c' = a$. (b) $T = 30.55$ μm. $c = c' = a$. (c) $T = 50$ μm. $c > c' = a$.

Figure 3.3: Simulated uncooled targets of final ice layer thicknesses (a) less than the modeled relationship inversion threshold, (b) at the threshold and (c) greater than the threshold. Targets are viewed from 90°above horizontal (top) and at horizontal (bottom). Below the threshold, the meniscus bubble (blue) is larger when viewed 90°above horizontal. Above the threshold, the meniscus bubble is larger when viewed directly at horizontal.

model made more accurate predictions. Above the threshold, the opposite was observed.

The thickness predetermination model was tested against 19 CFTF fills of cryogenic DT targets with $\theta = 0$. Experiments in which ice layers exhibited more than 10% of surface area being at least 16 μm outside the mean radius of the ice layer were considered poor quality targets. The testing dataset size was reduced to 14 after poor quality targets were excluded. For these 14, thickness predictions were compared against x-ray measurements for accuracy because shadowgraphy measurements exhibited more variability. X-ray images are also known to provide more accurate thickness measurements. The predicted thickness was on average within 2 μm of the measured average layer thickness, as shown in Figure 3.4. This satisfies the 2-μm accuracy requirement of LLE's experimental program.

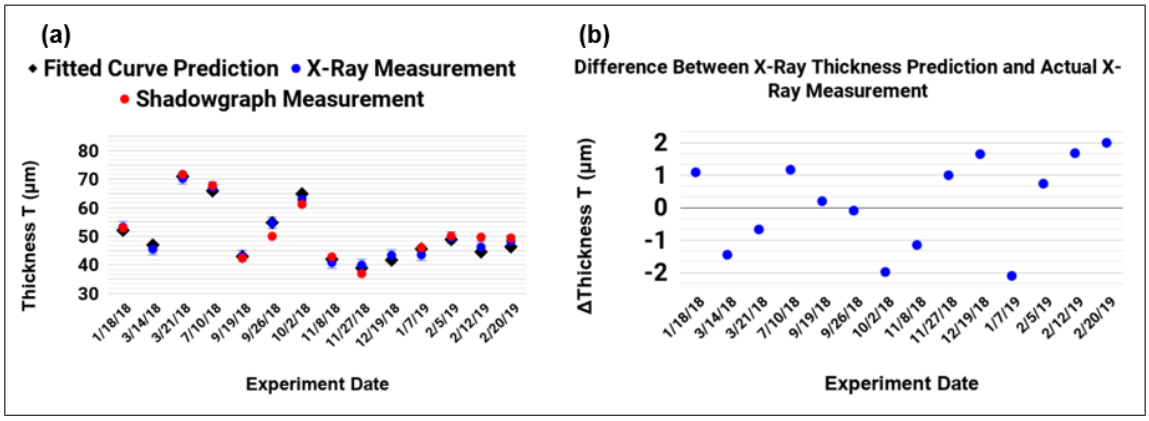

Figure 3.4: (a) Thickness prediction vs. measurements; (b) difference between prediction and x-ray measurement. The difference represents the distance between the black diamond and the blue circle for a given target.

Having satisfied the experimental program accuracy requirement, the developed thickness prediction formulas in Equations (5) and (6) will be implemented into the automated control loop of Ref. 7. Thus, cryogenic target filling can now be automated for OMEGA fill tube targets when viewed from 23.97°. It can also be automated for any other arbitrary angle.

4 Machine Learning Model

The second goal of this work was (1) to quantify the improvement that a new cryogenic filling mechanism can deliver to the neutron yield of a cryogenic DT implosion and (2) to use this measure to improve yield predictions.

4.1 Feature Selection

In order to quantify the yield increase that a new cryogenic filling mechanism can deliver, a group of features relating to cryogenic targets was selected from a dataset of implosion experiments conducted on the OMEGA laser within the past two years. Older shots were omitted to avoid externalities (e.g., new modules that would skew the data). These data were augmented with features that had been used to develop a previous model.[8]

The features collected from the dataset are listed in Table 1. The previously used features (those that are unrelated to target quality) are the last six entries. I_{RMS} represents the root mean square (RMS) nonuniformity of the ice layer of frozen targets. This estimate is calculated from the nonuniformity of the optical shadowgraphy bright ring. The same process is applied to the target shell ring to calculate S_{RMS}.

A_S, A_M, C_E, A_D, and C_D are measurements of the quality of the exterior polymer target that holds DT inside a target. Increases in all these values negatively impact implosion yield. Large C_E and C_D decrease implosion yield more than large A values because they indicate that target imperfections are skewed toward either the top or bottom. For LLE experiments, this skew is generally toward the top of the target. Elliptical and dendrite defects are two types of target imperfections that result from the current diffusion-filling process. Dendrite defects have a more negative impact on yield than elliptical defects.

Exploratory Data Analysis (EDA) of these features revealed that the initial horizontal offset of the crystal seed held no relationship with neutron yield nor implosion velocity. EDA also revealed (1) a negative correlation between between Y and T and (2) an unexpected positive correlation between Y and I_{RMS}. However, high-RMS ice layers are known to reduce implosion velocity and neutron yield.[9] The data's positive correlation between B-band RMS and yield contradicts a physical property. Thus, this trend was assumed to reduce the accuracy of a model's predictions. This was investigated by plotting the density of I_{RMS} for relatively low as well as relatively high thicknesses T because layer thickness has been shown to significantly influence Y (see Figure 4.1). The density plot in Figure 4.1 shows that as T increases, I_{RMS} decreases. This is why Y exhibits a positive correlation with I_{RMS} when

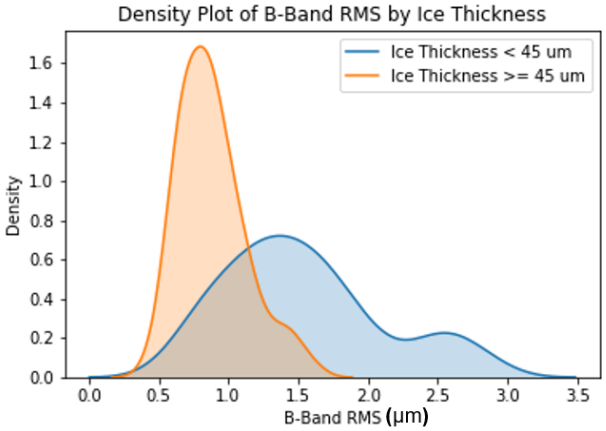

Figure 4.1: Density Plot of B-band RMS by Layer Thickness. At higher thicknesses, I_{RMS} is approximately normal and centered at $\sim$ 0.75 μm. At lower thicknesses, I_{RMS} is bimodal and generally greater, with centers at $\sim$ 1.3 μm and $\sim$ 2.6 μm.

Inputs	
Symbol	Name
I_{RMS}	Estimated thickness nonuniformity of solid DT layer (μm)
T	Final ice layer thickness (μm)
τ	Age of DT fuel (s)
d_X	Initial crystal seed horizontal offset (μm)
d_Y	Initial crystal seed vertical offset (μm)
S_{RMS}	RMS of target shell (μm)
A_S	Area of small-sized elliptical defects on target (μm^2)
A_M	Area of medium-sized elliptical defects on target (μm^2)
C_E	Centroid of elliptical defects on target (μm)
A_D	Area of dendrite defects on target (μm^2)
C_D	Centroid of dendrite defects on target (μm)
δ_{SSD}	Application of SSD (binary)
R_T	Range of ion temperature measurements (K)
V_{sim}	Simulated implosion velocity (m/s)
M_{sim}	Simulated target mass at stagnation (μg)
ρR_{sim}	Simulated areal density (kg/μm^2)
R_0	Outer radius of target (μm)

Output	
Symbol	Name
$\hat{Y}_{exp}$	Predicted neutron yield

Table 1: Symbols and descriptions of the initial feature space and output of the model developed to predict neutron yield.

considered independent of T. T impacts yield more than I_{RMS}. So, for low-I_{RMS} targets (large T), yield was lower than high-I_{RMS} targets not because of I_{RMS} itself, but because of T. To account for this in training the model, a second-order feature

$$Q_I = (I_{RMS})(T) \tag{7}$$

was added to the dataset to describe the quality of the solid layer more generally. Q_I accounts for both layer uniformity and thickness. This eliminated the incorrect trend that

was occurring between I_{RMS} and Y. Q_I correlates negatively with Y. Ultimately, the dimensionality of the model dataset was reduced by omitting the horizontal offset of the initial crystal seed, the bright ring RMS, and the layer thickness from training data; the latter two were replaced with layer quality Q_I.

4.2 Model Development

After dimensionality reduction, an investigation into the possibility of using a neural network to analyze the data was conducted on the entirety of the experimental dataset of cryogenic target shots at LLE within the past two years. This dataset contains 400 distinct features but only 215 data points. Each feature is either a simulated or observed measurement (e.g., those in Table 1). Each data point is a set of feature values corresponding to an imploded target (a "shot"). Having more features than data points suggested a neural network would have a low probability of successfully predicting neutron yields in this context. One of the more commonly used configurations for training neural networks was used. This was a 12-layer neural network with rectified linear unit (ReLU) activation. This was also configured with Sigmoid activation functions on deeper neurons. This performed with an accuracy of 0.12%, verifying that neural networks are currently not applicable for yield prediction in the context of cryogenic shots.

Subsequently, various predictive models were trained on the cryogenic target shot data using five-fold cross-validation, wherein 5 distinct 20% portions of the dataset were used as holdout testing data to be used for model evaluation after the model was trained on the other 80%. The metrics calculated from evaluating the different models on these 5 groups were the mean absolute error (MAE) and root mean square error (RMSE). For each model, these two metrics were averaged across the 5 runs and subsequently used for evaluation. Figure 4.2 shows a comparison of various models, ranked based on these metrics. The MAE and RMSE were compared against those of (a) a naive model that exclusively predicts the median yield and against (b) a developed model that does not factor in target data.[8] Both (a) and (b), the control models, are shown in black in Figure 4.2. (a) is labeled "Median"; (b) is labeled "Omitting Target Data."

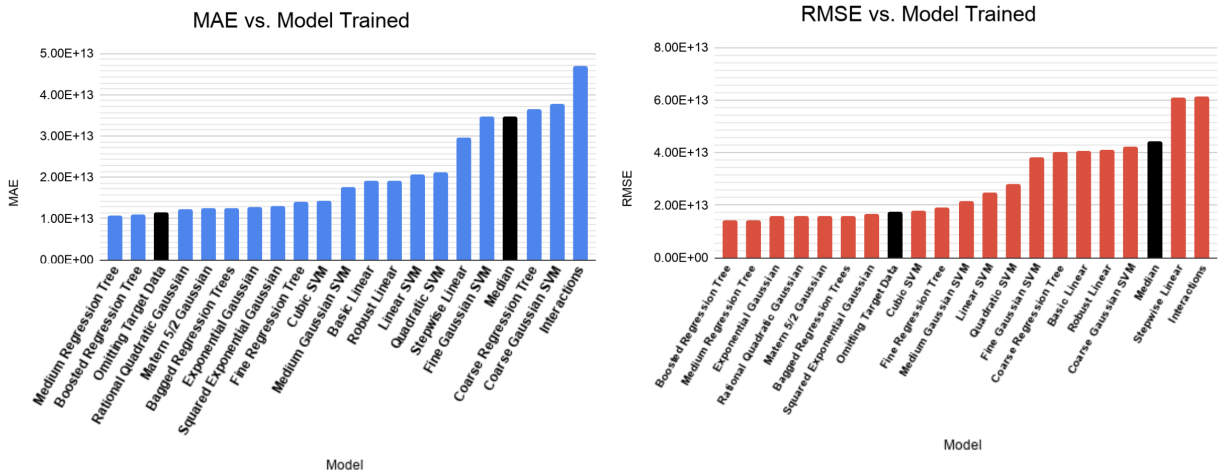

Figure 4.2: Mean absolute error (MAE) and root-mean-squared error (RMSE) compared across various yield prediction models.

4.3 Analysis of Model Output

Two models showed improvement when trained on data augmented with target parameters. The medium-grained regression tree showed the smallest MAE from experimental data. At 1.08×10^{13} neutrons, this demonstrated a 5.46% decrease from the model trained without target data (1.14×10^{13} neutrons). The ensemble of boosted trees showed the smallest RMSE. At 1.43×10^{13} neutrons, this demonstrated a 17.17% decrease from the model trained without target data ($1.73 \cdot 10^{13}$ neutrons). Having lower error values demonstrates that these two models performed better than the others.[10]

The best performing models were decision trees, which generally "overfit" data (fit noise in the data rather than physical trends).[11] Models that overfit data are observed to perform better on training data at the cost of performance on testing data; this performance can be be compared using MAE and RMSE. Overfitted models tend to mistake noise in data for physical relationships. As shown in Figure 4.3, the two best performing models had lower MAE and RMSE values on their training data. With the ensemble model, RMSE increased 142% between training and testing data; MAE increased 138%. The medium regression tree RMSE increased 21% between training and testing data; MAE increased 25%. These results indicate that the ensemble model overfit the data significantly more than the medium regression tree. This overfitting was mitigated through cross-validation but still present. By

separating the dataset into 5 groups of data, each model is iteratively trained on the first four randomly selected samples ("folds") of data. Then, the final fold is used to test the accuracy of the model. Because the model is trained on all four folds iteratively, it is less likely to overfit noise in a single fold. This thus mitigates overfitting.

Neutron yields for experiments conducted on OMEGA are generally on the order of 10^{13} or 10^{14} neutrons. Because the RMSE of the models were also on the order of 10^{13}, none of these machine learning models are suitable for real-time high-precision predictions; however, they quantifiy the impact of target quality on neutron yield.

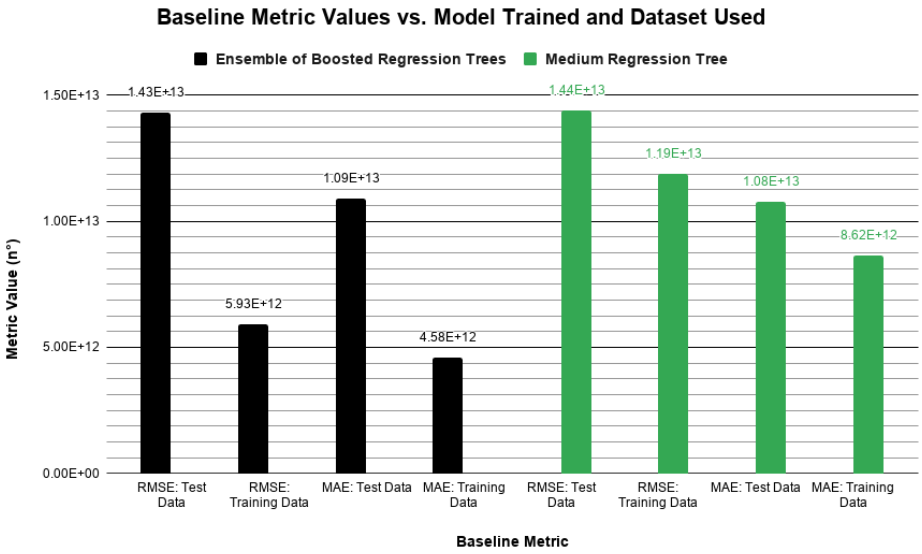

Figure 4.3: Comparison of the RMSE and MAE values of the boosted ensemble and medium regression decision tree machine learning models on testing and training datasets.

The decision tree models in Figure 4.3 were computed by the following process for each of the five folds of the cross-validation.[12] Twelve different numeric yield outcomes (evenly spaced based on the distribution of yields) were algorithmically established. An array of rules were then automatically fit to the training data (e.g., if δ_{SSD} is disabled, then Y will not exceed 1.2×10^{14} neutrons). For testing, a distinct tree would, given a data point with the input parameters in Table 1, assign a certainty (percent confidence) to each outcome. The final prediction for the data point was the weighted average of these outcomes.

Decision trees are inherently different from other models tested such as linear regression

(where the relationship between the prediction $\hat{Y}_{exp}$ is assumed to be linear with the input variables) and gaussian regression (where all input variables are assumed to be normally distributed).[13] The other models are less optimal for highly complex datasets but they generally do not overfit to the extent that decision trees do.

This verified that the neutron yield of implosions is multivariate and nonlinear. This also showed that cryogenic target quality highly correlates with neutron yield. Finally, the increased accuracy of the model resulting from training with target data shows the material importance of target quality in the goal of achieving nuclear ignition and burn.

5 Conclusion

In this work, two models were created. The first, a ray-tracing model *SPARROW*, is for use in filling cryogenic targets on the new fill-tube system on the OMEGA laser. The second leverages machine learning to predict neutron yield and quantify the significance of target quality on that yield.

SPARROW was developed to predetermine the final solid layer thickness of cryogenic targets filled using the fill-tube fixture. This was previously not possible for targets viewed from any angle. *SPARROW* was created using relationships previously learned from x-ray images of liquid fills viewed in the horizontal plane. Results from this model were fit to linear and quadratic polynomials. These give analytic expressions that allow the thickness to be determined for any viewing angle. For the angle at which the fill tube will be fielded on OMEGA, the linear model is optimal. The model will be implemented to fill cryogenic targets automatically to a desired thickness. Preexisting target fills imaged perpendicular to gravity were used as testing data. The model performed within the 2 μm accuracy specification of LLE's experimental program on these data.

The machine learning model was created to quantify the significance of target quality to fusion yield. Cryogenic shot data from OMEGA was first compiled for training. Then, nineteen types of predictive models were trained and compared for performance. The ensemble of boosted trees model was the most accurate. Testing of this model showed that target

quality data improved neutron yield predictions by 17%. This indicates that target quality improvements using the cryogenic fill-tube fixture have a material impact on experimental yields.

When the cryogenic fill-tube is fielded on OMEGA and used for implosions, data from the fill-tube fixture can be used in the yield prediction machine learning model. Data such as the range in temperature from the start to the end of the filling process, and the length of time required for filling could be included. Including these might provide insight into physical properties and further improve yield prediction accuracy.

6 Acknowledgements

I am thankful to Mr. Mark Wittman, Mr. Dean Bredesen, Dr. R. Stephen Craxton, Carwyn Collinsworth, and the 2019 high school students at LLE. Mr. Wittman and Mr. Bredesen provided mentorship. Dr. Craxton has managed the high school program since 1998, enabling over 260 students to participate in fusion research; he also provided advice for this work. Carwyn Collinsworth, a 2018 high school student, contributed to the foundation for this project. The thirteen other summer high school students of 2019 provided feedback.

References

[1] R. S. Craxton, K. S. Anderson, T. R. Boehly, V. N. Goncharov, D. R. Harding, J. P. Knauer, R. L. McCrory, P. W. McKenty, D. D. Meyerhofer, J. F. Myatt, A. J. Schmitt, J. D. Sethian, R. W. Short, S. Skupsky, W. Theobald, W. L. Kruer, K. Tanaka, R. Betti, T. J. B. Collins, J. A. Delettrez, S. X. Hu, J. A. Marozas, A. V. Maximov, D. T. Michel, P. B. Radha, S. P. Regan, T. C. Sangster, W. Seka, A. A. Solodov, J. M. Soures, C. Stoeckl, and J. D. Zuegel, "Direct-drive inertial confinement fusion: A review," *Physics of Plasmas*, vol. 22, no. 11, p. 110501, 2015.

[2] D. R. Harding, J. Ulreich, M. D. Wittman, R. Chapman, C. Taylor, R. Taylor, N. P. Redden, J. C. Lambropoulos, R. Q. Gram, M. J. Bonino, and D. W. Turner, "Requirements and Capabilities for Fielding Cryogenic DT-Containing Fill-Tube Targets for Direct-Drive Experiments on OMEGA," *Fusion Science and Technology*, vol. 73, no. 3, pp. 324–334, 2018.

[3] T. C. Sangster, R. Betti, R. S. Craxton, J. A. Delettrez, D. H. Edgell, L. M. Elasky, V. Y. Glebov, V. N. Goncharov, D. R. Harding, D. Jacobs-Perkins, R. Janezic, R. L. Keck, J. P. Knauer, S. J. Loucks, L. D. Lund, F. J. Marshall, R. L. McCrory, P. W. McKenty, D. D. Meyerhofer, P. B. Radha, S. P. Regan, W. Seka, W. T. Shmayda, S. Skupsky, V. A. Smalyuk, J. M. Soures, C. Stoeckl, B. Yaakobi, J. A. Frenje, C. K. Li, R. D. Petrasso, F. H. Séguin, J. D. Moody, J. A. Atherton, B. D. MacGowan, J. D. Kilkenny, T. P. Bernat, and D. S. Montgomery, "Cryogenic DT and D2 targets for inertial confinement fusion," *Physics of Plasmas*, vol. 14, no. 5, p. 58101, 2007.

[4] A. J. Martin, R. J. Simms, and R. B. Jacobs, "Beta energy driven uniform deuterium–tritium ice layer in reactor-size cryogenic inertial fusion targets," *Journal of Vacuum Science & Technology A: Vacuum, Surfaces, and Films*, vol. 6, pp. 1885–1888, 5 1988.

[5] D. R. Harding, D. Whitaker, and C. Fella, "Growth of a solid D-T crystal from the liquid inside inertial confinement fusion targets," in *Fusion Science and Technology*, vol. 70, pp. 173–183, American Nuclear Society, 8 2016.

[6] D. H. Edgell, R. S. Craxton, L. M. Elasky, D. R. Harding, L. S. Iwan, R. L. Keck, L. D. Lund, S. J. Verbridge, M. D. Wittman, A. Warrick, T. Brown, and W. Seka, "Three-dimensional characterization of cryogenic target ice layers using multiple shadowgraph views," in *Fusion Science and Technology*, vol. 49, p. 624, American Nuclear Society, 2006.

[7] C. R. Collinsworth, "Real Time X-Ray Analysis of Liquid-DT Fill Level in Fill-Tube Capsules to Control Solid-Layer Thickness," Project Report, Laboratory for Laser Energetics Summer High School Research Program, 2018.

[8] V. Gopalaswamy, R. Betti, J. P. Knauer, N. Luciani, D. Patel, K. M. Woo, A. Bose, I. V. Igumenshchev, E. M. Campbell, and K. S. Anderson, "Tripled yield in direct-drive laser fusion through statistical modelling," *Nature*, vol. 565, no. 7741, p. 581, 2019.

[9] R. L. McCrory, S. P. Regan, S. J. Loucks, D. D. Meyerhofer, S. Skupsky, R. Betti, T. R. Boehly, R. S. Craxton, T. J. B. Collins, J. A. Delettrez, D. Edgell, R. Epstein, K. A. Fletcher, and others, "Direct-drive inertial confinement fusion research at the Laboratory for Laser Energetics: charting the path to thermonuclear ignition," *Nuclear Fusion*, vol. 45, pp. S283–S290, 10 2005.

[10] D. H. Wolpert and W. G. Macready, "No free lunch theorems for optimization," *IEEE Transactions on Evolutionary Computation*, vol. 1, pp. 67–82, 4 1997.

[11] L. Breiman, "Statistical Modeling: The Two Cultures (with comments and a rejoinder by the author)," *Statist. Sci.*, vol. 16, no. 3, pp. 199–231, 2001.

[12] J. R. Quinlan, "Generating production rules from decision trees," (Cambridge, MA), pp. 304–307, 1987.

[13] J. Quiñonero and C. E. Rasmussen, "A Unifying View of Sparse Approximate Gaussian Process Regression," *Journal of Machine Learning Research*, vol. 6, pp. 1939–1959, 2005.

Enhancements to the Calorimetric Measurement System on the Omega Laser

Max Neiderbach

Geneseo Central School

Advisors: Michael Sharpe, Vinitha Anand, & Robert Peck

Laboratory for Laser Energetics

University of Rochester

November 2019

1. Abstract

Different analogue-to-digital converter (ADC) systems and calorimeter insulations were tested to improve calorimetric measurements for the OMEGA laser. It has been demonstrated that the current 16-bit ADC used on OMEGA has a less than optimal accuracy at low calorimetric energy readings of 0.1 J or less. The first three new systems tested were (1) a 24-bit version of the current system, (2) a system that used the Fluke 8508A reference multimeter, and (3) an ADC that was controlled by a Raspberry Pi computer (PiADC). These tests were carried out on three different calorimeters, at 1.0 and 0.1 J of energy, and in an insulated or non-insulated state. The PiADC performance was comparable to the Fluke 8508A at a much lower cost. A newer, smaller, and cheaper PiADC was then developed. This new PiADC system (without additional calorimeter insulation) was tested on a 1” calorimeter in OMEGA and was able to obtain energy measurements with an accuracy ten-times better than the current ADC system. Bench tests with additional insulation around the calorimeter demonstrated that an accuracy 32-times better than the current ADC system is possible.

2. Introduction

The calorimeters on the 60-beam OMEGA laser work by absorbing incoming energy in an absorbing glass (Fig. 2.1). This glass then heats up, and the heat transfers from the glass through several Peltier cooling modules to a heat sink. The Peltier modules consist of two junctions between dissimilar metals, where one junction receives the heat and the other is tied to a heat sink that acts as a thermal reference. When the calorimeter absorbs light and heats up, a voltage is created in the Peltier cooling modules that is proportional to the temperature difference between the heated junction and the heat sink. This voltage is then measured by an analogue-to-digital converter (ADC) over the time it takes the system to regain thermal equilibrium, the resulting graph resembling Fig. 2.2. From these graphs the time constants of the calorimeters, sensitivity of the calorimeters, and energy absorbed by the calorimeters can be calculated. Different calorimeters have different time constants and sensitivities [1] due to their different thermal masses and amplification circuitry. The time constant (in seconds) is a measure of how quickly the calorimeter

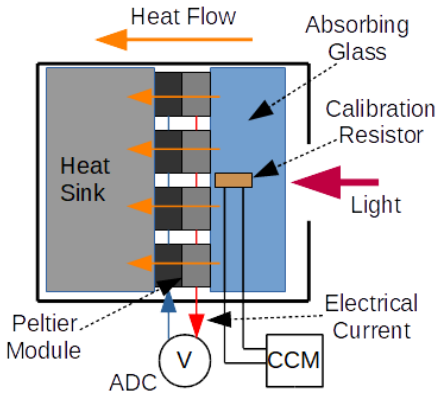

Fig. 2.1 Calorimeter Cut-away
The calorimeter absorbs light and then the heat flows through the Peltier modules to the heat sink and a measurable voltage is produced.

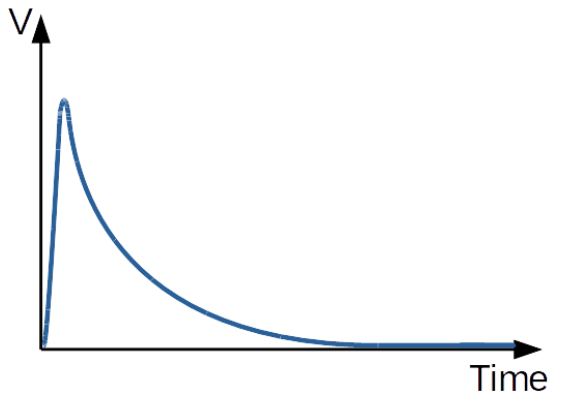

Fig. 2.2 Ideal Calorimeter Voltage Curve
Energy is applied to the calorimeter, causing the spike. The system then slowly loses heat and returns to thermal equilibrium.

dissipates the heat absorbed, while the sensitivity is how many Volt*seconds (Vs, the area under the curve in Fig. 2.2) of signal correspond to a Joule of energy. The approximate time constants and calorimeter sensitivities for the calorimeters used are listed in Table 2.1.

Table 2.1 Constants for Three Different Calorimeters

Calorimeter:	Time Constant in Seconds:	Sensitivity in Volt*Seconds/Joule (Vs/J):
1” Calorimeter without an Amplifier	12.6	0.5
1” Calorimeter with an Amplifier	10.8	10.3
2” Calorimeter with an Amplifier	25.5	9.0

The values above were found through calorimeter calibration. Calorimeters are calibrated using the Calorimeter Calibration Module (CCM). The CCM produces a voltage across the calibration resistor in the calorimeter (Fig. 2.1) for a short time to deliver heat energy to the calorimeter. The resulting voltage curve from the calorimeter is then integrated to get Vs, and then divided by the energy delivered by the CCM to get Vs/J. The time constant is found by fitting an exponential curve to the voltage curve from the calorimeter.

In order to improve the accuracy of the calorimeter’s energy measurements the noise in the voltage curve must be reduced. This noise increases uncertainty during both integration for calorimeter calibration and integration for an actual measurement. To decrease the noise different ADCs and calorimeter insulations were tested. At 0.02 J of energy, which is a typical 1” scatter calorimeter measurement at low OMEGA shot energies, the 16-bit ADC has a signal-to-noise ratio of between 10:1 and 32:1, whereas an ADC controlled by a Raspberry Pi computer (PiADC) has a signal-to-noise ratio of between 316:1 and 1000:1. The PiADC resulting from this

work was able to perform with a ten-times greater accuracy than the current ADC used on OMEGA, and has the ability to perform 32-times better if additional insulation around the calorimeter is present.

3. Experimental Setups

3.1 LON-Based ADC System

The currently used 16-bit ADC and the 24-bit version that was further tested in this work run on a Local Operating Network (LON) system (Fig. 3.1). Both the Calorimeter Calibration Module (CCM) and the Generic Analogue-Digital Module (GADM) cards are hooked into a box known as a LON "cart" or "rack" that interfaces with a PC.

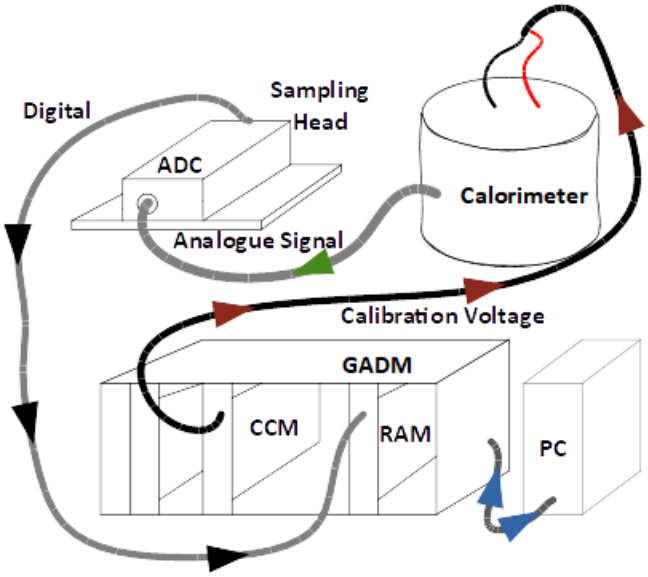

Fig. 3.1 LON-based ADC system
Both the CCM and GADM cards are hooked into a box known as a LON "cart" or "rack" which is then controlled by a PC. The CCM sends a known energy to the calorimeter, and the sampling head measures the resulting voltage. The GADM then records the digital voltage values and sends them to the PC.

The CCM operates by receiving an energy request from a PC. The CCM then sends a specific current at 24 V for a period of time through a heater in the calorimeter, which delivers the energy that was requested by the PC [2]. The sampling head converts the resulting voltage values from the calorimeter into digital values, which are then processed by the GADM [3] and sent to an Excel file on the PC. When running tests, the GADM was set to take 600 samples at a sample rate of 5 Hz. More samples could not be taken due to the GADM board's 8 kilobytes of RAM.

3.2 Fluke 8508A Based System

The Fluke 8508A is a high-precision 7.5-digit-accuracy reference multimeter. The system that was built around it (Fig. 3.2) was used to determine the limits of the calorimeters' performance so the effects of an ADC on the signal could be distinguished. However, its large size and prohibitively high price disqualified it from further consideration as an implementable system. In this system the CCM is still controlled by the PC and delivers a specified energy to the calorimeter, but the GADM and the sampling head are only used to supply the calorimeter with ±15 V and ground. The Fluke 8508A is controlled by a LabVIEW program on the PC that sets the sample rate to 5 Hz and collects the signal data from the calorimeter.

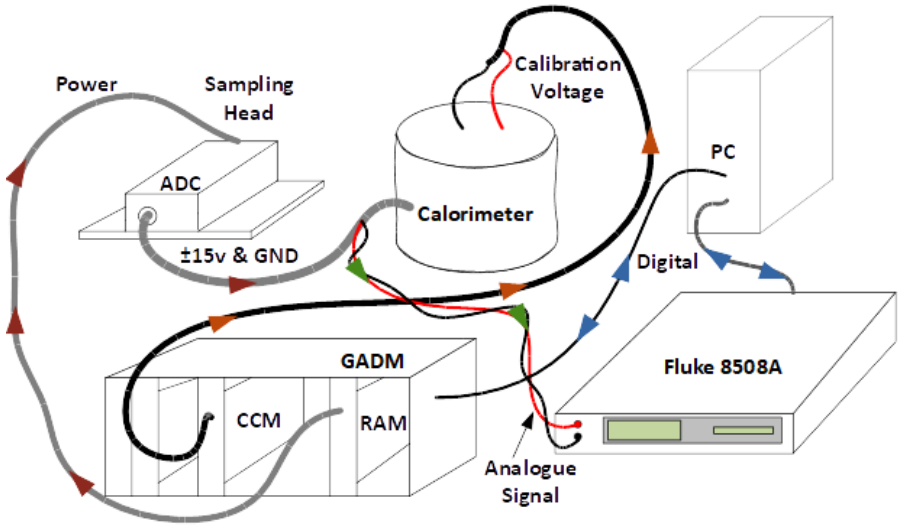

Fig. 3.2 Fluke 8508A based system
The CCM operates in the same way as Fig. 3.1. However, the GADM and sampling head are no longer used to collect data. Their sole function is to power the calorimeter's amplifier with ±15 V and Ground. The Fluke 8508A measures the voltage and writes the data to a LabVIEW program on the PC.

3.3 First PiADC System

The first PiADC system (Fig. 3.3) was developed at LLE and was originally designed to read pressure transducers [4], which added some extra complexity to the setup. Pull-up and pull-down resistors, hereafter referred to as terminations, had to be added in order to create a positive offset voltage so the system would be stable. It was found that these terminations had to be "tuned" to a very specific offset on the positive and ground wires in order to get the best performance out of the system. The analogue voltage from the calorimeter goes through the terminations and then is converted to a digital signal by the ADS1256. This signal is sent through a couple of field-programmable gate arrays before going to the Raspberry Pi, hereafter referred to as Pi, which sends the data to a Real Time Socket Server (RTSS). The RTSS system operates at 40 Hz and communicates with its clients every 25ms. A LabVIEW program on the PC then reads the data from the RTSS. Due to the design, setting an exact sample rate of 5 Hz was not possible.

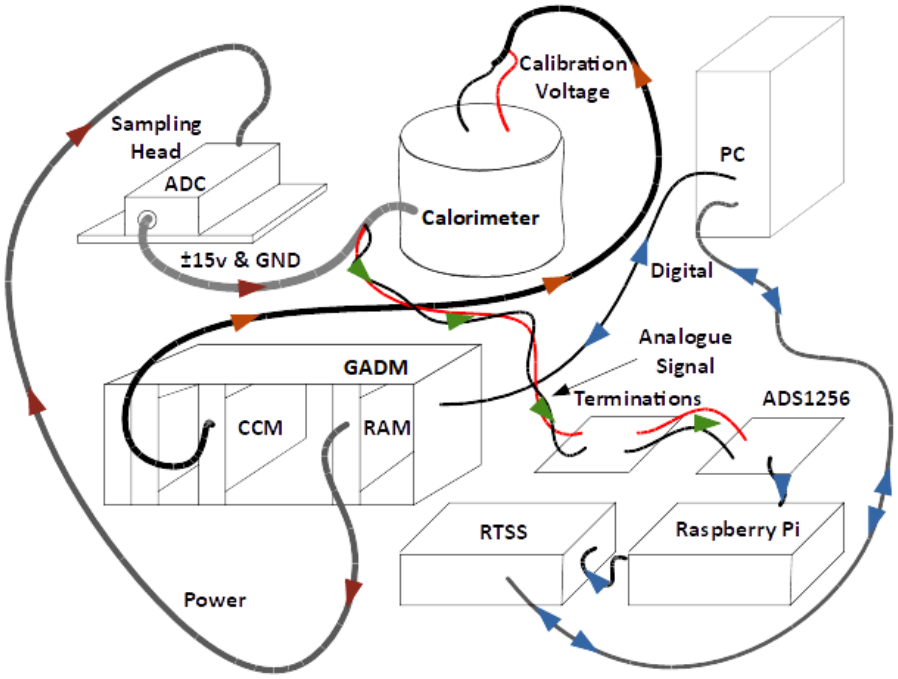

Fig. 3.3 First PiADC system
The CCM, GADM, and sampling head operate in the same way as described in Fig. 3.2. The analogue signal from the calorimeter goes through terminations to the ADS1256 ADC which outputs a digital signal. This signal eventually goes to the Pi to the RTSS, where a LabVIEW program on the PC reads the data from the RTSS.

3.4 Second PiADC System

The second PiADC system (Fig. 3.4) was built to simplify the issues present in the first system and be able to operate in OMEGA. The analogue signal from the calorimeter is processed in the ADS1256 on a commercial board [5], which is controlled by a C program [6] that was modified for file manipulation on the Pi. A Python program was used to interface with the LEDs and buttons on the control panel and calls the C program to start sampling. For the tests on OMEGA, another cable was added to remotely enable the Pi to begin acquiring data 20 seconds before the shot.

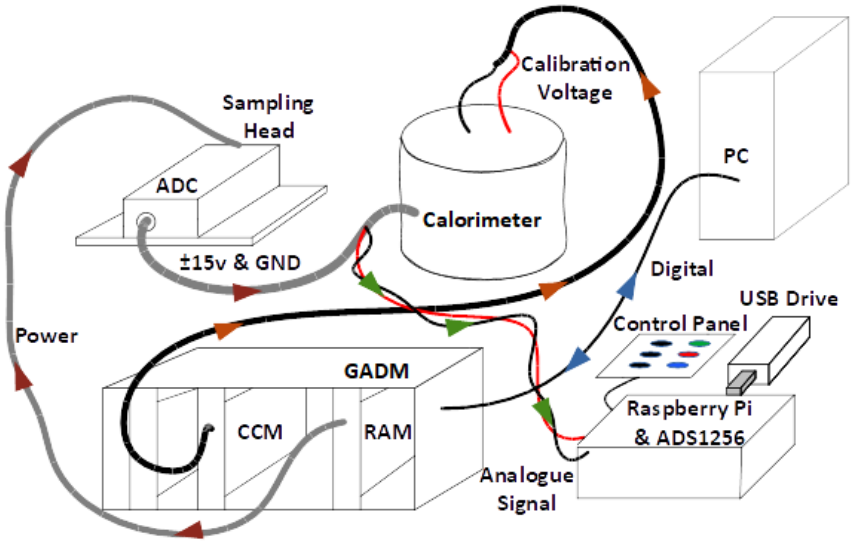

Fig. 3.4 Second PiADC system
The CCM, GADM, and sampling head operate in the same way as described in Fig. 3.2. The analogue signal from the calorimeter goes to the ADS1256 and then the digital signal travels directly to the Pi and is recorded on a USB drive. Unlike the first PiADC, this system was not connected to RTSS because OMEGA network clearance could not be acquired within the timespan of the project. The control panel is used to run the Pi without a monitor or keyboard.

The general procedure for all the systems while using the CCM to deliver energy was to begin data acquisition five to ten seconds prior to the calorimeter receiving energy so a baseline signal could be established. With the 1" calorimeter the sample time was around two minutes for 0.1 J of energy, and with the 2" calorimeter the sample time was around three minutes for 0.1 J of energy. It is important to note that a 1" calorimeter without an amplifier was also tested; in this case, the sampling head and GADM were not needed to power an

amplifier. Therefore, for the 1” calorimeter without an amplifier the GADM and the sampling head were not used in the Fluke 8508A system or the PiADC systems. The advantage of the non-amplified calorimeter was that no noise was added by an amplifier. However, the signal was so small that only the Fluke 8508A system could get a substantial dynamic range with it.

4. Data Processing

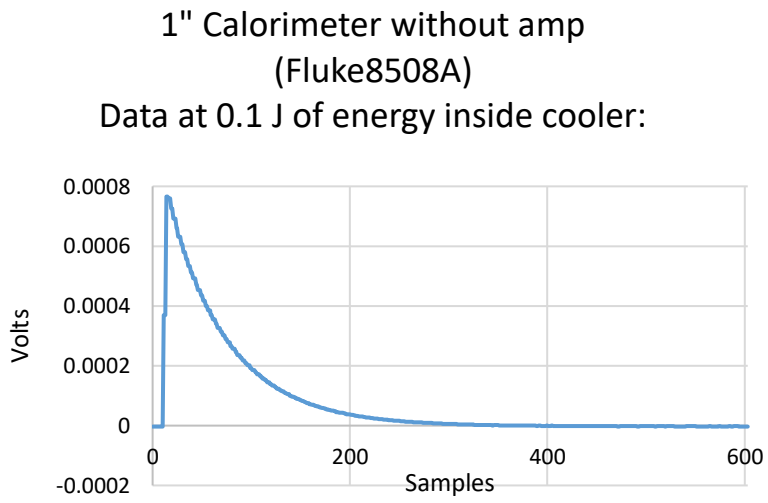

Fig 4.1 Graph of data before processing
A graph of the raw signal data directly from sampling. The samples were taken at 200 ms intervals, so the total sampling time was 120 seconds.

Fig. 4.1 is a graph of the raw signal obtained from the Fluke 8508A for the 1” calorimeter without an amplifier at an energy of 0.1 J, used to illustrate how data are analyzed.

The data are first adjusted by subtracting out a negligible amount less than the minimum (to avoid a zero on a logarithmic plot) from all values and then normalized by dividing all values by the new maximum. The data now have a maximum of one. The sample numbers on the horizontal axis are also multiplied by $\frac{1\ second}{5\ samples}$ to get seconds. These data are then plotted on a semi-logarithmic graph as in Fig. 4.2. As the signal approaches smaller orders of magnitude on the y-axis, the noise is magnified. This format makes comparisons between experiments much easier because a more successful test will reach lower

orders of magnitude. One order of magnitude is the distance between 1 and 0.1 on Fig. 4.2, two orders of magnitude are the distance between 1 and 0.01, etc. The 32:1 signal-to-noise ratio of the 16-bit ADC corresponds to about 1.5 orders of magnitude, since $10^{1.5}$=31.6 (Fig. 4.3). If the signal's beginning is at 0.1, peak at 1.0, and end at 0.1, then the graph is said to have a dynamic range of one order of magnitude. In Fig. 4.2, the graph has a dynamic range of three orders of magnitude. All subsequent plots of signal vs time are given in the same form as Fig. 4.2.

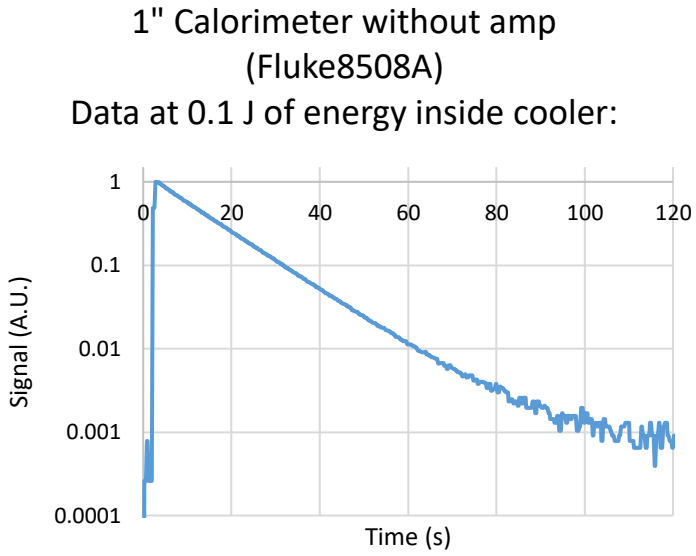

Fig 4.2 Graph of data after processing
A graph of the normalized data in arbitrary units on a semi-log plot, with the sample numbers converted to seconds.

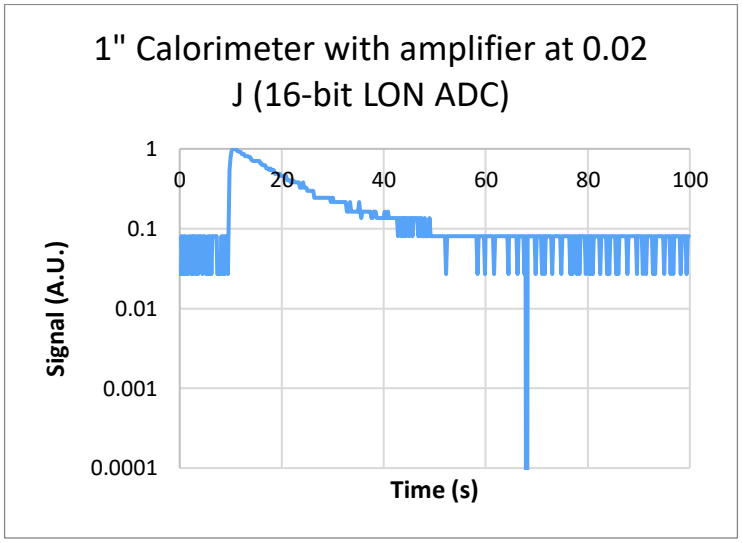

Fig. 4.3 Dynamic range of the 16-bit LON-based ADC that is currently used on OMEGA
As seen on the graph the 16-bit ADC can reach a dynamic range of 1.5 orders of magnitude at 0.02 J.

5. Effect of Insulation on Variability in Early ADC Experiments

Experiments started out with the three calorimeters listed in Table 2.1 (1” with and without an amplifier and a 2” with an amplifier), using three ADC systems at two energy levels (0.1 and 1.0 J), and the calorimeter being either inside or outside a Styrofoam cooler. Tests at 1.0 J or outside the cooler were not found to be useful and are not presented in this report. 1.0 J is much higher than what any 1” calorimeter will measure on OMEGA and is the highest that any 2” calorimeter will measure. Some of the tests outside the cooler were found to reach a thermal equilibrium tens of microvolts above the baseline signal due to room temperature effects, but this behavior (known as drift) was not consistent. Fig. 5.1 demonstrates these effects in a test where no energy was supplied to the calorimeter.

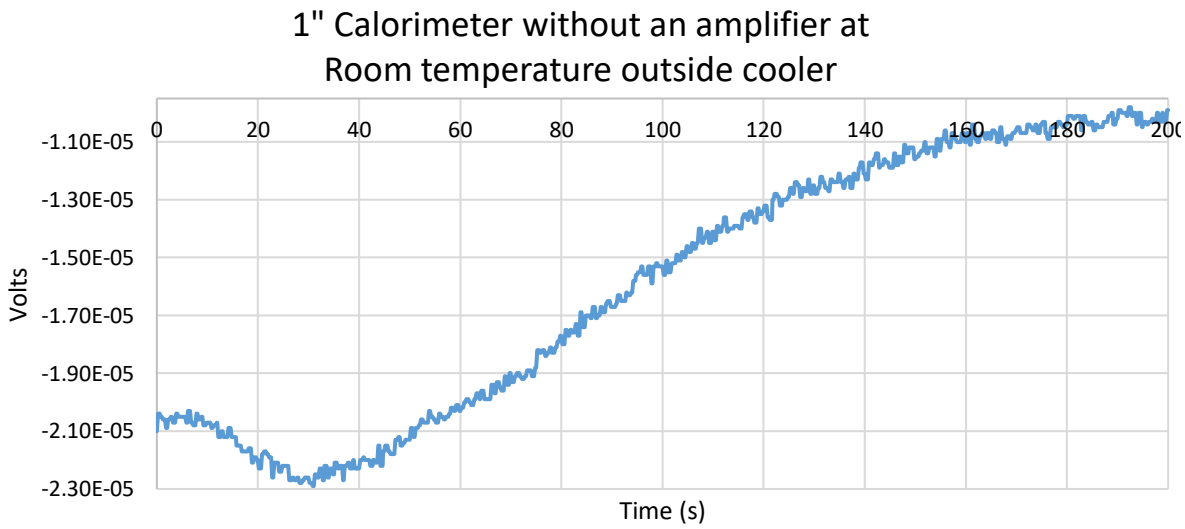

Fig 5.1 Voltage fluctuations caused by temperature fluctuations recorded by the calorimeter
As shown in the graph, temperature fluctuations can cause a drift of 12 microvolts over the course of 3 minutes.

The peak signal of the 1” calorimeter without an amplifier, from which these data were acquired, is 750 microvolts at 0.1 J of energy (see Fig. 4.1). This means that the drift could

account for 1.6% of the signal (12 microvolts), but the temperature change is not linear and isn't always present. Thus, when drift like this is present, it is impossible to have a measured-energy calculation that has a smaller margin of error than ±1.6%. Fig. 7.4 (below) is an example of drift when energy was supplied to the calorimeter.

In order to better control the test temperature, all further tests were performed inside the cooler. It is important to note that this drift issue wasn't completely solved by the cooler, and some tests still showed limited drift. Table 5.1 summarizes the results from the three calorimeters and the three ADC systems. The numbers in the table are the orders of magnitude for the dynamic range and drift for each specified case. For example, "Drift: 3 to 2" means that the signal's baseline (initial value before energy was supplied to the calorimeter) on a plot such as Fig. 7.4 (below) was 0.001 and the signal's final value was 0.01. A drift of none indicates that the baseline is equal to the signal at the end.

Table 5.1 Dynamic Range and Drift for 3 ADC Systems with 3 Different Calorimeters*

Data taken at 0.1 J of energy inside a cooler	24-bit LON-based ADC (Fig. 3.1)	Fluke 8508A System (Fig. 3.2)	First PiADC** (Fig. 3.3)
1" Calorimeter without an amplifier	Dynamic Range: 1 Drift: None	Dynamic Range: 3 Drift: None	Dynamic Range: 2 Noise Issue Present
1" Calorimeter with an amplifier	Dynamic Range: 1.5 Drift: 3 to 1.5	Dynamic Range: 2 Drift: 3 to 2	Dynamic Range: 2 Drift: 2 to 3
2" Calorimeter with an amplifier	Dynamic Range: 2 Drift: None	Dynamic Range: 1.5 Drift: 3 to 1.5	Dynamic Range: 1.75 Drift 2.5 to 1.75

**Numbers indicate orders of magnitude*

***These tests were before the PiADC was "fine-tuned" with the terminations shown in Fig. 3.3*

These data weren't very consistent and were more a demonstration of what was possible across all the systems at 0.1 J. The test with the Fluke 8508A system measuring the 1" calorimeter without an amplifier, shown in Figs. 4.1 and 4.2, revealed that a dynamic range of three orders of magnitude was possible. That result became known as the "gold standard" that all future tests would be compared against. The PiADC was very inconsistent during these tests but was still able to perform between the 24-bit LON-based ADC and the Fluke 8508A system. From these tests, a new goal of getting the PiADC to consistently perform as well as the gold standard with the other calorimeters was put in place. Note that because the 1" calorimeter without an amplifier isn't used on OMEGA, testing with it stopped.

6. First PiADC Fine-Tuning

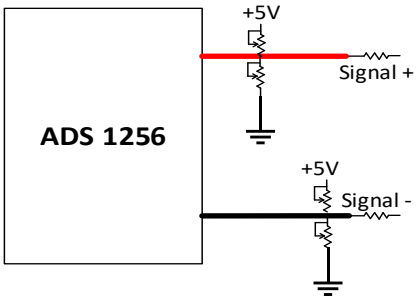

Fig. 6.1 First PiADC Terminations
The terminations consist of four tunable 10 k Ω potentiometers. Two additional series resistors on the Signal + and Signal – wires were added to reduce noise.

Due to an oddity of the C code on the PiADC, a 1.4 millivolt offset would come into effect if the analogue value came too close to zero, creating 1.4 millivolts of noise. Terminations were added before the ADS 1256 ADC to create a tunable offset (Fig 6.1) that both solved the 1.4 millivolt offset issue and further reduced noise. Resistors in series with the "signal +" and the "signal –" wires as shown in Fig. 6.1 were also found to reduce smaller-amplitude noise. The best offset was found to be +2.498 volts on the positive signal wire and -2.495 volts on the negative signal wire with 10 k Ω series resistors on both wires. The results of tests with this offset are all similar

to Fig. 6.2, which demonstrated that a PiADC could perform as well as the Fluke 8508A system. Further tests were performed in order to obtain the gold standard at 0.1 J with the 2" calorimeter. However, due to the 2" calorimeter's larger thermal mass the signal was smaller. This smaller signal meant that the 10 k Ω series resistors had to be replaced with 5 k Ω series resistors. Table 6.1 summarizes the 2" calorimeter test results, where 0.4 and 1.0 J were also tested because the 2" calorimeters usually handle higher energies than the 1" calorimeters.

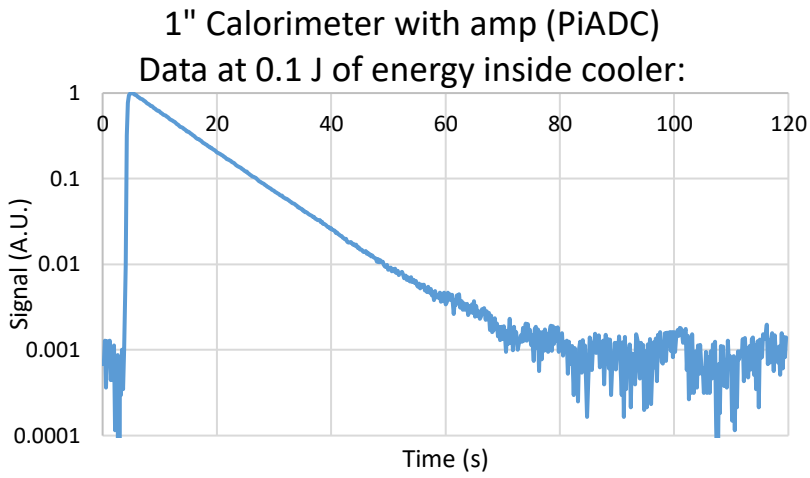

Fig. 6.2 Graph of the first PiADC reaching the gold standard
With the proper offset and 10 k Ω series resistors the first PiADC system was able to have a dynamic range of three orders of magnitude.

Table 6.1 Dynamic Range and Drift for Different Offsets and Energies on a 2" Calorimeter with 5 k Ω Series Resistors

Positive signal wire offset: Negative signal wire offset: Energy Level:	+2.558 V -2.548 V 0.1 J	+2.498 V -2.495 V 0.4 J	+2.498 V -2.495 V 1.0 J
2" Calorimeter with an amplifier	Dynamic Range: 2.5 Drift: None	Dynamic Range: 3 Drift: None	Dynamic Range: 3 Drift: None

By adding the terminations, tuning them, and creating an offset, the drifts that were present in Table 5.1 were practically eliminated. The tests also had consistently large dynamic ranges of 2.5 to 3 orders of magnitude. However, this PiADC was designed for different applications. In order to further improve measurement accuracy and make the PiADC practical

to use in OMEGA, the PiADC had to be made cheaper, smaller, easier to use, and developed for calorimetric measurements on OMEGA.

7. Second PiADC System

After setting up the second PiADC system, tests at 0.1 J inside the Styrofoam cooler demonstrated that the system could reach a dynamic range of at least 3 orders of magnitude (Fig 7.1). Further noise reduction using voltage regulators to supply a 1.5 V reference to the ADC was attempted but was found to be ineffective. At that level of accuracy, the temperature drift and noise from the calorimeter's amplifier were the dominant noise producers.

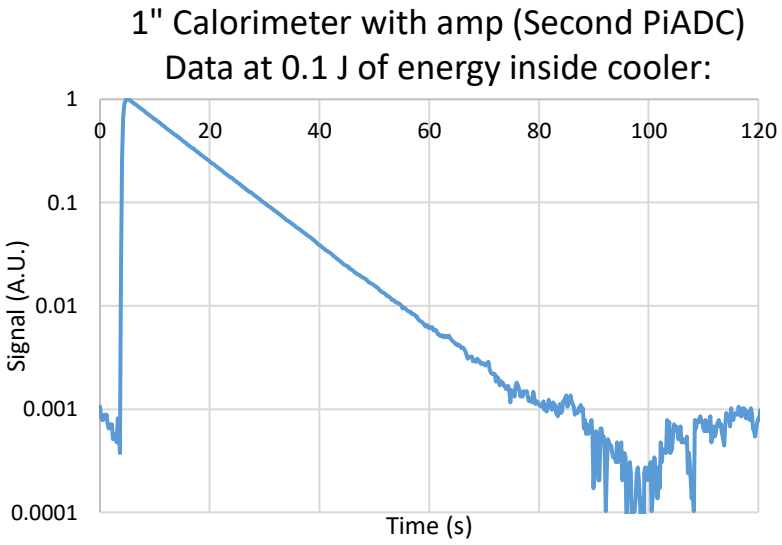

Fig. 7.1 Graph of the second PiADC reaching the gold standard with less noise than the previous version.
With this test the second PiADC demonstrated better performance than the first PiADC (Fig. 6.2) with a smaller size and lower price.

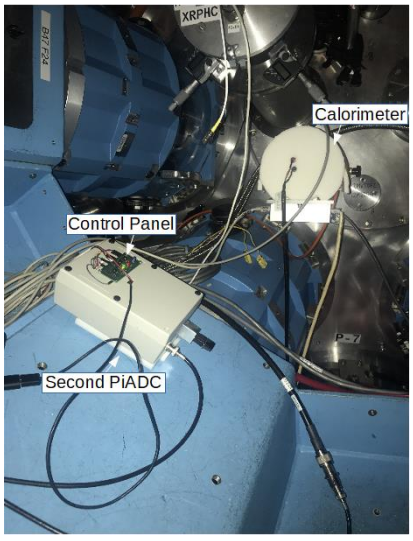

Fig. 7.2 Second PiADC on OMEGA
The PiADC in a box is left of center, and the H8 calorimeter with extra insulation is right of center.

The next set of tests were performed on the H8 scatter calorimeter on the OMEGA target chamber (Fig. 7.2), but without the extra insulation around the calorimeter that is depicted in Fig. 7.2. High energy shots on OMEGA involve all

60 beams, but these tests were with six-beam shots, so the calorimeter only detected about 0.02 J of energy that scattered off the target. The resulting data can be seen in Figs. 7.3 and 7.4. Due to the lower energy level and lack of extra insulation around the calorimeter, the best result (Fig. 7.3) had a dynamic range of only 2.5 orders of magnitude. However, there were also multiple tests that showed drift, such as Fig 7.4 where the signal leveled out at a value one order of magnitude higher than the signal's baseline.

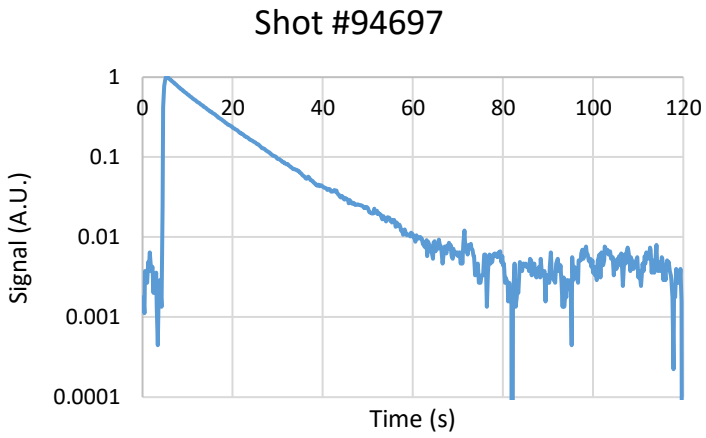

Fig. 7.3 Best result from the first set of OMEGA tests
The data have a dynamic range of 2.5 orders of magnitude and no drift due to temperature fluctuations.

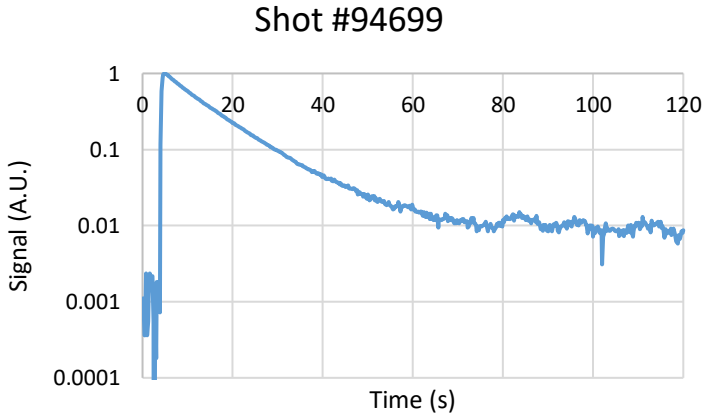

Fig. 7.4 Typical result with drift from the first set of OMEGA tests
The data could have a dynamic range of 2.5 to 3 orders of magnitude, but there is an order of magnitude of drift due to temperature fluctuations.

Even at an energy that was 20% of what the PiADC was tested at and on a calorimeter without extra insulation, the PiADC was able to collect some data with a dynamic range of 2.5 orders of magnitude. However, the results with drift showed a need for additional insulation around the calorimeters to further improve consistency and accuracy.

Insulation bench-tests on the 1” calorimeter with an amplifier at 0.02 J of energy followed. Thick paper, paper folded in a corrugated design around the calorimeter, bubble wrap, one layer of foam, and two layers of foam with a 7 mm air gap in between (Fig 7.5) were all tested. Only the one layer and two layers of foam showed a noticeable reduction in drift.

Each layer of foam reduced the drift by a considerable amount (Fig. 7.6). Tests without additional insulation around the calorimeter resulted in 1.5 orders of magnitude of drift; tests with one layer of insulation resulted in 1 order of magnitude of drift; and tests with two layers of foam insulation showed little to no drift. There was a consistent dynamic range of 2.5 to 3 orders of magnitude in the tests with two layers of foam insulation.

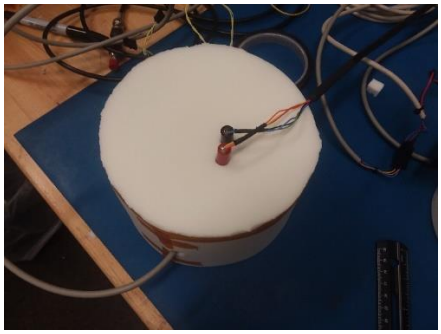

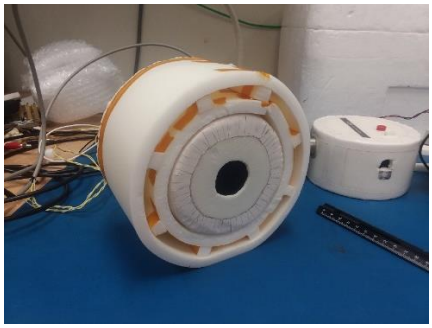

Fig. 7.5 (a) Top view of two-layer foam insulation on a 1” calorimeter

Fig. 7.5 (b) Side view of two-layer foam insulation on a 1” calorimeter

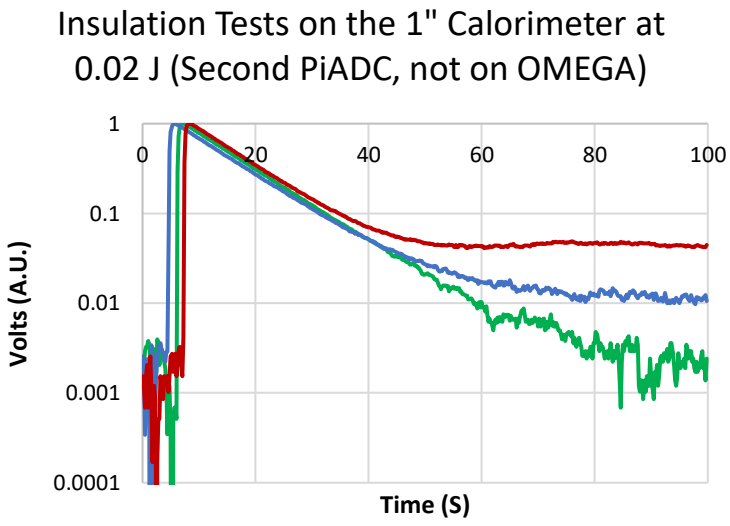

Fig. 7.6 A comparison of drift between no insulation, 1 layer of foam insulation, and 2 layers of foam insulation.
Red is the plot with no insulation
Blue is the plot with one layer of insulation
Green is the plot with two layers of insulation

This insulation was tested on OMEGA as depicted in Fig. 7.2, but the PiADC’s program

stopped working during the shots. The probable cause was that the PiADC logged-in two users, which doubled the processor usage. This drew power away from the ADS1256 and caused an error. This error was corrected in the latest version of the PiADC's program.

8. Conclusion and Future Research

This work has made it possible to improve the accuracy of calorimetric measurements on OMEGA by an order of magnitude, with the potential to be 1.5 orders of magnitude better than the current system if the calorimeter is insulated as shown in Fig. 7.5. After three different ADC systems were tested, a fourth system using a PiADC was created to further improve accuracy. Before the second PiADC is to be installed on OMEGA it must be configured with RTSS to improve reliability and properly shielded from neutron radiation. Connecting the second PiADC to RTSS would enable real-time data collection and a way of detecting program errors. The current plan to shield the PiADC is to separate the Raspberry Pi from the ADS1256 ADC and run fiber optic between them so that the ADC can still be close to the analogue source.

The simplest way to further improve energy measurement accuracy is to add the two layers of insulation depicted in Fig. 7.5 onto OMEGA calorimeters. Once temperature-based drift is no longer an issue, linear regulators can be added to the circuitry. A linear regulator is an integrated circuit that adjusts its resistance based on the current, resulting in a very steady voltage. Linear regulators could be used to supply the ±15V required to power the calorimeter's amplifier in order to potentially reduce amplifier-based noise. They could also be used to supply the ADS1256 with a smaller and less noisy reference voltage. Beyond that, additional optics would have to be installed to increase the amount of light absorbed by the calorimeter.

This additional absorbed energy would create a larger analogue signal, which means a larger dynamic range. Further accuracy would require either calorimeters that are designed for lower energies or the use of bolometers. Bolometers do not use a thermal reference like calorimeters. In theory the heat sink that acts like a thermal reference in calorimeters could drift due to room temperature effects, meaning bolometers could be more resistant to drift than calorimeters. However, the cost and effectiveness of many of these concepts would need to be addressed.

9. Acknowledgments

Special thanks to my advisors Mike Sharpe, Vinitha Anand, and Robert Peck for guiding and supporting my work on this project.

Thanks to Christian Stoeckl for guidance organizing the tests that were done on OMEGA.

Thanks to Heath Ferry for letting me borrow the First PiADC system.

Thanks to Dr. Craxton for his work organizing the High School program at LLE.

10. References

[1] Scientech. Astral Series Calorimeters Setup and Operating Procedures. PN9458P.

[2] Mark Donovan. Calorimeter Calibrator Operation Manual. E-CA-M-03 Laboratory for Laser Energetics. 06/25/2004

[3] John Canosa et al. Hardware Description Generic A/D Module. E-AD-M-02 Laboratory for Laser Energetics. 02/23/1994

[4] Heath Ferry. In-person communication. 07/17/2019

[5] Waveshare. High-Precision AD/DA Board

(https://www.waveshare.com/wiki/High-Precision_AD/DA_Board)

[6] John Beale. DataAcq / ADS1256_read.c

(https://github.com/jbeale1/DataAcq/blob/master/ADS1256_read.c)

Investigations of the Hydrogen-Palladium and Deuterium-Palladium Systems

Stephen Rosa

Eastridge High School

Rochester, NY

Advisors: Dr. Walter T. Shmayda & Dr. Matthew Sharpe

Laboratory for Laser Energetics

University of Rochester

Rochester, NY

January 2020

Abstract:

Palladium is a metal that is used to store hydrogen and its isotopes. It can interact with hydrogen by either physically storing it in the spaces between palladium atoms, or by reacting with it chemically to form palladium hydride, which can be separated later to release the stored hydrogen. This work examines the change in vapor pressure over palladium as hydrogen is added to change the ratio of hydrogen atoms to palladium atoms, with the temperature held constant. This data is represented as an isotherm. Little data exists for the formation of palladium hydride at temperatures below 0°C. This work serves to expand the data available at low temperatures. Data has now been collected at temperatures ranging from 140 K to 393 K (-133°C to 120°C). The formation of palladium hydride at low temperatures has been observed to deviate from high temperature data, following a separate trend on the van ‘t Hoff plot. This created a total of two lines on the van ‘t Hoff plot, one for the high temperature data and a separate one for the low temperature data. This is likely due to the physical adsorption of hydrogen onto the surface of the bed. A relationship between temperature and the surface coverage of the palladium bed by hydrogen via physical adsorption was calculated using this new data.

1. Introduction:

Studying the formation of palladium hydride is important because of its use as a method to store, transport and release hydrogen and its isotopes, deuterium and tritium. This is especially significant to the Laboratory for Laser Energetics (LLE) because LLE carries out inertial confinement fusion experiments using cryogenic targets filled with deuterium and tritium, isotopes of hydrogen. Using palladium hydride to release these isotopes is being investigated as a method of filling the targets with fuel.

The interaction between palladium and hydrogen is well-studied at temperatures above 0°C, [1], [2], [3], [4] but the data for sub-zero temperatures is very limited.[5] Isotherms, which relate the vapor pressure of the system to the H/Pd atom ratio of the bed, need to be measured for palladium hydride at low temperatures in order to fill in the data gap that exists for sub-zero temperatures, and can be used to predict how the composition of mixed isotopes (deuterium and tritium) in the hydrogen changes as a bed of palladium hydride is unloaded at low temperatures. From this experiment, it was found that the formation of palladium hydride did not behave the same at low temperatures as it did at high temperatures.

2. Theory:

Palladium interacts with hydrogen to form palladium hydride according to the following reaction:

$$\frac{x}{2}H_2(g) + Pd(s) \rightleftharpoons PdH_x(s) \quad (1)$$

The letter "x" represents the number of moles of hydrogen as palladium hydride, "s" indicates the solid state and "g" indicates the gaseous state. The formation of palladium hydride passes through three different stages: the first being the alpha stage, the second stage being the alpha-beta stage (or plateau stage) and the third being the beta stage. In each of these stages the palladium and hydrogen interact in different ways as shown in figure 1.

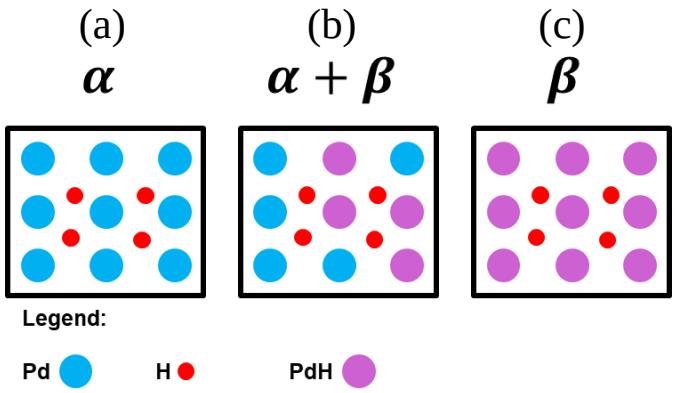

Figure 1: Diagram of the stages of palladium hydride formation

As hydrogen is added, the system progresses through the alpha, alpha+beta, and beta stages. Figure 1(a) shows the alpha stage of palladium hydride formation. Figure 1(b) shows the alpha+beta stage, or plateau stage. Figure 1(c) shows the beta stage.

As hydrogen is introduced to the palladium metal in the alpha stage, hydrogen atoms do not begin to chemically bond with the palladium. Instead they enter the interstitial spaces between palladium atoms to physically store themselves in the palladium atomic lattice as shown in figure 1(a). Next, hydrogen atoms begin interacting chemically with the palladium atoms to form

palladium hydride. This is the beginning of the plateau stage. During this stage there are both free palladium atoms and palladium hydride molecules as well as hydrogen in the palladium atomic lattice as shown in figure 1(b). The beta stage begins when all the palladium has been chemically bonded with hydrogen to form palladium hydride. In this stage, there are no additional free palladium atoms and the palladium lattice is now a palladium hydride lattice. Additional hydrogen is physically stored in the spaces in this new lattice of palladium hydride molecules, as shown in figure 1(c).

The vapor pressure of the system follows different trends during each stage. The relationship between H/Pd ratio and pressure at a given temperature is exemplified in figure 2. As the

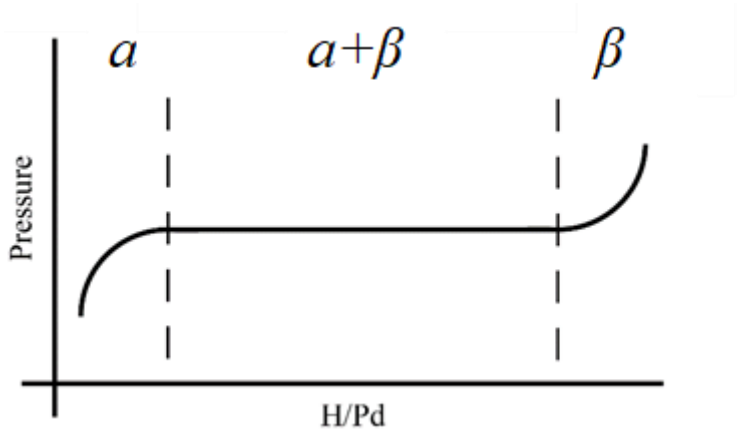

Figure 2: Diagram of the relationship between pressure and H/Pd ratio

The three stages of palladium hydride formation are represented by the three separate parts of the figure. The alpha region is the leftmost separation, labeled "a," the plateau region is in the middle, labeled "a+b," and the beta region is on the left, labeled "b."

H/Pd atom ratio increases during the alpha stage, the pressure increases also, but less rapidly as the plateau stage is approached. The plateau region sees no increase in pressure as more hydrogen is added to the system, and the H/Pd ratio continues to increase during this phase. During the beta stage, any additional hydrogen added to the system increases the pressure of the system once again.

This relationship between pressure and the H/Pd ratio at a given temperature creates a distinct s-shaped curve as shown in figure 2. This curve is known as an isotherm curve, which means "same temperature," because the various data points that are collected to form this curve are found while the system is held at constant temperature. The formation of palladium hydride always follows the same general s-shaped curve, but at higher temperatures the pressure for the entirety of the formation curve is higher and at lower temperatures the pressure is lower. This is shown in figure 3.

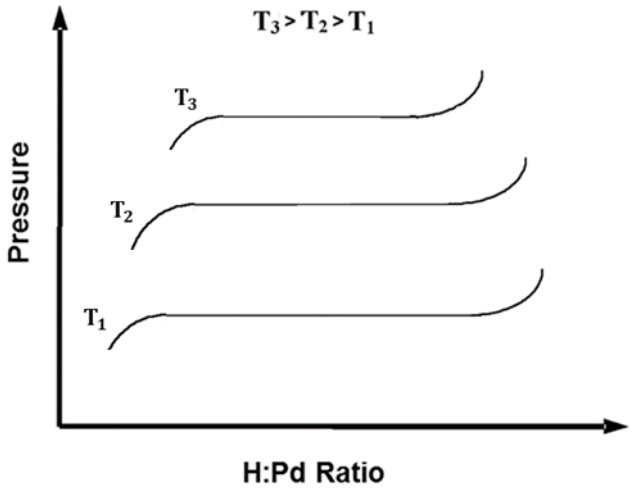

Figure 3: Diagram of the effect of temperature on isotherm position

The lowest temperature, T_1, features the lowest pressures of all three isotherms shown. As the temperature increases to T_2 and then to T_3, the overall pressure increases. It can be thought of as translating the isotherm up and down on the figure depending on the temperature.

The effect of temperature on the pressure of the system shown in figure 3 can be modeled using the van 't Hoff equation which relates the change in pressure to the change in temperature as shown in the following equation:

$$ln(P_{eq}) = \frac{2\Delta H}{xR} * \frac{1}{T_K} - \frac{2\Delta S}{xR} \quad (2)$$

The variable "P_{eq}" epresents the equilibrium pressure of the system, "ΔH" represents the enthalpy of formation of the system, "ΔS" represents the entropy of formation of the system, "x" represents the number of moles of hydrogen in the system, "R" is the universal gas constant and "T_K" represents temperature in Kelvin. This equation relates temperature to pressure for the

formation of palladium hydride, showing the effect that temperature has in "translating" the isotherm curve up or down on the graph as described in figure 3.

The van 't Hoff equation follows a linear relationship when plotted on a semilog scale, which is easy to see when comparing it to the equation of a straight line:

$$y = m * x + b \tag{3}$$

where "y" is the natural log of pressure, "m" represents the slope of the line, "x" is the inverse of temperature, and "b" represents the y-intercept of the line. In comparing equation 2 to equation 3, it becomes clear that the y-intercept is related to the entropy of formation of the system and the slope is related to the enthalpy of formation of the system.

Each point on a van 't Hoff plot represents the same H/Pd ratio, but different pressures depending on the isotherm, and therefore different temperatures. These points are then plotted on a graph of ln(pressure) vs. (1/temperature), according to the van 't Hoff equation and the result is a straight line as shown in figure 4(b), which shows the van 't Hoff plot created from the example isotherms in figure 4(a).

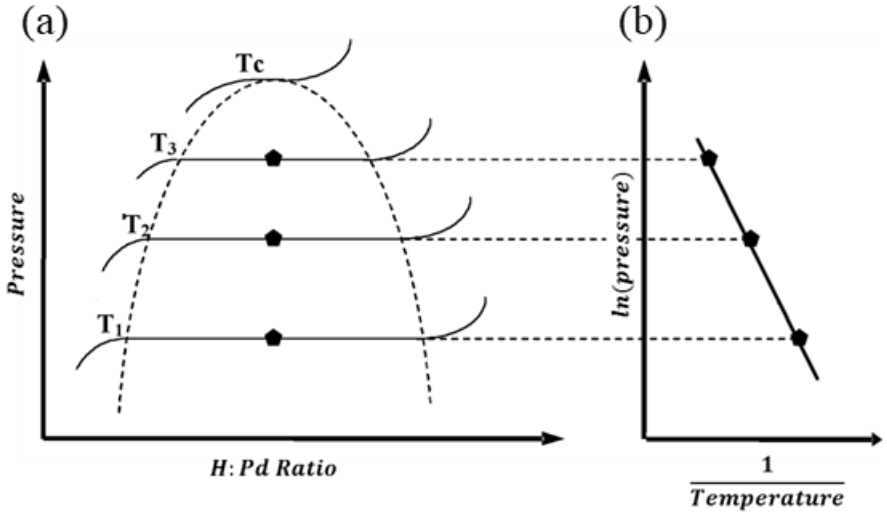

Figure 4: Diagram of the derivation of the van 't Hoff plot from isotherm curves

Figure 4(a) shows various example isotherms with a single point at a fixed H:Pd ratio highlighted on each curve. Figure 4(b) shows the corresponding van 't Hoff plot.

3. Experimental Setup:

A diagram showing the setup of the equipment to measure the pressure-composition isotherm for a range of temperatures is shown in figure 5.

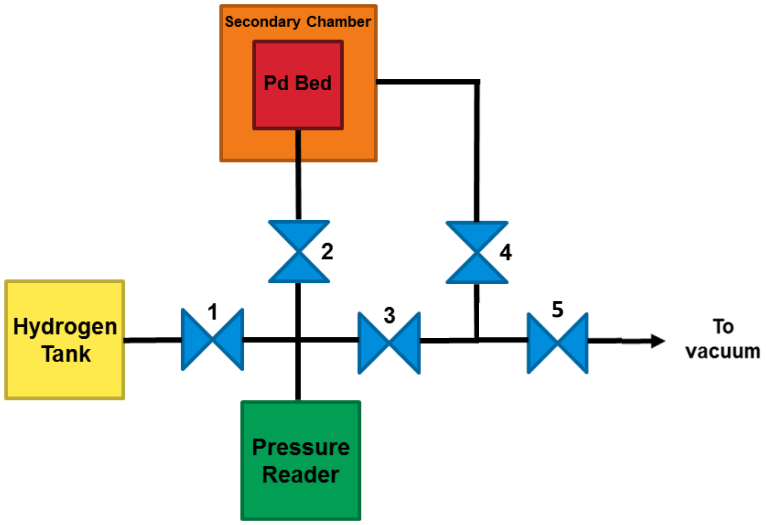

Figure 5: Diagram of lab setup

Black lines represent the tubing between each component, and blue hourglasses represent valves. The arrow that reads "to vacuum" represents the tubing that leads to a turbomolecular pump and a scroll pump. A Q-Drive cryocooler and Sorenson heaters (not pictured) control the temperatures of the Secondary Chamber and Pd Bed.

The palladium bed is made up of 2.5 g of palladium sponge. It is surrounded by a secondary chamber that is vacuum sealed to minimize heat loss or heat gain from the environment. A turbomolecular pump backed by a scroll pump was used to maintain a high vacuum in this chamber. Different valves were used to direct the flow of hydrogen gas to the system and to maintain a vacuum in the secondary chamber as well as to pump the hydrogen out of the system at the end of each run. The volume between valves 1, 2, and 3, including the pressure transducer, known as the charge volume, is 20.1 ± 0.1 cm^3. The volume between valve 2 and the Pd bed is 4.76 ± 0.05 cm^3.

The quality of the vacuum was measured with an ion gauge, which uses a heated filament to emit electrons that ionize gas molecules that pass through it. The ions are collected on a cathode, and the current measured from this cathode can be used to determine the gas density in the vacuum. The system was cooled to subzero temperatures by a Q-Drive, a Stirling pulse-tube cryocooler which uses the compression and expansion of helium to pull thermal energy from a cold head that in turn cools the palladium bed. A Sorenson power supply delivered a DC current to a heater embedded in the body of the palladium bed.

The system's properties such as its temperature and pressure were recorded using a computer running a LabVIEW program to collect real-time measurements. The LabVIEW data was updated every 5-second interval and analyzed using MATLAB.

4. Procedure:

A procedure was developed that outlines the step-by-step process used to add hydrogen to the system to form palladium hydride. Once the system is under vacuum and the desired temperature has been reached and is maintained, the steps to collect data are shown below using the valve diagram shown in figure 5. The load procedure is as follows.

Load Procedure:

1) Close valves V_1, V_2, and V_3, open valves V_4 and V_5
2) Record pressure of system as background pressure
3) Slowly open V_1 to allow hydrogen to enter the charge volume
4) Close V_1 when the desired pressure of hydrogen is reached, and record this pressure as charge pressure

5) Open V_2 to allow hydrogen to enter the palladium bed and interact with the palladium
6) Wait for the pressure to stop changing and reach equilibrium, record the pressure of the system as the equilibrium pressure
7) Repeat steps 4-6 until the isotherm is complete
8) After the isotherm is complete, run unload procedure

This process increases the H/Pd ratio of the system little by little with each iteration of the load procedure to slowly form an isotherm. The H/Pd ratio of the system is found using the following equation:

$$H/Pd = \frac{2*(P_{load}*V_{charge}+P'_{eq}*V_{bed}-P_{eq}*(V_{bed}+V_{charge}))}{R*T_{room}*n_{Pd}} \quad (4)$$

This equation relates the total amount of hydrogen that has entered the system to the total amount of palladium, "n_{Pd}," where "P_{load}" represents the charge pressure of the hydrogen before it's put onto the bed (see load procedure), "V_{charge}" represents the volume the charged hydrogen is put into, "P'_{eq}" represents the equilibrium pressure after the previous loading, or the background pressure of the system if this is the first charge of a new isotherm (see load procedure), "V_{bed}" is the volume between valve 2 and the Pd bed, "T_{room}" is the room temperature, and "R" is the universal gas constant.

After each isotherm is completed, the hydrogen that was loaded onto the bed must be removed. The removal of this hydrogen is known as "unloading." The process for unloading at the end of a run is outlined as follows:

Unload Procedure:

1) Close V_4 and V_5 to prevent the vacuum in the secondary chamber from being degraded
2) Open V_2 and V_3 to allow the hydrogen in the Pd bed to escape into the charge volume and surrounding tubing
3) Turn off the turbomolecular pump, Q-Drive, and ion gauge
4) Open V_5 to remove the gas stored in the tubing and Pd bed by evacuating the loop out with the scroll pump
5) Turn on the Sorenson heater to bake off any residual hydrogen in the palladium bed
6) Turn on the turbomolecular pump to improve the vacuum
7) Evacuate for several hours
8) Turn off the Sorenson heater, turn off the turbomolecular pump
9) Close V_3, open V_4 to start maintaining the vacuum of the secondary chamber
10) Turn on the turbomolecular pump, turn on the ion gauge, turn on the Q-Drive
11) Run load procedure

5. Results:

Figure 6 shows isothermal data collected during the current study quantifying the relationship between the H/Pd ratio and pressure for subzero temperatures ranging from -120°C to -36°C. These isotherms are also shown in figure 7 together with high temperature isotherms[4], [6] and additional low-temperature isotherms[6] obtained independently by other LLE researchers.

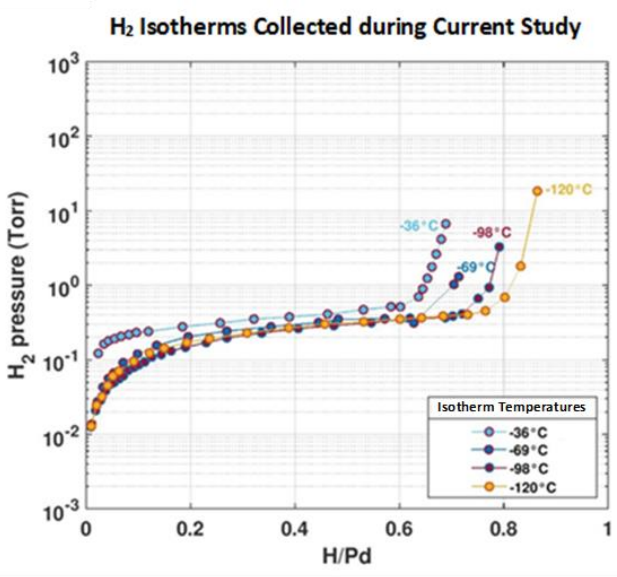

Figure 6: Palladium hydride isotherms collected during the current study

Isotherms were obtained for temperatures ranging from -120°C to -36°C.

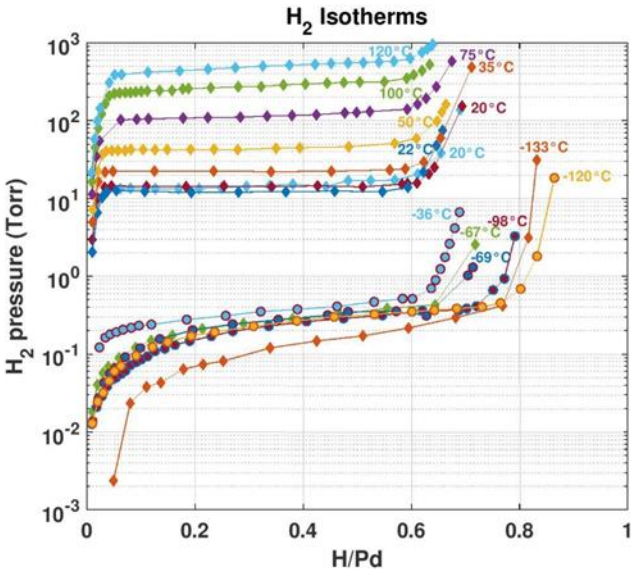

Figure 7: Complete set of palladium hydride isotherms

Figure 7 shows the palladium hydride isotherms of figure 6 together with isotherms collected by other LLE researchers using the same experimental setup[4], [6].

Figure 7 features two groups of isotherms: a low temperature group clustered in the 100 mTorr range with temperature ranging from -133°C to -36°C, and a high temperature group spanning pressures from 10 Torr to 600 Torr with temperatures from 20°C to 120°C. The H/Pd

ranges for the lower temperature isotherms are broader than for the higher temperature isotherms suggesting that more hydrogen can be stored at lower temperatures for a given amount of palladium before the pressure starts increasing dramatically. The slope of the plateau regions of the low temperature isotherms is more of an upwards slope rather than the traditional flat plateau shown in the high temperature data.

It should be noted that the yellow isotherm collected at -120°C in figure 7 seems to have been collected with substantial error. The other isotherms in this figure all follow the trend outlined in figure 4, where a decrease in isotherm temperature shows a decrease in overall isotherm pressure, causing the isotherms to vertically shift downwards as the temperature decreases. The isotherm at -120°C, however, is shown to be in line with or above collected isotherms of higher temperatures, such as the -98°C isotherm. Because of this error, the yellow -120°C isotherm was not included in data sets used to calculate van ‘t Hoff lines.

The isotherms of figure 7 were used to create a van ‘t Hoff plot for the formation of palladium hydride with a selected H/Pd ratio of 0.4, shown in figure 8. It is seen that

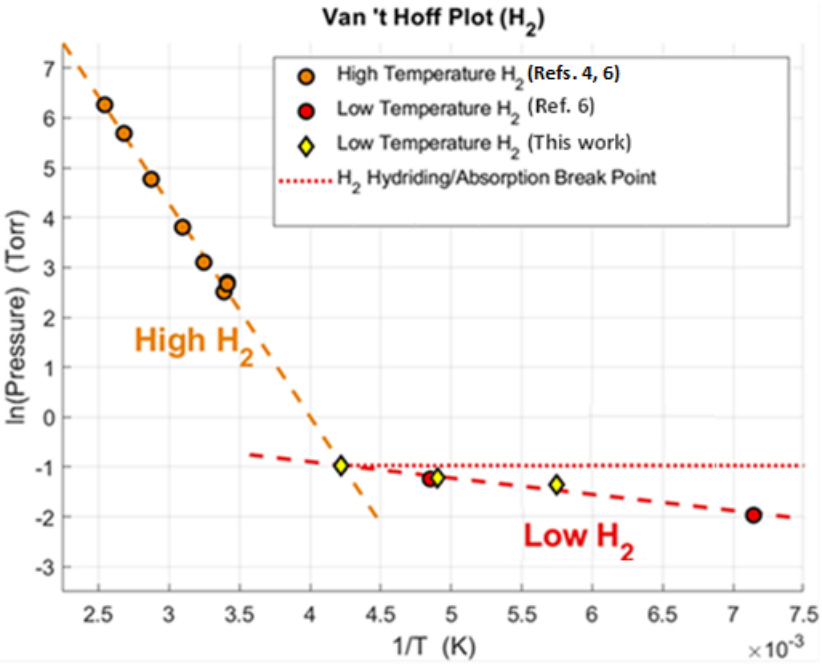

Figure 8: Van ‘t Hoff plot of collected palladium hydride isotherms

The higher temperature isotherms follow a different van’ t Hoff line than the lower temperature isotherms. This suggests a different interaction is occurring at lower temperatures.

the low temperature points deviate from the high temperature points. The points that are shown in orange represent the high temperature isotherms from figure 7. The van ‘t Hoff line for these high temperature isotherms is shown as the dashed orange line. The points shown in red represent the low temperature isotherms from reference 6 shown in figure 7. The van ‘t Hoff line for low temperature isotherms is shown as the dashed red line. The points represented as yellow diamonds are from the current study and are part of the low temperature data set.

The different trends of the low and high temperature van ‘t Hoff lines suggest that the interaction between hydrogen and palladium changes below a critical temperature. In other words, at low temperatures the interaction between hydrogen and palladium is no longer solely the formation of palladium hydride. According to figure 8, this shift occurs at the intersection of the two van ‘t Hoff lines, at -36°C ($1/T \approx 4.22\times10^{-3}$ K^{-1}). The dotted pink line is a horizontal reference line passing through this intersection. An isotherm that was collected at this temperature is shown in figure 8 as the yellow diamond in the intersection.

6. Discussion

This new interaction was theorized to be physical adsorption of hydrogen onto the surface of the palladium bed. This process begins with the hydrogen that enters the system pooling onto the surface of the palladium sponge rather than entering the palladium atomic lattice or bonding with palladium atoms to form palladium hydride. Next, some of the hydrogen particles bond with the palladium on the surface of the sponge and form palladium hydride, which heats up the palladium slightly because of the exothermic nature of the hydride formation reaction. This slight increase in temperature allows some of the hydrogen to diffuse deeper into the palladium sponge, but only allows it to permeate the first few layers of particles, while the rest of the hydrogen

continues to adsorb onto the surface. Because only the first few layers of palladium are permeated, there is a fixed quantity of hydrogen that can absorb into the palladium. This theory was investigated using Brunauer-Emmett-Teller (BET) theory[7] to find the percent surface area of palladium covered by hydrogen at different temperatures. The equation used is as follows:

$$PSAC = 100 \times \frac{\Delta p * V_f * \left(3.53 * 10^{16} \frac{particles}{cc-torr}\right) * \left(\frac{273K}{T_K}\right) (2r_H)^2}{\left(\frac{SA}{g}\right) * (m_{Pd})} \quad (5)$$

where "PSAC" stands for Percent Surface Area Covered, and "Δp" is the change in pressure calculated by finding the difference in pressure between a selected low-temperature isotherm point (the yellow diamond points in figure 8) and the pressure value of the pink horizonal reference line from figure 8 that shows where the high and low temperature van 't Hoff lines intersect. This difference in pressure is a result of hydrogen adsorbing onto the surface instead of forming a hydride. Hydrogen that enters the system will form a hydride until the system reaches the critical point (1/T~4.25x10^{-3} in figure 8), at which point new hydrogen added to the system will begin to adsorb onto the surface or form a hydride within the first few layers, which results in this pressure difference. "V_f" represents the free volume of the system, estimated to be 22.1 cc. "(3.53*10^{16} particles/(cc-torr))" is the number of particles per cc-torr at 273K, a constant found using equation 6 below. "T_K" is the temperature in Kelvin. In the numerator, "r_H" is the Van der Waals radius of the hydrogen atom. Thus, "$(2r_H)^2$" represents the area associated with a hydrogen atom. "(SA/g)" represents the surface area per gram rating of the palladium sponge used, and "(m_{Pd})" represents the total amount of palladium used, in grams.

The value "(3.53*10^{16} particles/(torr-cc))" was found using the following equation:

$$\frac{(6.02*10^{23}\frac{particles}{mol})}{(22.414\frac{L}{mol})(1000\frac{cc-atm}{L})(760\frac{cc-torr}{cc-atm})} = 3.53 * 10^{16}\ \frac{particles}{cc-torr} \quad (6)$$

This equation takes the number of particles per mol, "(6.02*10^{23} particles/mol)," and converts it to particles per liter using the conversion rate of "22.414 L/mol." Next, the liters are converted to cc-atm using the conversion rate of "1000 cc-atm/L." Then, this value of particles per cc-atm is converted to particles per cc-torr using the conversion rate of "760 cc-torr/cc-atm," which is used in this case because our pressures are measured in torr, not atmospheres. This leaves us with the number of particles per cc-torr, which we can use in equation (5) to find the percent surface area covered.

The entire numerator of equation (5) computes the amount of surface area covered by hydrogen at that temperature, while the entire denominator computes the surface area available. Dividing the amount of surface area covered by the total surface area available and multiplying by 100 gives the percent surface area covered.

The expected percent surface area covered at the four low temperature isotherm points shown in figure 8 is shown on figure 9. The surface coverage was found to be much less than 1%, varying from 0.01% to 0.1% in the range of temperatures studied.

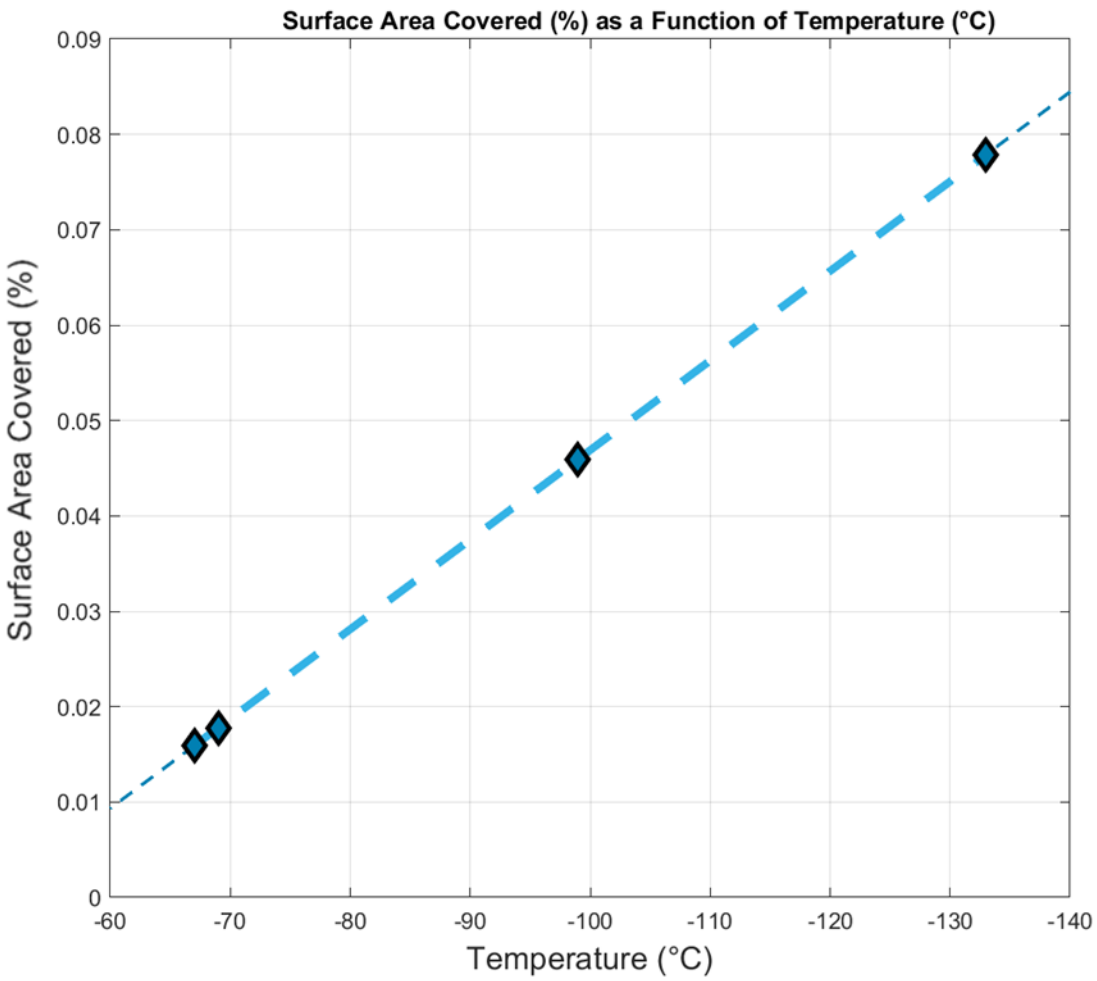

Figure 9: Percent surface area covered as a function of temperature

The four points represented by blue diamonds correspond to the temperatures of the four low temperature isotherm points in figure 8. The light blue dashed line represents the line of best fit for these data points. The thinner dark blue dashed line represents this line of best fit extrapolated outside of the domain of data.

This data set does not include the low temperature isotherm point that lies at the intersection of the high and low temperature van 't Hoff lines shown on figure 8, as this is the point at which it is theorized that the process of adsorption begins, and therefore there would be no adsorbing species. All of the hydrogen will absorb and form a hydride at this temperature. It also omits the -120°C isotherm from figure 7 that was collected with substantial error. The calculated low surface coverages indicate that the surface has more than enough space to accommodate the measured quantities of hydrogen taken up by the bed.

In the future, isotherms of mixed isotopic composition (hydrogen and deuterium) will be collected at varying hydrogen to deuterium ratios. Data for deuterium isotherms was collected [2] and a van 't Hoff line created for the deuterium palladium system. The deuterium and hydrogen van 't Hoff lines are shown together in figure 10.

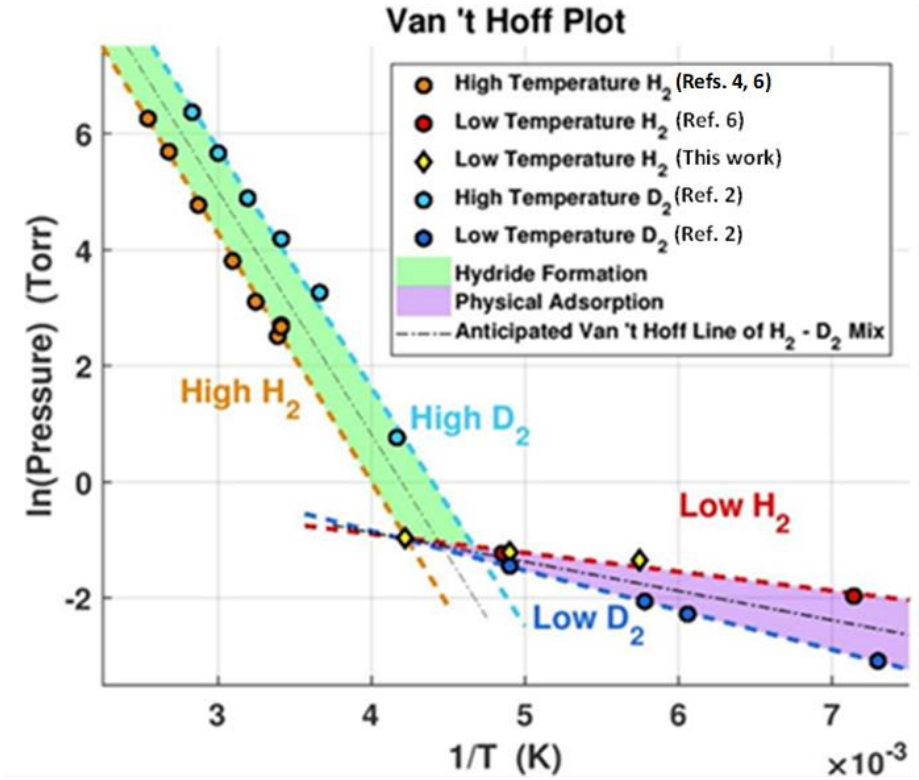

Figure 10: Hydrogen and deuterium van 't Hoff plot

The red, orange and yellow data points and van 't Hoff lines are the same as those in figure 8 and represent the isotherms and van 't Hoff lines collected for hydrogen. The light blue points represent high temperature deuterium isotherms, and the light blue line is the van 't Hoff line for these points. The dark blue points represent low temperature deuterium isotherms, and the dark blue line is the van 't Hoff line for these points. The shaded regions represent the regions between the hydrogen and deuterium van 't Hoff lines, with green representing the high temperature region and purple the low temperature region.

The low temperature deuterium isotherms follow a different trend than the high temperature deuterium isotherms, similar to the shift in trends between high and low temperature hydrogen. This again suggests a shift in interaction between deuterium and palladium at low temperatures.

The shaded regions between the deuterium and hydrogen lines represent the expected locations of the mixed isotopic composition van ‘t Hoff lines. A perfect 50/50 ratio of hydrogen to deuterium is expected to fall on the dashed black line shown in the shaded regions.

7. Conclusions:

The formation of palladium hydride has been well studied at temperatures above 0°C. This work has obtained new data for low temperatures from -120°C to -36°C that have not been studied previously. The new data show a trend that deviates from the higher temperatures. Two separate van ‘t Hoff lines can be created from the high and low temperature data, with an intersection at about -36°C. This deviation suggests a shift in the interactions between hydrogen and palladium at lower temperatures. This different interaction was theorized to be physical adsorption onto the surface of the palladium. This is consistent with the low percent surface area coverage, obtained using BET theory.

A higher amount of hydrogen can be stored at lower temperatures. By forming palladium hydride at a low temperature and then subsequently heating it to a set temperature, large hydrogen pressures can be generated. This could be highly beneficial to LLE for loading precise amounts of fuel into cryogenic targets.

In the future, isotherms of mixed isotopic composition using hydrogen and deuterium will be collected. These are expected to behave similarly to the hydrogen and deuterium isotherms. A mixed isotope van ‘t Hoff line is expected to fall between the hydrogen and deuterium van ‘t Hoff lines.

8. Acknowledgements:

The opportunity to conduct research at LLE was made possible by Dr. Stephen Craxton and Jean Steve, who I thank immensely for organizing the University of Rochester's Laboratory for Laser Energetics High School Summer Research Program. The things I have learned and people I have met are all thanks to you two. I would also like to extend my thanks to Dr. Walter T. Shmayda and Dr. Matt Sharpe, who guided me through my project and taught me everything I learned. I am so incredibly grateful to both of you for your patience with and dedication to me and my learning, and I hope the data I collected helps move the work forward! I would also like to thank the other members of the high school summer program, Adam Mroueh, Will Wang, Jude Kukla, Simon Narang, Michele Lin, George Morcos, Henry Berger, Anthony Mazzacane, Max Neiderbach, Adelyn Carney, Ji-Mi Jang, Ka-Hyun Nam, and Hanna Wiandt. You all made this summer the most memorable one of my entire life. My final thanks are extended to my physics teacher, Ms. Robinson, for introducing me to this amazing opportunity. I wouldn't have and couldn't have done it without you!

9. References:

1) Gillespie, Louis. "The Palladium-Hydrogen Equilibrium and New Palladium Hydrides." J. Am. Chem. Soc. **58**, 2565 (1936).

2) Gillespie, Louis. "The Palladium-Deuterium Equilibrium." J. Am. Chem. Soc. **61**, 2496 (1939).

3) Lasser, R. & Klatt, K.-H. "Solubility of Hydrogen Isotopes in Palladium." Phys. Rev. B **28**, 748 (1983).

4) Glance, Katherine. "Measuring Isotherms of the Hydrogen-Palladium System." Laboratory for Laser Energetics High School Research Program Project Report (2018).

5) Cross, Griffin. "Study of the Hydrogen Palladium System." Laboratory for Laser Energetics High School Research Program Project Report (2017).

6) Sharpe, Matthew & Shmayda, Walter. Unpublished.

7) Brunauer, S., Emmett, P.H., and Teller, E. "Adsorption of Gases in Multimolecular Layers." J. Am. Chem. Soc. **60**, 309 (1938).

Development of a Beam Configuration for the SG4 Laser to Support both Direct and Indirect Drive

William Wang

Pittsford Sutherland High School

Pittsford, NY

Advisor: Dr. R. Stephen Craxton

Laboratory for Laser Energetics

University of Rochester

Rochester, NY

August 2020

Abstract

Recent papers (e.g., K. Lan et al. Phys. Plasmas 21, 010704 (2014)) have proposed "octahedral," or six-hole, hohlraums for the planned SG4 laser. Octahedral hohlraums aim to increase indirect drive uniformity on the capsule (compared with the cylindrical hohlraums currently used on the National Ignition Facility). The SG4 target chamber uses 48 quads (each quad is a group of 4 laser beams) to drive the octahedral hohlraum with 8 quads/hole. This work proposes an amended target chamber that will provide the option of direct drive along with indirect drive. A view-factor program, *LORE*, has been created for the purpose of calculating the capsule nonuniformity for indirect drive. *LORE* simulations have confirmed the results obtained by Lan et al. for octahedral hohlraums and predict a nonuniformity ranging from 0.44% at early times (when the capsule is irradiated primarily by x rays from the laser spots) to 0.11% at later times (when the heated hohlraum wall dominates). The beam pointings for direct drive have been optimized using the 2-D hydrodynamics simulation code *SAGE* such that an RMS nonuniformity of $\sim 1\%$ in the deposited laser energy can be achieved while beams are repointed by no more than 9°. Further improvements to the uniformity are expected with additional optimization. Experiments on the 60-beam OMEGA laser using a seven-hole hohlraum are proposed as a platform for studying uniformity in spherical hohlraums.

I Introduction

An important criterion for achieving ignition and gain through inertial confinement fusion (ICF) is obtaining high levels of uniformity on a spherical capsule [1]. The capsule contains two isotopes of hydrogen, deuterium and tritium, as fuel, which are held inside a shell typically made of plastic or glass. As the capsule shell heats to high temperatures, it turns to plasma, both ablating outwards and compressing inwards. This process compresses the fuel to high temperatures and densities, allowing the strong nuclear force to overcome the electrostatic force between the positively charged nuclei, and the deuterium and tritium fuse into a helium nucleus and release large amounts of energy, mostly in the form of energetic neutrons.

The two current approaches to laser-driven ICF are known as direct and indirect drive (Fig. 1). In direct drive, laser beams are pointed at the fuel capsule, and the capsule is directly irradiated by the beams. During indirect drive, the fuel capsule is placed inside of a case, known as a hohlraum, which is made of a high-Z material (typically gold). The laser beams enter the hohlraum through laser entrance holes (LEH's) and rather than directly irradiating the capsule, the beams deposit energy onto the hohlraum wall. The hohlraum wall then emits x rays, which irradiate the capsule and heat other parts of the hohlraum wall. Indirect drive is therefore less sensitive to small-scale nonuniformities on the laser beams, which are caused by imperfections in the laser beams. Indirect drive, however, is less energy efficient since only a small fraction of the laser power (often 10 to 20%) is absorbed by the capsule.

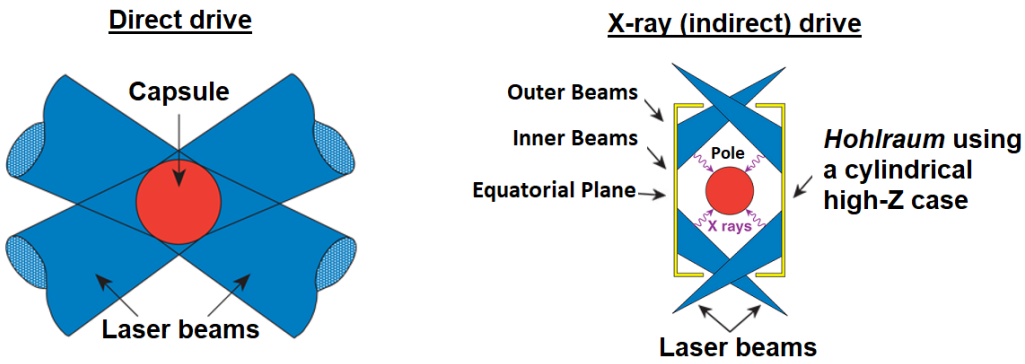

Figure 1: *The difference between the two main approaches to ICF, direct and indirect drive. The drawing on the right is a cross-section of a cylindrical hohlraum*

The cylindrical hohlraum is currently used at the National Ignition Facility (NIF) [2] at the Lawrence Livermore National Laboratory, which is the current largest ICF facility and is intended primarily for indirect drive. One potential flaw with this hohlraum design is that the fuel capsule implodes nonuniformly. At earlier phases of the implosions, the majority of the drive on the capsule is from the deposited laser energy spots. At later times, the majority of the drive is due to the heated hohlraum wall. During the implosion, material ablates from the hohlraum wall, and it becomes difficult for the inner beams to reach the equator of the hohlraum, reducing drive on the equatorial region of the capsule. The cylindrical hohlraum, however, can be "tuned," in which the specific pointings of the beams can be adjusted prior to the experiment, and/or the powers of the beams can be varied during the pulse (e.g., a laser pulse shape in which the powers of the inner beams are increased at later times) such that a greater uniformity can be achieved. However, tuning the beam powers to achieve uniform implosions is challenging to accomplish.

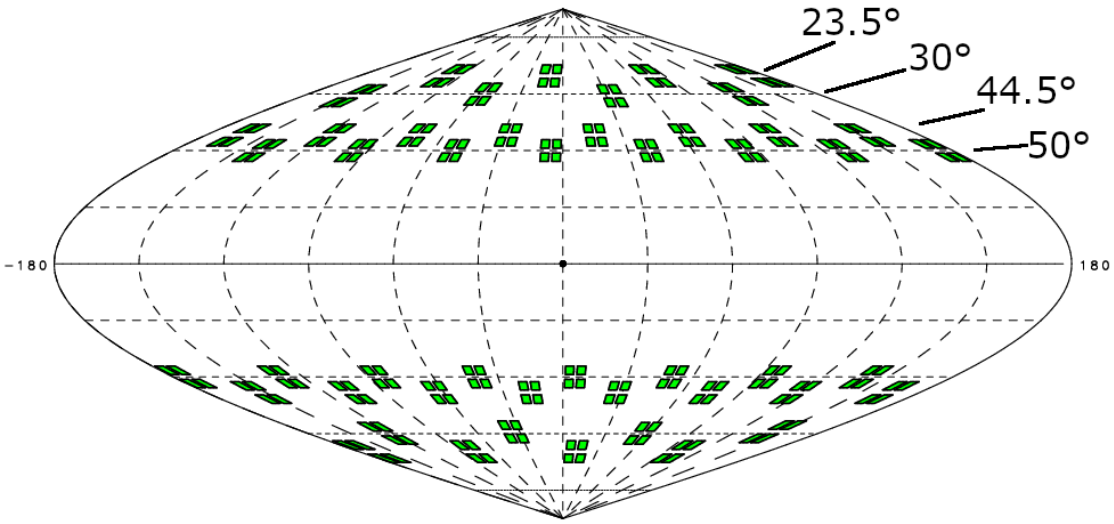

Figure 2: *Location of laser beam ports on the NIF target chamber*

In addition, direct drive is not a practical option with the current NIF target chamber design since the NIF beam ports are designed to perform predominantly indirect drive experiments with the cylindrical hohlraum. Figure 2 depicts the beam ports on the NIF, which are arranged in four rings at angles of 23.5°, 30.0°, 44.5°, and 50.0° from the vertical, and similarly for the lower hemisphere. The NIF contains 48 quads, which are groups of four beams. If the NIF beams are

pointed at normal incidence to the fuel capsule for direct drive experiments, the poles of the capsule are overdriven as compared to the equatorial region. To perform direct drive experiments on the NIF, beams must be repointed towards the equator of the target. Some beams are repointed as much as 35° (from 50° to 85°) [3, 4], which can cause undesired levels of nonuniformity since beams that are repointed by a large angle may "miss" the target as the capsule compresses (energy in the beam refracts around the edge of the capsule without being significantly absorbed). The NIF target chamber is therefore not suited to provide uniform implosions during direct drive.

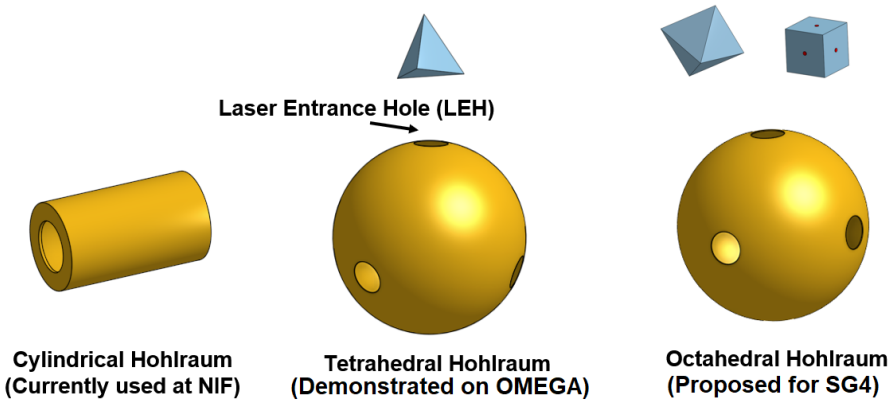

Figure 3: *Shown from left to right: Cylindrical, Tetrahedral, Octahedral Hohlraums*

The tetrahedral hohlraum was proposed to provide better uniformity for indirect drive [5, 6, 7]. As shown in Fig. 3 (middle), the tetrahedral hohlraum has four laser entrance holes located corresponding to the vertices of a tetrahedron. The tetrahedral hohlraum has been tested on the 60-beam OMEGA laser and has been shown to provide high levels of uniformity [8, 9].

Recently, octahedral hohlraums have been proposed as a more uniform alternative to the cylindrical hohlraum [10, 11, 12]. As shown in Fig. 3 (right), the octahedral hohlraum has six laser entrance holes corresponding to the centers of cube faces or the vertices of an octahedron. Due to the better geometric symmetry, the octahedral hohlraums should provide higher levels of uniformity during indirect drive as compared to the cylindrical and tetrahedral hohlraums. The NIF, however, does not match the cubic symmetry of the hohlraum and is not suited to drive it.

The SG4 Laser [13] is currently a concept in China and is planned to be a NIF-sized system (also with 48 quads) intended to drive the octahedral hohlraum. This work proposes amendments to the current SG4 target chamber design so that the SG4 laser can be used for direct drive in addition

to indirect drive. Minor modifications are made to the current design to allow for high levels of uniformity when driving the octahedral hohlraum along with good levels of uniformity for direct drive. A new 3-D view-factor code, *LORE*, was created to model the capsule uniformity during indirect drive using spherical hohlraums. *LORE* predicts that the proposed target chamber achieves similar levels of uniformity as compared to the current design. In addition, the 2-D hydrodynamics code *SAGE* was used to find beam pointings which would produce good direct drive uniformity.

The Appendix proposes a hohlraum with 7 LEH's for experiments on the 60-beam OMEGA laser to study uniformity in spherical hohlraums. Five LEH's are arranged on the equator based on the vertices of a pentagon with 2 LEH's on the poles.

II Amended Design of SG4 Target Chamber

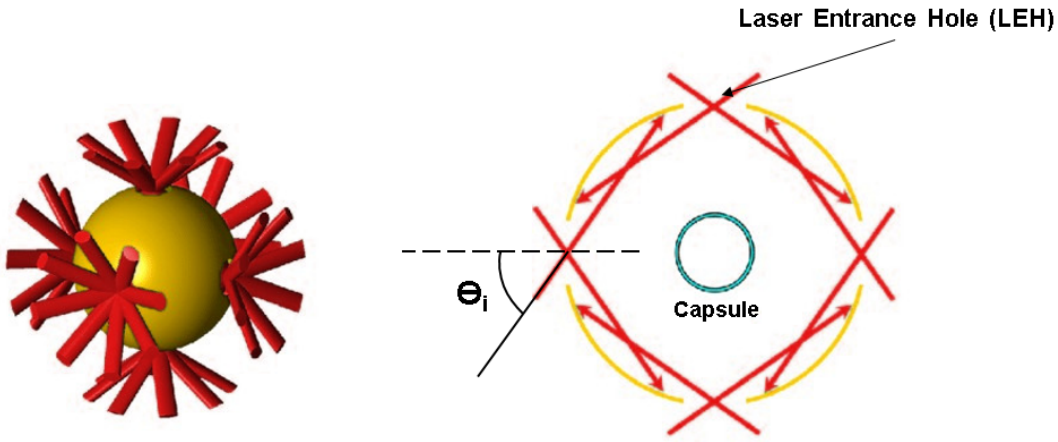

Figure 4: *3-D view of incident beams (left) and 2-D cross section of incident beams (right). From Ref. 10*

The beam arrangement envisaged for the SG4 laser to drive the octahedral hohlraum is shown in Fig. 4. Beams must enter this hohlraum at acceptable angles. Ideally, the angle of incidence θ_i ranges from 50° to 60° [10]. Beams entering at angles less than 50° have the risk of leaving through another LEH, crossing with other beams, or depositing energy onto the capsule. On the other hand, if the angle of incidence is greater than 60°, the beam may come too close to the edge of an LEH and ablate the gold [10]. This can cause unwanted plasma physics in which the beam

deposits its energy into the plasma rather than the hohlraum wall.

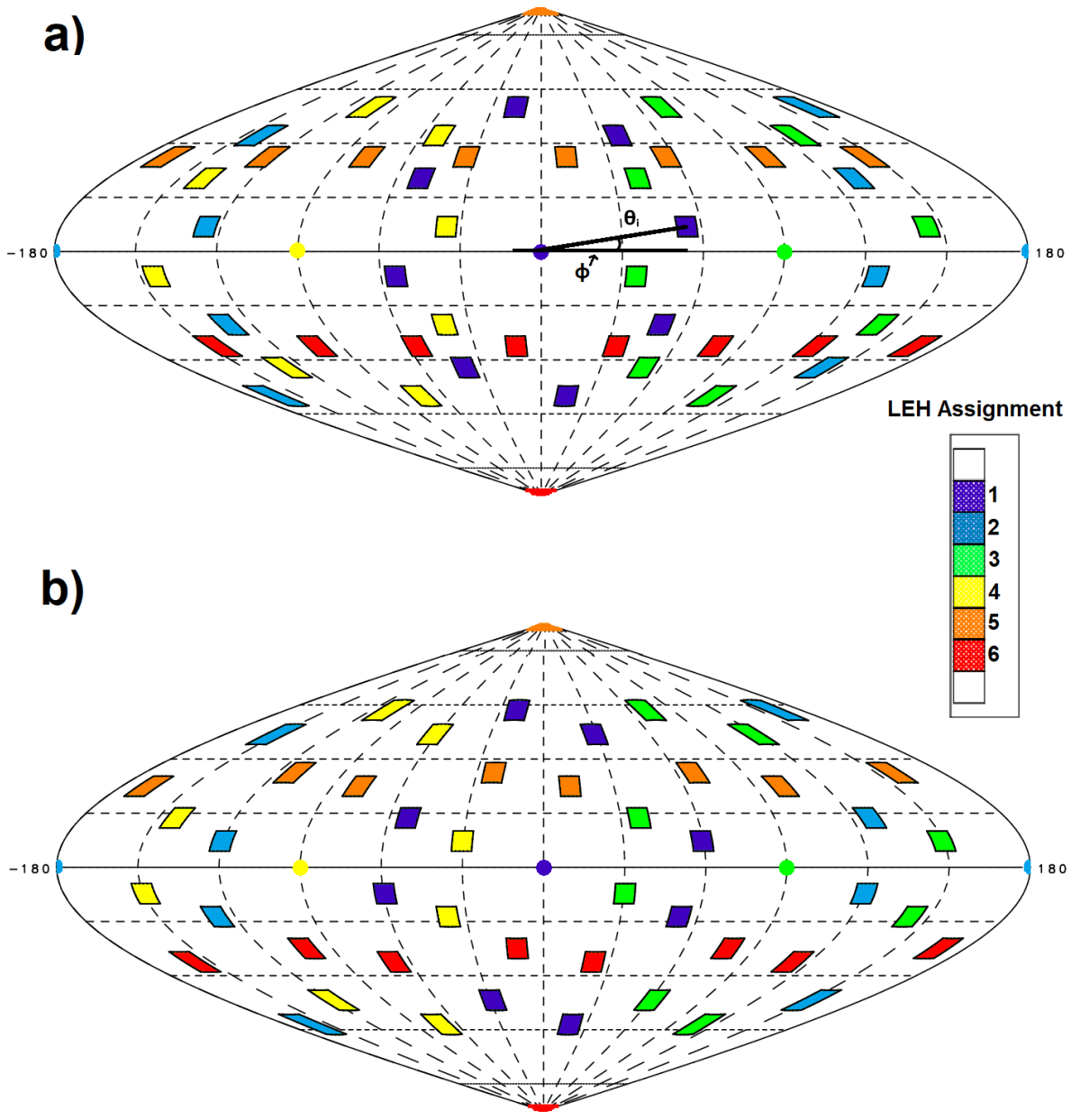

Figure 5: *Location of beam ports on the current target chamber (a) and the amended/proposed target chamber (b). The colored circles indicate the locations of the hohlraum LEH's (not drawn to scale)*

Figure 5 shows the location of beam ports on both the current and proposed target chambers. The colors of the beam ports correspond to the LEH through which the beam enters, with locations

indicated by the colored circles (4 LEH's around the equator and 2 on the poles). The laser ports are configured in such a way that there are eight laser ports assigned to each LEH of the octahedral hohlraum (8 quads x 6 holes = 48 quads). Ports are placed on a "ring" which is θ_i degrees from the LEH, and ϕ denotes the angle of the beam on the ring. The current design, as shown in Fig. 5(a), sends all beams at an angle θ_i of 55° and uses 11.25° for ϕ to avoid overlapping laser spots [10, 11]. Although this target chamber is optimal for indirect drive with the octahedral hohlraum, the "clustering" of beam ports translates to an overall lower uniformity during direct drive. However, this design can be amended to be better suited for direct drive.

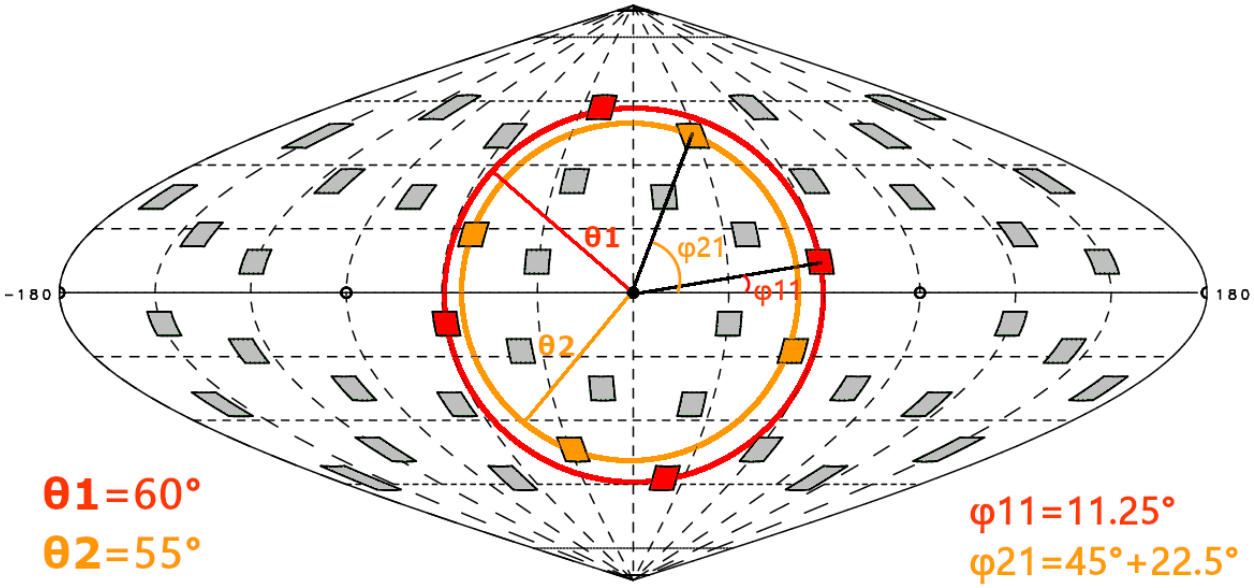

Figure 6: *Locations of odd beams (red) and even beams (orange) assigned to one LEH in the proposed design. The four beams of each group are spaced* 90° *in* ϕ

In the proposed design, as shown in Fig. 5(b) and Fig. 6, the θ and ϕ values for "odd" ports differ from the "even" ports in the group of eight. The odd half of the beams are sent at an angle of 60°, and the even half at an angle of 55°. The proposed chamber is still capable of driving the octahedral hohlraum as all the incident angles are within the acceptable range.

The odd ports are placed on a "ring" in which θ_1 is 60° from the center of the LEH (see Fig. 6). The ϕ values of the odd ports, ϕ_{1n}, are defined by:

$$\phi_{1n} = 11.25^\circ + 90.0^\circ * (n-1),\ n = 1-4 \tag{1}$$

Each even port is placed on a ring with a θ_2 value of 55° from the center of the LEH and the ϕ values are defined by:

$$\phi_{2n} = 45^\circ + 22.5^\circ + 90.0^\circ * (n-1),\ n = 1-4 \tag{2}$$

The laser ports on the proposed design are more evenly dispersed as compared with the current design, in which many beams are clustered together. This allows the amended chamber to provide good levels of uniformity during direct drive implosions, as later shown in Section V. The uneven spacing around the circles (the difference between 11.25° and 22.5°) is also to avoid ports associated with different LEH's from interfering.

III 3-D View-Factor Code *LORE*

The 3-D view-factor code *LORE* evaluates the capsule uniformity during indirect drive with a spherical hohlraum. *LORE* uses the same physics as is included in the code *Buttercup*, described in Ref. 6. *Buttercup* handles cylindrical and tetrahedral hohlraums, whereas *LORE* handles spherical hohlraums with any number of LEH's. While the description of *LORE* given here is focused on the octahedral hohlraum, the code can handle an arbitrary number of holes and beam ports.

III.1 Ray Trace Beams

LORE begins raytracing beams in the center of the entered LEH. The user specifies the LEH radius (r_{LEH}) and the beam cross sectional shape in the plane of the LEH (either circular or elliptical). The user also inputs the radius of the beam, r_o, which is typically $\frac{1}{2}r_{LEH}$. The beam cross section is then converted into a 2-D grid (shown in Fig. 7) of one million individual rays, each parallel to the beam direction and containing its own power.

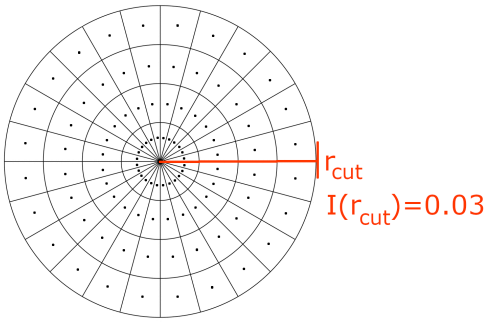

Figure 7: *2-D (r, θ_{ray}) grid of a circular beam cross section. Each grid cell contains one ray. Black circles indicate starting locations of rays. r_{cut} is the maximum distance r that rays are defined*

The power of each ray is determined by the area of its grid cell and the beam's intensity, $I(r)$, which is based on the distance r from the beam center and is assumed to be given by:

$$I(r) = I_o e^{-(\frac{r}{r_o})^n} \tag{3}$$

The constant, I_o, is determined from the total power in the beam such that the sum of all the ray powers equals the power of the beam. All the ray powers in all beams add up to P_{las}, the total

power of the laser. Rays are first defined in (r, θ_{ray}) coordinates, but are later translated to Cartesian coordinates. r_o is the distance from the center to the $\frac{1}{e}$ intensity contour of the circular/elliptical cross section (for elliptical cross sections, r_o is based on the specific ray's angle of rotation θ_{ray}). The parameter, n, is taken to be around 8-12. A higher value for n signifies a greater "drop-off" in intensity for rays near the edge of the beam. In Fig. 7, r_{cut} is the maximum value of r for which rays are defined, and typically occurs when $e^{-(\frac{r}{r_o})^n} = 0.03$ (a "cutoff" value).

Using vector equations, *LORE* then finds the intersection of each ray with the hohlraum wall. At that intersection, *LORE* calculates the fraction of energy deposited, $A(\theta)$, with θ being the angle of incidence on the hohlraum wall. An assumption can be made that $A(\theta) = 1$ (beams deposit all their energy at the first intersection) as large hohlraums have shown high levels of absorption [1]. *LORE* can, however, include a bounce, in which the fraction of energy deposited is based on the formula:

$$A(\theta) = 1 - \exp(-b * \cos^r(\theta)) \tag{4}$$

As in Ref. 7, the parameters b and r are taken to be 3 and 1, respectively. Thus, the absorption of one intersection is around 80% for $\theta_i = [55, 60]^\circ$. After finding the first intersection, the bounce is calculated by reflecting the ray and then determining a second intersection. According to *LORE*, when either the current design or the proposed design is used to drive the octahedral hohlraum, no beam energy is directly deposited onto the capsule, and no energy is lost to the LEH's after two intersections.

LORE defines points on the hohlraum wall according to a cube grid. Each of the six faces of a cube contains 100x100 grid points, each of which defines a direction that corresponds to a location on the hohlraum wall (making 60,000 points on the hohlraum wall). Quantities such as deposited laser energy and effective radiation temperature are defined at each point on the cube grid. After an intersection between a ray and the hohlraum wall is found, the deposited laser energy is distributed amongst the nearest four grid points using bilinear interpolation. (The cube grid was used in Ref. 14 to describe a nonuniform ice layer in a cryogenic ICF capsule and illustrated in Fig. 12 of Ref. 15)

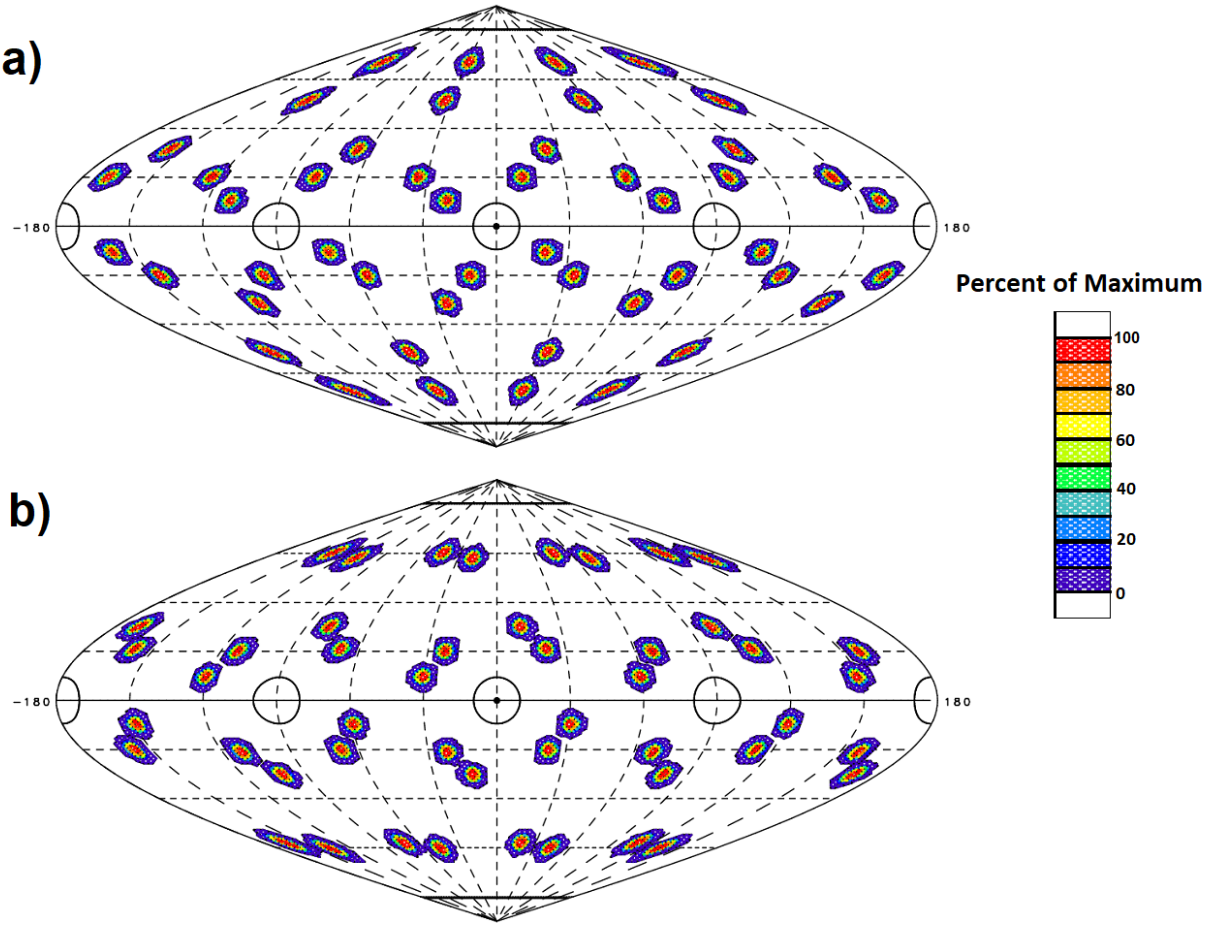

Figure 8: *Deposited laser energy per unit area on an octahedral hohlraum for the current target chamber design (a) and the proposed design (b). The LEH's are indicated with outlines*

Figure 8 depicts the deposited laser energy per unit area on an octahedral hohlraum for just one intersection ($A(\theta) = 1$). In both target chamber designs, there is no overlap of deposited energy. In addition, for both designs, the locations of deposited energy are spread fairly uniformly around the hohlraum wall. Thus, there are only minor differences between the two chamber designs when driving the octahedral hohlraum.

III.2 Determine Effective Radiation Temperature

After tracing all the beams, *LORE* determines a background, or equilibrium radiation temperature T_r by assuming an equilibrium Planckian radiation field in the hohlraum. The temperature T_r is calculated by balancing power entering the radiation field with power lost due to the LEH's and absorption by the hohlraum wall and capsule [Equation (2) of Ref. 6].

$$P_{las}\eta_L = \sigma T_r^4 (NA_h + B_w A_w + B_c A_c) \tag{5}$$

P_{las} is the total absorbed power of the laser (simulations for the proposed design use 410 TW as P_{las}) and A_h, A_w, A_c are the areas of the LEH's, hohlraum wall, and capsule, respectively. σ is the Stefan-Boltzmann constant, so σT_r^4 is the intensity of the background radiation in power/unit area. η_L is the efficiency of the conversion of laser energy to x-ray energy and is taken to be 0.8 [11]. B_w and B_c are the fractions of the background radiation energy absorbed by the hohlraum wall and the capsule, respectively. B_c is taken to be large (0.9). B_w is equal to $1 - \alpha_w$, where α_w is the wall albedo, or the fraction of radiation energy reflected by the hohlraum wall. α_w generally increases as the hohlraum walls heats up. Thus, wall albedo is a time-dependent variable. N is the number of LEH's.

Next, *LORE* calculates the effective radiation temperature T_e at every point on the wall, which is determined by the background radiation that is reflected by the hohlraum wall plus the fraction of absorbed laser power that is converted to radiation at that point (in Eq. (6), I_L is the absorbed laser power per unit area at that point):

$$\sigma T_e^4 = \alpha_w \sigma T_r^4 + \eta_L I_L \tag{6}$$

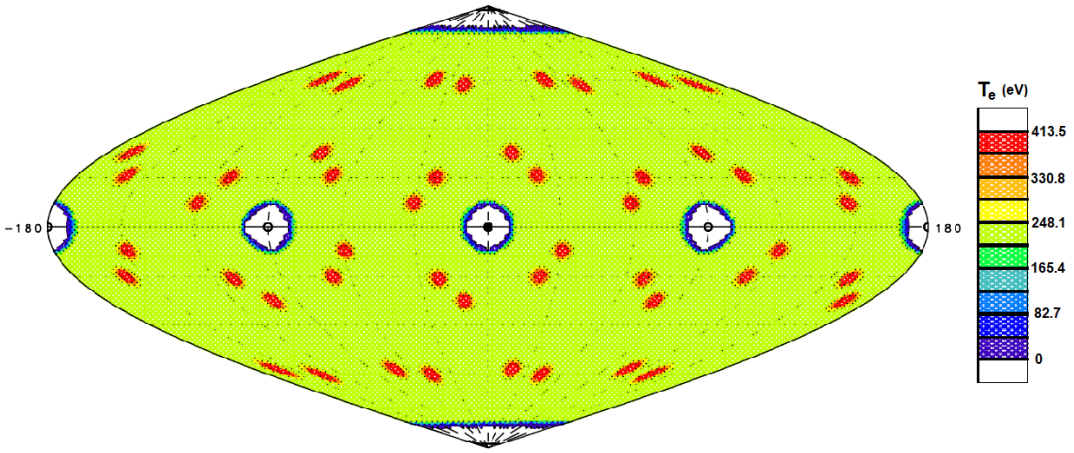

Figure 9: *Contour plot of effective radiation temperature T_e of the hohlraum wall at an albedo α_w of 0.85. $T_r \sim 244$ eV*

Figure 9 depicts the effective radiation temperature at all points on the hohlraum wall for the same parameters as were used for Fig. 8(b). The white circles, which represent LEH's, emit no radiation. It should be noted that the most intense (red) spots correspond to the laser spots on Fig. 8(b) and emit more radiation flux than the rest of the hohlraum wall, but this difference is less substantial at a higher albedo α_w. In addition, the associated area of these spots is only a small fraction of the hohlraum wall.

The parameters used for Fig. 9 are based on the dimensions given in Section IV for a typical octahedral hohlraum and an albedo of 0.85. T_r, the background radiation temperature determined from Eq. (5), is approximately 244 eV. A background radiation temperature of 270 to 300 eV is generally desired for ignition. Ignition occurs when helium nuclei produced by fusion redeposit their energy in the compressed fuel, causing more fusion to occur.

III.3 Integrate Radiation Flux

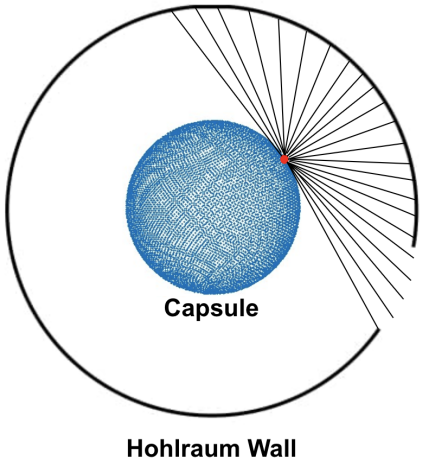

Figure 10: *Schematic of the algorithm used by LORE to determine the radiation flux at each point on the capsule. LORE scans over multiple points on the capsule, looks over a number of directions, and accumulates spectral brightness to determine the radiation flux. [Based on Fig. 4 of Ref. 6]*

After determining the effective radiation temperature at all points on the hohlraum wall, *LORE* scans over multiple points on the capsule. For each point, as indicated in Fig. 10, *LORE* integrates the spectral brightness over various angles of θ (direction altitude) from 0 to $\frac{\pi}{2}$ and ϕ (direction azimuth) from 0 to 2π to determine the radiation intensity at that point:

$$I = \int_0^{\frac{\pi}{2}} \int_0^{2\pi} B(\theta,\phi)\cos(\theta)\sin(\theta)d\phi d\theta \tag{7}$$

The brightness, $B(\theta,\phi)$, is $\sigma T_e^4/\pi$, or the power emitted per unit area per unit solid angle from the hohlraum wall. The $\sin(\theta)$ accounts for the solid angle and the $\cos(\theta)$ considers the angle between the surface element of the capsule and the incoming ray [6]. These integrals typically involve scanning 60,000 points on the capsule and for each point, looking over $\sim$ 100,000 directions.

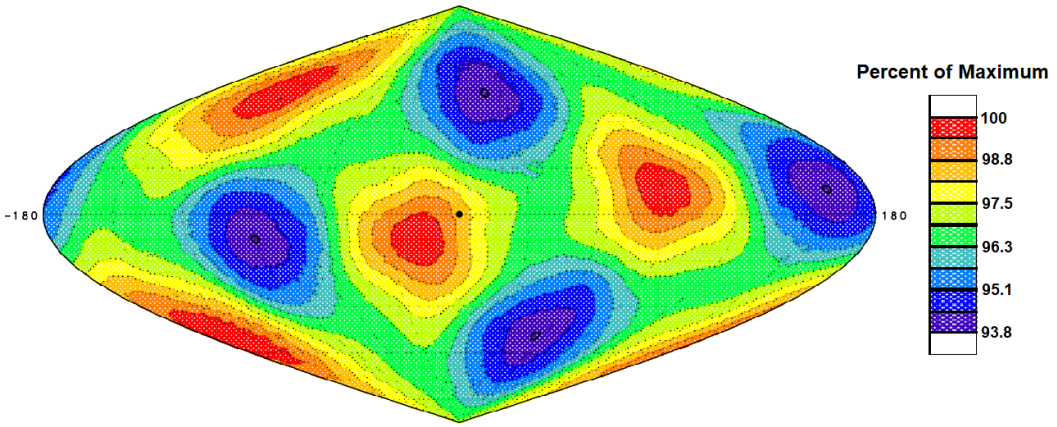

(a) Tetrahedral, Albedo=0.85, RMS $\sim$ 1.44%

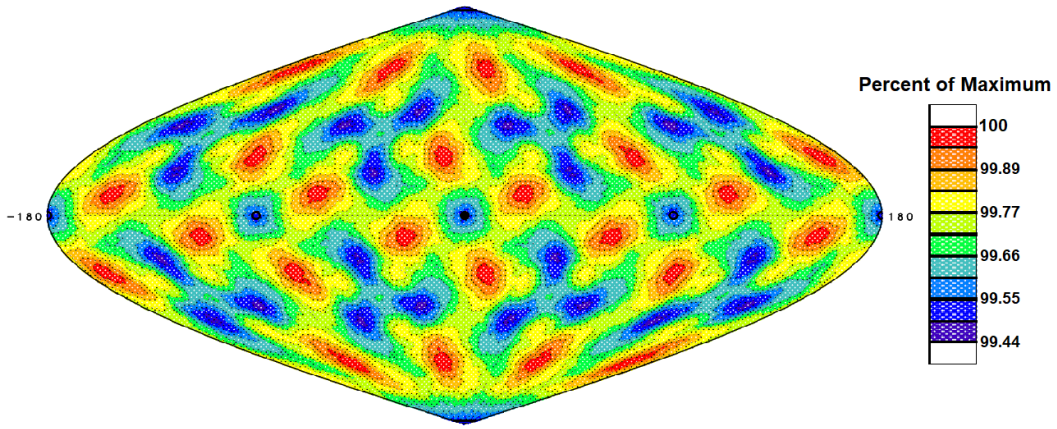

(b) Octahedral, Albedo=0.85, RMS $\sim$ 0.10%

Figure 11: *Capsule uniformity contour plots for tetrahedral (a) and octahedral (b) hohlraums at albedos α_w of 0.85*

Figure 11 depicts the uniformity of radiation flux on the capsule at an albedo α_w of 0.85 produced by *LORE* simulations comparing tetrahedral and octahedral hohlraums. The octahedral hohlraum produces lower levels of nonuniformity than the tetrahedral hohlraum (0.10% compared to 1.44%; note the difference in scales)

The octahedral hohlraum simulation, shown in Fig. 11(b), uses the parameters outlined in Section IV, different from the parameters used in the tetrahedral hohlraum simulation (based on Ref. 7). If the capsule radius, hohlraum radius, and laser pulse were the same as those used in the tetrahedral hohlraum simulation, however, *LORE* predicts that the octahedral hohlraum would provide a nonuniformity rms of 0.15%, still significantly lower than 1.44%.

IV Results from *LORE* for Indirect Drive

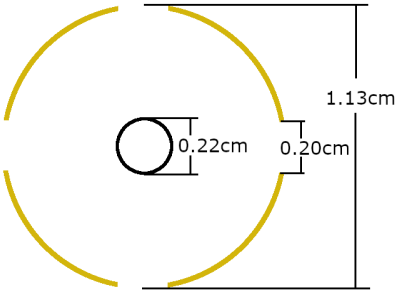

Figure 12: *Dimensions of octahedral hohlraum used in this paper*

Figure 12 depicts the the octahedral hohlraum dimensions used for the *LORE* simulations, unless otherwise noted. These dimensions are based on the "golden" octahedral hohlraum of Ref. 10. $R_{capsule} = 0.11$ cm, $R_{LEH} = 0.1$ cm, $R_{hohlraum} = 0.5654$ cm ($R_{hohlraum}$ is taken to be $5.14 * R_{capsule}$, which is referred to as the "golden ratio" for octahedral hohlraums [12]).

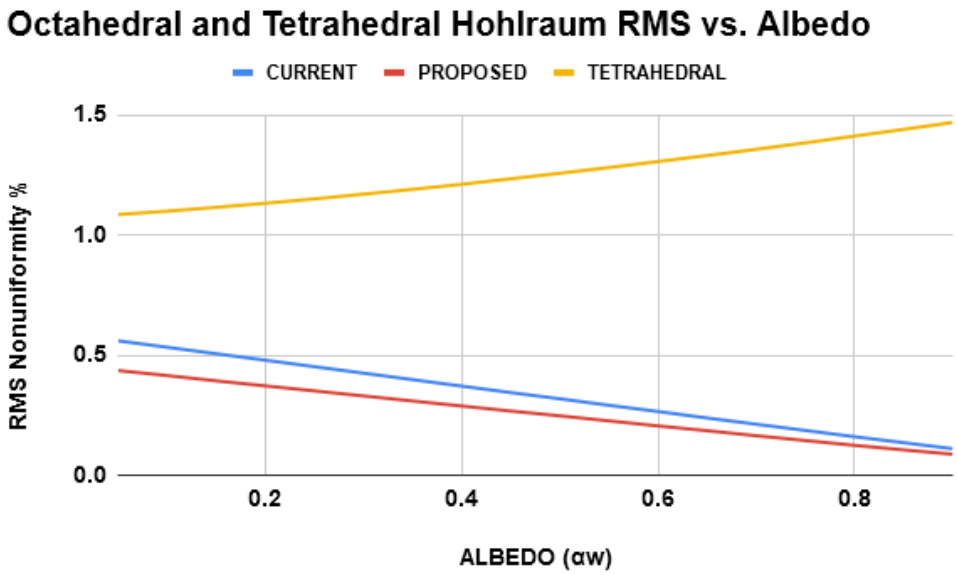

Figure 13: *RMS nonuniformity for octahedral (blue-current, red-proposed) and tetrahedral (yellow) hohlraums for various albedo* α_w

Figure 13 shows a comparison of capsule uniformity between the current and proposed designs for the octahedral hohlraum. The results for the tetrahedral hohlraum are included as a benchmark,

using parameters corresponding to the optimized "Scale 1.2" tetrahedral hohlraum of Fig. 1 of Ref. 7 ($R_{capsule} = 275$ μm, $R_{LEH} = 350$ μm, $R_{hohlraum} = 1400$ μm $= 5.09$*$R_{capsule}$). Different from Ref. 7, the beams are assumed to propagate with parallel rays (as described in Sec. III.1) and pass through the center of each LEH with a circular cross section in the plane of the LEH. Interestingly, the hohlraum-to-capsule ratio used in Ref. 7 is close to the "golden ratio" of Ref. 12.

According to Fig. 13, the octahedral hohlraum provides notably better uniformity than the tetrahedral hohlraum and the x-ray nonuniformity is less than 1% over all values of albedo. At lower albedos, the deposition pattern of the laser spots plays a dominant role in the capsule uniformity. At higher albedos, the majority of the capsule drive is from the heated hohlraum wall, and the uniformity is determined predominantly by the geometric symmetry of the hohlraum. The octahedral/cubic symmetry clearly provides better uniformity than the tetrahedral symmetry.

The proposed design provides higher levels of uniformity than the current design, but only by a slight margin. This is primarily due to the difference in the location of deposited laser energy (Fig. 8). This shows that the proposed target chamber achieves similar results to the current chamber when driving the octahedral hohlraum.

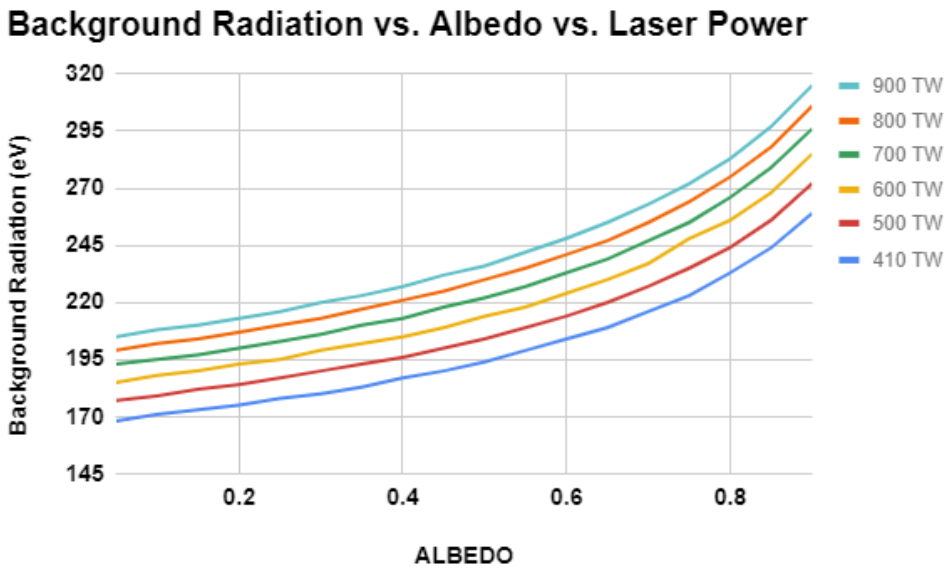

Figure 14: *Background radiation temperature T_r as a function of albedo α_w for various laser powers, for a hohlraum-to-capsule ratio of 5.14*

Figure 14 shows the octahedral hohlraum background radiation temperature T_r as a function of

albedo α_w for multiple laser powers. Since T_r is proportional to the $\frac{1}{4}$th power of the laser power, significant increases in the laser power result in small changes in the background temperature. With the hohlraum-to-capsule radius ratio of 5.14, a large laser power, above the upper limit of the NIF peak power of around 500 terawatts, is required in order to achieve the 270-300 eV required for ignition. A smaller hohlraum radius is therefore desirable to increase the background radiation temperature. Therefore, another topic of interest is how the hohlraum-to-capsule-radius ratio affects the uniformity.

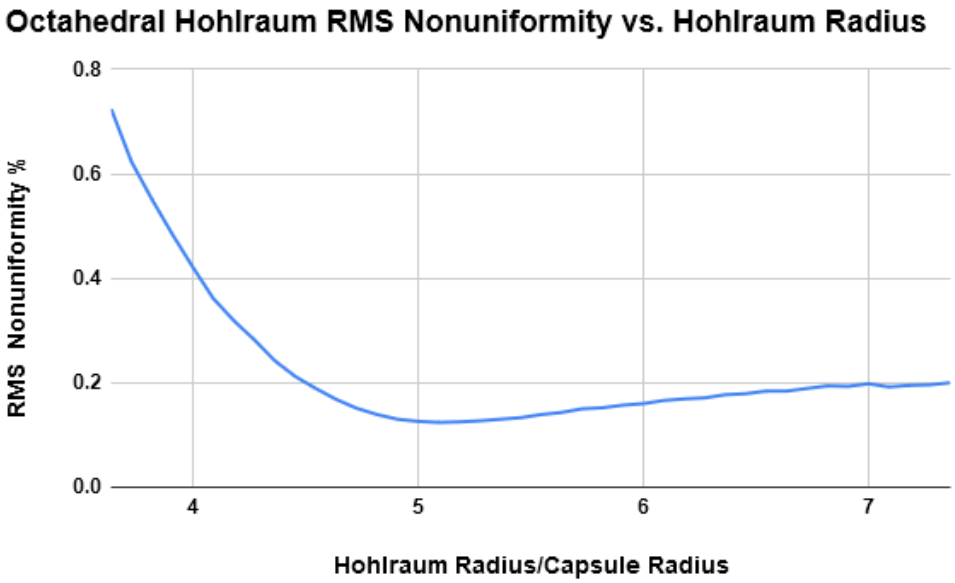

Figure 15: *RMS nonuniformity for octahedral hohlraums as a function of the ratio of hohlraum-to-capsule radius at an albedo α_w of 0.8. The capsule radius (0.11 cm) and LEH radius (0.1 cm) are fixed*

This is illustrated in the *LORE* simulations of Fig. 15. Here the capsule and LEH radius are kept the same, and the hohlraum radius is varied (note the albedo α_w is 0.8, not 0.85). A hohlraum-to-capsule ratio of around 5.1 presents a local minimum of $\sim$0.12% in RMS nonuniformity. This is consistent with the "golden ratio" of 5.14 found in Ref. 12. A smaller ratio will provide a greater background radiation temperature, but at the expense of uniformity, as nonuniformity steeply increases as this ratio decreases.

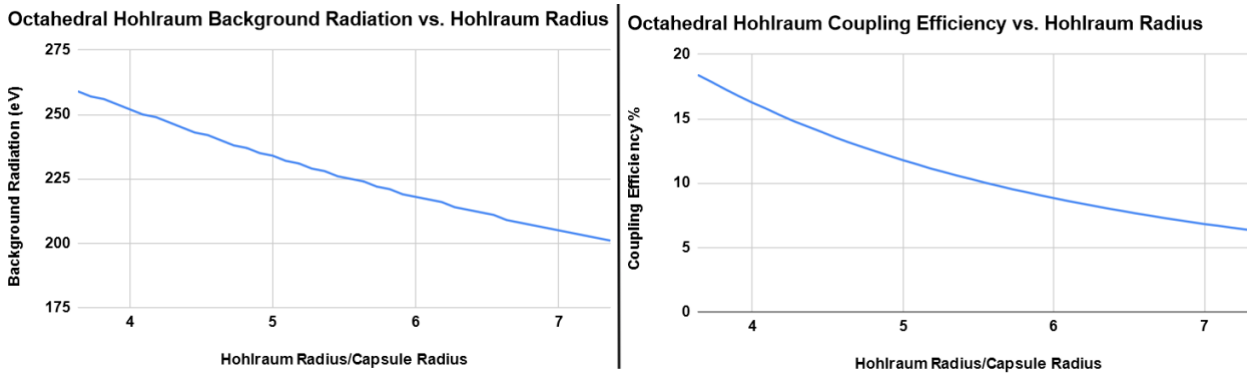

Figure 16: *Background radiation temperature (left) and coupling efficiency (right) for octahedral hohlraums for various values of hohlraum-to-capsule-radius ratio at an albedo of 0.8 and fixed capsule and LEH radii (0.11 cm and 0.1 cm, respectively). The laser power is 410 TW*

As shown in Fig. 16, as the hohlraum radius increases for a fixed capsule radius, the background radiation temperature and the coupling efficiency steadily decrease. The coupling efficiency is the fraction of the incident laser power absorbed on the capsule. These results guide the choice of a hohlraum-to-capsule-radius ratio that will accommodate this tradeoff. Different octahedral hohlraum shapes are being considered to increase the radiation temperature and coupling efficiency [16].

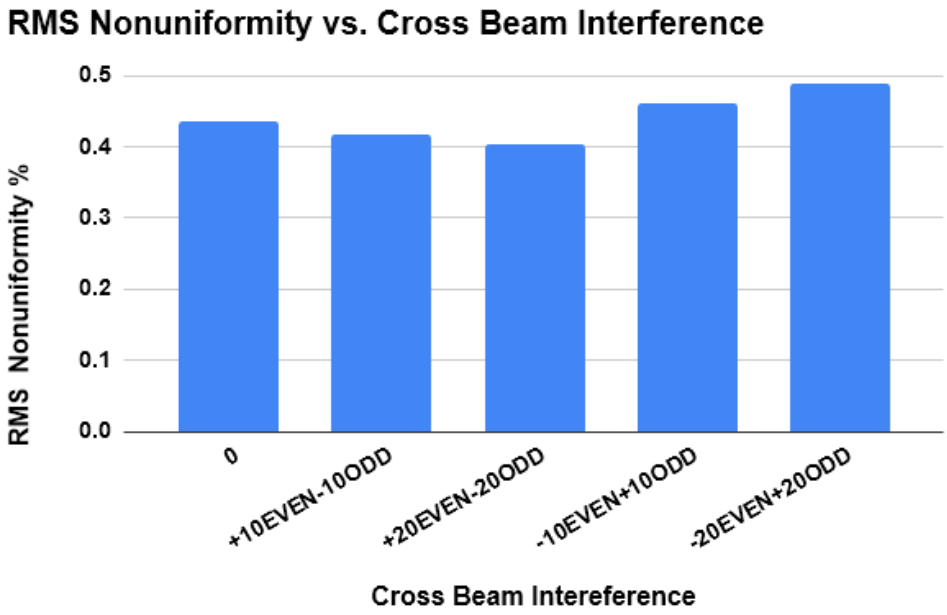

Figure 17: *RMS nonuniformity for an octahedral hohlraum with various scenarios of cross beam energy transfer. (+10EVEN-10ODD signifies a 10% power increase to even beams and -10% in odd beams). Albedo* α_w*=0.05*

Another factor to take into consideration is the effect of cross beam energy transfer (CBET) [17] on the uniformity on the capsule. CBET is the phenomenon in which, when two beams cross, energy from one beam can transfer to the other (this occurs when beams pass through the LEH's). According to Ref. 10, this does not occur when all beams have the same angle of incidence because all beams are essentially equivalent. CBET is unlikely to be significant for the minor differences ($\theta_i = 55^\circ$ vs. $\theta_i = 60^\circ$).

Figure 17 demonstrates this for various hypothetical energy shifts. The fractions of power for the odd (θ_i =60°) and even (θ_i =55°) beams are altered by $\pm$ 10-20%. The albedo used in Fig. 17 is 0.05. At low albedos, the background radiation contributes little to the drive on the capsule and the beam spots are more significant. Thus, an albedo of 0.05 was used as it demonstrates the biggest effect on nonuniformity. Even with drastic changes to the beam powers, however, there are no significant effects on uniformity. At higher albedos, the effect of CBET on uniformity is lessened, as the heated hohlraum wall dominates the drive on the capsule.

V Results from the 2-D Hydrodynamics Code *SAGE* for Direct Drive

As shown from *LORE* simulations, the proposed target chamber is capable of producing similar levels of uniformity for indirect drive of an octahedral hohlraum as compared to the current design (with beams entering at 55°). The main difference between the two designs, however, is that the proposed chamber allows for the option of direct drive experiments.

The following *SAGE* simulations assume a spatial profile given by Eq. (3) with a beam radius r_o of 0.11 cm and a supergaussian index n of 3.0 in the best-focus plane.

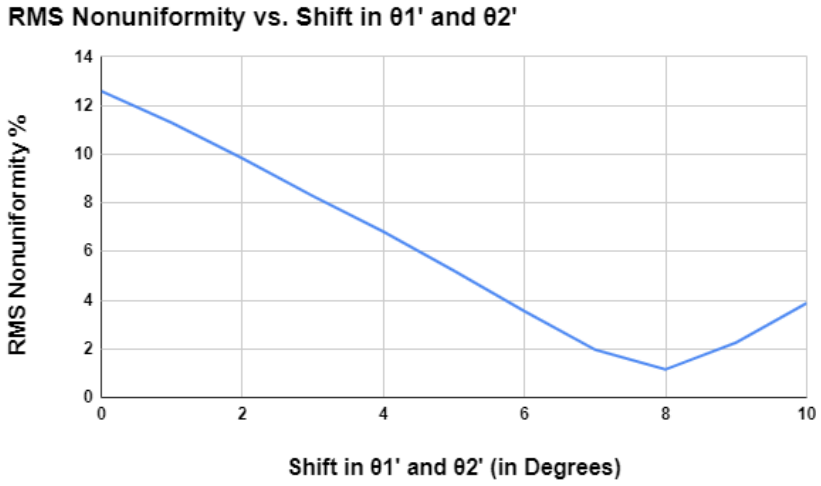

Figure 18: *RMS nonuniformity on the capsule as a function of beam pointing shifts* $\Delta\theta_1$ *and* $\Delta\theta_2$ *(assumed equal here) for direct-drive SAGE simulations using the proposed target chamber design*

Figure 18 depicts the nonuniformity of the cumulative deposited laser energy on the capsule as a function of beam repointing angles based on *SAGE* simulation results. In these runs, the beams are not pointed at normal incidence; instead, they are slightly shifted and aimed towards a different location on the capsule. Each beam is repointed by:

$$\theta_j' = \theta_j + \Delta\theta_j,\ j = [1,2] \tag{8}$$

$$\phi_{jn}' = \phi_{jn} + \Delta\phi_j,\ j = [1,2] \text{ and } n = 1-4 \tag{9}$$

θ_1 (odd) and θ_2 (even) represent the theta value of a laser port with respect to its associated

LEH (60° for odd ports, 55° for even ports). A value of ∼8.0° for both $\Delta\theta_1$ (odd beams) and $\Delta\theta_2$ (even beams) presents a local minimum of around 1.15% RMS nonuniformity. In the series of runs in Fig. 18, the values of ϕ'_{1n} and ϕ'_{2n} are unchanged ($\Delta\phi_1 = \Delta\phi_2 = 0$).

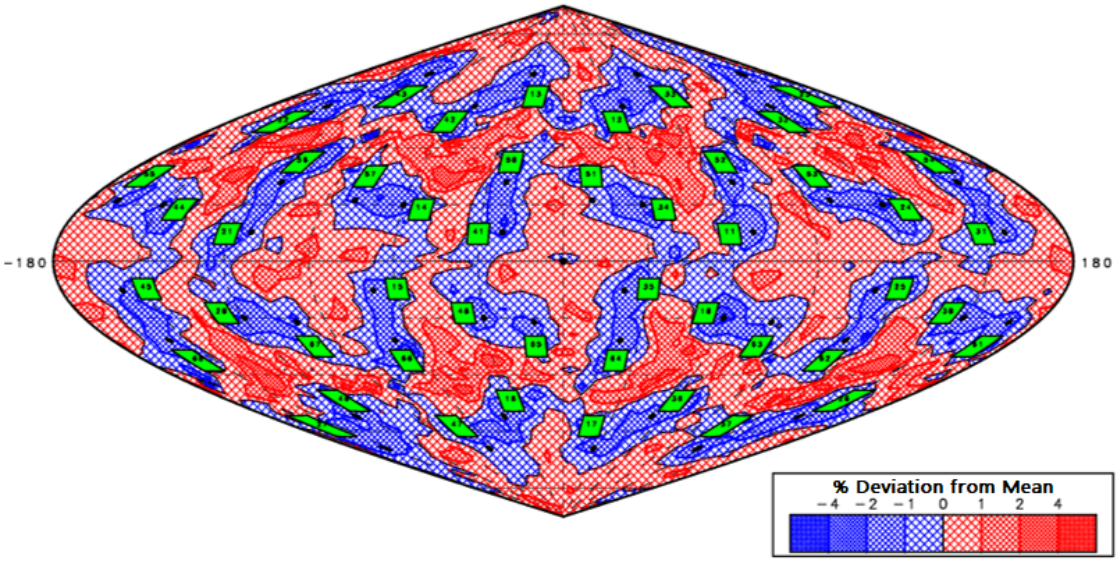

Figure 19: *Target uniformity of deposited laser energy for direct drive using beam repointings optimized for the assumed spatial profile. RMS∼1.06%. Green boxes represent locations of the laser ports, and black dots depict locations on the capsule to which the beams are pointed*

After further optimization of beam repointings including nonzero $\Delta\phi_1$ and $\Delta\phi_2$, Fig. 19 depicts the uniformity of the cumulative deposited laser energy on the capsule. The green boxes represent the locations of the laser ports, and the small black dots (excluding the one in the center) depict the locations on the capsule to which the beams are pointed. For the purpose of testing the performance of the target chamber configuration, each quad is considered to be one beam. Without altering the specific pointings of each of the four beams in a quad, the optimum design shown in Fig. 19 gives a nonuniformity rms of 1.06%.

In Fig. 19, the odd beams are pointed at $\theta'_1 = \theta_1 + 8.5°$, with $\theta_1 = 60°$. The theta values of the even beams are repointed by 7.1°, thus $\theta'_2 = \theta_2 + 7.1°$, with $\theta_2 = 55°$. In addition, the ϕ value of each beam is shifted by -0.2° ($\Delta\phi_1 = \Delta\phi_2 = -0.2°$).

The *SAGE* simulation parameters used in Figs. 18 and 19 are of a 4 mm diameter CH capsule imploded with 1.1 MJ (typical for a NIF experiment). These specifications are comparable to what

would be expected for a direct drive target experiment on the SG4 laser at a comparable energy.

With further optimization, separate repointing of the four beams of a quad, and using a different spatial profile (e.g., with a larger beam radius r_o), a nonuniformity rms of $<1\%$ can be expected. As opposed to the direct drive experiments on the NIF, in which the beams are repointed by as much as 35°, the beams in the proposed design are repointed by less than 9°. The proposed design is therefore well suited for direct drive experiments.

VI Conclusion

This work proposes minor modifications to the current SG4 target chamber design to allow for direct drive in addition to indirect drive. A view-factor code, *LORE*, was built to calculate the capsule uniformity for spherical hohlraums. The proposed target chamber, as shown by *LORE* simulations, is capable of achieving high levels of capsule uniformity when driving the recently proposed octahedral hohlraum. Without making adjustments to the pointings of the different groups of laser beams and without using different laser pulse shapes for different groups of beams, the uniformity for indirect drive ranges from 0.44% at earlier times in the implosion to 0.11% during later stages, both comfortably less than the 1% generally thought to be required. Further, simulation results from the 2-D hydrodynamics code *SAGE* demonstrate that, with slight repointing of the 48 quads, the proposed target chamber can provide good levels of uniformity ($\sim$1%) for direct drive experiments. Further optimization of the 192 beam pointings and spatial profiles can be expected to achieve results of higher uniformity.

Acknowledgements

I must give my sincerest thanks to my advisor and program director, Dr. R. Stephen Craxton, for all of his assistance. Dr. Craxton was always eager and willing to devote countless hours when providing me with help throughout the entire program. I would also like to thank Ms. Jean Steve for helping organize this eight-week high school program. Finally, I would like to thank Eugene Kowaluk for taking incredible pictures throughout the program and my fellow interns for providing a comfortable work environment.

Appendix (7-hole hohlraum)

The recent interest in spherical hohlraums based around octahedral designs has been extended by Ref. 18, which analyzed symmetry properties for values of n, the number of LEH's, up to 12, including a design for $n = 7$ of "a pentagon at the equator with two points at the poles." This Appendix proposes a hohlraum design with 7 holes to be used for experiments on the 60-beam OMEGA laser, which may be used to explore the performance of spherical hohlraums. Simulations of the Scale 1.2 tetrahedral hohlraum experiments carried out on OMEGA predicted low levels of nonuniformity (less than 1% during most of the laser pulse) [7]. Simulations from *LORE* of the 7-hole design predict a nonuniformity ranging from 1.10% at early stages to 0.6% at final stages.

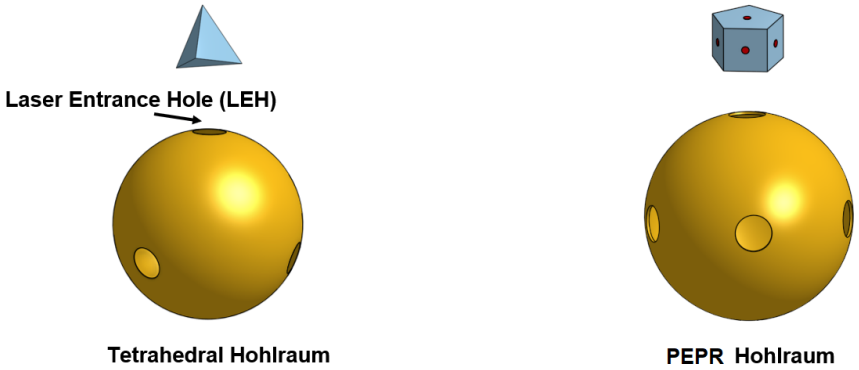

Figure A1: *Shown from left to right: Tetrahedral, PEPR hohlraums*

As shown in Fig. A1 (right), the locations of the LEH's on the 7-hole hohlraum are based on the centers of the faces of a pentagonal prism (this paper will refer to the 7-hole hohlraum as the "*PEPR*" hohlraum).

The following *LORE* simulations of the tetrahedral hohlraum use the same hohlraum dimensions as Section IV (based on Ref. 7) and the parameters of the OMEGA laser. The parameters used for the *PEPR* hohlraum are the same as those used for the tetrahedral hohlraum, except for the number of LEH's and locations of LEH's (the LEH radii are kept the same to avoid laser clearance issues).

LEH	(θ,ϕ)	Beams
1	(90°, 36°)	31, 10, 66, 24, 15, 35, 67, 14, 21, 50
2	(90°, 108°)	11, 13, 65, 32, 47, 18, 42, 23, 57, 62
3	(90°, 180°)	68, 58, 48, 59, 60, 53, 49, 69, 51, 54
4	(90°, 252°)	55, 52, 28, 40, 36, 63, 16, 44, 38, 29
5	(90°, 324°)	26, 20, 33, 41, 27, 37, 34, 43, 39, 12
6	(0°, 0°)	22, 56, 61, 46, 17
7	(180°, 0°)	30, 25, 45, 64, 19

Figure A2: *LEH assignments used in LORE simulations for a PEPR hohlraum. Numbers in the third column indicate OMEGA beam names*

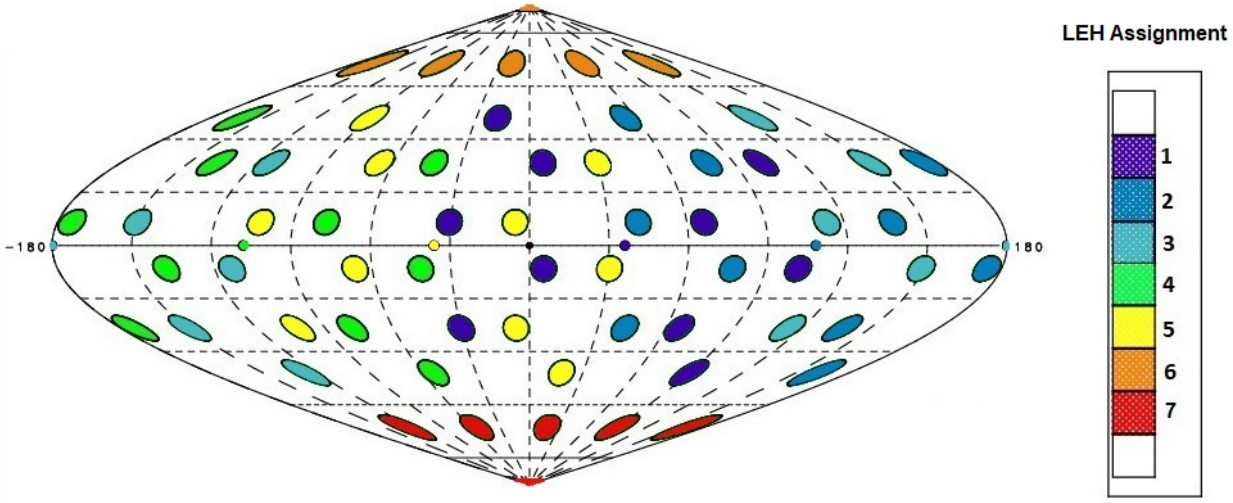

Figure A3: *LEH assignments used in LORE simulations for a PEPR hohlraum. Colors of beam ports represent LEH assignment. The small colored circles indicate the LEH locations*

Figures A2 and A3 depict one viable set of beam assignments of the OMEGA laser for driving the *PEPR* hohlraum. The angle of incidence θ_i ranges from 21.4° (beams sent to the two LEH's on the poles) to 69.7°. For comparison, θ_i ranges from 23.2° to 58.8° for the tetrahedral hohlraum [7].

When driving the tetrahedral hohlraum, each of the 60 beams must be sent through the nearest LEH due to the angle of separation between the 4 LEH's. For the *PEPR* hohlraum, however, there

are options for which LEH each beam may be sent through. As an example, the beam located at (θ=21.4°, ϕ = 54°) may enter either LEH 1 (with θ_i=69.7°) or LEH 6 (with θ_i=21.4°). Therefore, Figs. A2 and A3 are not the only plausible set of beam pointings; additional pointings may be devised for a variety of experiments.

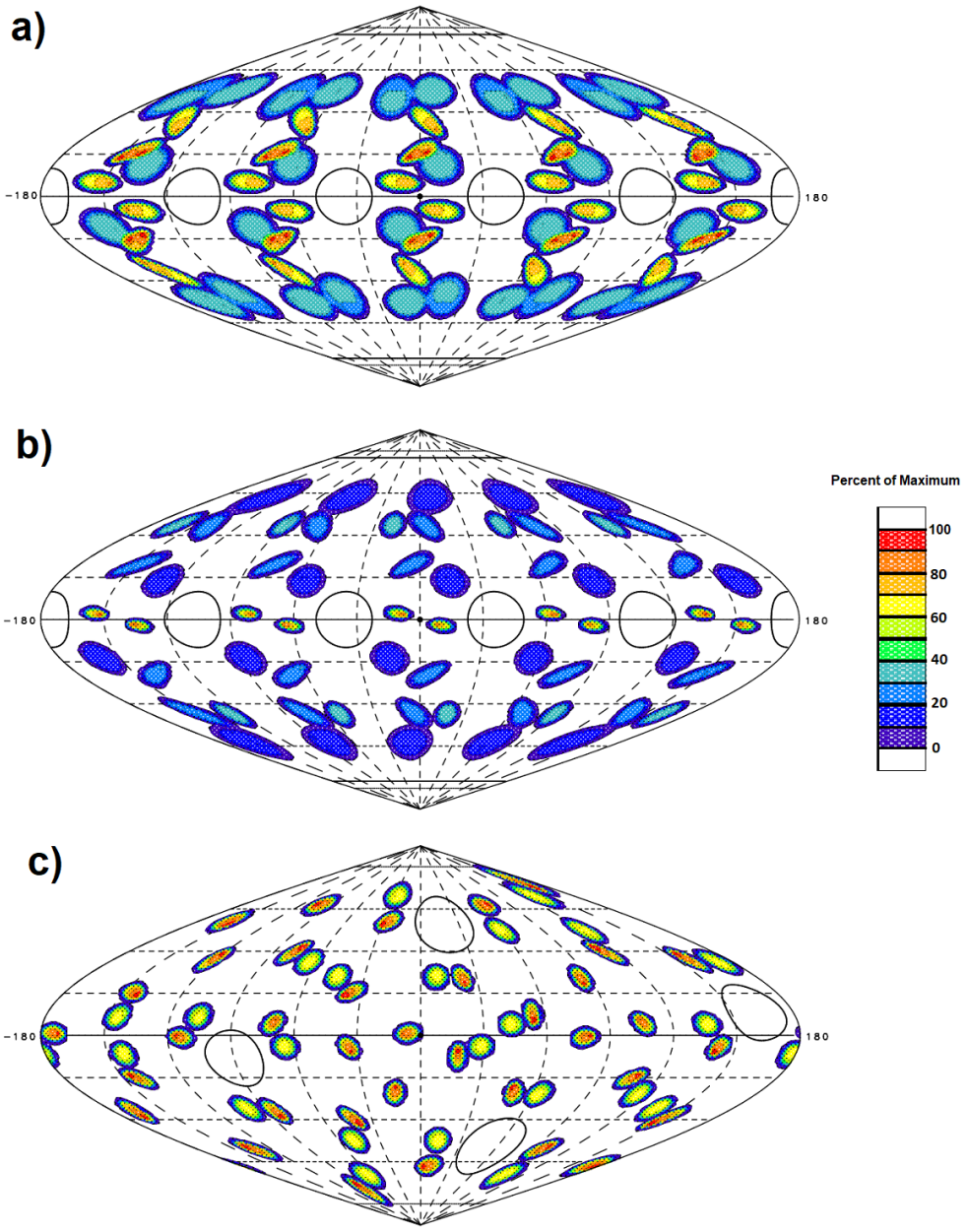

Figure A4: *Deposited laser energy per unit area on a PEPR hohlraum without beam repointing (a), with repointing (b), and on a tetrahedral hohlraum (c). The LEH's are indicated with outlines*

The beams may also be repointed by changing their best focus point. In Sec. IV, the tetrahedral hohlraum simulations assumed the use of phase plates, so the beams were modeled as parallel rays with a circular cross section in the plane of the LEH. The beams also travelled through the center of each LEH. For the following *PEPR* and tetrahedral hohlraum simulations, *LORE* uses the parameters of the 60-beam OMEGA laser, the beams are modeled as circular cones with an $f/6$ focus, and the best focus points are specified as user input. As for the experiments of Refs. 8 and 9, phase plates are not used.

Figures A4(a) and A4(b) both represent deposited laser energy (for just one intersection) on a PEPR hohlraum using the beam assignments shown in Figs. A2 and A3. For Fig. A4(a), the best focus point of each beam is in the center of the entered LEH, whereas Fig. A4(b) shifts the best focus points to improve capsule uniformity (see Fig. A9), increase clearance with the capsule (see Fig. A6), and maintain at least a 50 μm clearance when entering the LEH's (see Fig. A7). In addition, after repointing the beams, the locations of deposited energy are well clear of the LEH's and there are fewer overlaps.

Figure A4(c) shows the deposited laser energy on a tetrahedral hohlraum for just one intersection ($A(\theta) = 1$). The parameters used for the tetrahedral hohlraum are based on the tetrahedral hohlraum experiments modeled in Ref. 7, but the beam pointings have been optimized to improve uniformity. The tetrahedral hohlraum simulations will be used as benchmarks for the *PEPR* hohlraum.

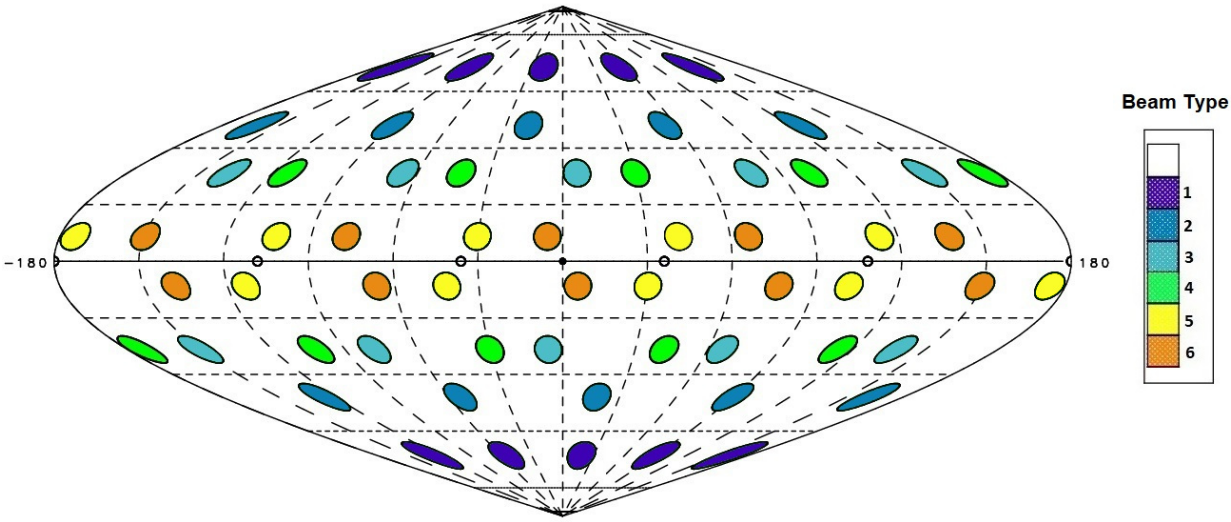

Figure A5: *Six types of beams entering the PEPR hohlraum. Based on the LEH assignments of Fig. A3*

Figure A5 depicts the six "types" of beams used to drive the *PEPR* hohlraum. The beam type is based on the angle at which the incident beam enters the LEH (in contrast to Fig. A3, where the colors indicate LEH assignments). For example, the beams which enter the polar LEH's are all considered to be the same type of beam. All the beams of a specific beam type have a similar travel path within the hohlraum and are repointed similarly for the current optimized pointings. The symmetries for each equatorial LEH and both polar LEH's are therefore maintained after the beams are repointed.

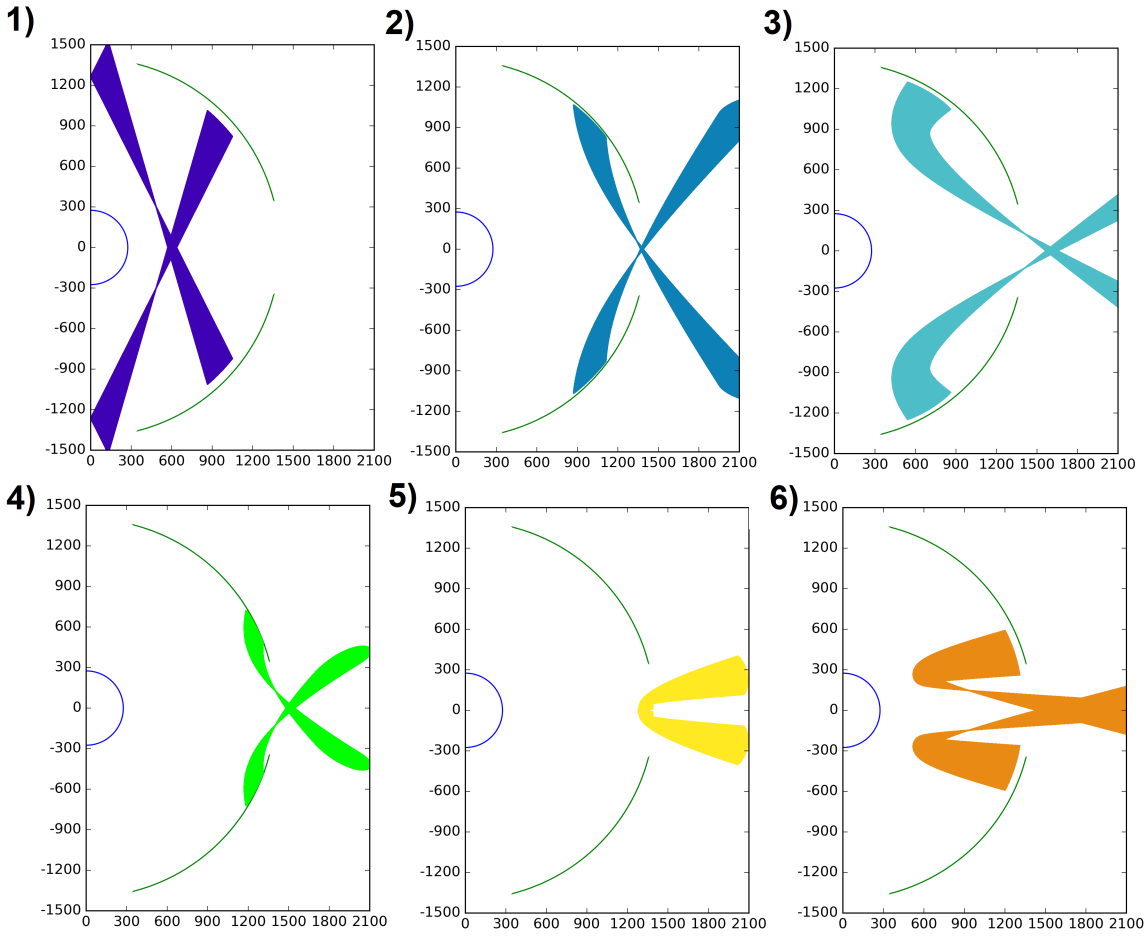

Figure A6: *2-D view of the six types of beams entering the PEPR hohlraum (using optimized pointings). The z-value is plotted on the vertical axis, with* $\sqrt{x^2+y^2}$ *on the horizontal axis. Units are in microns*

Figure A6 depicts 2-D views of the six types of beams entering the *PEPR* hohlraum with optimized pointings. The color of each beam type follows the color code of Fig. A5. The blue inner semi-circle depicts the capsule, while the larger green semi-circle depicts the hohlraum wall. The segments of the hohlraum wall that are not drawn represent the LEH's. Since the equatorial LEH's are equivalent under rotations about the vertical axis, only one equatorial LEH is shown.

For each 2-D view, $\sqrt{x^2+y^2}$ is plotted on the horizontal axis, enabling one to check the clearance with the capsule and to see the θ of where the laser beam strikes the wall. The repointed beams offer more clearance with the capsule. Beam type 1 is shifted away from the capsule, and the best focus point is positioned near the capsule to provide greater clearance. The ϕ values are

not shown in Fig. A6. For example, for beam type 6, no rays exit through an LEH; the spots are close to the equator but clear of the LEH's (see the approximately circular spots in Fig. A4(b) $\sim$ 20° from the equator), hitting the wall with ϕ different by $\sim$ 25°.

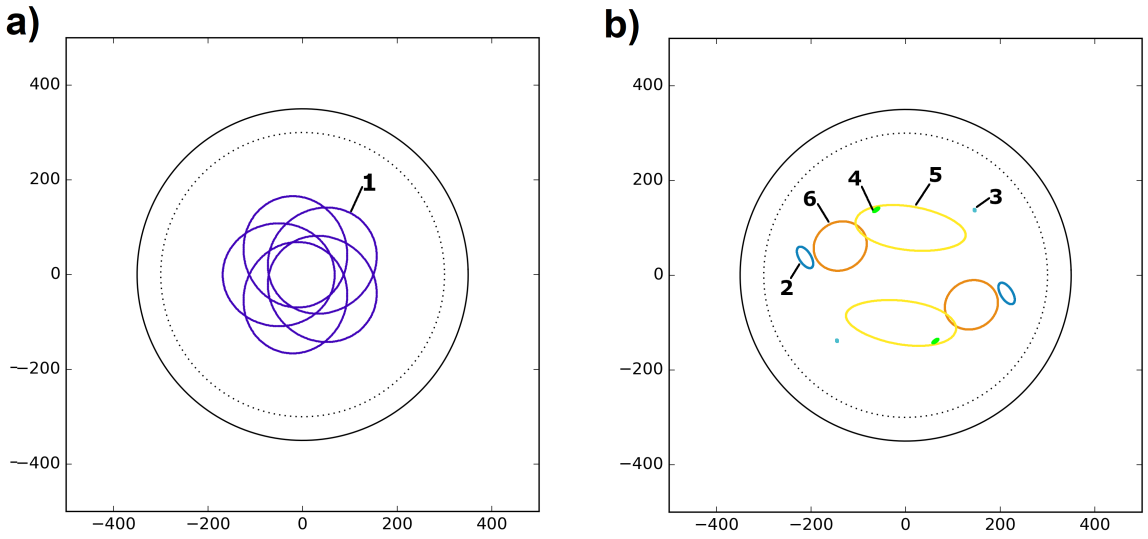

Figure A7: *2-D cross section view of the optimized pointed beams entering the PEPR hohlraum polar LEH's (a) and equatorial LEH's (b) in the plane of the LEH. The dotted circle depicts a 50 μm clearance. The beam cross sections are labeled and colored according to type as defined in Fig. A5. Units are in microns*

Figure A7 represents the incident beam cross section in the plane of the LEH for both the polar LEH's (a) and the equatorial LEH's (b). The colors of the beam cross sections in Fig. A7 correspond to the six beam types. The current optimized pointings of the beams also satisfy the clearance with the LEH. The dotted circle is drawn to demonstrate that the beams clear the LEH's with at least a 50 μm clearance, based on Ref. 6.

Some of the beam cross sections in the equatorial LEH (Fig. A7(b)) appear as small dots, since the best focus point is close to the LEH and *LORE* does not model the diffraction of the beams, which would widen the spots. In reality, the spot size would be about 50 μm in diameter at best focus [7]. Regardless, there would still be greater than 50 μm clearance with the actual spot sizes.

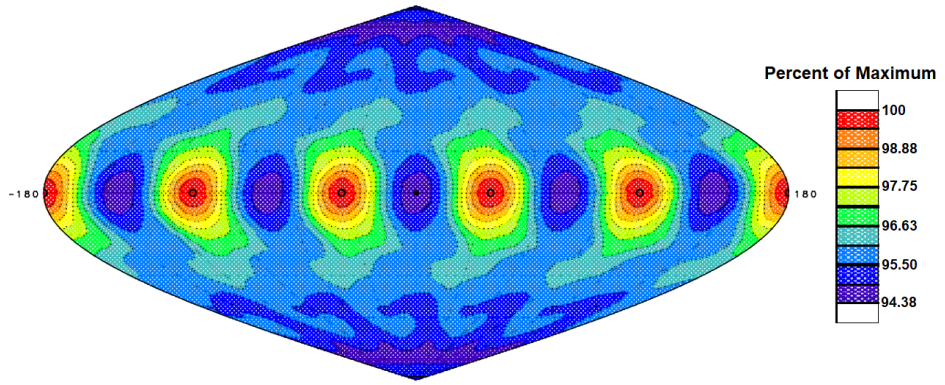

(a) *PEPR*, Albedo=0.05, RMS $\sim$ 1.10%

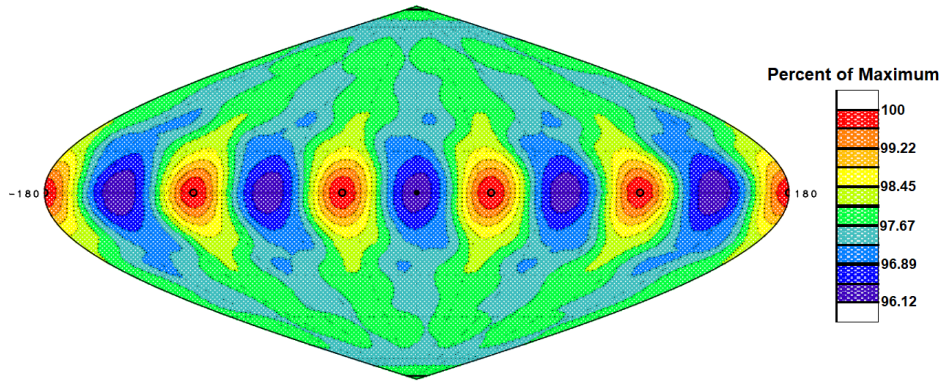

(b) *PEPR*, Albedo=0.50, RMS $\sim$ 0.67%

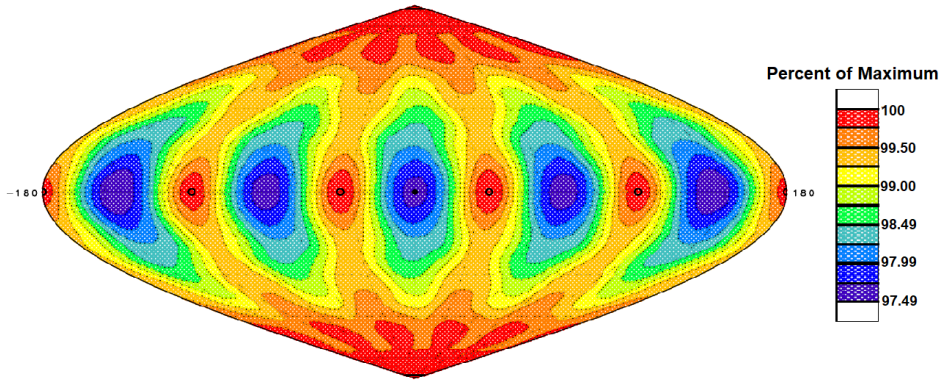

(c) *PEPR*, Albedo=0.85, RMS $\sim$ 0.60%

Figure A8: *Capsule uniformity contour plots for the optimized PEPR hohlraum at albedos α_w of 0.05 (a), 0.50 (b), and 0.85 (c). (Note the difference in scales)*

Figure A8 depicts the capsule uniformity when driving a *PEPR* hohlraum with optimized beam pointings at albedos α_w of 0.05, 0.50, and 0.85 produced by *LORE* simulations. At lower levels of albedo, the laser spots dominate, and since the locations of deposited laser energy are more

"clumped" around the equator than around the poles (Fig. A4(b)), the equatorial region of the capsule receives slightly more drive. However, at higher values of albedo, the heated hohlraum wall provides the dominant contribution to the drive. Due to the two LEH's on the poles being spaced further from other LEH's than the five equatorial LEH's, the poles of the capsule receive greater drive.

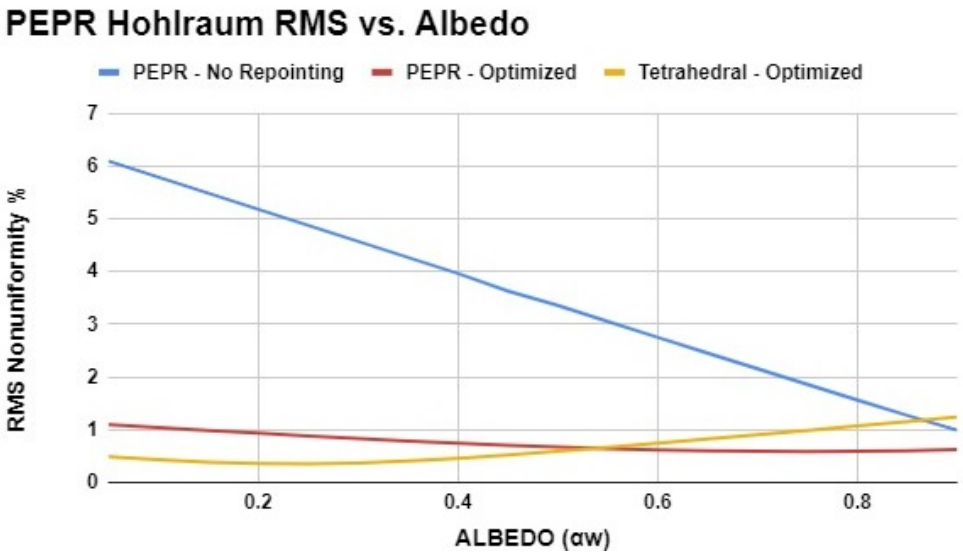

Figure A9: *RMS nonuniformity for unoptimized (blue) and optimized (red) PEPR hohlraums and tetrahedral hohlraums (yellow) for various albedo* α_w*. The tetrahedral curve uses optimized beam pointings and is different from the curve in Fig. 13*

Figure A9 shows a comparison of capsule uniformity between the tetrahedral and *PEPR* hohlraums (with and without repointing). Without repointing, there are significantly greater nonuniformities for the *PEPR* hohlraum, as the locations of deposited laser energy are not as uniformly dispersed (compare Figs. A4(a) and A4(b)). With the optimized pointings, however, the uniformity is improved at all values of albedo. The nonuniformity is reduced by a factor of 5 to 6 (6.10% to 1.10%) at an early time (albedo = 0.05), and at later times (albedo > 0.8) by about a factor of 2.

At lower values of albedo, the tetrahedral hohlraum provides better uniformity than the optimized *PEPR* hohlraum because the locations of deposited laser energy on the tetrahedral hohlraum are more evenly spread out (demonstrated in Fig. A4). At albedos greater than 0.5, however, the capsule nonuniformity is lower for the *PEPR* hohlraum, with the nonuniformity consistently around 0.6%.

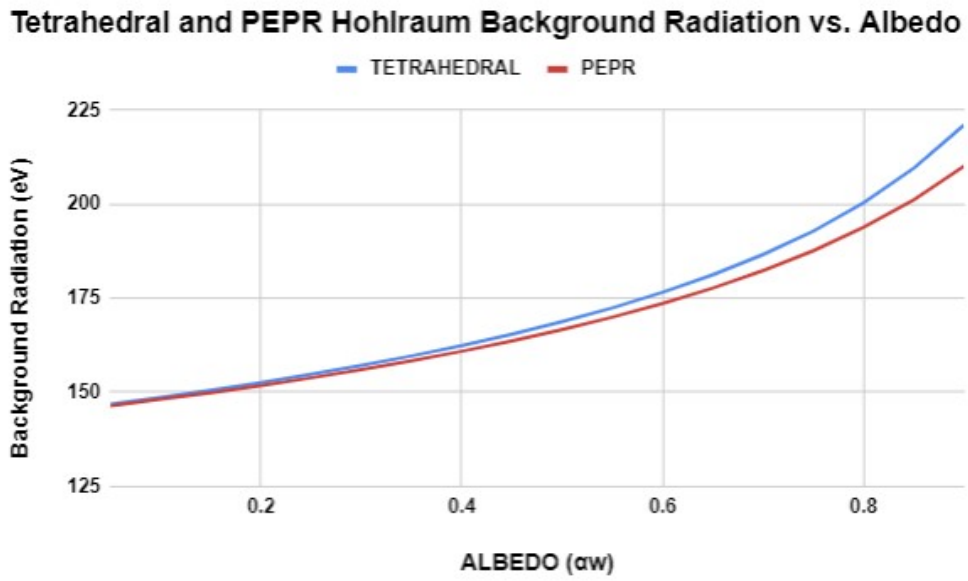

Figure A10: *Background radiation temperature T_r as a function of albedo α_w for tetrahedral (blue) and PEPR (red) hohlraums*

Figure A10 depicts the background radiation temperature T_r for tetrahedral and *PEPR* hohlraums as a function of albedo α_w. The total power of the 60-beam OMEGA laser P_{las} is taken to be 18 TW, approximately the peak power of the "PS22" laser pulse shape used to drive the tetrahedral hohlraums of Refs. 8 and 9. Due to the presence of three more LEH's, the *PEPR* hohlraum provides a lower T_r as compared to the tetrahedral hohlraum. Reducing the hohlraum radius somewhat (with the LEH radius fixed) to increase T_r would be plausible since the deposited laser energy is clear of the LEH's (as shown in Fig. A4).

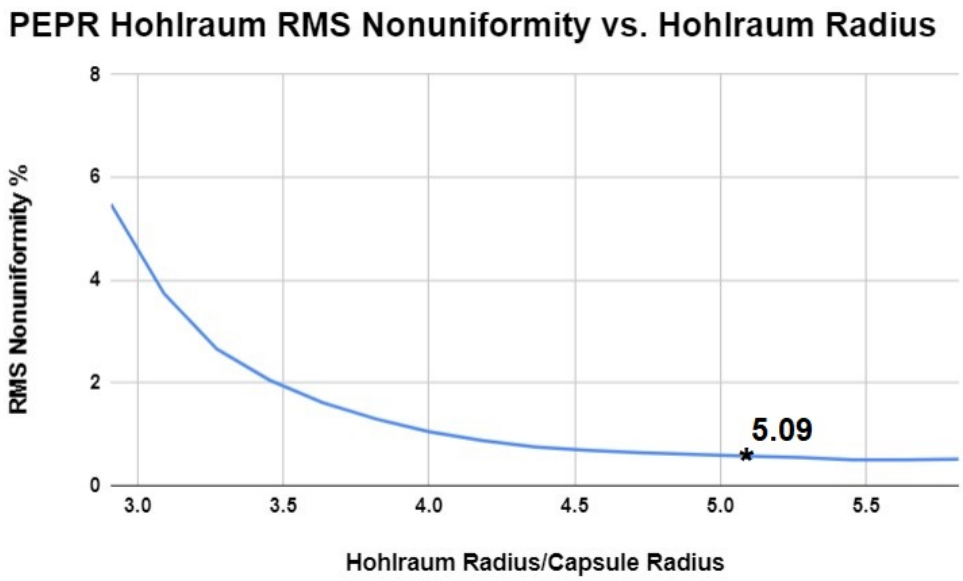

Figure A11: *RMS nonuniformity for PEPR hohlraums as a function of the ratio of hohlraum-to-capsule radius at an albedo α_w of 0.8. The capsule radius and LEH radius are fixed. The asterisk indicates the ratio for the standard PEPR and tetrahedral hohlraums used in this paper*

Figure A11 depicts the capsule nonuniformity while the hohlraum radius is varied (the capsule and LEH radii are kept the same). Each simulation used beam pointings that are similar to those optimized for a case-to-capsule ratio of 5.09. For different ratios, the beams are repointed in the same direction, but the distance shifted is based on the hohlraum radius. For example, each type 1 beam is repointed by 1200 μm for a standard *PEPR* hohlraum, but is repointed by 1.2*1200 μm for a case-to-capsule ratio of 1.2*5.09.

As opposed to the octahedral hohlraum, for which a hohlraum-to-capsule ratio of around 5.1 presents a local minimum, there does not appear to be a "golden ratio" for *PEPR* hohlraums. The RMS nonuniformity consistently decreases as the hohlraum-to-capsule ratio increases. As an example of the tradeoff between uniformity and radiation temperature, a hohlraum-to-capsule ratio of 4.35 would give a nonuniformity of 0.88% and increase T_r to 202 eV, a little higher than the 200 eV shown in Fig. A10 for the tetrahedral hohlraum. Since the beam pointings were initially optimized for a case-to-capsule ratio of 5.09, Fig. A11 is likely an overestimate of the nonuniformity that can be achieved at different ratios. Nevertheless, Fig. A11 gives a good indication of the tradeoff.

A possible method to improve capsule uniformity while minimally decreasing the background radiation temperature is to increase the size of the LEH's on the poles, as the regions near the poles of the capsule receive greater drive at higher albedos.

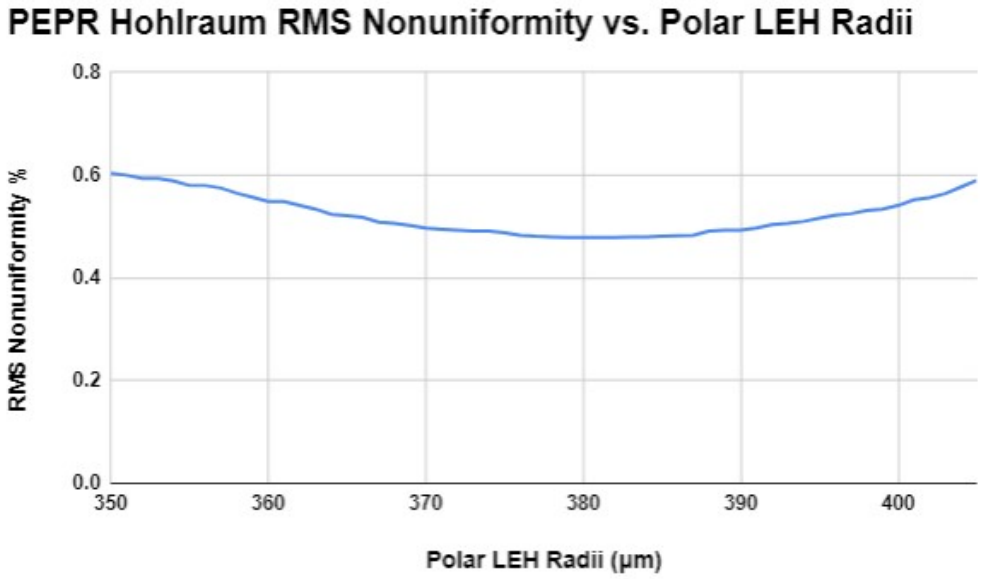

Figure A12: *RMS nonuniformity for PEPR hohlraums as a function of polar LEH radii at an albedo α_w of 0.85. The equatorial LEH radii are kept the same (350 μm)*

Various radii of polar LEH's are tested in Fig. A12, while the radii of the equatorial LEH's remain at 350 μm. At an albedo α_w of 0.85, a relative minimum for RMS nonuniformity of 0.48% occurs at a polar LEH radius of 380 μm, a minor improvement over the value of 0.60% found for equal LEH radii in Figs. A8(c) and A9. The background radiation temperature T_r is approximately 200 eV, compared to 201 eV for a standard *PEPR* hohlraum with equal size LEH's.

The simulations to create Fig. A12 used a higher resolution to reduce the "steps" in the curve which resulted from the way effective radiation temperature is defined in the vicinity of the LEH's. Each cube grid face contains 200x200 grid points, creating four times more points on the hohlraum wall than the 100x100 grid points used in the rest of the simulations in this paper (see Section III.1). The results with increased resolution are consistent with the rest of the paper and only deviated slightly (a difference of $\sim 0.05\%$ in the RMS values) compared to the "standard resolution."

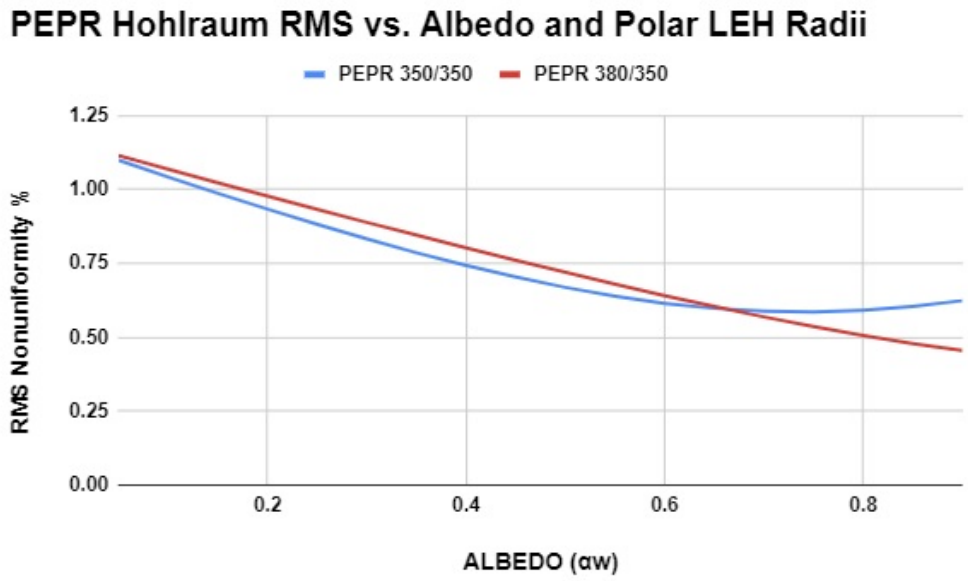

Figure A13: *RMS nonuniformity for the standard PEPR hohlraum (blue) and a PEPR hohlraum with polar LEH radii of 380 μm (red) as a function of albedo α_w. Both hohlraums use optimized beam pointings. The equatorial LEH radii are kept the same (350 μm). The standard PEPR curve is the same as that in Fig. A9*

Another point of consideration for *PEPR* hohlraums with increased polar LEH radii is the dependence of their uniformity on albedo. In Fig. A13, results for increasing the radii of the polar LEH's to 380 μm are compared with results for a standard *PEPR* hohlraum. The radii of the equatorial LEH's remain the same (350 μm), and the beam repointings are unaltered.

The *PEPR* hohlraum with increased polar LEH radii produces slightly higher nonuniformities compared to the standard *PEPR* hohlraum at low values of albedo. However, lower nonuniformities are achieved at all albedo values greater than 0.7. This is due to the poles being underdriven at low albedo values but overdriven at high albedos (Fig. A8). Thus, to obtain minimum overall nonuniformity, the radii of the polar LEH's may need to be greater than those of the equatorial LEH's, depending on the hohlraum and capsule dynamics.

References

[1] J. D. Lindl. "Development of the indirect-drive approach to inertial confinement fusion and the target physics basis for ignition and gain". In: *Physics of Plasmas* 2.11 (1995), pp. 3933–4024. DOI: 10.1063/1.871025. eprint: https://doi.org/10.1063/1.871025. URL: https://doi.org/10.1063/1.871025.

[2] C. A. Haynam et al. "National Ignition Facility laser performance status". In: *Appl. Opt.* 46.16 (2007), pp. 3276–3303. DOI: 10.1364/AO.46.003276.

[3] P. B. Radha et al. "Direct drive: Simulations and results from the National Ignition Facility". In: *Physics of Plasmas* 23.5 (2016), p. 056305. DOI: 10.1063/1.4946023. eprint: https://doi.org/10.1063/1.4946023. URL: https://doi.org/10.1063/1.4946023.

[4] T. J. B. Collins et al. "A polar-drive-ignition design for the National Ignition Facility". In: *Physics of Plasmas* 19.5 (2012), p. 056308. DOI: 10.1063/1.3693969. eprint: https://doi.org/10.1063/1.3693969. URL: https://doi.org/10.1063/1.3693969.

[5] D. W. Phillion and S. M. Pollaine. "Dynamical compensation of irradiation nonuniformities in a spherical hohlraum illuminated with tetrahedral symmetry by laser beams". In: *Physics of Plasmas* 1.9 (1994), pp. 2963–2975. DOI: 10.1063/1.870537. eprint: https://doi.org/10.1063/1.870537. URL: https://doi.org/10.1063/1.870537.

[6] J. D. Schnittman and R. S. Craxton. "Indirect-drive radiation uniformity in tetrahedral hohlraums". In: *Physics of Plasmas* 3.10 (1996), pp. 3786–3797. DOI: 10.1063/1.871511. eprint: https://doi.org/10.1063/1.871511. URL: https://doi.org/10.1063/1.871511.

[7] J. D. Schnittman and R. S. Craxton. "Three-dimensional modeling of capsule implosions in OMEGA tetrahedral hohlraums". In: *Physics of Plasmas* 7.7 (2000), pp. 2964–2977. DOI: 10.1063/1.874148. eprint: https://doi.org/10.1063/1.874148. URL: https://doi.org/10.1063/1.874148.

[8] J. M. Wallace et al. "Inertial Confinement Fusion with Tetrahedral Hohlraums at OMEGA". In: *Phys. Rev. Lett.* 82 (1999), pp. 3807–3810. DOI: 10.1103/PhysRevLett.82.3807. URL: https://link.aps.org/doi/10.1103/PhysRevLett.82.3807.

[9] G. R. Bennett et al. "Moderate-convergence inertial confinement fusion implosions in tetrahedral hohlraums at Omega". In: *Physics of Plasmas* 7.6 (2000), pp. 2594–2603. DOI: 10.1063/1.874101. eprint: https://doi.org/10.1063/1.874101. URL: https://doi.org/10.1063/1.874101.

[10] K. Lan et al. "Octahedral spherical hohlraum and its laser arrangement for inertial fusion". In: *Physics of Plasmas* 21.5 (2014), p. 052704. DOI: 10.1063/1.4878835. eprint: https://doi.org/10.1063/1.4878835. URL: https://doi.org/10.1063/1.4878835.

[11] K. Lan and W. Zheng. "Novel spherical hohlraum with cylindrical laser entrance holes and shields". In: *Physics of Plasmas* 21.9 (2014), p. 090704. DOI: 10.1063/1.4895503. eprint: https://doi.org/10.1063/1.4895503. URL: https://doi.org/10.1063/1.4895503.

[12] K. Lan et al. "High flux symmetry of the Spherical Hohlraum with Octahedral 6 LEHs at the hohlraum-to-capsule radius ratio of 5.14". In: *Physics of Plasmas* 21 (2014). DOI: 10.1063/1.4863435.

[13] X. He and W. Zhang. "Advances in the national inertial fusion program of China". In: *EPJ Web of Conferences* 59 (2013), pp. 01009–. DOI: 10.1051/epjconf/20135901009.

[14] G. J. Balonek. "How Good is the Bright Ring Characterization for Uniformity of Deuterium Ice Layers within Cryogenic Nuclear Fusion Targets?" In: *LLE Summer High School Research Program* (2004). URL: http://www.lle.rochester.edu/media/publications/high_school_reports/documents/hs_reports/2004/Balonek_G.pdf.

[15] T. Mo. "X-Ray Backlighting of Shock Ignition Experiments on the National Ignition Facility". In: *LLE Summer High School Research Program* (2010). URL: http://www.lle.rochester.edu/media/publications/high_school_reports/documents/hs_reports/2010/Mo_Tom.pdf.

[16] L. Jing et al. "Comparison of three hohlraum configurations with six laser entrance holes for indirect-drive inertial confinement fusion". In: *Nuclear Fusion* 58.9 (2018), p. 096017. DOI: 10.1088/1741-4326/aacec8. URL: https://doi.org/10.1088%2F1741-4326%2Faacec8.

[17] R. K. Kirkwood et al. "Observation of Energy Transfer between Frequency-Mismatched Laser Beams in a Large-Scale Plasma". In: *Phys. Rev. Lett.* 76 (1996), pp. 2065–2068. DOI: 10.1103/PhysRevLett.76.2065. URL: https://link.aps.org/doi/10.1103/PhysRevLett.76.2065.

[18] W. A. Farmer et al. "High-temperature hohlraum designs with multiple laser-entrance holes". In: *Physics of Plasmas* 26.3 (2019), p. 032701. DOI: 10.1063/1.5087140. eprint: https://doi.org/10.1063/1.5087140. URL: https://doi.org/10.1063/1.5087140.

Optimization of the Uniformity of 12-Quad Direct Drive Targets for the National Ignition Facility

Hanna Wiandt

Pittsford Mendon High School

Advisor: Dr. Stephen Craxton

Laboratory for Laser Energetics

University of Rochester

August 2019

1. Abstract

The National Ignition Facility (NIF) has a total of 192 beams, divided amongst 48 quads located at 23.5˚, 30˚, 44.5˚, and 50˚ from the top and bottom of the target chamber. A proposed experiment requires the use of 24 quads to irradiate a cylindrical hohlraum and 12 quads to compress each of two spherical capsules using direct drive. A sample would be exposed to the high fluxes of x rays and neutrons produced by the hohraum and capsules, respectively. Glass (SiO_2) and plastic (CH) spheres of 1600 μm and 2000 μm diameter were considered for the direct drive capsules. To compensate for the uneven coverage provided by only 12 quads, individual beams were defocused and repointed in the θ (vertical) and φ (horizontal) directions, increasing the uniformity of the imploding capsules. Simulations that varied beam selections, pointings, and defocuses were used to identify an optimum design for each capsule. Nonuniformities as low as 3-4% rms were obtained in all cases.

2. Introduction

Nuclear fusion could one day produce clean energy. One method used to achieve nuclear fusion relies on the irradiation of a capsule using laser beams. The capsule, composed of a spherical shell containing the hydrogen isotopes deuterium and tritium, ablates outward in response to being irradiated. This ablation results in a compressive force inward, creating a high temperature and pressure environment at the core of the capsule. As the hydrogen isotopes are compressed, their strong nuclear forces overcome the repulsive Coulomb forces between them, and the isotopes fuse to form a helium nucleus and an energetic neutron. A fraction of the energy produced by the reaction is redeposited, which in turn leads to more fusion reactions. Provided that there is enough energy redeposited, the fusion reactions can become self-sustaining in a

process known as ignition. The National Ignition Facility (NIF) was built in the hopes of achieving ignition.

The NIF is capable of depositing laser energy in two processes: direct and indirect drive. A comparison of these two methods can be seen in Figure 1. The former requires that laser beams hit a capsule directly [Fig. 1(a)], whereas the latter utilizes a cylindrical container referred to as a hohlraum [Fig. 1(b)]. The hohlraum allows laser beams to enter through openings located at the top and bottom of its structure, and emits x rays when irradiated by laser energy. It is these x rays which then compress the capsule. While this allows for more uniform compression, the energy absorbed in the process of creating x rays, coupled with the loss of energy through the openings, make indirect drive much less energy efficient than direct drive.

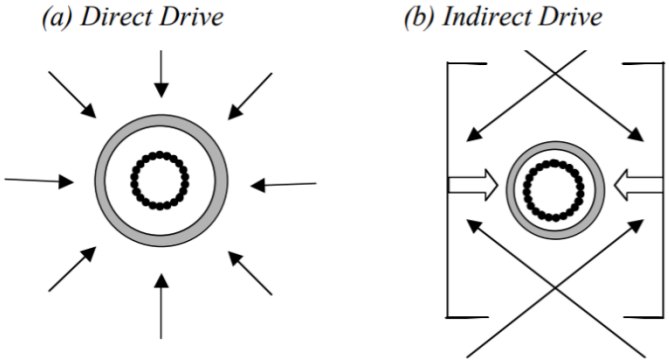

Figure 1. Two approaches to nuclear fusion using lasers. (a) Direct drive uses laser beams (shown here as thin arrows) to irradiate a capsule directly. (b) Indirect drive relies on a hohlraum to produce x rays (shown here as thick arrows), which then compress the capsule. (From Ref. 1)

The NIF was originally intended for indirect drive. Accordingly, its beam ports are located in four rings at angles θ of 23.5º, 30º, 44.5º, and 50º from the vertical in the upper and lower hemispheres. Because they rest at such a great angle from the equator, its beams have to be repointed in order for the NIF to achieve direct drive. The locations of beams and the necessary

adjustments can be seen in Figure 2. The beams cannot simply be pointed towards the center of the capsule. Doing so would place much more energy near the poles than the equator, resulting in uneven compression and a compromised neutron yield. To ensure a successful experiment, then, some beams have to be repointed towards the equator, in a process known as polar direct drive.[2,3]

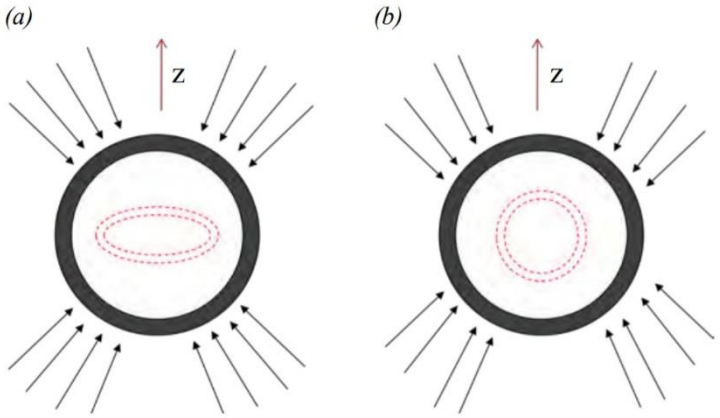

Figure 2. NIF beam pointings (thin arrows) and resultant compression pattern of the capsule (pink rings). (a) If the laser beams are pointed towards the center of the capsule, uneven energy deposition results in a flat compression. (b) Polar direct drive compensates for beam placements by repointing beams towards the equator for a more uniform compression. (From Ref. 4)

As a high amount of energy is being deposited by laser beams in direct drive, a plasma forms around the capsule. This plasma, a gas which contains both ions and electrons, is comparable to the conditions found in space. By mimicking the densities, temperatures, and pressures found in stars, the NIF serves as a way to bring distant phenomena into a laboratory environment. Neutrons and x rays from fusion experiments can also be applied to observe the reaction of materials to large amounts of energy.

The combined environment target was proposed by Dr. Yeamans of Lawrence Livermore National Laboratory as a means of studying a sample's reaction to x rays and neutrons.[5] The 48

quads of the NIF are divided into three groups, providing energy to a hohlraum and two spherical capsules, as shown in Figure 3.

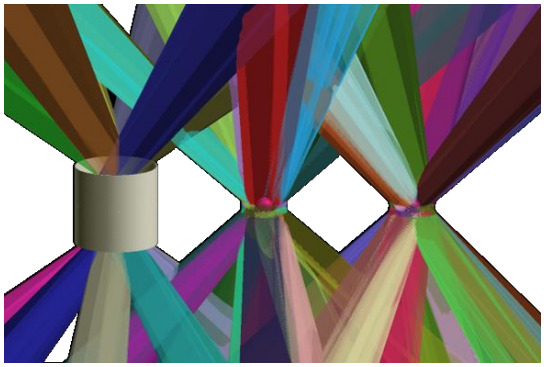

Figure 3. Laser beams being used to irradiate a cylindrical hohlraum and two spherical capsules. (From Ref. 5)

The irradiation of the hohlraum produces x rays, in a fashion similar to indirect drive. Unlike indirect drive, however, the hohlraum does not contain a capsule, as the objective of the hohlraum is solely that of producing x rays. The compression of the two spherical capsules in direct drive produces neutrons. While the number of quads required for each target is fixed—24 quads for the hohlraum and 12 for each direct drive target—the division of the quads can vary.

It is important that the spherical capsules implode as evenly as possible, to maximize their neutron yield. However, with the use of only a quarter of all the NIF's quads for each capsule, large areas of the target surface can easily be left with less compression than average, while other regions become over compressed. In this work, combined environment targets were designed, with plastic (CH) and glass (SiO_2) capsules, in 1600 µm and 2000 µm diameter sizes, for two different sets of quads. The pointings and defocuses of each beam were adjusted to optimize implosion uniformity, with each capsule achieving uniformities between 3-4% rms.

3. Factors that Influence the Implosion

The beam selection, laser pulse shape, and beam pointings and defocuses of an experiment on the NIF are discussed in Sections 3.1-3.3, respectively, as they contribute to the uniformity of a capsule's implosion. The beam selection determines the locations of beams

relative to the target surface. The laser pulse shape determines the amount of energy delivered to a capsule. Lastly, the beam pointings and defocuses increase the uniformity of a capsule's implosion by distributing energy in certain patterns.

3.1 Beam Selection

The NIF has eight rings of quads, with four rings each in the upper and lower hemispheres. Figure 4 shows the layout of quads relative to a capsule on the NIF. The whole surface of the capsule can be seen, with lines of constant θ and φ indicated by dashed lines. For each direct drive target, there need to be six quads from each of the upper and lower hemispheres of the NIF. Of these six, two have to be inner quads (from rings 1 and 8 in Figure 4), and four have to be outer quads (from rings 4 and 5 or 3 and 6). This division between upper and lower hemispheres allows for similar configurations to be used for each capsule, and helps to achieve a uniform compression. Alternating quads were used in both inner and outer rings, for optimal azimuthal symmetry. The selection of quads from rings 4 and 5 was limited by the architecture of the NIF; certain 50º quads—those shown in Figure 4 as colorless—are linked to 30º quads in such a way that they must be fired simultaneously. It was therefore decided that quads from rings 2 and 7 (the 30˚ quads) would be reserved for the irradiation of the hohlraum, along with the 50˚ quads that they are linked to.

This reduces the number of available 50˚ quads in such a way that if one capsule were to use 50˚ quads, the other would have to use 44.5˚ quads. As these quads are even further from the equator, the nonuniformity of implosions at the equator is magnified. This makes designs using the 44.5˚ quads especially challenging.

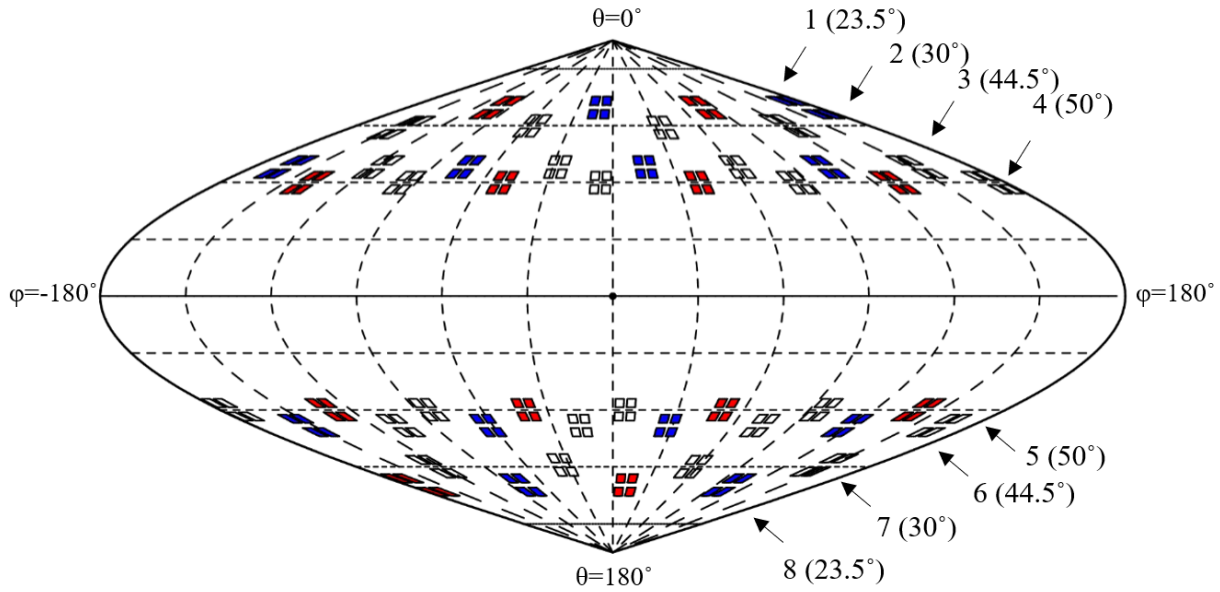

Figure 4. One option for division of NIF quads among direct drive targets. In the configuration shown, the quads irradiating capsule 1 are marked in red and those irradiating capsule 2 in blue. The colorless quads irradiate the hohlraum. Rings have been labeled 1-8.

3.2 Laser Pulse Shape

To avoid damaging the optics of the NIF and thus lower the cost of a shot, a maximum total energy of 534 kJ was selected. Each group of 12 quads would therefore require 133.5 kJ. This led to the laser pulse shown in blue (incident) in Figure 5. To determine the maximum power, P_{max}, of the laser pulse required to deliver this amount of energy, the following equation was used, where P represents power, E energy, and t time:

$$E = \int P dt = \frac{1}{2}\left(t_4 + (t_3 - t_2)\right)P_{max} \quad (1)$$

The times t_2-t_4 from Eq. (1) can be seen in Figure 5.

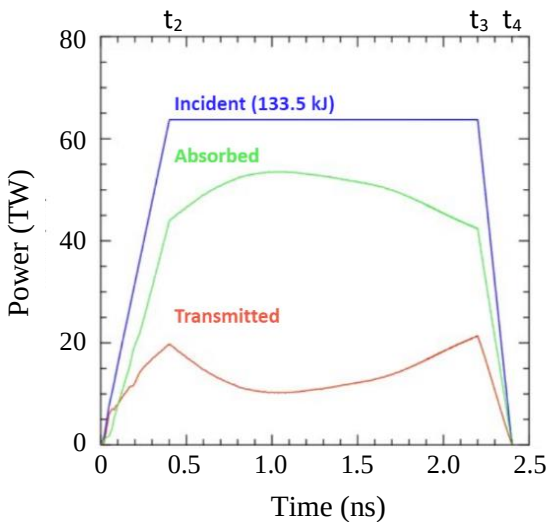

Figure 5. Graph of incident, absorbed, and transmitted power delivered to a spherical capsule.

The time t_2 was taken to be 0.4 ns to allow the laser adequate time to reach the maximum power desired, t_4 was set at 2.4 ns, and t_3 had to be 0.2 ns less than t_4, to allow the laser enough time to power down. Substituting into Eq. (1), the maximum power was found to be 63.75 TW for each group of 12 quads, which is comfortably less than the 112.5 TW that the NIF is capable of.

Furthermore, as the shape of the laser pulse and the amount of energy delivered to the capsule had been set, each capsule's shell thickness served as a valuable variable for adjusting the implosion time of the capsule, with thinner capsules imploding faster. To minimize wasted laser energy, the implosion would ideally occur towards the end of the laser pulse, between 2.2 ns and 2.4 ns. The energy that is deposited onto the surface of the capsule becomes absorbed energy, while the energy that continues past the capsule becomes transmitted energy, which risks causing damage to the optics of the NIF if it is too large. A later implosion therefore allows for more absorbed and less transmitted energy.

3.3 Beam Shifting and Defocusing

Each of the individual beams on the NIF can be repointed to a specific location on the initial capsule surface determined by the angles θ and φ, and can also be defocused by adjusting the distance of the focus lens to the capsule [Figure 6].

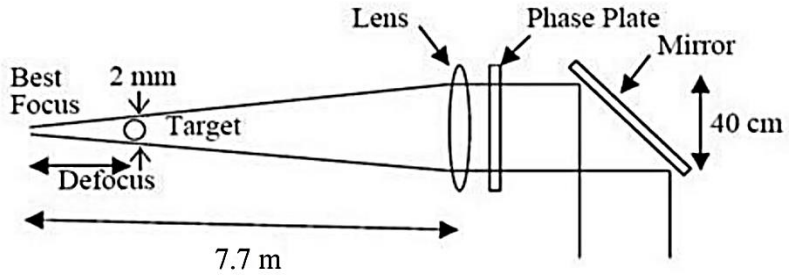

Figure 6. Diagram (not to scale) representing the defocusing and pointing mechanisms of a laser beam. Defocus can be adjusted by moving the lens closer to or further from the capsule along the axis of the laser beam. Changing the angle of the mirror controls beam pointing. (From Ref. 4)

These three parameters function as a means of controlling the pattern of energy deposition on the surface of a direct drive target. Repointing a beam allows for a different area on the surface of the capsule to be irradiated. Defocusing a beam changes its focal point, hence altering the size and intensity of the beam spot. Using only 25% of the beams of the NIF for a capsule increases the risk of uneven energy deposition, which can greatly compromise the neutron yield of an experiment. Therefore, finding the optimum beam pointings and defocuses is especially important.

4. Sample Optimized Design

The aim of the optimization process was to develop compatible designs that would implode at an optimum time with maximum uniformity, using only 12 NIF quads each. The time when peak density occurs can be used to define the implosion time, as there is no precise

moment when the capsule implodes. Thus, the implosion time was determined by graphs of the maximum density of the capsule plotted versus time [Figure 7].

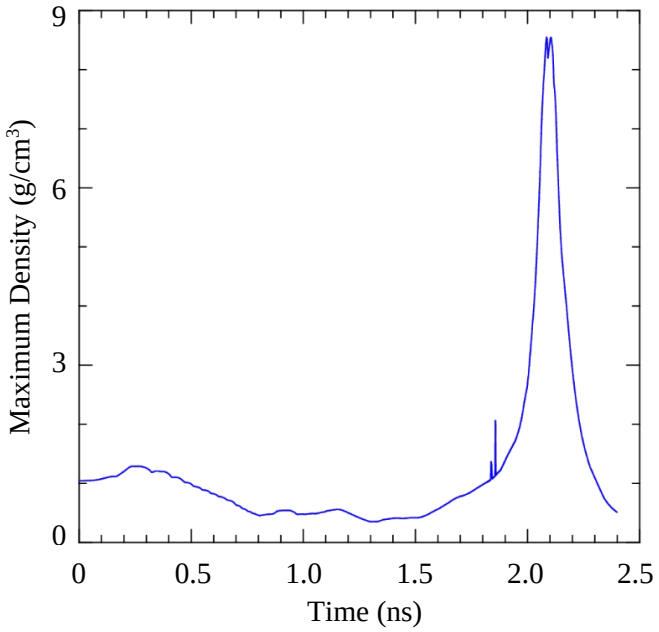

Figure 7. Plot of maximum density versus time in an optimized design. Peak density occurs at 2.1 ns, indicating that the implosion will happen near the ideal 2.2-2.4 ns range.

Using such graphs, optimum thicknesses were determined for glass and plastic capsules in 1600 µm and 2000 µm diameters. These thicknesses, and the corresponding implosion times, can be seen in Table 1. All of the thicknesses are reasonable in terms of manufacturability, and would be capable of holding the required pressures of hydrogen isotopes. The capsules also implode late enough in the laser pulse to reduce transmitted energy to an amount that would not damage the optics of the NIF.

Table 1. Comparison of shell thicknesses and implosion times for four capsule designs with two quad selections.

Capsule	Thickness (µm)	Implosion time (ns)	
		50˚ quads	45˚ quads
1600 µm glass	8	2.15	2.4
1600 µm plastic	14	2.1	2.35
2000 µm glass	5	2.1	2.3
2000 µm plastic	10	2.1	2.3

The 1600 μm diameter glass capsule with a shell thickness of 8 μm, using 50˚ quads, was chosen as a sample case for initial study, and is discussed in the remainder of this section, while the other designs are reserved for Section 5. Both the azimuthal and vertical directions were considered to determine uniformity during optimization. The use of 2-D hydrodynamic simulations, run using the code SAGE, allowed for comparisons between models with different beam groupings, pointings, and defocuses. The basic effects of adjustments can be seen in raytrace plots of the capsule implosion, which display density contours as the implosion progresses [Figure 8]. The shell expands as the capsule implodes, creating an area of higher density towards the center of the capsule. These simulations average the density of an imploding capsule in the azimuthal direction. The more circular the density contours, the more spherical the implosion.

The rays from a θ=50˚ beam are plotted as red lines in Figure 8. Once a ray has deposited 99% of its energy, the line representing it stops. Hence, any lines that continue on, curving away from the capsule, represent rays that possess at least 1% of their original energy. The energy deposited onto the capsule by the rays contributes to the absorbed energy graphed in Figure 5, whereas any energy carried beyond the capsule becomes transmitted energy. The further from its angle of origin that a beam is pointed, the less of its energy is absorbed by the capsule. This leads to the rebounding of the rays that are closest to the equator in Figure 8. Energy absorption is further weakened when 44.5˚ beams are used as opposed to 50˚ beams, due to the fact that 44.5˚ beams pointed towards the equator are repointed a greater θ from their angle of origin than 50˚ beams. This leads to the difference in implosion times seen in Table 1; 44.5˚ capsules implode slower because they absorb less energy.

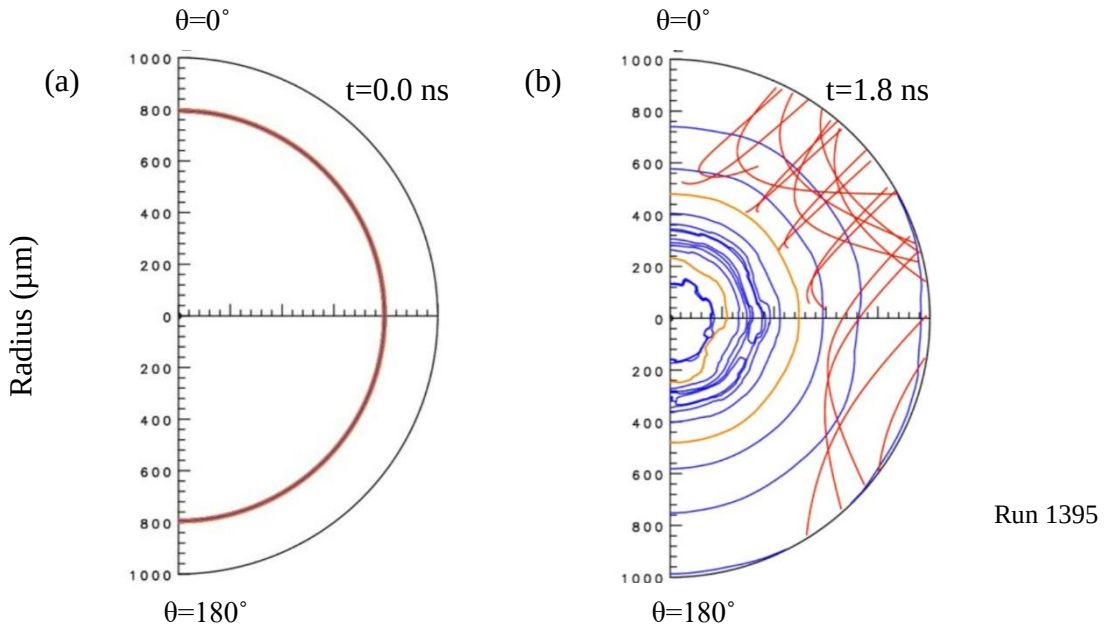

Figure 8. Two raytrace plots depicting the implosion of a 1600 μm diameter glass capsule with shell thickness 8 μm. (a) The capsule prior to implosion is spherical in shape. (b) As the capsule implodes, it compresses inwards, remaining as similar as possible to its initial spherical shape as a result of beam placement. At 1.8 ns, the capsule has imploded just past 400 μm, half of its initial radius. The red lines represent laser rays from a beam incident at θ=50˚. The blue lines are density contours, while the yellow lines represent critical density (the maximum density that the laser can reach).

For each radial line in these 2-D raytrace plots, from θ=0˚ to 180˚, the center-of-mass radius was calculated. This was then plotted as a function of θ in Figure 9 to more clearly illustrate the differences in nonuniformity between unoptimized and optimized designs. This radius was averaged over all φ. The root-mean-square (rms) deviation from the average radius averaged over all angles was calculated to compare nonuniformities. The graph on the left shows an unoptimized design, while the graph on the right is for a final, optimized model of the implosion for the same capsule. As can be seen in the first graph, Figure 9(a), the initial design has a larger center-of-mass radius at the equator than at the poles, indicating that the capsule is

losing its spherical shape and compressing into a flatter mass. The final graph, Figure 9(b), which corresponds to Figure 8(b), is much more uniform, displaying a more even radius throughout the shell and therefore indicating a more uniform, spherical implosion. These differences are owed to adjustments in beam pointings and defocusing. To compensate for the protrusion at the equator in Figure 9(a), beams were pointed further towards the equator. Simultaneously, to slow the compression of the capsule near the poles, the beams closest to the poles were given larger defocus distances. Between these two models, the use of different beam pointings and defocuses reduced the rms from 2.59% to 1.00% in the vertical direction.

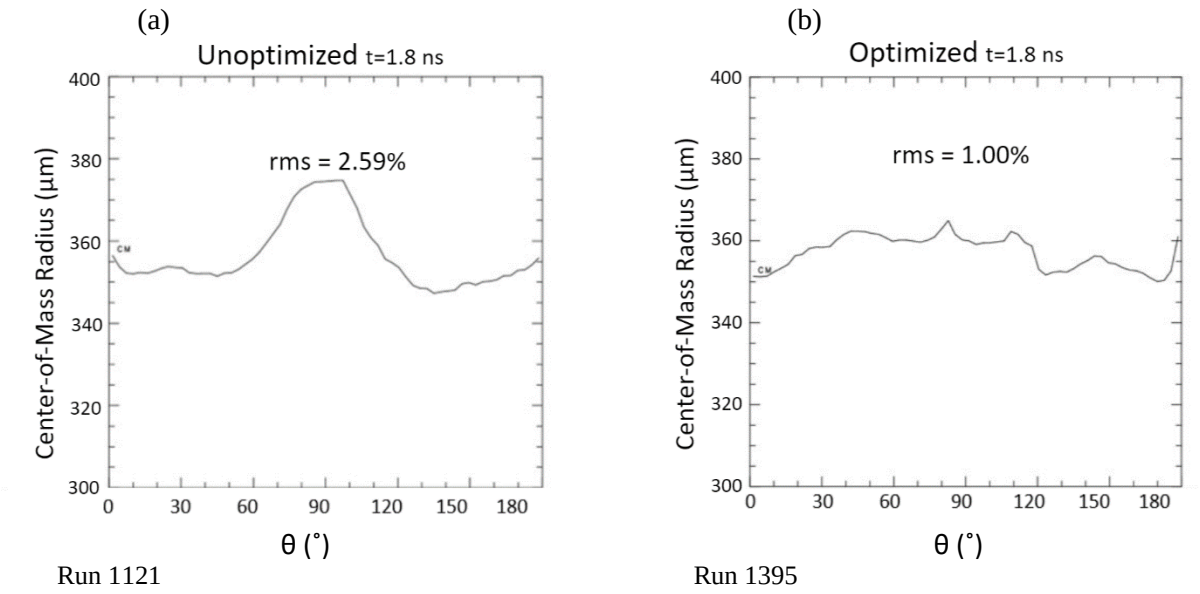

Figure 9. Graphs of center-of-mass radius with respect to the angle θ from the z axis for an initial design (a) and a final design (b) .

The extent of azimuthal nonuniformity is more clearly illustrated by 3-D center-of-mass profiles like Figure 10, which display the distribution of compression on the three dimensional surface of the capsule projected onto a two dimensional profile.[4] SAGE calculates both the azimuthally averaged center-of-mass radius [Fig. 9] and the rays' three dimensional distribution

of energy onto the target surface. At each θ, SAGE adjusts the center-of-mass radius in the φ direction to be consistent with the variations in φ of energy deposition onto the capsule. In Figure 10, which is an initial attempt at optimization, areas in red have compressed further than areas in blue. The quads being used to irradiate the capsule, shown here in green, correspond to the quads marked in red in Figure 4. Each black dot represents the aim point of a laser beam. However, even with the dispersal of aim points, a laser beam still deposits much of its energy near its point of origin. The use of only 12 quads for each capsule, therefore, distributed the laser energy in such a way that large areas of the capsule were left with less compression. Simply spacing the equatorial aim points evenly did not lead to even compression. The 3-D rms of Figure 10, which was calculated similarly to the rms of Figure 9, except averaged over the whole sphere, was determined to be 5.07%.

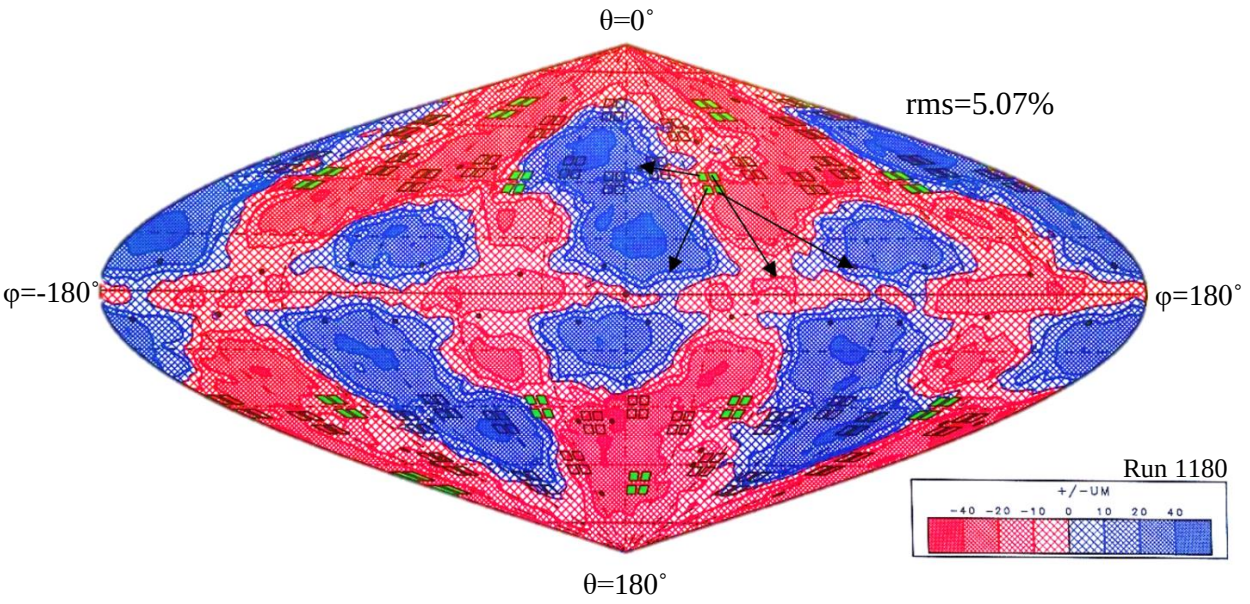

Figure 10. 3-D center-of-mass profile (contours corresponding to the deviation of the center of mass from the average in μm) of a 1600 μm diameter glass capsule at 1.8 ns. Areas in red have compressed further than areas in blue. The quads being used for this capsule, marked in green, correspond with the areas of greatest compression. Black dots represent aim points.

To compensate for the large swathes of red shown above, each beam in a 50˚ quad was pointed further outward from its point of origin, bridging the gaps in between active quads. As the beams were moved further to either side, a different pattern emerged, indicating a more uniform capsule implosion with an rms of 2.82% [Figure 11]. The equatorial aim points have moved further outwards; they are no longer evenly spaced, as they were in Figure 10. The areas of greatest compression have thus shifted and diminished, with the areas in red changing from thick vertical patches to narrower, slanted regions. As Figures 10 and 11 are on the same scale, it can also be seen that the dark red and blue patches are not as dark, nor as large, in Figure 11 indicating that there is less variation in compression than in Figure 10.

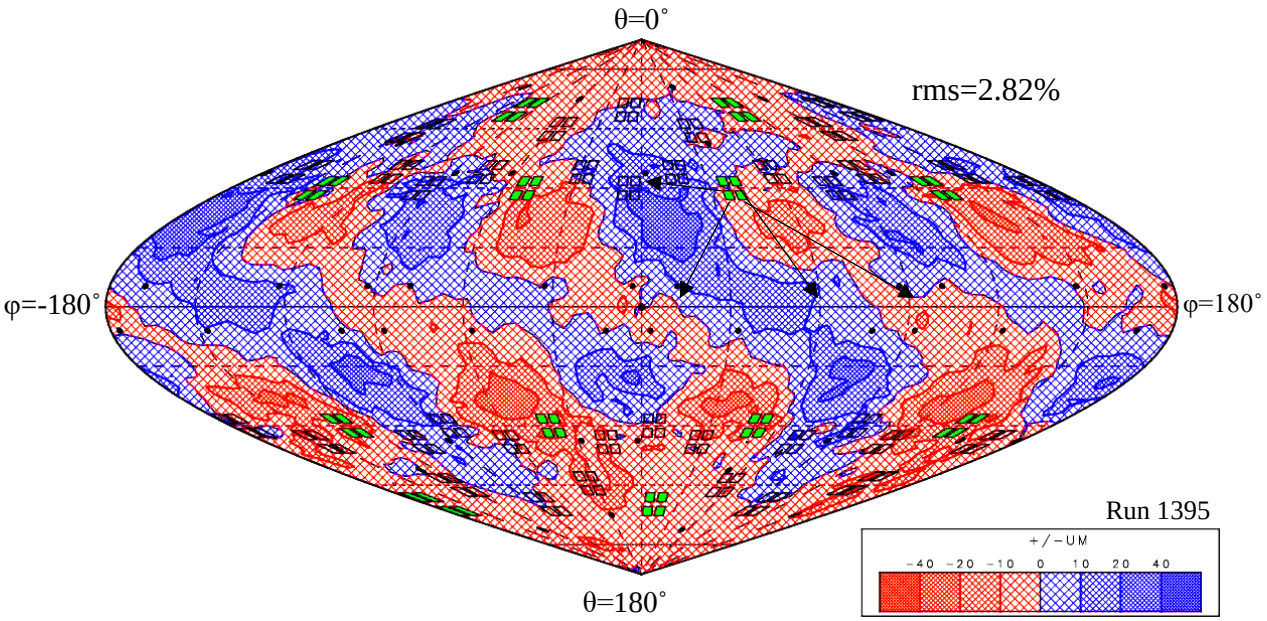

Figure 11. 3-D center-of-mass profile of a 1600 µm diameter glass capsule with adjusted beams at 1.8 ns.

5. Set of Optimized Designs

The approach from this model was then applied to the other cases listed in Table 1. In order to run the experiment, two compatible designs—that is, one 44.5˚ and one 50˚ capsule—

need to have acceptable nonuniformities. The most successful designs for the two 1600 µm glass capsules are shown in Table 2 and Figure 12. Figure 12 is a pictorial representation of the aim points specified for the 50˚ capsule detailed in Table 2. θ_0 refers to the angle of origin of the quad, while θ_1 is the angle to which the beam has been pointed. For the 50˚ capsule, any beam pointed towards the poles was given a defocus of 1.4 cm, while those pointed towards the equator were given a defocus of 1 cm. This prevented the poles of the capsule from being overdriven and compressing faster than the equator. The beams that were pointed towards the equator were actually pointed either 7˚ or 8˚ above or below it (no beams were pointed over the equator, as this would have greatly increased transmitted energy), instead of directly at the equator, to prevent the equator from compressing in a localized band.

Table 2. Optimized beam pointings and defocuses for two capsules. These are all the specifications needed to set up the laser. Both capsules are 1600 µm diameter glass. Each beam is labeled as follows: ring number-top(A)/bottom(B)-left(L)/right(R). Each quad in a ring followed the same specifications.

	50˚ capsule			Run 1395		44.5˚ capsule			Run 1308
beam	θ_0 (˚)	θ_1 (˚)	Δφ (˚)	defocus (cm)	beam	θ_0 (˚)	θ_1 (˚)	Δφ (˚)	defocus (cm)
1A-L	23.5	16	-35	1.4	1A-L	23.5	45	-32	2.3
1A-R	23.5	20	35	1.4	1A-R	23.5	20	32	2.3
1B-L	23.5	35	-35	1.4	1B-L	23.5	40	-32	2.3
1B-R	23.5	45	35	1.4	1B-R	23.5	45	32	1.2
4A-L	50	45	-35	1.4	3A-L	44.5	45	-32	1.2
4A-R	50	83	15	1	3A-R	44.5	90	12	1.2
4B-L	50	83	-25	1	3B-L	44.5	90	-22	1.2
4B-R	50	83	45	1	3B-R	44.5	90	42	1.2
5A-L	130	98	-45	1	6A-L	135.5	90	-42	1.2
5A-R	130	98	25	1	6A-R	135.5	90	22	1.2
5B-L	130	98	-15	1	6B-L	135.5	90	-12	1.2
5B-R	130	135	35	1.4	6B-R	135.5	135	32	1.2
8A-L	156.5	135	-35	1.4	8A-L	156.5	135	-32	1.2
8A-R	156.5	145	35	1.4	8A-R	156.5	140	32	2.3
8B-L	156.5	160	-35	1.4	8B-L	156.5	160	-32	2.3
8B-R	156.5	165	35	1.4	8B-R	156.5	135	32	2.3

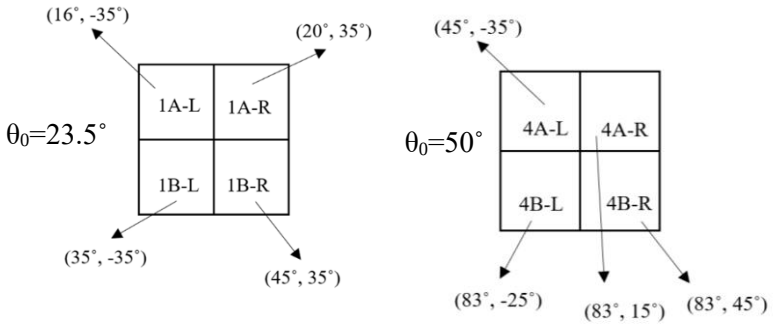

Figure 12. Diagram of pointings of individual beams in two quads for the 50˚ capsule of Table 2.

In the 44.5˚ case, to compensate for their increased distance from the equator, beams were pointed directly at the equator, as opposed to just above or below it. Beams were also given larger defocus distances, so that they would distribute less of their energy in concentrated areas. The three beams closest to the poles for the 44.5˚ capsule have a defocus of 2.3 cm, while all others have a defocus of 1.2 cm. This resulted in the 3-D center-of-mass profile seen in Figure 13.

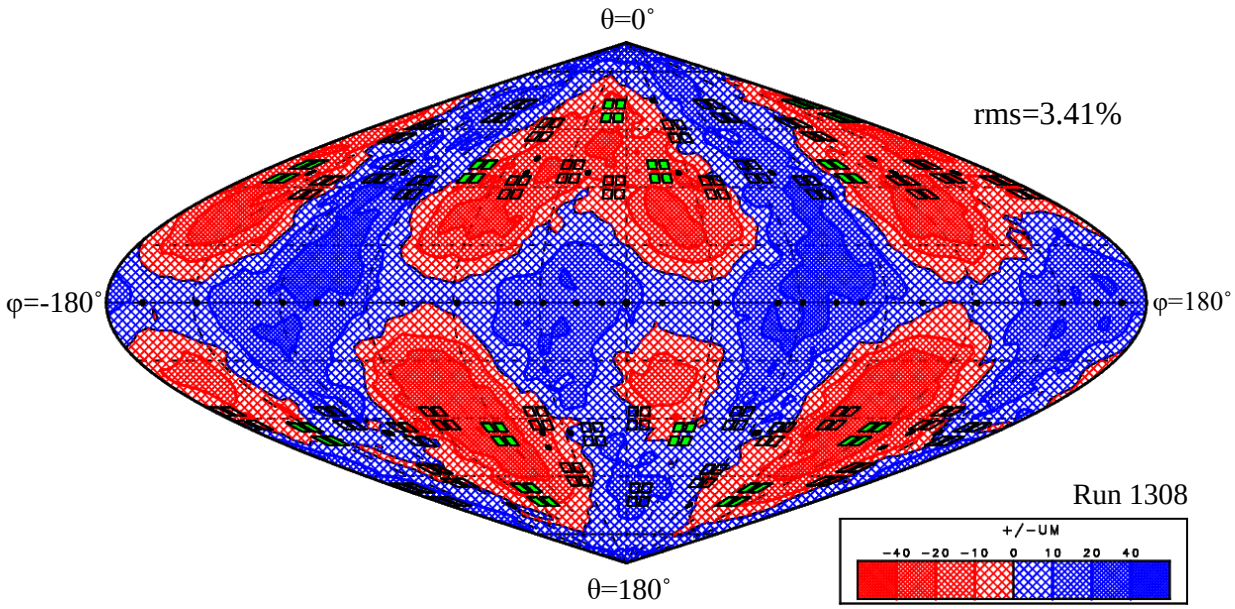

Figure 13. 3-D center-of-mass profile of a 1600 µm diameter glass capsule irradiated with 44.5˚ quads at 1.8 ns.

While Figure 13 does not seem as uniform as Figure 11 visually, the differences in their rms deviations are small, with Figure 11 having an rms of 2.82% and Figure 13 having an rms of

3.41%. In the case of the 44.5˚ capsule, the over compressed regions did not cross the equator as they did in the 50˚ case, due to the increased distance of the 44.5˚ quads from the equator. These over compressed regions also tended to be more concentrated, as the 44.5˚ and 23.5˚ quads are closer to one another than the 23.5˚ and 50˚ quads. The areas of over compression therefore correspond with the areas where the greatest number of quads are in closest proximity to one another.

The rms for all cases is shown in Figure 14. Although the use of 44.5˚ quads did not achieve quite as uniform implosions as the use of 50˚ quads, with an average 0.35% rms difference between corresponding capsules, all capsule nonuniformities achieved rms deviations as low as 3-4%.

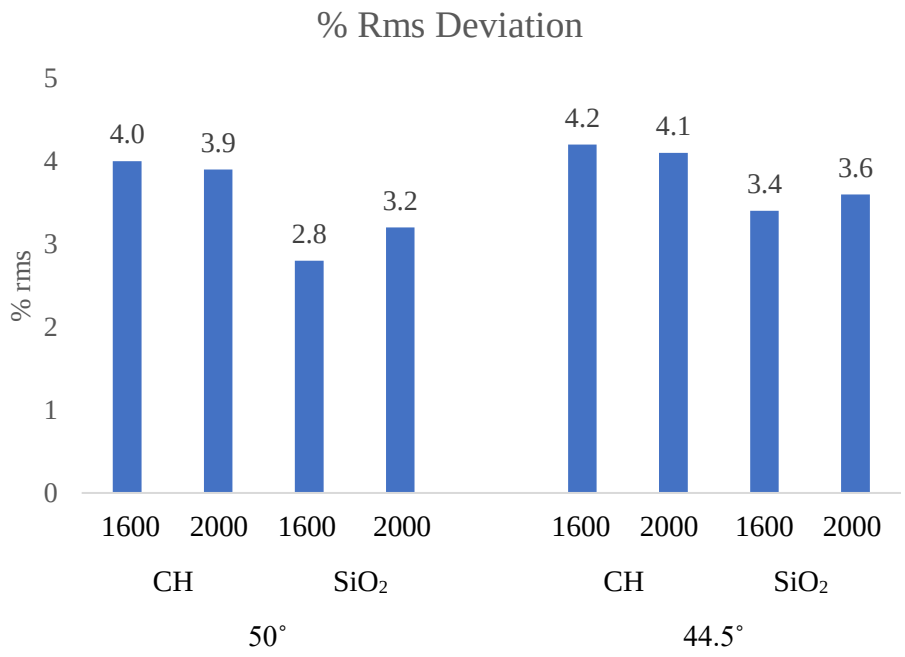

Runs 1455, 1490, 1395, 1437, 1367, 1354, 1308, 1303

Figure 14. Bar graph comparing nonuniformities at 1.8 ns of eight models, categorized by size (in µm), composition, and beam configuration.

The absorbed energies, shown in Figure 15, result from the size, composition, and beam selection of each capsule. 50˚ capsules, for example, have higher absorbed energies than 44.5˚ capsules, because the beams pointed towards the equator do not have to travel as far from their point of origin. Plastic capsules tend to absorb energy less efficiently than glass capsules, as absorption increases with atomic number, which is larger for Si and O than for C and H. Capsules of larger diameter absorb more energy than smaller ones, because laser rays travel a greater distance through the plasma around the capsule. The differences in implosion time between a 44.5˚ and 50˚ capsule [Table 1] are due to the differences in absorbed energy; a target that absorbs more energy implodes sooner than one that absorbs less.

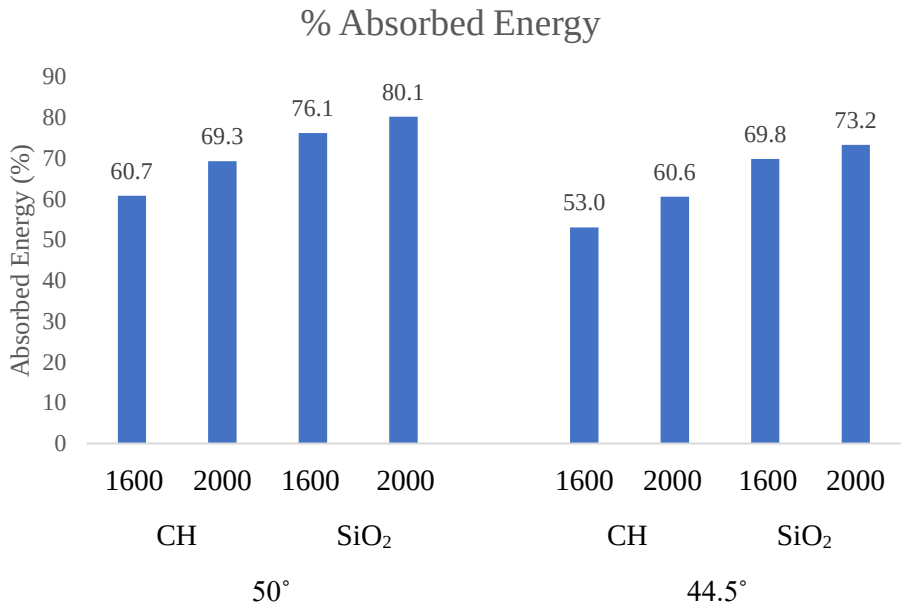

Runs 1455, 1490, 1395, 1437, 1367, 1354, 1308, 1303

Figure 15. Graph of absorbed energies of capsules of different size, composition, and beam selection.

6. Conclusion

The irradiation designs for various capsules were optimized in order to be used for the generation of neutrons in a combined x ray/neutron environment. Due to the number of targets—

one hohlraum and two spherical capsules—each capsule could only utilize 12 of the NIF's 48 quads. The capsules were composed of either glass or plastic, with 1600 μm or 2000 μm diameters. Working with a pre-determined laser pulse shape, the thicknesses of the shells of these capsules were adjusted so that they would implode towards the end of the laser pulse, making use of as much available laser energy as possible. For each capsule, beam pointings and defocuses were varied to determine designs with maximum implosion uniformity. Using hydrodynamic simulations that included 3-D ray tracing, 1-D center-of-mass radius and 3-D center-of-mass profiles were generated to determine optimum uniformity in the vertical and azimuthal directions. Using these designs, it will be possible to irradiate x ray/neutron combined environment targets using only 12 of the NIF's 48 quads for each spherical capsule, with each capsule imploding with an rms nonuniformity of around 3-4%.

7. Acknowledgements

I would like to thank Dr. Craxton; his feedback and patience as my advisor made this internship an amazing learning opportunity. I would also like to thank Ms. Johnston for all of her support, both for my love of the sciences and in pursuing this program. Lastly, I owe a debt of gratitude to everyone in the LLE community; their support of the high school summer internship program contributes to a truly unique resource.

8. References

1. A. M. Cok, “Development of Polar Direct Drive Designs for Initial NIF Targets,” Laboratory for Laser Energetics High School Summer Research Program (2006).

2. S. Skupsky, J. A. Marozas, R. S. Craxton, R. Betti, T. J. B. Collins, J. A. Delettrez, V. N. Goncharov, P. W. McKenty, P. B. Radha, T. R. Boehly, J. P. Knauer, F. J. Marshall, D. R. Harding, J. D. Kilkenny, D. D. Meyerhofer, T. C. Sangster, and R. L. McCrory, “Polar Direct Drive on the National Ignition Facility,” Phys. Plasmas 11, 2763 (2004).

3. R. S. Craxton, F. J. Marshall, M. J. Bonino, R. Epstein, P. W. McKenty, S. Skupsky, J. A. Delettrez, I. V. Igumenshchev, D. W. Jacobs-Perkins, J. P. Knauer, J. A. Marozas, P. B. Radha, and W. Seka, “Polar Direct Drive: Proof-of-Principle Experiments on OMEGA and Prospects for Ignition on the National Ignition Facility,” Phys. Plasmas 12, 056304 (2005).

4. L. A. Tucker, “A Design for a Shock Ignition Experiment on the NIF Including 3-D Effects,” Laboratory for Laser Energetics High School Summer Research Program (2011).

5. Dr. Charles Yeamans, Lawrence Livermore National Laboratory, private communication.